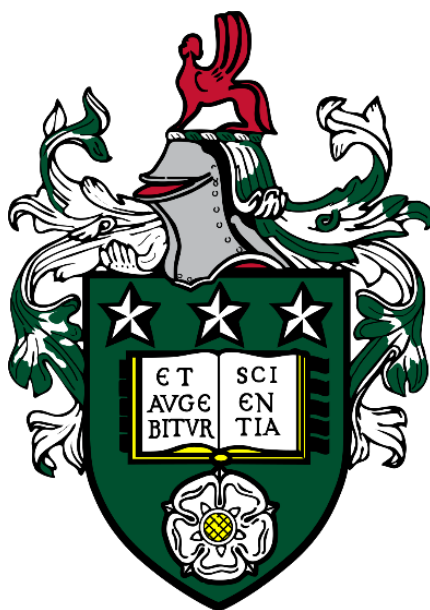


**Polyelectrolyte Complex Templated Synthesis of Silica
Nanoparticles with Intrinsic Functionality for Biomedical
Application**

George Newham

**Submitted in accordance with the requirements for the degree of
Doctor of Philosophy**



**University of Leeds
School of Physics and Astronomy
June 2022**

Declaration

The candidate confirms that the work submitted is his own, except where work has formed part of jointly authored publications and has been included. The contribution of the candidate and the other authors of this work have been explicitly indicated below. The candidate confirms that appropriate credit has been given within the thesis where reference has been made to the work of others.

The work discussed in chapters 3 & 4 of this thesis has appeared in publication as follows:

G. Newham *et al.* Polyelectrolyte complex templated synthesis of monodisperse, sub-100 nm porous silica nanoparticles for cancer targeted and stimuli-responsive drug delivery *J. Colloid Interface Sci.* 584 (2021) 669–683

GN was responsible for experimental data collection and analysis.

The work discussed in chapters 5 & 6 of this thesis has appeared in publication as follows:

G Newham *et al.* Mechanically Tuneable Physical Nanocomposite Hydrogels from Polyelectrolyte Complex Templated Silica Nanoparticles for Anionic Therapeutic Delivery *J. Colloid Interface Sci.* 617 (2022) 224–235.

GN was responsible for experimental data collection and analysis

This copy has been supplied on the understanding that it is copyright material and that no quotation from this thesis may be published without proper acknowledgement. The right of George Newham to be identified as author of this work has been asserted by him in accordance with the Copyright, Designs and Patents Act 1988.

Acknowledgements

First and foremost I wish to thank my supervisors Dr. Zhan Yui Ong and Prof. Stephen Evans for providing the opportunity of this PhD project, and for their continued support and guidance. Without them, none of this would have been possible.

I would also like to acknowledge the efforts and work of each of the other researchers who have contributed to this thesis, particularly Dr. Ryan K. Mathew and Dr. Heiko Wurdak for their contributions to Chapters 3 and 4 of this work.

Finally my deepest thanks are extended to the Molecular and Nanoscale Physics Research Group at the University of Leeds. I could not wish for a better group of colleagues, friends, and mentors. The support and care I have received extends far beyond research and academia, and has made a profound difference to my time at the university. For that, I am extremely grateful.

Abstract

Coacervation, the liquid-liquid phase separation of a solution of charged macromolecules into macromolecule rich and depleted phases, can give both nano- and macro- scale polyelectrolyte complexes (PECs) that are desirable for biomedical application. The ease of formation under mild conditions makes the PECs ideal candidates for the encapsulation of therapeutic molecules, while the range of macromolecules which may be incorporated allows the introduction of biomedically beneficial properties for example cancer targeting or stimuli responsive drug release. However, their sensitivity to environmental changes in pH, ionic strength, and temperature can lead to poor stability which can limit their potential application. Silica nanoparticles (SiNPs), on the other hand, demonstrate good stability under these environmental changes, but typically do not exhibit biomedically desirable surface functionalities without extensive multi-stage synthetic protocols. This thesis aims to use PECs as multifunctional scaffolds for SiNP synthesis, hence combining the ease of PEC formation and intrinsic macromolecule functionality to enhance anticancer drug delivery.

This is first demonstrated with the formation of arginine (Arg)/poly(acrylic acid) (PAA) PECs which serve as templates for the synthesis of highly monodispersed sub-100 nm porous SiNPs with intrinsic Arg and PAA surface functionality (Arg/PAA-PSiNPs). The retention of PAA enabled a high doxorubicin hydrochloride (Dox) loading capacity and a 4-fold increase in drug release under weakly acidic pH compared to physiological pH. The surface presentation of Arg conferred significantly higher intracellular accumulation of Arg/PAA-PSiNPs in patient-derived glioblastoma cells compared to non-tumorigenic neural progenitor cells, which effectively translated to lower IC_{50} values with Dox-loaded Arg/PAA-PSiNPs than non-functionalised PSiNPs. The synthesis pathway was also extended to the synthesis of poly(ethyleneimine) functionalised SiNPs (PEI-SiNPs) formed from soft PEC templates of PEI and glutamic acid. Through their polycationic surface functionality, the PEI-SiNPs acted as multifunctional electrostatic crosslinkers with hyaluronic acid to form nanocomposite coacervate hydrogels with tunable mechanical stiffness. The reversible electrostatic interactions within the hydrogel networks enabled self-healing and thixotropic properties, and the excess positive charge present within the PEI-SiNPs facilitated high loading and retarded the release of the anionic anti-cancer drug methotrexate. These systems show great potential for further evaluation in *in vivo* animal models, and bring forward new insights for the development of SiNPs with built-in functionalities for biomedical applications.

Table of Contents

1	Introduction	21
1.1	Overview and Thesis Outline	21
1.2	Polyelectrolytes.....	22
1.3	Coacervation and Polyelectrolyte Complexes.....	24
1.3.1	Theoretical Considerations	25
1.3.2	Simple Coacervation.....	27
1.3.3	Complex Coacervation.....	32
1.4	PEC Templated Silica Nanoparticle Synthesis.....	40
1.4.1	Stober method.....	41
1.4.2	PEC templated SiNPs.....	42
1.5	Table of Definitions.....	47
1.6	Chapter Overview	48
2	Materials and Methods.....	50
2.1	Materials	50
2.1.1	Arginine/Poly(acrylic acid) Polyelectrolyte Complex Templated Silica Nanoparticle Synthesis and Application	50
2.1.2	Poly(ethyleneimine)/Glutamic Acid Polyelectrolyte Complex Templated Silica Nanoparticle Synthesis and Poly(ethyleneimine)-Silica Nanoparticle/Hyaluronic Acid Hydrogel Formation.....	51
2.2	Arg/PAA Polyelectrolyte Complex Templated Silica Nanoparticle Synthesis.....	51
2.2.1	Preparation of Arginine/Poly(acrylic acid) Polyelectrolyte Templates	51
2.2.2	Synthesis of Arg/PAA and NH ₄ OH/PAA Porous Silica Nanoparticles.....	52
2.3	Quantification of Doxorubicin Loading and Release from Arg/PAA-PSiNPs and NH ₄ OH/PAA-PSiNPs	52
2.4	Live Cell Experiments	54
2.4.1	Preparation of Culture Flasks and Well Plates.....	54
2.4.2	Cell Culture	55
2.4.3	Cytotoxicity Studies	55
2.4.4	Cellular Uptake Studies	56
2.4.5	Statistical Analysis.....	57
2.5	PEI/Glu Polyelectrolyte Complex Templated Silica Nanoparticle Synthesis.....	57
2.5.1	Preparation of PEI/Glu Polyelectrolyte Templates	57
2.5.2	Synthesis of PEI-SiNPs.....	58
2.6	PEI-SiNP/HA and PEI/HA Nanocomposite Hydrogel Formation	58

2.6.1	Quantification of SiNP surface-bound PEI Concentration.....	58
2.6.2	PEI-SiNP/HA Hydrogel Formation.....	59
2.6.3	Quantification of Residual PEI in the Supernatant after PEI-SiNP/HA Hydrogel Formation.....	60
2.6.4	Quantification of Residual HA in the Supernatant After PEI-SiNP/HA Hydrogel Formation.....	60
2.7	Nanoparticle Characterisation	62
2.7.1	Dynamic Light Scattering	62
2.7.2	Zeta Potential.....	65
2.7.3	Transmission Electron Microscopy	67
2.7.4	UV-Vis-NIR Spectroscopy.....	70
2.7.5	Fluorescence Spectroscopy.....	71
2.7.6	Thermogravimetric Analysis.....	71
2.7.7	Fourier-Transform Infrared Spectroscopy.....	71
2.7.8	Gas Adsorption Porosimetry	72
2.8	PEI-SiNP/HA and PEI/HA Hydrogel Characterisation	74
2.8.1	Quantification of the PEI-SiNP/HA Hydrogel Swelling Ratio	74
2.8.2	Haemolysis Testing of PEI-SiNP/HA Hydrogel.....	74
2.8.3	Rheological Characterisation of PEI-SiNP/HA Hydrogels.....	75
2.8.4	Macroscopic Self Healing Test of PEI-SiNP/HA Hydrogels.....	76
2.9	Drug Loading and Release of Methotrexate from PEI-SiNP/HA Hydrogels.....	77
3	Synthesis and Characterisation of Arginine/Polyacrylic Acid Polyelectrolyte Complex Templated Porous Silica Nanoparticles.....	79
3.1	Motivation	79
3.2	Effect of Isopropanol/Water Volume Ratio on the Formation and Size of Arg/PAA Polyelectrolyte Droplets	82
3.3	Effect of Varying Arg, NH ₄ OH, and PAA on the Size and Dispersity of Arg/PAA and NH ₄ OH/PAA Templates.....	87
3.4	PAA/Arg PEC Template Directed Porous Silica Nanoparticle Synthesis.....	91
3.5	The Scalability of Arg/PAA-PSiNP and NH ₄ OH/PAA-PSiNP Syntheses.....	97
3.6	Chemical Characterisation of Arg/PAA-PSiNPs and NH ₄ OH/PAA-PSiNPs	100
3.7	Porosity Measurements of Arg/PAA-PSiNPs and NH ₄ OH/PAA-PSiNPs	103
3.8	Synthesis of FITC-Labelled Arg/PAA and NH ₄ OH/PAA Templated PSiNPs	105
3.9	Conclusion	107

4 Application of Arginine/Polyacrylic Acid PEC Templated SiNPs for Cancer Targeted and pH-Responsive Drug Delivery	108
4.1 Motivation	108
4.2 Drug Loading and Release of Doxorubicin Hydrochloride From PAA/Arg PSiNPs 109	109
4.3 <i>In vitro</i> Cytotoxicity Testing and Selective Uptake of Arg/PAA-PSiNPs in Primary Human Glioblastoma Cells.....	115
4.4 The Effect of Arg/PAA-PSiNP Overgrowth on Cellular Uptake	119
4.5 Enhanced Anticancer Efficacy in Patient-Derived Glioblastoma Cells.....	122
4.6 Conclusion	124
5 Synthesis and Characterisation of Poly(ethyleneimine)/Glutamic Acid Polyelectrolyte Complex Templated Porous Silica Nanoparticles	125
5.1 Motivation	125
5.2 Formation and Size Control of PEI/Glu PEC Templates	126
5.2.1 The Effect of Alcohol Co-Solvent Choice on Alcohol-Induced PEC Formation.....	127
5.2.2 The Effect of PEI Molecular Weight on the Alcohol-Induced Coacervation of PEI/Glu 130	130
5.2.3 The Effect of Varying PEI and Glu concentrations on the PEI/Glu PEC Templates	133
5.3 PEC Templated Synthesis of PEI-Functionalised SiNPs.....	136
5.4 Conclusions	140
6 Application of PEI-SiNPs as Multifunctional Crosslinkers in Physical Nanocomposite Hydrogels.....	141
6.1 Motivation	141
6.2 PEI-SiNP/HA Hydrogel Formation	144
6.3 The Effect of PEI-SiNP Incorporation on Hydrogel Morphology	150
6.4 Rheological Characterisation of PEI-SiNP/HA and PEI/HA Hydrogels	152
6.5 The Equilibrium Swelling Ratio of PEI-SiNP/HA and PEI/HA Hydrogels.....	155
6.6 Shear Thinning and Self-Healing Properties of PEI-SiNP/HA Hydrogels.....	157
6.7 Hemolytic Activity of PEI-SiNP/HA and PEI/HA Hydrogels	159
6.8 Methotrexate Drug Loading and Release.....	161
6.9 Conclusion	165
7 Conclusions and Future Work.....	166
7.1 Conclusions	166
7.2 Future Work	169

7.2.1	Additional Assessment of Selective Arg/PAA-PSiNP Uptake into Malignant Tissues	169
7.2.2	Cellular Toxicity and Anti-Tumour Efficacy of PEI-SiNP/HA Hydrogels.....	170
7.2.3	Assessment of the PEC Internal Structure, and its Influence on the SiNP Properties	170

List of Figures

- Figure 1.1 (A) The mixing, (B) formation of metastable phase droplets, and (C) coalescence of phase droplets into a bulk coacervate phase for oppositely charge polymers. Reproduced with permission from Elsevier.¹⁴24
- Figure 1.2. The three possible types of liquid-liquid phase separation (LLPS): Segregative phase separation, in which two species separate into distinct single-macromolecule phases; associative phase separation (complex coacervation) where two species form a macromolecule-rich coacervate phase in a dilute solvent; and simple coacervation, where a single macromolecule phase separates to form a concentrated coacervate phase in a dilute solvent. Adapted and reproduced with permission from the Royal Society of Chemistry.⁵²27
- Figure 1.3 (A) A schematic representation of complex coacervation. (B) A typical phase diagram showing the salt concentration against polymer concentration with an exemplary photograph of a complex coacervate from poly(4-styrenesulfonic acid) and poly(diallyldimethylammonium chloride). Reproduced with permission from the Royal Society of Chemistry.³⁰32
- Figure 1.4 The coacervate forming molar fractions, as indicated by high turbidity, for mixtures of PAA and pAH at pH 6.5 and 8.5, and with and without salt. Reproduced with permission under a CC-BY licence.⁶⁶34
- Figure 1.5 A schematic showing the progression from solid precipitate to coacervate, and then dissolved polymer solution on the addition of salt to mixtures of (PSS) and (PDADMA). Reproduced with permission under a CC-BY licence.³⁴35
- Figure 1.6 Optical microraphs of PVBTMA/PSS mixtures prepared with ethanol:water volume ratios between 0:10 and 7:3, and salt concentrations between 0 and 4 M. The red line indicates the salt and alcohol concentrations above which coacervates are formed, and the blue line indicates their transition to liquid. Reproduced with permission un a CC-BY licence⁷⁹38
- Figure 1.7 A phase diagram for mixtures of PAA sodium salt with (degree of polymerisation between 25 and 695) and 0.5 wt % PAH as a function of PAA and NaCl salt

concentration. Open and filled symbols represent concentrations at which either a coacervate or precipitate were observed respectively. Reproduced with permission from Ref 68. Copyright 2013 American Chemical Society ⁶⁸	40
Figure 1.8 A schematic representation of a PEC templated hollow SiNP synthesis showing (A) the mixing of PAA and either a monovalent or divalent cation before (B) the addition of ethanol for the formation of the PEC templates. (C) On the addition of tetraethoxysilane (TEOS) silica condensation occurs at the template surface, and (D) the template is removed to yield hollow SiNPs. Reproduced and adapted with permission from Elsevier. ⁹⁹	45
Figure 2.1 A calibration plot of Dox in ultrapure water obtained using UV-vis-NIR spectroscopy at 480 nm used to determine the amounts of Dox loaded and released from Arg/PAA-PSiNPs and NH ₄ OH/PAA-PSiNPs.....	53
Figure 2.2 A calibration plot of obtained from the absorbance of CBBG dye at 595 nm with increasing concentration of PEI.	59
Figure 2.3 Control measurements of HA with the CBBG assay and PEI-SiNPs without the CBBG dye showing their negligible contribution to the measured PEI concentration. A typical PEI concentration measurement from the hydrogel supernatant is included for comparison.	60
Figure 2.4 The calibration plot obtained from the CTAB turbidimetric assay used to determine the hyaluronic acid concentration remaining in the supernatant after PEI-SiNP/HA hydrogel formation.....	61
Figure 2.5 Control measurements of PEI and PEI-SiNPs in the HA concentration quantification assay with an exemplary PEI/HA hydrogel measurement to compare.....	62
Figure 2.6 Example correlation data from DLS measurements. (A) A ‘poor’ correlation curve characterised by several exponential decay functions indicative of a polydisperse sample. (B) A ‘good’ correlation function with a y-intercept close to 1, and a smooth, single exponential decay profile.	64
Figure 2.7 The stern layer and slipping plane created by ions bound to a charged particle in a polar solvent, and their relation to the zeta potential. Reproduced with permission under a CC BY-SA licence. ¹¹⁰	66

Figure 2.8 Example size analysis as completed for particles presented in Chapter 3, showing the particle diameter measured with imageJ analysis software.....	69
Figure 2.9 TEM size analysis of asymmetric SiNPs. (A) A typical TEM image of SiNPs (presented in Chapter 5), (B) the image after binary conversion using imageJ software, (C) ellipses drawn around each particle used for size calculation.	69
Figure 2.10 A TEM image (A) and corresponding size histograms without (B) and with (C) a size exclusion parameter to omit drying effects and overlapping particles from automated size analysis.....	70
Figure 2.11 An optical absorbance calibration plot collected for MTX at 303 nm for use in quantifying the MTX loading efficiency and release rates with PEI-SiNP/HA hydrogels.	77
Figure 3.1 A schematic showing the polyelectrolyte templated synthesis of Arg/PAA-PSiNPs. (A) PAA and Arg are initially dissolved in water, and (B) upon addition of 2-propanol (IPA), the electrostatically associated PAA and Arg assemble into aqueous PECs in bulk IPA. (C) The PECs act as a template for the hydrolysis and condensation of the silica precursor triethoxysilane (TEOS) to form hybrid Arg/PAA-PSiNPs with intrinsic PAA and amino acid surface functionality.	82
Figure 3.2 DLS correlation function curves for (A) Arg/PAA, (B) NH ₄ OH/PAA, and (C) PAA complexes formed at different IPA volume fractions.	83
Figure 3.3 A summary of data presented in Figure 3.2. Changes in the dynamic light scattering measured correlation function y-intercepts of Arg/PAA, NH ₄ OH/PAA, and PAA as a function of IPA volume and dielectric constants ¹³⁷	84
Figure 3.4 Intensity weighted size distributions of stable (A) Arg/PAA, (B) NH ₄ OH/PAA, and (C) PAA droplets formed at the critical range of IPA/water volume fractions corresponding to the coloured boxes shown in Figure 3.3.....	86
Figure 3.5 Changes in the dynamic light scattering measured hydrodynamic diameters and polydispersity index of Arg/PAA PECs formed by varying Arg with PAA fixed at 111 μM.....	88

Figure 3.6 Changes in the dynamic light scattering measured hydrodynamic diameters and polydispersity index of NH ₄ OH/PAA PECs formed by varying NH ₄ OH with PAA fixed at 111 μM.	89
Figure 3.7 Changes in the dynamic light scattering measured hydrodynamic diameters and polydispersity index of PECs formed by varying PAA with Arg fixed at 25.4 mM.	90
Figure 3.8 TEM images and corresponding size histograms for Arg/PAA-PSiNPs synthesised with (A) 7.7 mM, (B) 15.5 mM, (C) 25.4 mM, and (D) 30.8 mM Arg. The average diameters are 26 ± 3 nm (ignoring the presence small particles arising from unreacted reagents post-synthesis), 36 ± 3 nm, 42 ± 4.0, and 50 ± 5 nm respectively (n = 200 for all).....	92
Figure 3.9 (A) Intensity weighted DLS size distributions of the Arg/PAA-PSiNPs displayed in (C-F) with Z-average diameters of 61 ± 1 nm, 97 ± 3 nm, 152 ± 2 nm, and 256 ± 4 nm synthesised with 20, 40, 200, and 500 μL TEOS respectively. (B) The polydispersity index and zeta-potentials at pH 7.4 of the Arg/PAA-PSiNPs expressed shown in (A) as a function of the ratio of the particle and the polyelectrolyte template diameter showing the effect of the under- and over-growth regimes. TEM images and diameter histograms for Arg/PAA-PSiNPs synthesised by adding (C) 20, (D) 40, (E) 200, and (F) 500 μL of TEOS to 70 nm (by DLS) polyelectrolyte colloidal templates. The average diameters determined from the TEM images are (C) 42 ± 4 nm, (D) 66 ± 5 nm, (E) 100 ± 9 nm, and (F) 178 ± 28 nm, respectively (n = 200).	93
Figure 3.10 A schematic depiction of the three possible undergrowth and overgrowth regimes and their impact on surface functionality.	94
Figure 3.11 Z-average diameters and zeta-potentials of NH ₄ OH/PAA-PSiNPs synthesised with 50 μM PAA and 25.4 μM NH ₄ OH over a range of TEOS volumes.	96
Figure 3.12 Size distributions for Arg/PAA-PSiNPs synthesised in a 25-fold scaled-up synthesis. (A) Representative TEM image, (B) corresponding diameter histogram showing an average diameter of 49 ± 5 nm (n = 248), and (C) DLS size intensity distributions for 3 repeat syntheses with Z-average diameters of 131 ± 1 nm, 134 ± 1 nm, and 128 ± 2 nm (batch 1, 2, and 3). The PDI values from the 3 independent synthesis batches are 0.17, 0.10, and 0.13, respectively.....	98

Figure 3.13 (A) TEM image and (B) the corresponding size distribution histogram for NH₄OH/PAA-PSiNPs produced in a 250 mL scaled-up synthesis. The average diameter of the NH₄OH/PAA-PSiNPs is 55 ± 9 nm (n = 260). (B) The intensity size distribution determined using dynamic light scattering for 3 repeat syntheses with Z-average diameters of 132 ± 1 nm, 151 ± 1 nm, and 73 ± 2 nm for batch 1, 2, and 3, respectively. The PDI values from the 3 independent synthesis batches are 0.09, 0.25, and 0.12, respectively.....99

Figure 3.14 Chemical characterisation of Arg/PAA-PSiNPs and NH₄OH/PAA-PSiNPs. (A) Stacked ATR-FTIR spectra showing the fingerprint regions for PAA, Arg, Arg/PAA-PSiNP, and NH₄OH/PAA-PSiNP. TGA curves and the 1st derivatives of the weight loss curves for (B) Arg, (C) PAA, (D) Arg/PAA-PSiNPs and (E) NH₄OH/PAA-PSiNPs, where coloured peaks indicate the presence of a common organic compound between samples.....102

Figure 3.15 (A) N₂ gas adsorption/desorption isotherms collected at 77K for Arg/PAA-PSiNPs and NH₄OH/PAA-PSiNPs and (B) the corresponding pore size distributions determined using non-local density function theory analysis.104

Figure 3.16 (A) A typical UV-Vis absorbance trace and (B) fluorescence emission spectra for FITC-Arg/PAA-PSiNPs and FITC-NH₄OH/PAA-PSiNPs excited at 490 nm.105

Figure 3.17 TEM images and corresponding size histograms for FITC-Arg/PAA-PSiNPs synthesised using (A) 75 µL, (B) 400 µL, and (C) 1 mL of TEOS with 0.1 molar % of FITC-PEG-Silane. The average diameters are 23 ± 3 nm, 52 ± 5 nm, and 84 ± 10 nm respectively (n = 200 for all).106

Figure 4.1 Drug loading capacity of Arg/PAA-PSiNPs and NH₄OH/PAA-PSiNPs (1 mg/mL) incubated with 1, 2, and 4 mg/mL Dox for 48 h.110

Figure 4.2 (A) Intensity size distributions of empty and Dox-loaded Arg/PAA-PSiNPs and NH₄OH/PAA-PSiNPs measured by dynamic light scattering. Z-average diameters of empty Arg/PAA-PSiNP and NH₄OH/PAA-PSiNPs were 128.4 ± 2.4 and 132.1 ± 0.1 nm, respectively, while that of Dox-loaded Arg/PAA-PSiNP and NH₄OH/PAA-PSiNPs were 162.4 ± 3.4 and 152.2 ± 0.2 nm, respectively. (B) Zeta-potentials of Dox loaded Arg/PAA-PSiNPs and NH₄OH-PSiNPs measured in PBS (pH 7.4). The zeta-potential

values for Dox-loaded Arg/PAA-PSiNP and NH ₄ OH/PAA-PSiNPs were determined to be -16.0 ± 0.7 and -19.0 ± 0.9 mV, respectively.....	111
Figure 4.3 Cumulative Dox release curves from the Arg/PAA-PSiNPs and NH ₄ OH/PAA-PSiNPs over 48 h in PBS (pH 7.4) and sodium acetate buffer (pH 5.0).....	112
Figure 4.4 (A) A log-log plot of the first 60% of the drug release data where the gradient is the release exponent, <i>n</i> . (B) The Korsmeyer-Peppas fit, where <i>n</i> was found from (A) and used in Eq. 2-2 to determine the kinetic constant, <i>k_m</i>	113
Figure 4.5 Cytotoxicity of Arg/PAA-PSiNPs and NH ₄ OH/PAA-PSiNPs in patient-derived glioblastoma cell lines. Graphs show cellular viability of GBM1 (A), GBM20 (B), and the (C) non-tumourigenic human adult neural progenitor NP1 cells treated with 0-750 µg/mL of Arg/PAA-PSiNPs and NH ₄ OH/PAA-PSiNPs for 24 h.....	115
Figure 4.6 Enhanced targeting and uptake of Arg/PAA-PSiNPs by patient-derived glioblastoma cells. (A) Cellular uptake of FITC-labelled Arg/PAA-PSiNPs and NH ₄ OH/PAA-PSiNPs after treating GBM1, GBM20, and non-tumourigenic neural progenitor NP1 cells with 200 µg/mL of PSiNPs for 4 h. The fluorescence intensities of the internalized particles were normalized for cellular protein content using the bicinchoninic acid assay. Each data point represent mean ± standard deviation from at least two independent experiments performed with six replicates. *** P < 0.001; NS indicates lack of statistical significance (P > 0.05). (B) Confocal images of GBM20 and NP1 cells following treatment with FITC-labelled Arg/PSiNPs and NH ₄ OH/PAA-PSiNPs.....	118
Figure 4.7 (A) The intensity size distribution determined by DLS for Arg/PAA PECs with a Z-average diameter of 72.5 ± 1.3 nm used for the overgrowth synthesis of FITC-labeled Arg/PAA-PSiNPs. (B) Intensity size distributions for FITC-labelled Arg/PAA-PSiNPs and NH ₄ OH/PAA-PSiNPs synthesised in the overgrowth regime for use in nanoparticle uptake studies with z-average sizes of 226 ± 6.4 and 194.3 ± 2.9 nm respectively. (C) The zeta- potential distributions for the FITC-labelled Arg/PAA-PSiNPs and NH ₄ OH/PAA-PSiNPs with average values of -37.2 ± 1.2 and -36.7 ± 1.3 mV, respectively.....	120
Figure 4.8 Cellular uptake of overgrown FITC-labelled Arg/PAA-PSiNPs and NH ₄ OH/PAA-PSiNPs. GBM20 cells were treated with 200 µg/mL of PSiNPs for 4 h and the	

fluorescence intensity of the internalised particles was normalised for cellular protein content.....	121
Figure 4.9 Cell viability of GBM1 cells following 24 h treatment with Dox-loaded Arg/PAA-PSiNPs and NH ₄ OH-PSiNPs as determined using the WST-1 assay and fitted with a dose-response curve (Eq. 2-4). The dotted lines indicate the IC ₅₀ values. The results represent mean ± standard deviation from two independent experiments performed with six replicates.....	123
Figure 5.1 A schematic representation of the PEC templated synthesis of PEI functionalised SiNPs. (A) PEI and Glu are dissolved in water, and (B) on the addition IPA assemble into stable, monodispersed, aqueous PECs in bulk IPA. (C) On the addition of tetraethoxysilane (TEOS), the PECs act as scaffolds for the hydrolysis and condensation of silica. (D,E) The chemical structures of PEI and Glu respectively.	126
Figure 5.2 Dynamic light scattering correlation data for PEI/Glu PECs prepared in mixtures of water and differing alcohol co-solvents. (A) Changes in the dynamic light scattering correlation function y-axis intercept as a function of alcohol volume fraction and (B-D) the respective correlation curves for mixtures IPA, ethanol, and methanol.	128
Figure 5.3 (A) The dielectric constant for binary mixtures of water and alcohol ¹³⁷ . Circular or square points superimposed onto the dielectric constant data presented in panel A to indicate whether or not alcohol-induced coacervation of PEI/Glu was observed for (B) methanol, ethanol, and IPA.....	129
Figure 5.4 (A) Dynamic light scattering data for 2, 10, and 25 kDa PEI in binary water/IPA solvents as a function of IPA volume fraction, and (B – D) the contributing correlation function curves for 2, 10, and 25 kDa PEI respectively. Each data point represents the mean ± standard deviation of 3 repeat measurements.....	131
Figure 5.5 (A) Dynamic light scattering data for mixtures of PEI/Glu with varied PEI molecular weight in binary water/IPA solvents, and (B – D) the contributing correlation function curves for 2, 10, and 25 kDa PEI respectively. Each data point represents the mean ± standard deviation of 3 repeat measurements.....	132
Figure 5.6 Hydrodynamic diameters and PDI values for 25 kDa PEI/Glu PECs formed at 80 % IPA with (A) 64 μM PEI and varied glutamic acid, and (B) 1.09 mM glutamic acid and varied PEI.....	134

Figure 5.7 The Z-average diameter determined by DLS for PEI/Glu PECs prepared at 80 % v/v IPA with 2, 10, or 25 kDa PEI for varied (A) PEI concentration and (B) Glu concentration.	135
Figure 5.8 (A, B) TEM images showing the size and morphology of PEI-SiNPs and (C) their corresponding size histogram with an average diameter of 135 ± 37.7 nm (n = 188)....	136
Figure 5.9 (A) Intensity weighted size distribution collected by dynamic light scattering for PEI-SiNPs of diameter 187 ± 4.2 nm and PDI of 0.07 ± 0.02 and (B) The zeta potential of as-synthesised PEI-SiNPs in PBS (pH 7.4) showing a positive surface charge of 22.1 ± 1.1 mV.....	137
Figure 5.10 (A) Stacked FTIR spectra of glutamic acid, PEI, and PEI-SiNPs. (B) Weight loss curves from TGA analysis for glutamic acid, PEI, and PEI-SiNPs, and (C-E) their corresponding 1st derivatives.....	139
Figure 6.1 A graphical representation of the PEC templated synthesis of core-shell PEI-SiNPs and their subsequent use as multifunctional crosslinking junctions in the formation of coacervate nanocomposite hydrogels. (1) PEI and Glu are initially dispersed in an aqueous solution before (2) the addition of isopropanol (IPA) to form monodispersed nanoscale PECs. (3) On the addition of TEOS, the silanes selectively condense inside the PECs and each one becomes a PEI-functionalised SiNP (PEI-SiNP). (4) The PEI-SiNPs are mixed with HA and MTX to form a drug loaded, physical nanocomposite hydrogel with electrostatic crosslinks.	143
Figure 6.2 The chemical structures of (A) hyaluronic acid and (B) polyethylenimine.	144
Figure 6.3 Photographs of taken during PEI-SiNP/HA hydrogel synthesis showing (A) the white precipitates formed after the initial mixing of PEI-SiNPs and HA, and (B) the coacervate hydrogel formed in a transparent supernatant after reduction of the pH and the resultant syneresis.	145
Figure 6.4 The intensity weighted size distribution for unfunctionalised SiNPs measured by DLS with a diameter of 230 ± 4 nm and PDI of 0.17 ± 0.01 . (B) The zeta potential distribution of the SiNPs measured in pH 7.4 PBS with a negative surface charge of -29.5 ± 0.7 mV. (C) A photograph of a mixture of non-PEI functionalised SiNPs and HA showing no coacervation or gelation.....	146

Figure 6.5 Schematics showing the gel forming conditions for (A) PEI-SiNP/HA gels, and (B) PEI/HA gels.	147
Figure 6.6 Quantification of the PEI and HA concentration in the supernatant after gel formation normalised to the initial reagent concentration. (A,C) The PEI supernatant concentration as a function of decreasing PEI concentration and decreasing HA concentration respectively. (B,D) The HA supernatant concentration as a function of decreasing PEI concentration and decreasing HA concentration respectively.	149
Figure 6.7 The effect of PEI-SiNP incorporation on the structure and morphology of hydrogels. Cryo-SEM images of (A,B) pristine HA, (C,D) PEI/HA hydrogels, and (E-H) PEI-SiNP/HA hydrogels prepared with PEI/HA ratio 3.6/4.8.	151
Figure 6.8 (A) A frequency sweep at 1 % shear strain showing the storage and loss moduli for PEI-SiNP/HA and PEI/HA hydrogels synthesised with PEI/HA monomer ratio of 1.2/4.8. (B) The storage moduli measured at 1 % shear strain and a frequency of 1 Hz for PEI-SiNP/HA and PEI/HA hydrogels prepared at different PEI/HA monomer ratios (n = 3).	152
Figure 6.9 The loss factor at 1 % shear strain and 1 Hz for PEI-SiNP/HA and PEI/HA hydrogels prepared with varied composition.	154
Figure 6.10 A strain sweep for PEI-SiNP/HA and PEI/HA hydrogels (PEI/HA monomer ratio 1.2/4.8) at a frequency of 1 Hz.	155
Figure 6.11 Equilibrium swelling ratios determined in ultrapure water for (A) freshly prepared and (B) dried PEI-SiNP/HA and PEI/HA gels (n = 3).	156
Figure 6.12 (A) The storage modulus for PEI-SiNP/HA hydrogels (PEI/HA ratio 1.2/4.8; measurement frequency 1 Hz) under repeated cycles of 1 % and then 1000 % strain (interval time 30 s). (B) Two pieces of hydrogel, prepared with and without CBBG dye, placed in intimate contact to demonstrate their macroscopic self-healing properties. After 1 h the hydrogels support their own weight (C) and remain connected under mild mechanical stretching (D).	158
Figure 6.13 Hemolysis testing for (A) PEI-SiNP/HA and PEI/HA gels, and (B-D) HA, PEI, and PEI-SiNPs respectively.	160

Figure 6.14 MTX loading efficiencies for PEI-SiNP/HA and Free-PEI/HA gels synthesised with varied PEI monomer concentration and HA monomer concentration fixed at 4.8 mM (n = 3). 162

Figure 6.15 Cumulative release of MTX from PEI-SiNP/HA hydrogels of varied composition collected in pH 7.4 PBS at 37 °C (n = 3). 164

List Of Abbreviations

Arg	L-Arginine
ASS	Argininosuccinate synthetase
ATR FTIR	Attenuated Total Reflection Fourier Transform Infrared Spectroscopy
BCA	Bicinchoninic acid
BET	Brunauer–Emmett–Teller
bfFGF	Basic Fibroblast Growth Factor
CAT-1	Cationic Amino Acid Transporter 1
CBBG	Coomassie Brilliant Blue
CTAB	Cetrimonium Bromide
DLS	Dynamic Light Scattering
Dox	Doxorubicin Hydrochloride
FITC	Fluorescein isothiocyanate
Glu	Glutamic Acid
HA	Hyaluronic Acid
HSNP	Hollow Silica Nanoparticle
IC₅₀	Half Maximal Inhibitory Concentration
IPA	Isopropanol
LCST	Lower Critical Solution Temperature
MTX	Methotrexate
NLDFT	Non-Local Density Functional Theory
NNLS	Non-Negative Least Squares
PAA	Poly(acrylic Acid)
PAH	Poly(allylamine hydrochloride)
PBS	Phosphate Buffered Saline
PDADMA	poly(diallyldimethylammonium)
PDMAEMA	Poly(2-(N,N-dimethylamino) ethylmethacrylate)
PE	Polyelectrolyte
PEC	Polyelectrolyte Complex
PEI	Polyethylenimine
PEI-SiNP	Polyethylenimine Functionalised Silica Nanoparticle

PGA	Poly(glutamic acid)
PNIPAM	Poly(N-isopropylacrylamide)
PSiNP	Porous Silica Nanoparticle
PSS	Poly(styrenesulfonate)
PVBTMA	Poly((vinylbenzyl) trimethylammonium chloride)
rhEGF	Recombinant Human Epidermal Growth Factor
SEM	Scanning Electron Microscopy
SiNP	Silica Nanoparticle
T_c	Critical Temperature
TEM	Transmission Electron Microscopy
TEOS	Tetraethoxysilane
TGA	Thermogravimetric Analysis
UCST	Upper Critical Solution Temperature
WST-1	(4-[3-(4-Iodophenyl)-2-(4-nitro-phenyl)-2H-5-tetrazolio]-1,3-benzene sulfonate)

1 Introduction

1.1 Overview and Thesis Outline

The mixing of two oppositely charged polyelectrolytes (PEs) can lead to the formation of nanoscale polyelectrolyte complex coacervates (PECs). Their formation in aqueous conditions under mild changes to pH and ionic strength make them effective tools for the encapsulation and delivery of drug molecules. High loading capacities may be achieved without risk of damage to liable drugs or payloads¹, and the coacervate can provide a protective environment for the loaded drug while potentially offering prolonged release to maintain therapeutic concentrations at the treatment site^{2,3}.

Many biologically derived polysaccharides, which are inherently non-toxic and biodegradable, carry ionisable carboxyl or amino groups allowing water solubility and electrostatically mediated formation of PECs. Among the most common formulations are those based on chitosan⁴⁻⁶, alginate⁷⁻¹⁰, and heparin^{11,12}. Compared to individual PEs, PECs can load and retain greater quantities of drug as shown by Janes *et al* with chitosan/dextran sulfate PECs, which showed a two-fold increase in loading efficiency with doxorubicin (Dox) than complexes of just chitosan and Dox alone¹³.

PEC drug delivery vehicles however are not limited to naturally occurring polysaccharides. Significant focus has also been applied to the synthesis and application of coacervate drug delivery vehicles based on synthetic polyelectrolytes¹⁴⁻¹⁷. The PECs may show stimuli-responsive behaviour, most often through pH mediated dissolution and corresponding drug release^{2,18,19}. For example, complexes of poly(2-(N,N-diethylamino) ethylmethacrylate) (PDMAEMA) and alginate have been reported for the loading and release of hydrophilic drugs with pH and ionic strength responsive drug release profiles²⁰. Under acidic pH associative interactions between the protonated alginate and Dox are weak compared to an alkaline environment leading to enhanced drug release. Similarly, high salt concentrations screened electrostatic interactions between the PEs and the Dox leading to destabilisation of the PECs and enhanced drug release²⁰.

The coacervation of PEs can also lead to macroscopic phase separation and the formation of coacervate hydrogels. Comprising of a porous, crosslinked polymer network with a high water content, tuneable mechanical properties, and the ability to encapsulate drugs, hydrogels

have long received attention for controlled drug delivery.²¹ However, clinical translation of chemical gels with covalent bonds has been limited by their brittle nature and lack of self-healing properties due to the networks inability to dissipate energy through its permanent and heterogeneous crosslinks^{22,23}. The non-covalent bonds (e.g. hydrogen bonding or electrostatic interaction) formed in coacervate hydrogels can lead to highly stretchable networks with self-healing and shear-thinning properties which are desirable in biomedical application²⁴⁻²⁶. In addition, the reversible crosslinking can impart stimuli responsive behaviours. For example Zhou and co-workers developed thermally responsive coacervate hydrogels through the use of poly(β -amino esters) that exhibit lower critical solution temperature²⁷, and Wang *et al.* demonstrated a pH responsive increase in mechanical stiffness through a change in ionisation state of a catechol-modified poly(acrylic acid) in the presence of Zn⁺ ions²⁸.

However, the reversible nature of coacervates and their sensitivity to pH, ionic strength, and temperature can lead to poor stability, and limit their application. As such, this thesis developed the use PECs as scaffolds for the synthesis of silica nanoparticles (SiNPs). The silica mineralisation inside the PEC template imparted stability to the PECs, while the PEs are retained at the SiNP surface as intrinsic organic functionalities. This approach was first applied to the development poly(acrylic acid) (PAA) and L-arginine (Arg) functionalised SiNPs for cancer targeted and pH responsive drug release (Chapters 3 and 4). Later, poly(ethyleneimine) (PEI) and L-glutamic acid (Glu) PECs were used to form PEI-functionalised SiNPs for incorporation into nanocomposite coacervate hydrogels with tuneable mechanical properties (Chapters 5 and 6).

1.2 Polyelectrolytes

Polyelectrolytes are macromolecules comprised of repeating ionisable groups which may dissociate into anions and cations in a polar solvent. In their uncharged state, the polyelectrolyte behaviour is similar to that of any other macromolecule, but on ionisation of electrolyte groups, interactions between monomers of individual chains or between adjacent polyelectrolytes can lead to specific behaviours such as the formation of PECs.

Similar to the classification of acids or bases and their salts, polyelectrolytes are also described as either 'strong' or 'weak'. Strong polyelectrolytes are those that fully dissociate at mild pH, while complete dissociation of a weak polyelectrolyte will only occur under

highly acidic or basic conditions. The ionisation state of a polyelectrolyte is calculated from the Henderson-Hasselbalch equation:

$$pH = pKa + \log \left(\frac{[base]}{[acid]} \right)$$

Eq. 1-1

Where the pH is that of the solvent, the pKa is the acid dissociation constant of the chemical group, and $\frac{[base]}{[acid]}$ is the ratio of ionised to un-ionised groups. In short, the degree of ionisation of an acidic group increases as the pH rises above the pKa value, while basic electrolytes become progressively more charged at pHs below their dissociation constants.

As polyelectrolyte properties are dependent on their charge state and resultant electrostatic interactions, their behaviour in solution is strongly influenced by the dielectric properties of the solvent. In addition to pH, the interactions between neighbouring polyelectrolytes and between a polyelectrolyte and itself may also be modulated via the solvent ionic concentration and dielectric constant. Tuning of each of these solvent properties can induce conformation change in the polymer, precipitation, or under specific conditions, coacervation and the formation of polyelectrolyte complexes.

Two commonly used length scales which describe these effects are the Debye length and the Bjerrum length²⁹. The Debye length, λ_d , is the distance over which the electrostatic force from an ionised polyelectrolyte is significantly reduced (by a factor of $1/e$). This can be viewed as the persistence length of any electrostatic interaction and is defined as follows:

$$\lambda_d = \left(\frac{\epsilon \epsilon_0 k_b T}{\sum_i c_i Z_i^2 e^2} \right)^{\frac{1}{2}}$$

Eq. 1-2

where ϵ is the dielectric constant, ϵ_0 is the permittivity of free space, k_b is the Boltzmann constant, T is temperature, c_i is the concentration of ion species i , Z_i is the charge of that ion species, and e is the elementary charge.

Notably, this length is dependent on the charge concentration and hence ionic strength of the solvent. Specifically, in the presence of high salt concentration the Debye length becomes very short and electrostatic interactions between neighbouring polyelectrolytes are diminished.

The Bjerrum length is defined as the distance at which the strength of electrostatic interaction between two charged bodies becomes comparable to the thermal energy $k_b T$.

$$l_B = \frac{e^2}{4\pi\epsilon\epsilon_0 k_B T}$$

Eq. 1-3

One can easily see from the terms in this equation the dependence of the Bjerrum length on the dielectric constant of the solvent, and how electrostatic interactions between charged polyelectrolytes can become increasingly relevant as it decreases. The dielectric constant is commonly controlled through the addition of alcohols to aqueous polyelectrolyte solutions, and is discussed in sections 1.3.2.3 and 1.3.3.3.

1.3 Coacervation and Polyelectrolyte Complexes

Coacervation is the term used to describe the macroscopic liquid-liquid phase separation of a homogeneous polymer solution into a polymer-rich phase and a dilute supernatant. Typically, the dense phase consists first of metastable, nano- or micro-scale phase droplets which when left to rest will coalesce into a single bulk phase (Figure 1.1). Dependent on the stability of the phase droplets, this coalescence can be near instantaneous, or can take several hours¹⁴. Coacervation, however, is not to be confused with precipitation, the liquid-solid phase transition observed in the case of strong inter-polymer interactions and poor solubility, which is a different phenomenon and not the focus of this discussion.

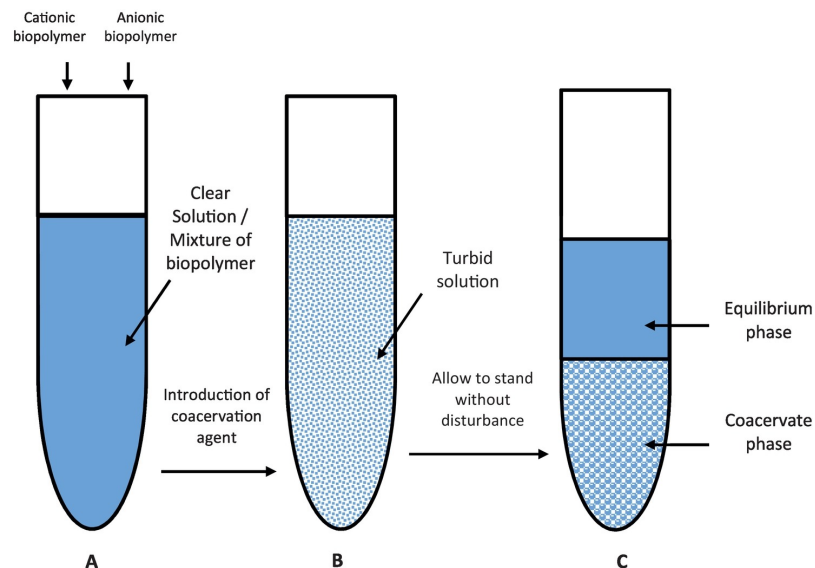


Figure 1.1 (A) The mixing, (B) formation of metastable phase droplets, and (C) coalescence of phase droplets into a bulk coacervate phase for oppositely charge polymers. Reproduced with permission from Elsevier.¹⁴

In general, coacervates may be classified as either simple coacervates (sometimes termed ‘self-coacervates’) comprising of only one macromolecular species whose self-assembly is mediated by charge neutralisation through changes to the solvent, such as pH, salt concentration, or the addition of dehydrating co-solvents like alcohols; or complex coacervates comprising of two or more components whose assembly is most commonly driven by cooperative electrostatic interactions^{30,31}.

Historically, the terms coacervate and PEC have been used interchangeably to refer to the polymer-rich phase prepared after liquid-liquid phase separation^{32,33}. In more recent literature, however, the term PEC may also refer to solid precipitate-like phases with fundamentally different properties to their liquid counterparts. Similarly, the term coacervate is widely used often without distinction to refer to both the dispersion of nano-scale polyelectrolyte rich phase droplets prepared in a dilute solution, and the single macro-scale phase prepared on their coalescence. Wang *et al.* use the distinction that ‘polyelectrolyte complex’ refers to dense, solid-like precipitates prepared typically at low salt concentration which when dried may be stiff or rubbery, while ‘polyelectrolyte coacervate’ or ‘polyelectrolyte complex coacervate’ is used to discuss micro and nano phases of loosely associated polyelectrolytes with more liquid like properties³⁴. Sing asserts a more quantitative definition where the intermolecular bonds in ‘complex coacervates’ are dynamic and transient in nature allowing the polyelectrolyte to diffuse and change places over observable timescales. ‘Polyelectrolyte complexes’, however, are in a state of kinetic arrest and the network conformation is fixed, which may manifest as solid-like behaviour in the complex³⁵. In this work, the focus is on the preparation of polyelectrolyte complex coacervates (as defined above) meaning nanoscale polymer-rich phase droplets bearing loosely packed networks and liquid-like behavior, and the terms ‘coacervate’, and ‘polyelectrolyte complex’ are used interchangeably to describe this state.

1.3.1 Theoretical Considerations

The earliest successful theoretical description of coacervation was brought by Voorn and Overbeek in 1957³⁶. The model was based in part on Flory-Huggins theory of polymer mixing in a small molecule solvent, and Debye theory to account for simple electrolytes. The

free energy expression for the 4 species in solution (the polyanion, polycation, and the anion and cation associated with salt species in solution) is given in Eq. 1-4:

$$\frac{a^3 F}{V k_b T} = \sum_i \frac{\phi_i}{X_i} \ln \phi_i + \sum_i \sum_{i < j} \chi_{ij} \phi_i \phi_j - \alpha \left(\sum_i \sigma_i \phi_i \right)^{\frac{3}{2}}$$

Eq. 1-4

where a is the size of the monomer, F is the free energy, V is the total volume, k_b is the Boltzmann constant, T is the temperature. The first two terms arise from Flory-Huggins theory for a polymer species i which occupies a volume fraction ϕ_i and has degree of polymerisation X_i , whose interaction with species j is described by the Flory-Huggins interaction parameter χ_{ij} . The final term accounts for the free energy contributions of weakly interacting electrolytes in solution and is dependent on the volume fraction ϕ_i of species i , which has charge density σ_i . The form of the electrostatic interaction parameter α is given below:

$$\alpha = \frac{2}{3} \sqrt{\pi} \left(\frac{e^2}{\epsilon \epsilon_0 k_b T a^3} \right)^{\frac{3}{2}}$$

Eq. 1-5

Phase separation into a polymer depleted phase and either a precipitate or coacervate phase will occur when the free energy F is minimised.

In recent history, more advanced theoretical frameworks have been developed to better describe complex systems³⁷, which incorporate non-ionic polyelectrolyte interactions³⁸, a non-zero ion size³⁹, polymer excluded volume effects⁴⁰, and charge connectivity between polyions^{41,42}. Despite this, the simplicity of Voorn-Overbeek theory is favoured by many and is often found to be in good agreement with experiments^{38,43}. Hence, it remains a widely used formalism for the description of complex coacervates and is used in this work to qualitatively describe the key parameters leading to liquid-liquid phase separation.

1.3.2 Simple Coacervation

Simple coacervation, or self-coacervation, is the phase separation of a solution containing one macromolecular species into a macromolecule-rich phase and a dilute supernatant, and has been widely reported in protein systems such as tropoelastin⁴⁴⁻⁴⁶ and muscle foot proteins^{47,48}, and synthetic polyampholytes (Figure 1.2)⁴⁹⁻⁵¹. Most commonly, single-component coacervation is entropic in nature and driven by charge neutralisation and the relative increase of hydrophobic interaction strength between polymer chains. The primary mechanisms that affect this include increased hydrophobicity (changes to pH and solvent ionic strength, temperature changes, and the addition of an alcohol co-solvent) which are discussed below.

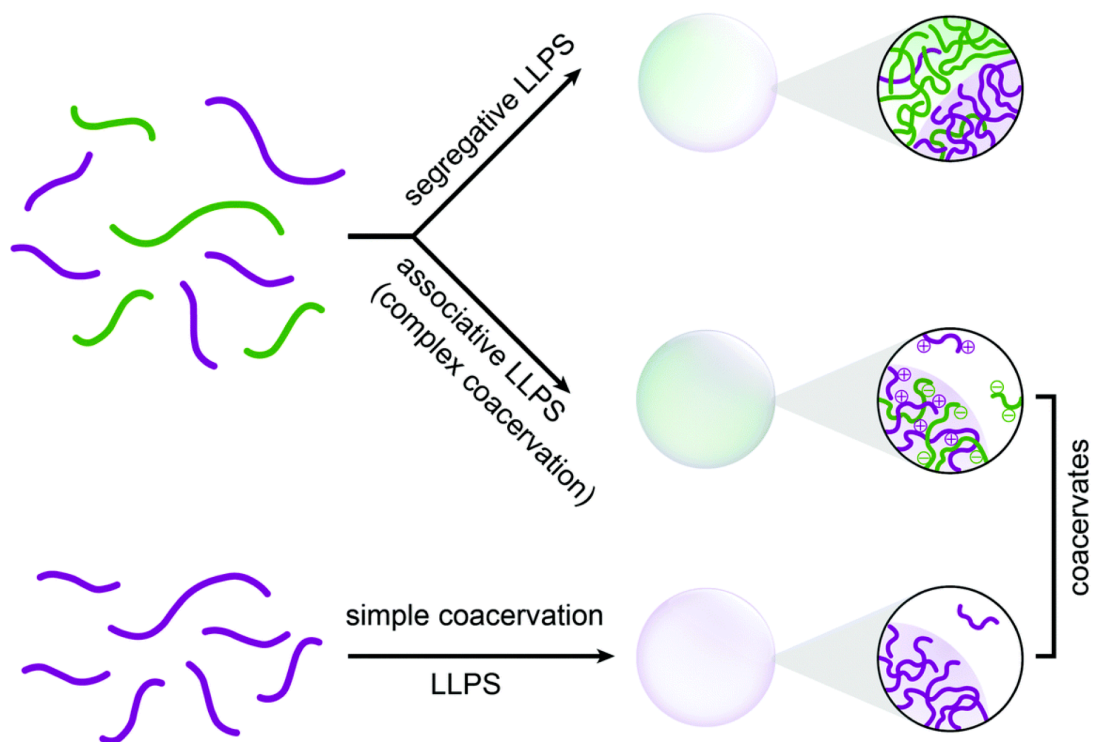


Figure 1.2. The three possible types of liquid-liquid phase separation (LLPS): Segregative phase separation, in which two species separate into distinct single-macromolecule phases; associative phase separation (complex coacervation) where two species form a macromolecule-rich coacervate phase in a dilute solvent; and simple coacervation, where a single macromolecule phase separates to form a concentrated coacervate phase in a dilute solvent. Adapted and reproduced with permission from the Royal Society of Chemistry.⁵²

1.3.2.1 pH and Ionic Strength

For polyampholytic macromolecules, those with positive and negative monomers, stabilised by repulsive electrostatic interactions, changes to the pH and salt concentration can be used to promote coacervation. In this case, similar to the complexation of oppositely charged polyelectrolytes, the assembly is driven by net charge neutralisation, local cooperative electrostatic interaction between oppositely charged groups, and the entropic gain from the release of counter ions.

This was observed by Perro *et al.* for a synthetic polyampholyte of anionic acrylic acid and cationic dimethylethylenediamine groups⁵¹. The charge state of a polyelectrolyte, and hence the strength of electrostatic interactions between adjacent polymer chains, is affected by the solution pH relative to the polyelectrolyte pK_a , and described by the Henderson-Hasselbalch equation (eq 1-1). On pH reduction to near the isoelectric point, a reversible liquid-liquid phase separation was observed forming microscale spherical coacervate droplets which remained stable for 12 days at 4 °C. Re-ionisation of the polymer by further pH reduction caused re-solvation of the polymer and dissolution of the coacervates. Investigations into the effect of cation grafting density revealed a strong dependence of phase separation on charge ratio. Indeed, when the cationic group grafting density was less than 5 % or greater than 30 %, no coacervation was observed regardless of pH, and for 25 % grafting density, solid precipitates were observed in place of the coacervates. The importance of cooperative electrostatic interactions was reinforced with zeta-potential measurements of the coacervates, which showed a negative surface charge. This is explained by a random distribution of cationic groups which form bridges between the excess anionic segments yielding a globally negative charge⁵¹.

pH mediated self-coacervation was also demonstrated with amphoretic carboxymethyl chitosan, which reversibly formed simple coacervates on pH reduction to near the isoelectric point. The coacervates showed good stability to high salt concentrations in excess of 1 M. In the presence of weak electrostatic interactions under a high salt environment, the polyelectrolyte becomes effectively uncharged and is hence sensitive to hydrophobic interactions which could maintain the state of coacervation².

However, when the solvent pH is not close to the isoelectric point, and the ionised macromolecules are stabilised by repulsive interactions, the effect of increased salt concentration becomes significant. The addition of salt to high concentrations is known to

screen electrostatic interactions by shortening the Debye length and is expected to disrupt interactions between adjacent polyelectrolytes. In an aqueous solvent below the isoelectric point (\sim pH 7.5), zwitterionic muscle foot protein-3 carries a net positive charge and remains stabilised in solution by long-range electrostatic repulsion. At high salt concentrations, suppression of the dielectric double layer causes the decrease and then disappearance of these forces motivating the formation of coacervates at pH 3⁴⁸.

It is evident that the reversible formation of simple coacervates on mild changes to pH and salt concentration gives ease of formation with minimal chemical processing, which could be beneficial if applied to drug delivery. However, the same reversible response to small environmental changes can make the coacervates potentially liable to disassembly or premature drug release. Furthermore, the choice of polyelectrolytes is limited to those that form coacervates under physiological pH and ionic strength, and at the disease site.

1.3.2.2 Temperature Mediated Coacervation

For single component solutions stabilised by hydrophilic interactions, temperature may be used to tune the relative strength of hydrophobic interactions and cause phase separation. Coacervation will occur when transient, hydrophobic interactions between adjacent macromolecules become more favourable than hydrophilic interactions with the bulk solvent. Above a critical temperature (T_c), when the kinetic energy of the solvent molecules exceeds the energy of the solvating hydrogen bonds, hydrophobic interactions between the polymer backbones and hydrophobic side chains become dominant. Dependent on the strength of inter-molecular interaction, this lower critical solution temperature (LCST) behaviour can elicit either liquid-solid phase separation (precipitation)⁵³ or reversible liquid-liquid coacervation⁵⁴.

Despite the dominance of hydrophobic interaction, ionic systems exhibiting LCST coacervation may still be affected by electrostatic interactions, and hence are often liable to changes in the solvent. This is widely reported with tropoelastin, a precursor to extracellular matrix protein elastin whose T_c decreases with increasing salt concentration and pH. In both cases the changes to solvent condition alter the balance of polar and non-polar residues, which otherwise promote stability, and lowers the energy barrier for coacervation⁴⁴.

Das *et al.* observed the opposite trend and an increase in T_c with salt concentration for carboxylated poly-L-lysine (PLL). The screening of electrostatic charges reduced the strength

of electrostatic interaction between cationic and anionic chain segments such that the addition of sodium chloride to a coacervate solution above T_c could reverse the phase separation. The critical temperature could be further controlled by tuning the molecular hydrophobicity through the length of the alkyl group in the side chain. The onset of coacervation occurred at progressively higher temperatures as the alkyl chain length (and hence hydrophobicity) was reduced from 4 to 1 carbon, until no LCST behaviour was observed when the methylene group was replaced with a hydrophilic ether group⁵⁵.

The potential liability of pH and ionic strength dependent coacervates prompted Narayanan *et al.* to develop non-ionic, tropoelastin-like polyesters which showed temperature dependent coacervation between pH 3 – 13, and ionic strengths between 0 – 1 M. Their increased stability to changes in solvent condition show potential for application where pH and ionic strength may fluctuate over large ranges⁴⁶.

In comparison to LCST behaviour, upper critical solution temperature (UCST) behaviour describes a stable polymer solution at high temperature that becomes partially or completely desolvated below T_c . At low temperatures, strong polymer-polymer interactions (e.g. electrostatic interactions) facilitate coacervation, and are broken by the added kinetic energy associated with temperature increase.⁵⁶ Although UCST behaviour is not commonly observed in aqueous conditions as the polymer-polymer ionic and hydrophobic interactions can be destabilised by water and salt, Zhang and co-workers used glycol-amide modified poly(N-(2-hydroxypropyl)methacrylamide) as a coacervate forming UCST polymer. Unlike LCST coacervates, whose assembly is mediated by hydrophobic interactions, the hydrophilic nature of UCST behaviour readily enables the encapsulation of hydrophilic cargos which was demonstrated here with bovine serum albumin⁴⁹. Notably, other examples of UCST polymers exist in literature but are reported to form precipitates below T_c , not coacervates⁵⁷.

1.3.2.3 Alcohol Induced Coacervation

The addition of alcohol, or another non-polar solvent, at a critical concentration to an otherwise aqueous solution can disrupt the solvating hydrogen bonds causing the dominance of hydrophobic interactions and the formation of simple coacervates.

In the case of polyampholytes, the self-assembly of coacervates is partially mediated by electrostatic interactions. This is seen in the final term of Eq. 1-4, which describes the electrostatic contribution to the free energy of mixing for weakly interacting polyelectrolytes in solution. The electrostatic interaction parameter scales with $\varepsilon^{-\frac{3}{2}}$ and hence on the addition of alcohols to an aqueous solution the free energy of mixing increases until a critical point where it exceeds that of the polymer-rich and polymer-depleted phases formed in coacervation. This explains the observed dependency of the critical alcohol volume fraction on the alcohol dielectric constant. In addition, the use of higher alcohols whose polarity and dielectric constants are lower than water caused coacervation at progressively lower alcohol concentrations^{58,59}.

In these systems where electrostatic interactions are also present, the pH and ionic strength of the buffer can have significant effect on the required volume of alcohol to elicit coacervation. For pH values high above the isoelectric point where repulsive interactions are dominant, highly charged and relatively stiff gelatin molecules required the addition of larger alcohol concentrations than those prepared closer to charge neutrality. Similarly, the addition of salt was able to screen repulsive electrostatic repulsion between charged monomers, and cause phase separations at lower alcohol concentrations^{58,60}.

Neutral polymers are reported to undergo coil-globule-coil conformation transitions on increasing alcohol concentration, although this does not typically yield coacervate phases. It has been shown with poly(N-isopropylacrylamide) (PNIPAM) that the polymer may be completely solvated in the coil conformation by either water or methanol but over a critical methanol concentration range the solvent is comprised almost exclusively of water/methanol complexes. These are a poor solvent for PNIPAM and cause a coil-globule conformation change^{61,62}. This conformation change is observed as a significant decrease in the hydrodynamic radius of the polymer suggesting individual polymer collapse and not associative assembly of polymers.

As is discussed later in Chapter 3, this re-entrant transition behaviour was observed for weak polyelectrolyte poly(acrylic acid) (PAA) but with an increase in diameter over the critical alcohol range suggesting the assembly of multiple polymers in the formation of coacervate droplets and not individual polymer globules as described above.

1.3.3 Complex Coacervation

Complex coacervation is the associative phase separation of two or more oppositely charged macromolecules to yield either PECs suspended in a polyelectrolyte-depleted solvent, or a single macroscale coacervate phase and a dilute supernatant phase (Figure 1.3). Most commonly this occurs through cooperative electrostatic interaction between oppositely charged chain segments.

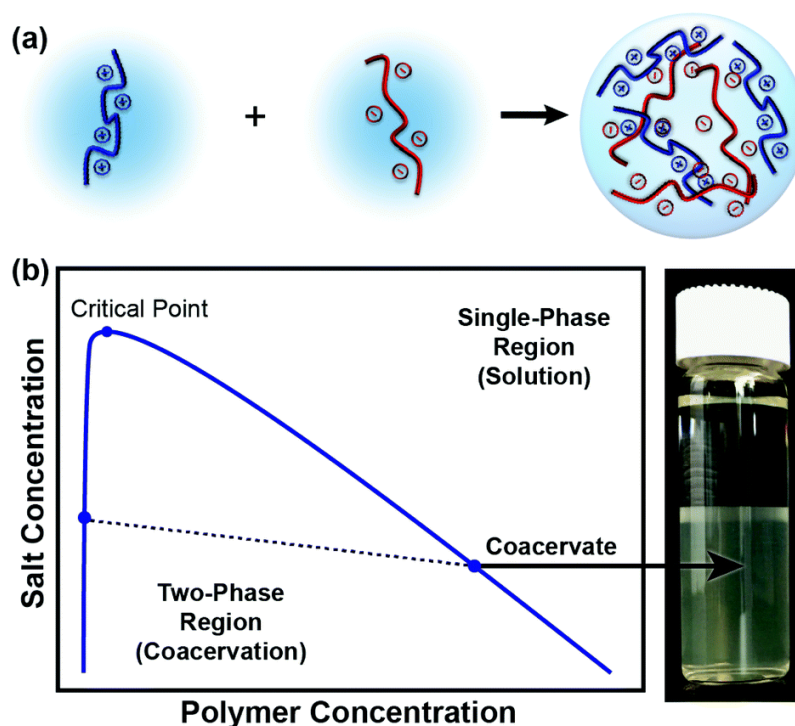


Figure 1.3 (A) A schematic representation of complex coacervation. (B) A typical phase diagram showing the salt concentration against polymer concentration with an exemplary photograph of a complex coacervate from poly(4-styrenesulfonic acid) and poly(diallyldimethylammonium chloride). Reproduced with permission from the Royal Society of Chemistry.³⁰

Considering the relationship between the solvent pH and polyelectrolyte ionisation state, and the effect of charge concentration and dielectric constant on the Debye and Bjerrum lengths, it comes as no surprise that these are key parameters in the formation and stability of complex coacervates. These, and the effect of stoichiometry, alcohol concentration, and polymer molecular weight are introduced in the following discussion.

1.3.3.1 Solvent pH and Ionic Strength

Similar to the discussion presented in section 1.3.2.1 about the effects of ionic strength and pH in simple coacervation, the ionisation state of a polyelectrolyte, and hence its ability to form coacervates via electrostatic interactions, is a function of the solvent pH. The extent of ionisation given by Eq. 1-1 describes how close to their respective pK_a values a high proportion of each polyelectrolytes ionisable groups will carry a charge, while at extremes of pH it is possible for one polyelectrolyte species to be completely ionised, while an oppositely charged species shows no dissociation and remains neutral. Hence, titration from highly acidic to highly alkaline pH for aqueous mixtures of oppositely charged polyelectrolytes can show a solvated solution under highly acidic or basic conditions, with a reversible coacervate phase between their respective pK_a values⁶³⁻⁶⁵.

Changes to the pH and ionisation state of either polyion can also affect the required molar stoichiometry. Coacervates of PAA and poly(allylamine hydrochloride) (pAH) formed at approximately 1:1 molar ratio at weakly acidic pH, but on increase to pH 8.5 the decreased ionisation state of the cation prevented coacervation at this ratio. Instead, approximately 66 % molar fraction pAH was required under an alkaline condition to achieve the charge ratio required for PEC formation (Figure 1.4)⁶⁶.

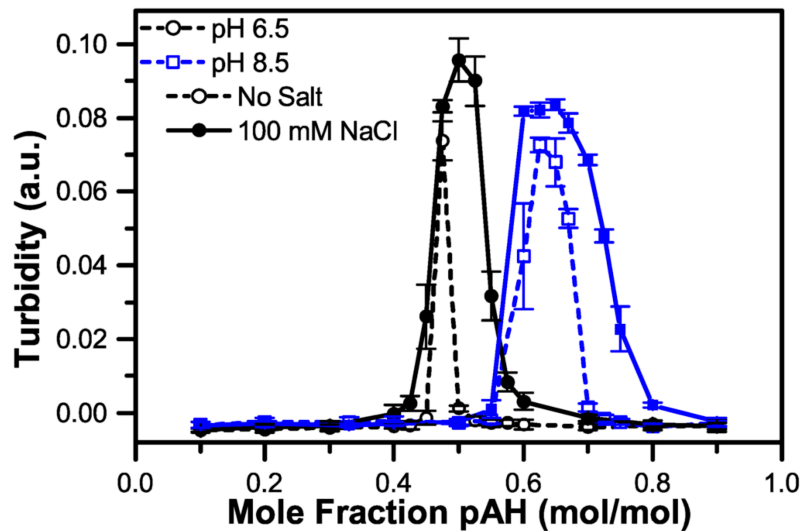


Figure 1.4 The coacervate forming molar fractions, as indicated by high turbidity, for mixtures of PAA and pAH at pH 6.5 and 8.5, and with and without salt. Reproduced with permission under a CC-BY licence.⁶⁶

At sufficient ionic strength, the increased salt content can screen long-range electrostatic interactions between charged polymers. In the case of simple coacervation, these are typically repulsive and their suppression will promote coacervation through charge neutralisation. In complex coacervation, associative electrostatic interaction is required and hence screening of electrostatic charges narrows the range in which complex coacervation will occur. Aqueous PECs of anionic hyaluronic acid and cationic chitosan show phase separation over a broad pH range of between 2 – 6 at 0.05 M. But the addition of sodium chloride progressively narrows the permissible pH range until no coacervation is observed over the full pH titration at 1.5 M⁶⁵.

In the case of strongly interacting polyelectrolytes, the weakening of electrostatic interaction by salt addition can promote the precipitate-coacervate transition. This was observed by Wang *et al.* with the progressive addition of potassium bromide to mixtures of poly(styrenesulfonate) (PSS) and poly(diallyldimethylammonium) (PDADMA). The strong electrostatic bonds which led to a dense solid complex under low salt conditions, were broken on increasing salt concentration leading first to a solid doped with KBr, then a coacervate, and ultimately a dispersed solution of solvated polyelectrolyte (Figure 1.5). The authors suggest that the effects of salt concentration arise not just from screening and shortening of the debye length, but also from competition between salt ions and charged monomers to form

electrostatic bond with an oppositely charged electrolyte. That is to say, as the salt concentration increases, the salt ions are able to break polyelectrolyte-polyelectrolyte ion pairs and replace one of the charged species, so the density of crosslinking in the polyelectrolyte complex progressively decreases³⁴. This was also commented by Spruijt *et al.* who studied PAA and PDMAEMA PECs and concluded that the critical salt concentration at which phase separation no longer occurred was too high to be derived purely from classical screening of electrostatic charges³⁸.

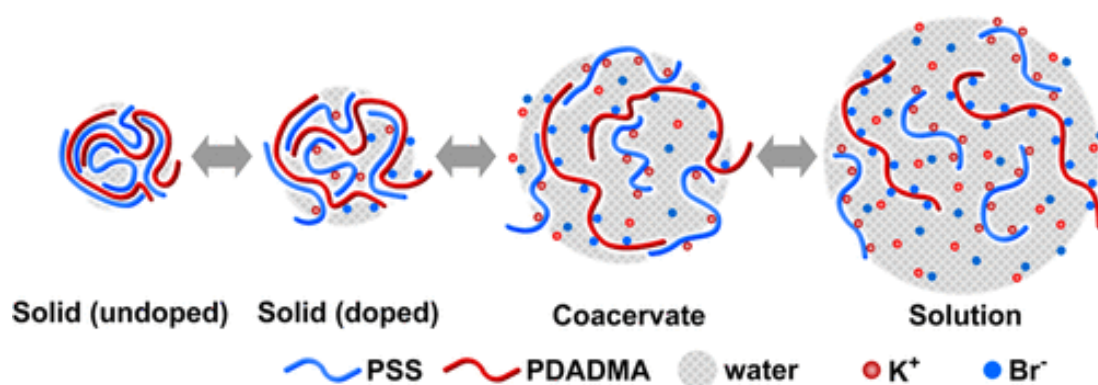


Figure 1.5 A schematic showing the progression from solid precipitate to coacervate, and then dissolved polymer solution on the addition of salt to mixtures of (PSS) and (PDADMA). Reproduced with permission under a CC-BY licence.³⁴

From this, one may draw the same conclusions as presented in the discussion of pH and ionic strength in simple coacervates; that is that the ready formation of PECs under moderate conditions show great potential for encapsulation of cargos, but their sensitivity to small changes in pH and salt concentration may significantly limit their application to dynamic or non-uniform environments. While formulations with appropriate pH and salt sensitivity for biological drug delivery do exist, they are relatively few in number compared to the broad scope of polyelectrolyte coacervation. A method to stabilise the coacervates and improve their utility in wider salt and pH environments is desirable.

1.3.3.2 Mixing Ratio and Stoichiometry

The ability of a solution to form a complex coacervate is governed by intermolecular electrostatic interactions. As such, the stoichiometry and hence charge ratio between the polyelectrolytes is a key parameter. However, the specific effect and required conditions for coacervation vary depending on the polyelectrolytes. It has been reported for many systems that a near 1:1 charge stoichiometry is prerequisite for complex coacervation⁶⁶⁻⁶⁸. For example, Priftis *et al.* used turbidity measurements to show that for mixtures of poly(L-lysine) and poly(glutamic acid) (PGA), coacervation occurred at the 1:1 acid/base ratio, independent of polymer molecular weight or total concentration⁶⁹. However, work by Kayitmazer *et al.* suggested the opposite, where for mixtures of hyaluronic acid and chitosan, coacervation was only observed for anion/cation charge ratios up to 0.46 where the zeta potential was highly positive. Above this point, phase separation caused precipitation of the polymer species⁶⁵. It may be that the non-stoichiometric ratio, and resultant charge mismatch, caused the formation of charged loops instead of the contact ion pairs seen in 1:1 charge matching, which was favourable for maintaining the hydration required for coacervation. This agrees with the findings of Schatz and co-workers who found that for mixtures of polysaccharides chitosan and dextran sulfate, stable polyelectrolyte complex coacervates could only be formed at non-stoichiometric mixing ratios⁷⁰. In fact, chitosan-alginate PECs were formed by Yilmaz at cation:anion molar charge ratios as high as 100:1 which were also destabilised when the ratio was tuned to 1:1⁷¹. It is evident that the charge mismatch performed a vital role in stabilising the coacervates against irreversible aggregation.

The use of mixing stoichiometry to tune the surface charge of the coacervates was further explored by Shiu *et al.* By varying the stoichiometric ratio of anionic PGA to cationic PDMAEMA, PECs with comparable size but tuneable zeta potentials were produced. When the cationic component was in excess, a positive zeta potential was recorded, but when the weight fraction of the anionic component exceeded 50 %, PECs of negative surface charge were produced⁷².

1.3.3.3 Alcohol-Induced PEC Formation

Similar to the alcohol-induced simple coacervation of polyampholytes, the addition of alcohol to an aqueous solution of oppositely charged polyelectrolytes can cause the formation of polyelectrolyte complex coacervates. The reduction of the solvent dielectric constant by the addition of a less polar co-solvent increases the free energy contribution of weakly interacting polyelectrolytes as described by Voorn-Overbeek theory (Eq. 1-4), which at a critical concentration can promote phase separation.

This has been studied by Fuji and group with weak polyanion poly(acrylic acid) (PAA) and cationic ammonium hydroxide in an 80 % ethanol solution. Their mixing yielded metastable PECs whose nanoscale diameter was tuneable via the concentration of PAA, its molecular weight, and the valency of the amine cation⁷³⁻⁷⁵. While the effect of varying the ethanol concentration was not studied in these works, it is known from Mechtaeva *et al.* that the aqueous mixing of PAA with diamines does not cause coacervation, and triamines or higher were required to electrostatically crosslink PAA in the formation of PECs⁷⁶. It is clear that where electrostatic interactions alone are insufficient to cause coacervation the addition of an alcohol co-solvent can act cooperatively to induce PEC formation. These alcohol-induced PAA/amine PECs were later used for the coacervate templated synthesis of silica nanoparticles, and are discussed more extensively in section 1.4.2.

As discussed above (Section 1.3.3.1), strongly interacting polyelectrolytes will precipitate in aqueous solutions and the addition of salt is required to facilitate a transition from precipitate to coacervate. In this case the addition of alcohols has been observed to tune the critical salt concentration⁷⁷. For hyaluronic acid and chitosan studied by Sun *et al.* a solid precipitate was observed in an aqueous solvent, and 280 mM of sodium chloride was required to weaken the electrostatic interactions and allow coacervation. On the addition of 8 % methanol the required salt concentration increased to 400 mM. The addition of higher alcohols further decreased the dielectric constant and increased the hydrophobic effects such that 450 mM of salt was required using the same concentration of ethanol, and no coacervation could be observed with the use of isopropanol⁷⁸.

Unusually, Meng and co-workers observed the opposite effect where increasing the alcohol concentration reduced the critical salt concentration required for coacervation (Figure 1.6). In other words, the addition of ethanol to high concentrations facilitated liquid-liquid phase separation, while more aqueous solvents yielded only precipitates. The study was performed with PSS and poly((vinylbenzyl) trimethylammonium chloride) (PVBTMA), both of which

have hydrophobic benzyl groups. Although both polyelectrolytes are water soluble, the addition of a less polar solvent may increase their solvation state and mediate the precipitate-coacervate transition⁷⁹. In this instance, it is clear that not only the dielectric constant is important in alcohol induced coacervation, but also the solvent hydrophilicity/hydrophobicity relative to the polyelectrolytes.

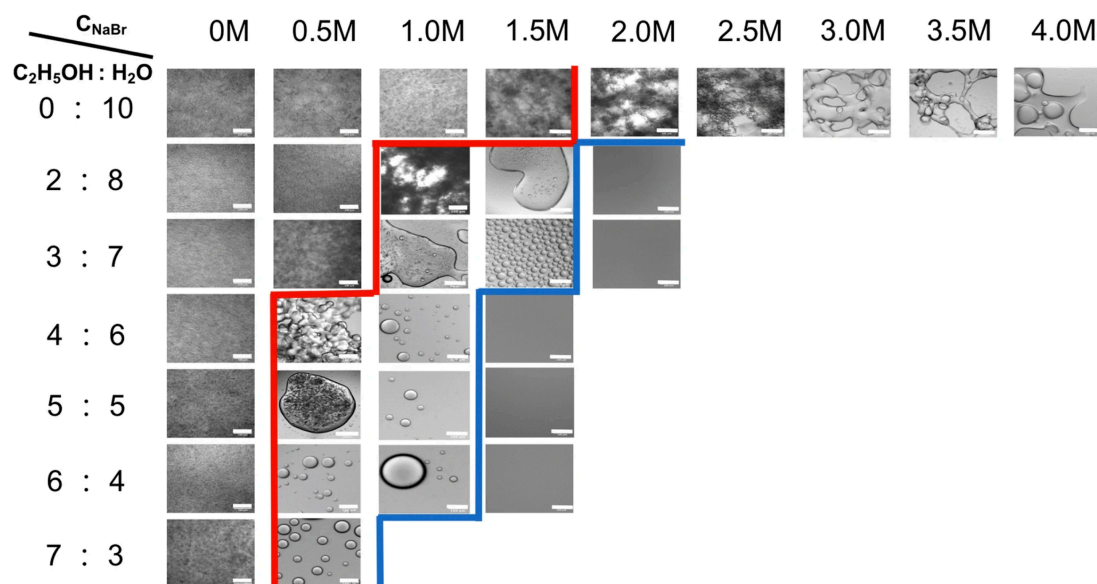


Figure 1.6 Optical micrographs of PVBtMA/PSS mixtures prepared with ethanol:water volume ratios between 0:10 and 7:3, and salt concentrations between 0 and 4 M. The red line indicates the salt and alcohol concentrations above which coacervates are formed, and the blue line indicates their transition to liquid. Reproduced with permission un a CC-BY licence⁷⁹.

Although the potential for drug retention and prolonged release has been demonstrated with gelatin in binary water/alcohol solvents⁵⁹, the coacervates are only metastable and highly dependent on alcohol concentration in the solvent. As such, alcohol-induced complex coacervates typically are unsuitable for biomedical application. To prevent immediate dissolution and to retain efficacy on delivery into an alcohol-free biological medium, additional stabilisation would be required.

1.3.3.4 Polymer Molecular Weight

From observation of the free energy equation presented in Section 1.3.1, (Eq. 1-4) we see that the first term, $\sum_i \frac{\phi_i}{X_i} \ln \phi_i$, is inversely proportional to the degree of polymerisation, X_i . From this, we can expect that an increase in polymer molecular weight, even at constant mass concentration, will decrease the free energy of mixing and facilitate coacervation. This effect was in fact described as early as 1977 by Abe *et al.* who observed a critical chain length for oligo(ethylenimine) when mixed with PGA, below which phase separation was not observed⁸⁰.

Spruijt and team went on to study the effects of molecular weight in mixtures of PAA and PDMAEMA on their resistance to changes in salt concentration. As discussed above, the addition of salt to a complex coacervate solution progressively screens the electrostatic charges and increases the concentration of polymer found in the dilute phase until it equals that of the concentrated phase. At this critical salt condition, the polymer concentration is constant throughout the medium and no phase separation occurs. However, the use of higher molecular weight polymers can stabilise the coacervates and increase this critical salt concentration and the range over which separation is observed. In fact, an increase in the degree of polymerisation of PAA from 20 to 510 more than doubled the critical salt concentration from approx. 0.5 – 1.3 M³⁸.

The same trends were documented by Chollakup *et al.* with aqueous solutions of PAA sodium salt, and PAH. In this case, the salt concentration required for the precipitate-coacervate transition was also shown to increase with the degree of polymerisation. Indeed for 100 mM ionic strength and a PAA polymerisation degree of 25, many coacervate forming polyelectrolyte ratios were identified, but on increase of X_{PAA} to 695, only precipitation was observed, and an increased salt concentration was required for coacervation (Figure 1.7). Interestingly, however, the PAA/PAH stoichiometry required for phase separation (either precipitation or coacervation) remained largely unchanged independent of X_i .⁶⁸

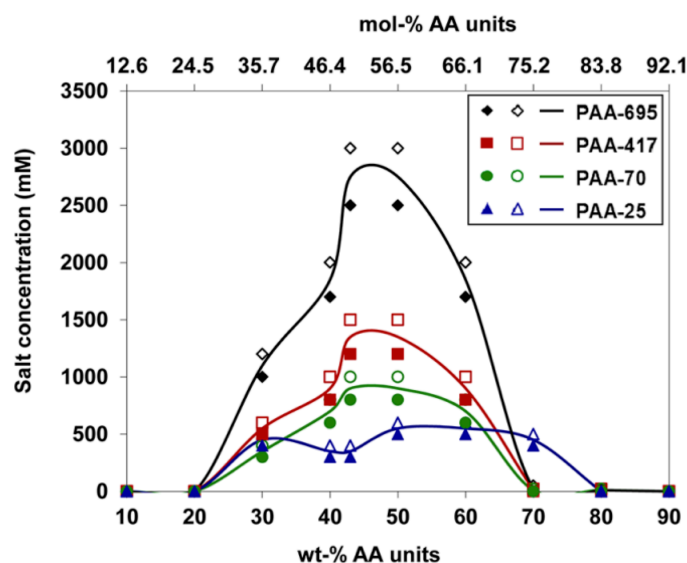


Figure 1.7 A phase diagram for mixtures of PAA sodium salt with (degree of polymerisation between 25 and 695) and 0.5 wt % PAH as a function of PAA and NaCl salt concentration. Open and filled symbols represent concentrations at which either a coacervate or precipitate were observed respectively. Reproduced with permission from Ref 68. Copyright 2013 American Chemical Society⁶⁸.

1.4 PEC Templated Silica Nanoparticle Synthesis

We see from the above discussion that coacervates are very sensitive to environmental changes such as pH, ionic strength, and temperature, which can make them unsuitable for use in drug delivery. However, the use of coacervates as templates for SiNP synthesis offers potential to stabilise the PECs.

Since their discovery, silica nanoparticles have attracted considerable attention in drug delivery and biomedical applications. Silica itself is inherently biocompatible and readily degraded by reactive oxygen species in the tumour microenvironment⁸¹⁻⁸³, while the synthesis of porous silica nanoparticles with large internal pore volumes and surface areas allow the loading and transport of therapeutic cargos^{84,85}.

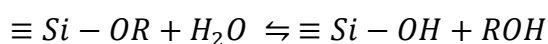
For biological application there exists an impetus for the synthesis of nanoparticles with functional surface ligands. For example targeting ligands to improve accumulation of the particles at the disease site, stimuli-responsive moieties for controlled or triggered release of

the cargo. However, as is discussed in the following section, conventional silica nanoparticle syntheses do not typically yield particles with biomedically desirable surface functionality, and extensive post-synthetic modification and conjugation steps are required before application.

An optimum drug delivery system may incorporate the ease of coacervate formation and cargo encapsulation with the stability of hard colloids such as silica. Hence in this thesis, PECs are used as scaffolds for the template-directed synthesis of silica nanoparticles with built-in application specific surface functionality to obviate the need to retrospective functionalisation.

1.4.1 Stober method

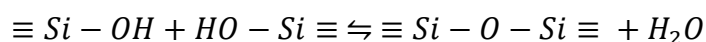
The Stöber method, first reported by Werner Stöber in 1968, is the most widely used synthetic pathway for the formation of silica nanoparticles. In this sol-gel process, the Si-OR bond in the silica precursor is first hydrolysed by nucleophilic attack of the oxygen in water on the silicon atom in the silica precursor (typically tetraethoxyorthosilicate)^{86,87}.



Eq. 1-6

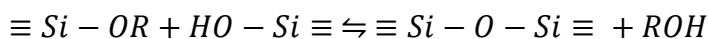
The condensation to form siloxane bonds from silica monomers or oligomers to ultimately yield silica nanoparticles also proceeds *via* nucleophilic attack in either water or alcohol producing condensation reactions:

Water Condensation:



Eq. 1-7

Alcohol Condensation:



Eq. 1-8

Both the rates of hydrolysis and condensation are highly pH dependent. Hydrolysis is quickest at extremes of pH with a minimum at neutral conditions, while the rate of condensation sees a minimum in the acidic regime and its maximum occurs at weakly alkaline pH. Hence in the Stöber method the formation of silica nanoparticles is base-catalysed by ammonium hydroxide.

In the absence of a template or predetermined nucleation site, the formation of silica particles is thought to proceed *via* one of two models, monomer-addition or controlled aggregation, both of which are based on nucleation and growth.

In the monomer addition model, the concentration of monomers produced by hydrolysis increases to the point of supersaturation, and a burst of nucleation is observed. This rapid formation of nuclei significantly reduces the monomer concentration to below the critical concentration and the energy barrier for further spontaneous nucleation becomes too great. This effectively prevents the formation of new nuclei, and the number of sites for nanoparticle growth becomes fixed. The ‘growth’ phase is characterised by the deposition of silica monomers onto the nuclei surfaces until colloidal particles are produced. As the number of nuclei is fixed after the burst phase, and the rate of monomer deposition during growth is constant across all nuclei, the synthesised silica nanoparticles have a high degree of monodispersity^{87,88}.

The controlled aggregation model assumes near continuous monomer formation throughout the synthesis through the condensation of silica monomers into polymeric species and ultimately dense particles. These nuclei however, are colloidally unstable and aggregate repeatedly to form larger, stable particles. The origins of the observed particle uniformity are less clear in this model, but could arise from a difference in aggregation rate between large and small particles. It is reported that the aggregation rate between particles increases for those with large size ratios which would effectively prevent aggregation of two large species and ultimately confer monodispersity to the particle population^{86,87,89}.

1.4.2 PEC templated SiNPs

The functionalisation of SiNPs with surface ligands for biomedical application has attracted considerable attention in literature, with many authors using a post-synthesis grafting strategy^{90,91}. Typically, unfunctionalised SiNPs are synthesised and cleaned to remove excess

reagents first, and then the surface is functionalised with amines *via* the condensation of 3-aminopropyl triethoxysilane, which act as grafting points for the retrospective conjugation of pH-responsive PAA^{92,93}. Similarly, the condensation of 3-methacryloxypropyl trimethoxysilane has also been used to functionalise the SiNP surface with methacrylate groups for the conjugation of temperature responsive PNIPAM⁹⁴. This process can add appreciable time, cost, and complexity to synthetic protocols, and there remains a need for new pathways that incorporate built-in surface functionalities.

As introduced above, coacervation is a facile tool that may be used to generate metastable nano- and micro- scale polyelectrolyte complexes. These PECs can incorporate a wide range of polyelectrolytes, but are potentially liable to changes in environmental pH, salt concentration, temperature, or alcohol concentration. As such, the choice of viable components for use in PECs is limited to those that will produce highly stable complexes in both the synthesis and application media.

The use of coacervate PECs as scaffolds for the synthesis of SiNPs can answer both of these problems. It is expected that silica growth within the PEC will add the colloidal stability associated with hard nanoparticles and prevent PEC dissolution under changing solvent condition, while the retention of polyelectrolytes in the silica matrix and at the surface will afford intrinsic and customisable organic functionality to the silica particle.

The desirable properties of a PEC template for functionalised SiNP synthesis are as follows:

- PECs are monodispersed and of nanoscale diameter.
- Their internal microenvironment may facilitate silica hydrolysis and condensation.
- The constituent polyelectrolytes carry desirable application-specific properties eg. cancer targeting, ability to load and retain therapeutic cargo, ect.
- The constituent polyelectrolytes are retained post-synthesis and present as surface functionalities.

While several authors have reported the use of PEC templates in the formation of hollow silica nanoparticles, the potential for in-synthesis functionalisation of SiNPs *via* this method remains poorly exploited. Most commonly, weakly anionic polyelectrolyte PAA is used with ammonium hydroxide in a binary water/ethanol solvent to form PECs via alcohol-induced coacervation. The ammonium hydroxide had a dual function as both a component of the PEC

for complexation with PAA, and also as a basic catalyst leading to the selective hydrolysis and condensation of silica precursors inside the coacervate scaffold. However, the particles synthesised from this approach exhibited a broad size distribution which could be attributed to the polydispersity of the coacervate scaffold^{95,96}. It is known that the cellular interaction and biological fate of nanoparticle systems are strongly dependent on particle size, and hence monodispersed populations are necessary for predictable drug delivery behaviour^{97,98}.

The PEC template monodispersity was improved by Nakashima *et al.* first with the use of polyamines. When used as PEC components with PAA, triethylenetetramine and diethylenetriamine (which have 4 and 3 ionisable amine groups respectively) were able to form smaller and more monodispersed complexes than ethylamine. Their higher charge density allowed increased electrostatic interaction with anionic PAA⁷⁵.

A similar effect was observed with divalent cations when compared to monovalent. On electrostatic interaction with the charged carboxyl side chains of PAA, monovalent species such as Na⁺ or K⁺ become neutralised. The lack of repulsion between previously charged PAA monomers in combination with solvent effects from the high alcohol concentration caused partial chain collapse and the formation of loosely packed complex coacervates. Divalent ions Ca²⁺ and Mg²⁺, however, may interact with two carboxyl groups simultaneously acting as crosslinks between adjacent PAA molecules. This additional electrostatic interaction led to denser PECs with smaller average diameters and greater monodispersity which was conferred to the final silica nanoparticles (Figure 1.8)⁹⁹. The condensation of silica around the PEC scaffolds also led to the formation of a microporous network in the shell of the hollow SiNPs. The use of Mg²⁺ gave a broader distribution of pore volumes with larger internal volumes than its monovalent counterparts, suggesting that the charge density and hence polyelectrolyte packing in the PECs may be a means of tuning porosity in the resultant SiNPs. Notably however, in each of these studies the PEC components were readily washed away after synthesis by centrifugation and rinsing in ethanol or water, and not retained as surface ligands for potential future application.

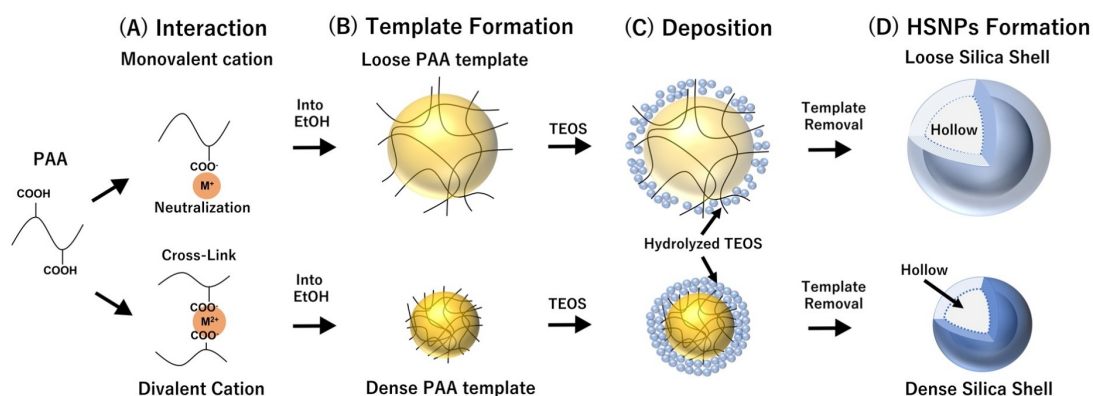


Figure 1.8 A schematic representation of a PEC templated hollow SiNP synthesis showing (A) the mixing of PAA and either a monovalent or divalent cation before (B) the addition of ethanol for the formation of the PEC templates. (C) On the addition of tetraethoxysilane (TEOS) silica condensation occurs at the template surface, and (D) the template is removed to yield hollow SiNPs. Reproduced and adapted with permission from Elsevier.⁹⁹

Shiu *et al* used PGA and PDEAEMA in distilled water for the formation of PECs with tuneable average diameter between 100 – 200 nm.⁷² Although tuning the size through variations in mixing stoichiometry and polymer chain length did also elicit changes in dispersity and only specific formulations exhibited monodisperse populations. The presence of polyamines in the PEC provided the basic environment required to catalyse the condensation of silica precursors, and then electrostatic interactions with silica oligomers caused their local concentration increase inside the templates. Hence, the PECs acted as scaffolds for the spatially selective condensation of silica nanoparticles. Unlike the alcohol-induced PAA/polycation based PECs, the polyelectrolytes in the coacervate template were retained after washing and purification steps to yield polymer-functionalised silica nanoparticles. This could be due to the higher polyelectrolyte valency of PDEAEMA compared to the relatively low valency cations described above that induced stronger electrostatic interactions between the polymers. The presence of the anionic peptide shell then facilitated the electrostatic loading and subsequent release of cationic anti-cancer therapeutic doxorubicin without the need for post-synthetic ligand conjugation.

A similar work from the same group expanded the choice of polyelectrolytes used to include PAA, PSS, and poly(L-lysine) (PLL). Hybrid silica particles were successfully prepared from coacervates of PLL/PAA, PLL/PSS, and PLL/PGA with retained organic functionality after

washing and purification steps. From the protonation state of the cationic and anionic polyelectrolytes decorating the silica particle surface, the zeta potential was positive under acidic conditions and strongly negative in the alkaline regime. Further, the choice of PEC components with differing pKa values was used to effectively tune the isoelectric point of the silica particles¹⁰⁰.

However, PEC templated SiNP syntheses that yield monodispersed populations and controllable sizes below 100 nm remain rare, and many existing systems do not incorporate PEs with biomedically desirable properties such as pH responsive drug release or cancer targeting. It is evident that the use of PECs as scaffolds for silica condensation is a potentially powerful tool in the synthesis of highly stable nanocomposites with intrinsic functionality, but to date remains severely under reported.

1.5 Table of Definitions

For clarity, this table is included to define key terms surrounding coacervation as they are used in this work.

Term	Definition
Coacervation	The macroscopic liquid-liquid phase separation of a homogeneous polymer solution into liquid polymer-rich and polymer-dilute phases. The polymer-rich phase may exist as a single bulk phase or as a suspension of phase droplets in the continuous polymer-dilute phase. The intermolecular bonds in the polymer-rich phase are typically dynamic and transient in nature allowing for diffusion of the polyelectrolytes.
Coacervate	The resultant polymer-rich phase obtained in coacervation.
Precipitation	The liquid-solid transition that creates a polymer-dilute phase, and a polymer-rich solid. The precipitate (solid) phase is typically in a state of kinetic arrest.
Simple Coacervation	The formation of coacervates comprising of only one macromolecular species.
Complex Coacervation	Coacervation involving two or more macromolecular components.
Polyelectrolyte Complex (PEC)	Used interchangeably with ‘coacervate’ in this work to describe the liquid-like polymer-rich phase obtained in coacervation.

1.6 Chapter Overview

This thesis aims primarily to develop polyelectrolyte complex coacervate templated silica nanoparticle syntheses that provide particles with customisable and intrinsic functionality without post-synthetic modification steps.

It is discussed above that coacervation can readily form nanoscale complexes of varied composition through a number of physical pathways, but the reversible nature of coacervation makes the formulations liable to small changes in the environment. Silica nanoparticles however, typically exhibit good stability in biological media but offer very little intrinsic functionality, and typically require extensive synthetic protocols to retrospectively conjugate surface functional groups. The novel protocols developed herein will incorporate the ease of coacervate formation from polyelectrolytes of potentially desirable properties with the stability associated with colloidal silica answering the concerns commonly associated with both materials.

This is developed first in Chapter 3 with the formation of poly(acrylic acid)/L-arginine functionalised porous silica nanoparticles (PAA/Arg-PSiNPs) from polyelectrolyte complex templates. Initially, the alcohol-induced formation of PAA/Arg PECs is explored and discussed. The effects of varying the alcohol, PAA, and Arg concentration are systematically investigated with the aim of characterising the PEC formation mechanism, and producing monodispersed, nanoscale templates for SiNP synthesis. The size tunability of the PAA/Arg-SiNPs is demonstrated and the relationship between the particle size and template size, and its influence on the presentation of surface ligands, is described.

Chapter 4 discusses the application of the PAA/Arg-PSiNPs to cancer targeted and pH responsive drug delivery. The ability of anionic PAA at the particle surface and in the internal pore spaces to encapsulate and retain cationic anti-cancer therapeutic doxorubicin was investigated. Furthermore, the pH responsive release of the drug at pH values corresponding to physiological pH and the weakly acidic microenvironment were characterised. It was hypothesised that Arg at the surface of the SiNPs may confer enhanced cellular uptake into tumorigenic cells *via* the overexpressed cationic amino acid transporter. As such, the cancer targeting activity was assessed *in vivo* using fluorescently labelled PAA/Arg-PSiNPs with patient derived glioblastoma cells (GBM1 and GBM20) and non-tumorigenic neural progenitors (NP1). Finally, the combined efficacy of the pH responsive

release mechanism and enhanced cellular uptake was assessed in comparison to control particles.

Chapters 5 and 6 demonstrate the versatility of this synthesis by using a different combination of polyelectrolytes in the coacervate scaffold. First we investigated the alcohol-induced formation of poly(ethylenimine) (PEI) and glutamic acid (Glu) coacervates in Chapter 5. In addition to determining the optimum PEI and Glu concentrations for stable monodispersed PEC formation, the use of higher and lower alcohols was investigated to better understand the mechanism of coacervation. Further, the molecular weight of the PEI was systematically varied to probe its effects on PEC size, dispersity, and stability during the condensation of silica species. Chemical characterisation of the as-synthesised silica particles confirmed that the PEI was retained at the particle surface as to yield PEI-SiNPs with a strongly positive zeta potential.

The final results chapter (Chapter 6) addresses the application of the PEI-SiNPs. The presence of polycationic PEI at the nanoparticle surface facilitated electrostatic interaction with anionic polysaccharide hyaluronic acid (HA) in the formation of a physical nanocomposite hydrogel. To demonstrate the tuneable mechanical properties and better understand their physical origin, a rheological characterisation of the hydrogels prepared at varied reagent ratios was completed and compared to gels prepared with pristine PEI. The hydrogel is intended as a drug carrier to provide prolonged drug release at the disease site. As such, the hemocompatibility of the gels was assessed and its relationship to gel composition. In addition to its role in gelation, the surface bound PEI was expected to enable the loading of anionic cancer therapeutic methotrexate into the hydrogel matrix. As such the drug loading and release profiles were evaluated.

2 Materials and Methods

2.1 Materials

2.1.1 Arginine/Poly(acrylic acid) Polyelectrolyte Complex Templated Silica Nanoparticle Synthesis and Application

L-arginine (Arg) and ammonium hydroxide (28-30 wt% NH₃ solution in water) were purchased from Acros Organics. 2-Propanol (IPA; ≥ 99.7%) was purchased from VWR. Poly(acrylic acid) (PAA; Mw = 1800), 4-[3-(4-Iodophenyl)-2-(4-nitro-phenyl)-2H-5-tetrazolio]-1,3-benzene sulfonate (WST-1) reagent, and poly-L-ornithine were purchased from Sigma- Aldrich. Tetraethoxysilane (TEOS; 99.9%) was purchased from Alfa Aesar. Fluorescein isothiocyanate-poly(ethylene glycol) silane (FITC-PEG-silane; Mw = 5000) was obtained from Nanocs. Pierce BCA Protein Assay kit, DMEM/F-12 medium with GlutaMAX, neurobasal medium, B-27 supplement, N2 supplement, and mouse laminin protein were purchased from Thermo Fisher Scientific. Spectra/Por 7 regenerated cellulose dialysis tubing (1 kDa MWCO) was purchased from Spectrum Chemical. Recombinant human epidermal growth factors (rhEGF) and basic fibroblast growth factors (bFGF) were purchased from Bio Techne and doxorubicin HCl (Dox; 95%) was purchased from Fluorochem Limited. All chemicals were of analytical grade and used without further purification. Ultrapure water (Millipore Milli-Q) with 18.2 MΩ cm resistivity at 25 °C was used in all experiments.

2.1.2 Poly(ethyleneimine)/Glutamic Acid Polyelectrolyte Complex Templated Silica Nanoparticle Synthesis and Poly(ethyleneimine)-Silica Nanoparticle/Hyaluronic Acid Hydrogel Formation

Branched polyethylenimine (PEI; $M_w = 25,000$, $M_n = 10,000$), Sodium hydroxide (pellets; $\geq 98\%$), cetrimonium bromide (CTAB; $\geq 98\%$), and polyacrylic acid (PAA; $M_w = 1800$) were purchased from Sigma Aldrich. Glutamic acid (Glu; 99%), L-Arginine (Arg; 98%), and phosphoric acid (85%) were purchased from Acros Organics. 2-propanol (IPA; $\geq 99.7\%$) was purchased from VWR. Tetraethoxysilane (TEOS; 99.9%) and hyaluronic acid sodium salt (HA; streptococcus equi, 91%, $M_w \geq 1.0 \times 10^6$ Da) were purchased from Alfa Aesar. Methotrexate sodium salt (MTX) was purchased from Toku-E, and Coomassie brilliant blue g-250 (CBBG) was purchased from Cayman Chemical Company. Ultrapure water (Millipore Milli-Q) with $18.2 \text{ M}\Omega \cdot \text{cm}$ resistivity at 25°C was used in all experiments.

2.2 Arg/PAA Polyelectrolyte Complex Templated Silica Nanoparticle Synthesis

2.2.1 Preparation of Arginine/Poly(acrylic acid) Polyelectrolyte Templates

To study the IPA-induced formation of Arg/PAA polyelectrolyte complexes (PECs) and determine the optimum water/alcohol ratio, Arg and PAA were first mixed in binary solvents of increasing IPA volume fraction. $100 \mu\text{L}$ of $1.1 \times 10^1 \text{ mM}$ PAA and $295 \mu\text{L}$ of $8.6 \times 10^2 \text{ mM}$ Arg were first added to $1605 \mu\text{L}$ of ultrapure water (2.0 mL final volume) before the solution was dispersed in an ultrasonic bath for 5 min. 0 – 8.0 mL of IPA was added under magnetic stirring at room temperature and the final volume was topped up with to 10.0 mL with ultrapure water and left to stir for 1 h.

For the synthesis of PEC templates with varying amounts of PAA or Arg an 80 % (v/v) IPA solvent was used. The total aqueous volume was maintained at 2.0 mL while the concentration of each reagent was varied, and 8.0 mL of IPA was added under stirring.

To form NH₄OH/PAA PECs, the same procedure was followed but with an equimolar amount of NH₄OH used in place of Arg. The final pH was 9.0 for both Arg/PAA and NH₄OH/PAA PECs.

2.2.2 Synthesis of Arg/PAA and NH₄OH/PAA Porous Silica Nanoparticles

For the porous silica nanoparticle (PSiNP) syntheses presented herein, PECs were prepared as described in Section 2.2.1 with 100 μ L of 1.1×10^1 mM PAA and 295 μ L of 8.6×10^2 mM Arg (or 295 μ L of 8.6×10^2 mM NH₄OH) in 80% v/v IPA (10 mL final volume). Subsequently, between 20-500 μ L of tetraethoxysilane (TEOS) was added and the mixture was stirred at room temperature for 24 h. The final product was collected by centrifugation ($17,000 \times g$ for 1 h) and purified by rinsing thrice with ultrapure water.

The reaction was also scaled up to 250 mL by increasing the volume of each reagent used by 25-fold using the same synthetic protocol.

Fluorescein isothiocyanate (FITC)-labelled PSiNPs were synthesised by the addition of ~ 0.1 mol % of FITC-PEG-silane and 1000 μ L of TEOS to 250 mL final volume of the PEC templates in 80% v/v IPA.

2.3 Quantification of Doxorubicin Loading and Release from Arg/PAA-PSiNPs and NH₄OH/PAA-PSiNPs

As discussed in Chapter 4, Arg/PAA-PSiNPs and NH₄OH/PAA-PSiNPs were loaded with anticancer therapeutic doxorubicin hydrochloride (Dox) and the drug release profile over time was quantified in buffers prepared at pH 5.0 and 7.0.

For the loading of Dox in the PSiNPs, 2 mg of as-synthesised Arg/PAA-PSiNPs or NH₄OH/PAA-PSiNPs were suspended in 1, 2, or 4 mg mL⁻¹ of Dox solution (1.0 mL). The mixture was stirred at room temperature under dark conditions for 48 h. The Dox-loaded particles were collected by centrifugation ($17,000 \times g$ for 10 min) and rinsed thrice with ultrapure water to remove excess drug. To determine the drug loading capacity, the amount of non-encapsulated drug remaining in the supernatants from each rinse was determined by

UV-vis-NIR spectroscopy at 480 nm; using a standard calibration curve prepared from solutions of known Dox concentrations (Figure 2.1).

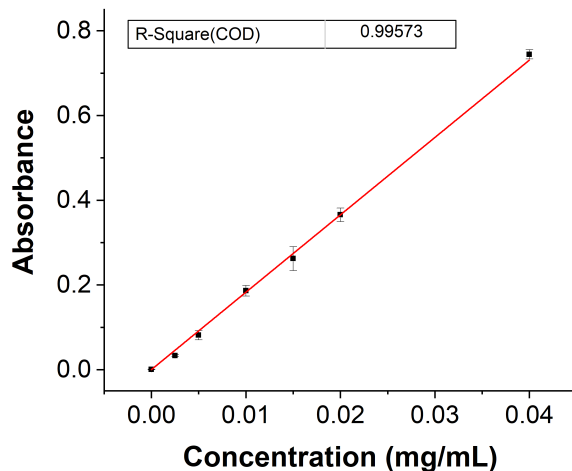


Figure 2.1 A calibration plot of Dox in ultrapure water obtained using UV-vis-NIR spectroscopy at 480 nm used to determine the amounts of Dox loaded and released from Arg/PAA-PSiNPs and NH₄OH/PAA-PSiNPs.

The total amount of non-encapsulated drug in the supernatants was subtracted from the initial amount of drug added to determine the mass of drug loaded into the PSiNPs. The drug loading capacity was calculated using the following formula:

$$\text{Drug loading capacity (\%)} = (\text{Mass of loaded drug})/(\text{Mass of particles}) \times 100\%$$

Eq. 2-1

To quantify the drug release rate, 9 mg of dox-loaded Arg/PAA-PSiNPs or NH₄OH/PAA-PSiNPs were suspended in 2.0 mL of water and transferred to a dialysis bag (1 kDa MWCO). The samples were dialysed against 50 mL of 1 × PBS (pH 7.4) or 239 mM sodium acetate buffer (pH 5.0) with equivalent ionic strengths at 37 °C under magnetic stirring. At regular time points, 1.0 mL of the dialysate was removed for analysis of Dox concentration and replaced with fresh buffer. The amount of drug released was quantified using UV-vis spectroscopy at 480 nm. The drug release kinetics and mechanisms were evaluated using the Korsmeyer-Peppas model:¹⁰¹

$$F = k_m t^n$$

Eq. 2-2

Where F is the fraction of drug released, k_m is the kinetic constant dependent on the structural and geometric properties of the particles, and n is the release exponent which indicates the drug release mechanism (Table 1). Data points up to 60% of drug release in the cumulative release curves were plotted on logarithmic scales, and the release exponent, n, was found from the gradient. The value for n was then substituted into Eq 2-2 to find the kinetic constant, k_m .

Table 1 Diffusion coefficients derived from the Korsmeyer-Peppas equation and their corresponding drug release mechanisms.¹⁰¹

Release Exponent (n)	Drug Diffusion Mechanism
0.5	Fickian diffusion
$0.5 < n < 0.85$	Anomalous non-Fickian diffusion
0.85	Case-II transport
$n > 0.85$	Super Case-II transport

2.4 Live Cell Experiments

2.4.1 Preparation of Culture Flasks and Well Plates

Flasks and well plates used in the culture of patient derived glioblastoma cells GBM1 and GBM20 were coated with poly-L-ornithine and mouse laminin.

Under sterile conditions, 75 μ L of 10 mg/mL poly-L-ornithine was added to 150 mL of ultrapure water and passed through a 0.22 μ m vacuum filter. 10 mL of the ornithine solution was added to each T75 flask, 3 mL per T25, and 43 μ L per well of the 96 well plates before incubation at room temperature for 1 h. Separately, 300 μ L of laminin was added to 150 mL

of phosphate buffered saline (PBS) and filtered in a 0.22 μm vacuum flask. The flasks were aspirated and rinsed with 5 mL of sterile ultrapure water before the addition of 10 mL of laminin to each T75 flasks, 3 mL to each T25, and 43 μL to each well of the 96 well plates. After incubation at room temperature overnight, the flasks were stored at $-20\text{ }^{\circ}\text{C}$ for up to 6 months. Immediately before use, each flask was thawed at room temperature, aspirated, and rinsed once with PBS.

2.4.2 Cell Culture

Patient-derived glioblastoma GBM1 and GBM20 cells, which have been confirmed to retain the histopathological features of their parent tumours,^{102,103} were cultured on poly-L-ornithine and laminin-coated T75 cell culture flasks in neurobasal medium supplemented with $0.5 \times \text{B-27}$, $0.5 \times \text{N-2}$, 40 ng/mL human fibroblast growth factor (bFGF), and 40 ng/mL recombinant human epidermal growth factor (rhEGF). Primary non-tumourigenic adult brain neural progenitor NP1 cells were cultured in Dibeco's modified eagle medium (DMEM)/F-12 medium supplemented with $0.5 \times \text{B-27}$, $0.5 \times \text{N-2}$, 20 ng/mL bFGF, and 20 ng/mL rhEGF, $1 \times \text{GlutaMax-1}$, and 5% fetal bovine serum. The cells were stored at $37\text{ }^{\circ}\text{C}$ with 5% CO_2 in a humidity-controlled incubator.

Each cell type was subcultured approximately every 4 days dependent on the rate of proliferation and confluency. Each flask was aspirated and then incubated with TrypLE dissociation reagent for 5 mins. 5 mL of media was added to deactivate the TrypLE and the cells were pelleted with centrifugation. The supernatant was replaced with fresh media and typically one third of the resultant cell suspension was added to a new T75 flask.

For long-term storage, each cell type could be frozen in a cryovial in cell culture media supplemented with 10 % dimethylsulfoxide (DMSO). The vials were frozen overnight in a Mr Frosty Freezing Container containing IPA in a $-80\text{ }^{\circ}\text{C}$ freezer before storage in the vapour phase of liquid nitrogen.

2.4.3 Cytotoxicity Studies

To assess their therapeutic efficacy, the cytotoxicity of the empty and Dox-loaded Arg/PAA-PSiNPs and $\text{NH}_4\text{OH/PAA-PSiNPs}$ was determined using the WST-1 assay. GBM1, GBM20,

and NP1 cells were seeded at a density of 8×10^3 cells per well in 96-well plates and left to adhere for 24 h. The cell culture media was replaced with fresh media containing 5 – 750 $\mu\text{g mL}^{-1}$ of PSiNPs or Dox-loaded PSiNPs containing 0.01 – 50 μM of Dox and incubated for 24 h. After incubation, the cells in each well were rinsed with PBS, and 100 μL of fresh media containing 10 μL of WST-1 reagent was added to each well. The cells were then incubated for 2 h at 37 °C before the absorbance was determined at 440 nm using a microplate spectrophotometer (Molecular Devices SpectraMax M2e). Blank wells containing cell culture media and WST-1 (without cells) were included to determine the background absorbance. The cell viability of treated cells was determined by comparison to untreated controls as follows:

$$\text{Cell viability (\%)} = [(A_{\text{Treated}} - A_{\text{Background}})/(A_{\text{Untreated Control}} - A_{\text{Background}})] \times 100\% \quad \text{Eq. 2-3}$$

Equation 2.4 was used to find the EC_{50} , where y is the cell viability, x is the drug concentration, $\log x_0$ is the concentration of half response (EC_{50}), p is the hill slope, and A_1 and A_2 are the top and bottom asymptotes respectively.

$$y = A_1 + \frac{A_2 - A_1}{1 + 10^{(\log x_0 - x)p}} \quad \text{Eq. 2-4}$$

2.4.4 Cellular Uptake Studies

GBM1, GBM20, and NP1 cells were seeded at a density of 8×10^3 cells per well in 96-well plates and allowed to adhere for 24 h. The cells were incubated with fresh media containing 200 $\mu\text{g mL}^{-1}$ FITC-labelled Arg/PAA-PSiNPs and NH_4OH /PAA-PSiNPs for 4 h before carefully rinsing the cells 5 times with PBS to remove non-internalised PSiNPs. The cells were lysed with 1% v/v triton-X100 in PBS and the fluorescence intensity of the lysate was determined at 420 nm excitation and 518 nm emission wavelengths with a microplate spectrophotometer. To determine the concentration of PSiNPs taken up by the cells, the measured fluorescence intensity was compared to a calibration curve prepared from known FITC-labelled PSiNP concentrations in the same 1% v/v Triton X-100 solution. The protein content of each well was determined using the BCA protein quantification assay. 15 μL of

the cell lysate was added to 200 μL of BCA reagent in a 96-well plate, and incubated at 37 $^{\circ}\text{C}$ for 30 min. The absorbance was measured at 562 nm with a microplate spectrophotometer and compared to a calibration curve prepared from known concentrations of bovine serum albumin.

For fluorescence imaging, cells were seeded onto 8-well chamber slides and treated with 200 $\mu\text{g mL}^{-1}$ of FITC-labelled Arg/PAA-PSiNPs and $\text{NH}_4\text{OH/PAA-PSiNPs}$. After 4 h incubation, the cells were rinsed 5 times with PBS and transferred to heated stage at 37 $^{\circ}\text{C}$ for imaging using a confocal laser scanning microscope (Leica DMI8/SP8).

2.4.5 Statistical Analysis

Results obtained from cell uptake experiments were analysed using the two-tailed Student's *t*-test to determine statistical significance. Differences between treatment groups were considered to be statistically significant when $P < 0.05$.

2.5 PEI/Glu Polyelectrolyte Complex Templated Silica Nanoparticle Synthesis

2.5.1 Preparation of PEI/Glu Polyelectrolyte Templates

To first determine the optimum water/alcohol ratio for the formation of PEI/Glu PECs, PEI and Glu were mixed in binary solvents of IPA volume fraction between 0 – 90 % (v/v). 200 μL of 5.45×10^1 mM Glu and 62.5 μL of 1.28×10^0 mM PEI were added to 737.5 μL of ultrapure water to a final volume of 1 mL. Between 0 – 9.0 mL of IPA was added under magnetic stirring at room temperature and the final volume was topped up to 10.0 mL with ultrapure water to give the desired IPA volume fraction and left to stir for 1 h.

To evaluate the effect of varying the PEI and Glu amounts an 80 % (v/v) IPA solvent was used. With the total aqueous volume kept constant at 2.0 mL, the concentration of each reagent was systematically varied before the addition of 8.0 mL of IPA. The optimum reagent

volumes were identified as 500 μL of 1.28×10^0 mM PEI and 200 μL of 5.45×10^1 mM Glu added to 1300 μL of ultrapure water to make a total volume of 2.0 mL before IPA addition.

To study the synthesis of PEI/Glu PEC templated SiNPs, the PEC synthesis was first scaled up 25-fold to a total volume of 250 mL while keeping all reagent ratios and concentrations the same. 12.5 mL of 1.28×10^1 mM PEI and 5 mL of 5.45×10^1 mM Glu were added to 32.5 mL of ultrapure water before the addition of 200 mL of IPA.

2.5.2 Synthesis of PEI-SiNPs

For the synthesis of PEI-SiNPs, PEC templates were prepared as described in Section 2.5.1 with 12.5 mL of 1.28×10^0 mM PEI and 5 mL of 5.45×10^1 mM Glu in a 250 mL total volume of 80% IPA (v/v). With the temperature maintained at 40 °C in a water bath, 1 mL of TEOS was added under stirring. After 24 h, the final product was purified by centrifugation at $17,000 \times g$ for 1 h and rinsed thrice with ultrapure water.

2.6 PEI-SiNP/HA and PEI/HA Nanocomposite Hydrogel Formation

2.6.1 Quantification of SiNP surface-bound PEI Concentration

For the future use of PEI-SiNPs in the formation of physical nanocomposite hydrogels, the concentration of SiNP surface bound PEI must be known.

To prepare a stock of coomassie stain, 8.5 mg of coomassie brilliant blue (CBBG) was dissolved in 4.1 mL of 95% ethanol and added to 8.4 mL of 85% phosphoric acid and 37.5 mL of ultrapure water. CBBG binds electrostatically with charged amines through its anionic sulfonic acid groups, where the number of bound dye molecules is proportional to the number of cations. This binding causes a colour change from blue to red-brown. To quantify the concentration of PEI conjugated to the PEI-SiNP surface, 200 μL of coomassie stock solution was added to 100 μL of diluted nanoparticle solution in a 96 well plate and after 5 minutes incubation, the absorbance was measured at 595 nm with the Molecular Devices SpectraMax M2e plate reader. The concentration of PEI at the PEI-SiNP surface was determined by comparison of absorbance values to a calibration curve of known PEI concentrations (Figure 2.2).

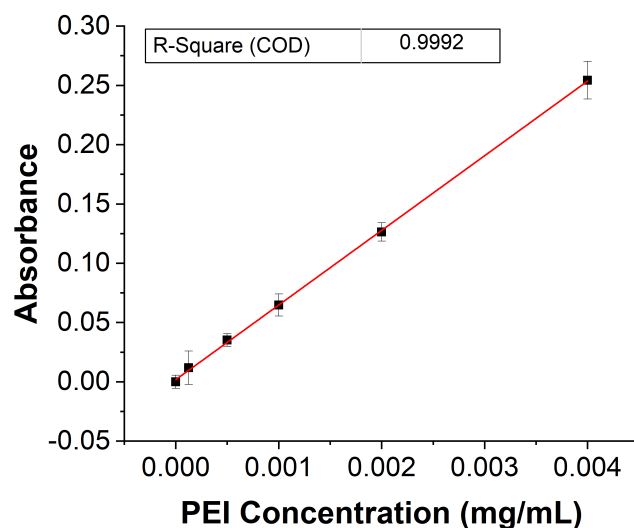


Figure 2.2 A calibration plot of obtained from the absorbance of CBBG dye at 595 nm with increasing concentration of PEI.

2.6.2 PEI-SiNP/HA Hydrogel Formation

For the preparation of PEI-SiNP/Hyaluronic Acid (HA) gels, 200 μL of PEI-SiNP stock containing 67.2 μM of silica surface bound PEI (3.65 mM PEI monomers) and 58.4 μL of 10 μM HA (25 mM HA monomers) were added to 36.6 μL of ultrapure water. After mixing using a vortex mixer, a suspension of white precipitates was formed. To this, 5 μL of 2 M hydrochloric acid was added (total volume 300 μL) before further mixing with a vortex mixer to induce the formation of a coacervate hydrogel in which a colourless liquid is formed above the white hydrogel. For the synthesis of PEI/HA gels, the same protocol was followed but with an equimolar solution of PEI in place of PEI-SiNPs. For the formation of gels with varied PEI and HA concentration the total volume was maintained at 300 μL .

2.6.3 Quantification of Residual PEI in the Supernatant after PEI-SiNP/HA Hydrogel Formation

To quantify the residual PEI remaining after hydrogel formation, 200 μ L of Coomassie stain (prepared as described in Section 2.6.1) was added to 100 μ L of diluted supernatant collected after hydrogel formation in a 96 well plate. After incubation for 5 min, the optical absorbance was measured at 595 nm and compared to a calibration curve of known PEI concentrations (Figure 2.2).

Control measurements were performed with HA and PEI-SiNPs without the CBBG dye. Neither had a significant contribution to the measurement of the PEI concentration in the supernatant.

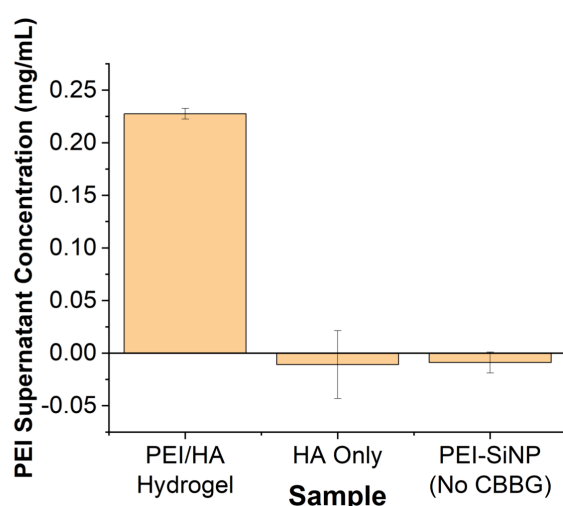


Figure 2.3 Control measurements of HA with the CBBG assay and PEI-SiNPs without the CBBG dye showing their negligible contribution to the measured PEI concentration. A typical PEI concentration measurement from the hydrogel supernatant is included for comparison.

2.6.4 Quantification of Residual HA in the Supernatant After PEI-SiNP/HA Hydrogel Formation

To evaluate the concentration of HA in the gel supernatants, the CTAB turbidimetric method was used. Electrostatic complexation of polyanionic HA and cationic CTAB forms insoluble

precipitates whose turbidity is proportional to the concentration of HA¹⁰⁴. The assay solution was prepared by dissolving 2.5 g of CTAB in 100 mL of 2% (w/v) NaOH. 100 μ L of CTAB solution was added to 50 μ L of the hydrogel supernatant in a 96 well plate and incubated for 10 min. The absorbance was measured at 600 nm and compared to a calibration curve of known HA concentrations (Figure 2.4). Control measurements were completed with PEI and PEI-SiNPs to show their negligible contribution to the measure HA concentration (Figure 2.5).

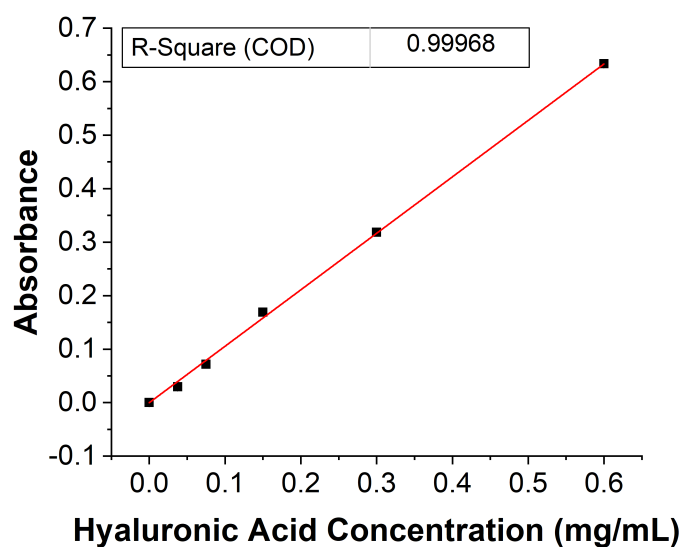


Figure 2.4 The calibration plot obtained from the CTAB turbidimetric assay used to determine the hyaluronic acid concentration remaining in the supernatant after PEI-SiNP/HA hydrogel formation.

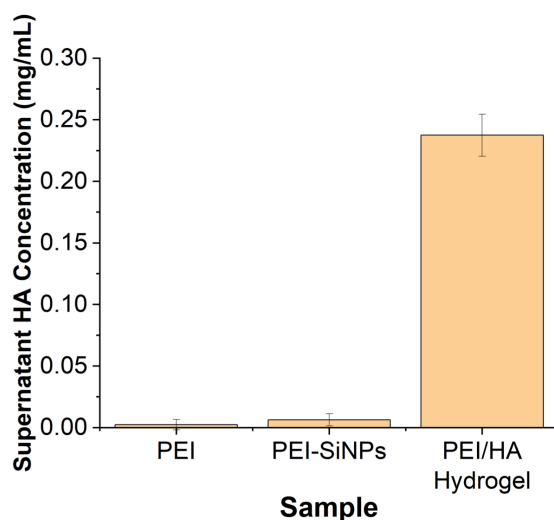


Figure 2.5 Control measurements of PEI and PEI-SiNPs in the HA concentration quantification assay with an exemplary PEI/HA hydrogel measurement to compare.

2.7 Nanoparticle Characterisation

2.7.1 Dynamic Light Scattering

The hydrodynamic diameters of the PECs and SiNPs were determined by dynamic light scattering (DLS) using Zetasizer Nano equipped with a 633 nm He-Ne laser and with scattered light detected at 173° (Malvern Instrument Ltd., Worcestershire, UK).

To measure the size distribution of a particle suspension, a scattering pattern caused by constructive and destructive interference between scattering events is collected from monochromatic light incident on the particle dispersion. As the particles diffuse with Brownian motion, the observed scattering intensity fluctuates with time. The correlation between successive light scattering patterns contains information about the time scales of particle movement and hence their hydrodynamic radii. This correlation is characterised by an autocorrelation function, $g(\tau)$, defined in Eq. 2-5.¹⁰⁵

$$g^2(\tau) = \frac{\langle I(t_0)I(t_0 + \tau) \rangle}{\langle I(t_0) \rangle^2}$$

Eq. 2-5

where $I(t_0)$ is the scattered light intensity at time $t = 0$, and $I(t_0 + \tau)$ the intensity after delay time τ . For a perfectly monodisperse population the autocorrelation function is described by the single exponential decay given in Eq. 2-6:

$$g(\tau) = e^{-\Gamma\tau} \quad \text{Eq. 2-6}$$

τ is the delay time, Γ is the decay rate given by $\Gamma = Dq^2$ with q as the scattering vector, and D as the translational diffusion coefficient. The scattering vector is defined as follows:

$$q = \frac{4\pi n}{\lambda} \sin \frac{\theta}{2} \quad \text{Eq. 2-7}$$

where λ is the wavelength of incident light, n is the refractive index, and θ is the angle of detection; and the hydrodynamic radius of the particles can be obtained from the diffusion coefficient using the Stokes-Einstein relation (Eq. 2-8).

$$D = \frac{k_B T}{6\pi\eta R} \quad \text{Eq. 2-8}$$

with k_B as the Boltzman constant, T is the temperature, η is the solvent viscosity, and R is the hydrodynamic radius of a sphere.

Throughout this thesis, the shape of the correlation function is used as a descriptor of PEC formation. As described above, the correlation function for a monodispersed population is characterised by a single exponential decay, while polydisperse populations show poor correlation described by multiple exponential decay functions (Figure 2.6). Hence, when investigating the onset of alcohol induced PEC formation the shape of the correlation curve was observed.

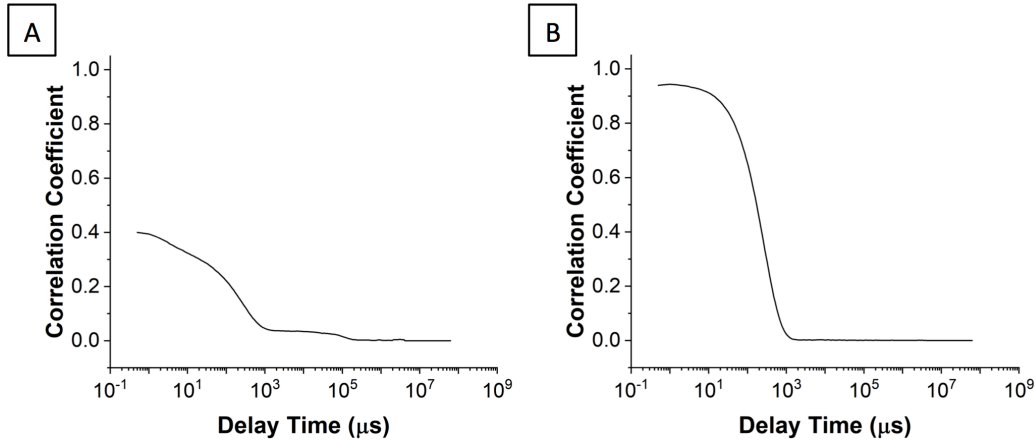


Figure 2.6 Example correlation data from DLS measurements. (A) A ‘poor’ correlation curve characterised by several exponential decay functions indicative of a polydisperse sample. (B) A ‘good’ correlation function with a y-intercept close to 1, and a smooth, single exponential decay profile.

In addition, the y-intercept of the plot of correlation against time is an indicator of the measurement signal-to-noise ratio, where values closer to 1 indicate high signal and are typically representative of stable particle formation. For ease of interpreting the relationship between alcohol concentration and PEC formation, the y-intercept as a function of alcohol volume fraction is presented and used as a preliminary assessment in conjunction with the correlation curve shape, the hydrodynamic radii and PDI, and the intensity weighted size distributions.

To obtain the z-average diameter and polydispersity index (PDI) values, the cumulants analysis method is used. For a monomodal but not perfectly monodisperse sample, $g(\tau)$ is treated as the sum of several exponential decay functions, each representative of a different particle size, multiplied by a function $G(\Gamma)$ describing the distribution of decay rates.

$$g(\tau) = \int G(\Gamma)e^{-\Gamma\tau}d\tau \tag{Eq. 2-9}$$

where

$$\int G(\Gamma)d\Gamma = 1 \tag{Eq. 2-10}$$

This is expanded using cumulant analysis to give Eq. 2-11 where $\bar{\Gamma}$ is the mean of $G(\Gamma)$, the first cumulant, $e^{-\bar{\Gamma}\tau}$, is used to find the average diameter as described above, and the second cumulant, $\frac{k_2}{\bar{\Gamma}^2}$, gives the PDI.

$$g(\tau) = e^{-\bar{\Gamma}\tau} \left[1 + \frac{1}{2} \frac{k_2}{\bar{\Gamma}^2} (\bar{\Gamma}\tau)^2 - \frac{1}{3!} \frac{k_3}{\bar{\Gamma}^3} (\bar{\Gamma}\tau)^3 + \dots \right]$$

Eq. 2-11

with

$$k_n = \int (\Gamma - \bar{\Gamma})^n G(\Gamma) d\Gamma$$

Eq. 2-12

This method however assumes a monomodal distribution and is hence not suitable for polydisperse samples.¹⁰⁵⁻¹⁰⁷

For broad monomodal or multimodal populations, other analytical approaches are required. Typically the non-negative least squares (NNLS) and constrained regularization method for inverting data (CONTIN) are applied to yield full size distributions^{108,109}. Notably, in the Rayleigh approximation the intensity of scattered light is proportional to the particle size to the 6th power (d^6). As such, the contributions of large particles in broad size distributions can lead to over estimation of the peak particle diameters.

For measurement, each 1 mL sample was run thrice in a polystyrene cuvette with 12 measurements per run at 25 °C, and the hydrodynamic diameters, polydispersity indices, and size distributions are displayed as the mean \pm standard deviation of the three runs.

2.7.2 Zeta Potential

The stability of a nanoparticle dispersion in a polar solvent is commonly mediated by charge, where electrostatic repulsion between particles of the same charge will prevent aggregation. Additionally, the surface charge of a nanoparticle population at a known pH can provide information about the chemical groups present at the surface and hence the success of any synthetic functionalisation steps.

Around a charged particle in a polar solvent exists a layer of strongly bound ions, known as the stern layer, which move as one with the particle. Beyond this, weaker electrostatic interactions between the particle and the solvated ions give rise to a slipping plane between fixed and diffuse ions in surrounding medium. The zeta-potential is defined as the potential between a point far away in the medium and this slipping plane at the edge of the electric double layer (Figure 2.7).

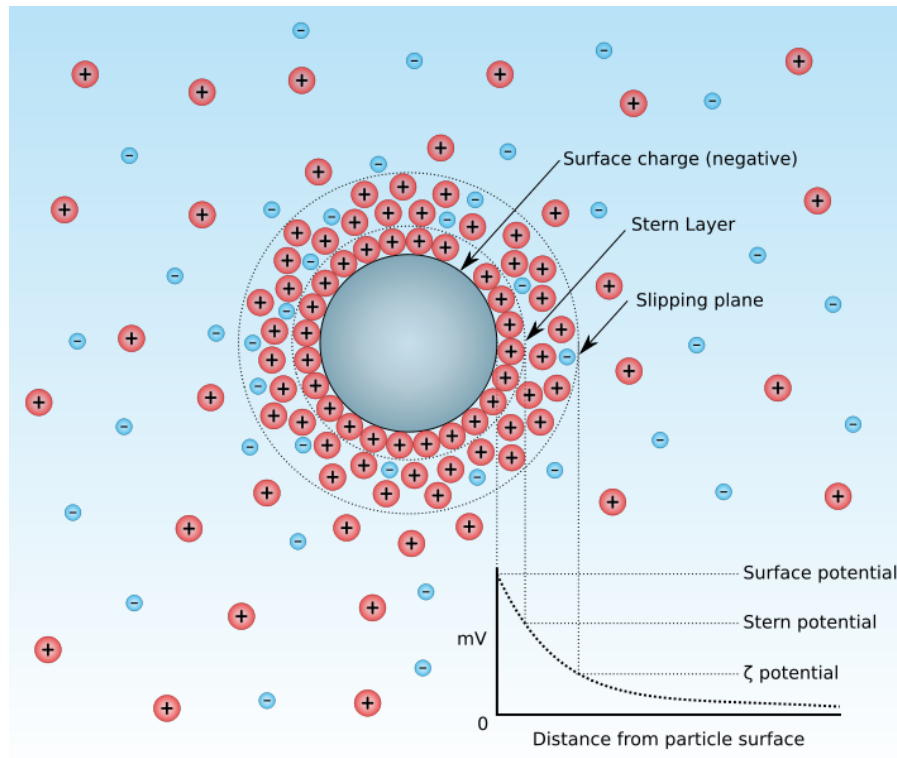


Figure 2.7 The stern layer and slipping plane created by ions bound to a charged particle in a polar solvent, and their relation to the zeta potential. Reproduced with permission under a CC BY-SA licence.¹¹⁰

As the potential is dependent on the surface charge density, nanoparticles with a high concentration of ionic functional groups or surface-bound ligands show more strongly positive or negative zeta-potentials and greater colloidal stability. As such, changes to the ionisation state at the particle surface in solvents of differing pH can have significant effects on the particle stability and must be controlled during zeta-potential measurement. This is also true of the ionic strength of the medium, where high ion concentrations decrease the thickness of the dielectric double layer and screen electrostatic interactions between colloids.

The determination of a particle's zeta-potential is most commonly achieved through measurement of the electrophoretic mobility. Referring to the velocity, v , of a charged particle in an infinite liquid under an applied electric field, E , electrophoretic mobility is defined as:¹¹¹

$$\mu_E = \frac{v}{E}$$

Eq. 2-13

This is related to the zeta-potential as follows:

$$\mu_E = \frac{\epsilon\zeta}{\eta}$$

Eq. 2-14

where ϵ is the permittivity, ζ is the zeta-potential, and η is the viscosity of the medium.

The particle velocity due to electrophoresis is measured using DLS. As described in Section 2.7.1, monochromatic light incident on a particle dispersion creates a scattering pattern which, due to Brownian motion of the particles and interference between scattering events, changes as a function of time and are used to determine the translational diffusion coefficient. In this instance however, movement of the particles occur under the influence of an electric field, and hence the correlation function is a combination of Brownian motion and electrophoresis (Eq. 2-15).¹¹¹

$$g(\tau) = Ae^{\pm iqv\tau}e^{-q^2D\tau}$$

Eq. 2-15

where A is some constant and v is the particle velocity used in Eq. 2-13.

For measurement, 1 mL of sample in an aqueous buffer of known pH and ionic strength was analysed in a folded capillary cell at 25 °C. The results are reported as the mean \pm standard deviation of the three runs.

2.7.3 Transmission Electron Microscopy

Using optical microscopy, the minimum achievable resolution is described by the Abbe limit:

$$d = \frac{\lambda}{2n \sin \theta}$$

Eq. 2-16

In this equation, d is the minimum resolvable distance, λ is the wavelength of light incident on the sample, and $n \sin(\theta)$ gives the numerical aperture with n as the material refractive index and θ as half the convergence angle of the lens focus. With optical wavelengths and a typical numerical aperture (~ 0.9) the maximum resolution is approximately several hundred nanometers, which is not suitable for the study and imaging of nanomaterials.

As described by wave-particle duality, the De Broglie wavelength for massive particles of momentum p , is given as:

$$\lambda = \frac{h}{p}$$

Eq. 2-17

Hence, the use of a focused electron beam, whose wavelength and hence diffraction limit is dependent on their momentum, may reach significantly lower resolution and are commonly used for the analysis of nanoparticle and nanostructured materials.

Transmission electron microscopy (TEM) uses electrons accelerated through a potential difference and focussed with condensing lenses to illuminate the sample. The incident electrons are then either scattered, absorbed by the sample, or pass through the sample grid onto the charge-coupled-device detector, thus creating a 2D image of the sample.

Herein, TEM imaging was performed with the FEI technai G²-Spirit microscope operated at 120 kV with a Gatan Ultrascan 4000 camera. To prepare silica nanoparticle samples for TEM imaging, 5 μ L of aqueous sample was pipetted onto a carbon coated copper grid and allowed to air dry. Particle solutions were used as synthesised without additional staining.

For all TEM size analysis presented, the size distributions were obtained using ImageJ analysis software. The data presented in Chapter 3 obtained for approximately spherical particles was obtained by measuring the largest diameter of each particle (Figure 2.8).

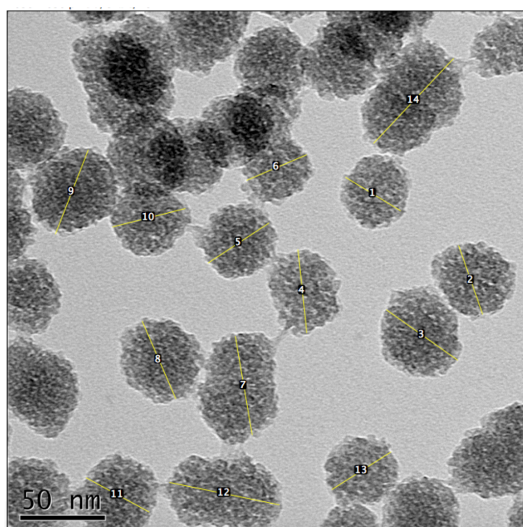


Figure 2.8 Example size analysis as completed for particles presented in Chapter 3, showing the particle diameter measured with imageJ analysis software.

To characterise the asymmetrical particles presented in Chapter 5, the reported size was defined as the major axis of the smallest possible ellipse that may encompass the whole particle (Figure 2.9)

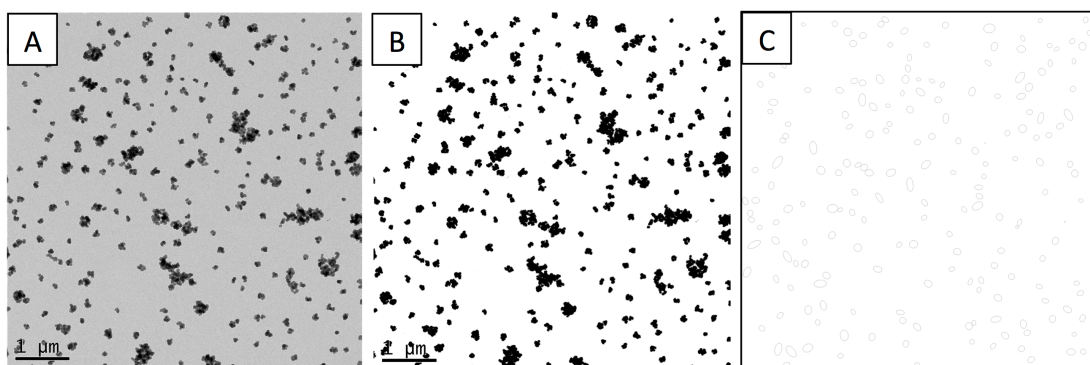


Figure 2.9 TEM size analysis of asymmetric SiNPs. (A) A typical TEM image of SiNPs (presented in Chapter 5), (B) the image after binary conversion using imageJ software, (C) ellipses drawn around each particle used for size calculation.

When the nanoparticle solution dries onto the TEM grid in sample preparation, it is common for particles to cluster together to giving to appearance of very large particles. Further,

discrete particles that overlap in the image are recognised as one particle in the automated sizing process. To provide a representative size distribution, a size exclusion parameter was placed to omit large clusters of overlapping particles (Figure 2.10).

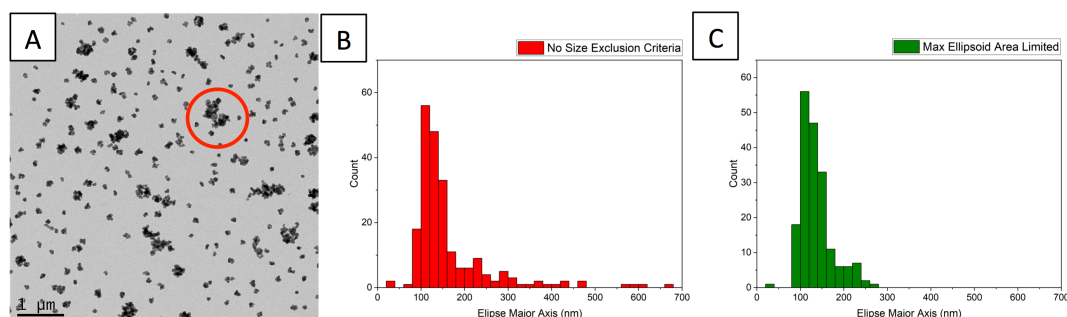


Figure 2.10 A TEM image (A) and corresponding size histograms without (B) and with (C) a size exclusion parameter to omit drying effects and overlapping particles from automated size analysis.

2.7.4 UV-Vis-NIR Spectroscopy

UV-VIS-NIR spectroscopy was used in this work to confirm the presence of SiNP-conjugated fluorescent dyes and to quantify the amount of anti-cancer drug encapsulated into the drug delivery systems.

The absorbance spectrum of a sample is determined by measuring the intensity of monochromatic light transmitted through a cuvette containing of the dispersion of interest over a range of wavelengths. The light intensity at the detector is compared to a 'blank' containing the same solvent or dispersant in an identical cuvette to obtain the sample absorbance as a function of wavelength.

The absorbance spectra for FITC-labelled PAA/Arg PSiNPs and NH₄OH/PAA-PSiNPs presented in Chapters 3, and spectra used for the quantification of the Doxorubicin loading capacity and release rate for Dox-loaded PAA/Arg-PSiNPs and NH₄OH/PAA-PSiNPs in Chapter 4 were collected with an Agilent Technologies Cary Series UV-Vis-NIR spectrophotometer.

2.7.5 Fluorescence Spectroscopy

Fluorescence spectroscopy is the measurement of fluorescent emission intensity of a sample as a function of wavelength. Typically, a monochromatic light source is used to excite the sample contained in cuvette, while a second monochromator is used at the detector to measure the intensity of fluorescence emission. For the fluorescence spectroscopy measurements presented herein the excitation wavelength was held constant and the emission intensity was measured across a range of wavelengths.

The FITC-conjugated SiNP spectra presented in this thesis were collected with the Edinburgh Instruments FLS 980 spectrometer. Typically, 1 mL of sample (~ 0.1 mg/mL) was excited at 488 nm in a quartz cuvette with 10 mm path length. The emission counts were accumulated over 3 repeat measurements recorded between 375 – 650 nm at intervals of 0.5 nm with a dwell time of 1 s.

2.7.6 Thermogravimetric Analysis

In thermogravimetric analysis (TGA) the mass of a sample is recorded as it is heated over time. This provides information about thermal stability and by comparison to reference spectra was used here to confirm the presence of specific organic functionalities on the nanoparticle internal and external surfaces.

Prior to analysis, SiNPs were lyophilised and approximately 20 mg was added to a crucible of known mass. Measurements were performed between 30 – 650 °C with the Mettler Toledo TGA/DSC Star System at a heating rate of 10 °C min⁻¹ under nitrogen flow. The first derivative of the mass as a function of temperature was used to identify thermal degradation peaks for comparison to spectra recorded of unreacted reagents. Pristine reagents were analysed for comparison and used without additional purification.

2.7.7 Fourier-Transform Infrared Spectroscopy

To confirm the presence of polymeric and amino acid functionality on the synthesised SiNPs, Fourier transform infrared spectroscopy (FTIR) spectroscopy was used throughout this thesis.

FTIR is a technique used to determine how much light is absorbed by a sample as a function of wavenumber. A broadband light source is used with a Michelson interferometer before passing through the sample to a detector, which records the light intensity as a function of time as the mirror position in the interferometer changes. The Fourier transform of the resultant interferogram is a plot of the signal intensity as a function of wavenumber and may be compared to the background to obtain the FTIR spectra of the sample. As molecules in the sample selectively absorb at characteristic wavelengths determined by their vibrational energy gap, peaks in the FTIR spectra may be assigned to specific functional groups. Most commonly solid samples are prepared for FTIR by incorporation into a pellet made of potassium bromide. The pellet acts as a carrier and is itself optically transparent in the infrared.

Attenuated total reflection (ATR) FTIR is a technique used to analyse samples without additional preparation. The internal reflection of incident light from the interferometer inside an ATR crystal causes an evanescent wave that will typically penetrate several microns into the sample dispersed in intimate contact with the crystal surface.

For the analysis of Arg/PAA-PSiNPs and NH₄OH/PAA-PSiNPs presented in Chapter 3, the ATR-FTIR spectra were collected using the Thermo Scientific Nicolet iS10 equipped with the Thermo Scientific Smart iTX ATR sampling accessory. In Chapter 5, PEI-SiNPs were prepared into a KBr pellet for analysis in the FTIR transmission mode also with the Thermo Scientific Nicolet iS10. Spectral data was collected between 650 – 4000 cm⁻¹ with a spectral resolution of 2 cm⁻¹. The as-synthesised PSiNP spectra were compared to reference spectra of pristine reagents to confirm their presence as internal and external particle functionalities.

2.7.8 Gas Adsorption Porosimetry

Gas adsorption porosimetry was used to assess the internal surface areas and porosity of the Arg/PAA-PSiNPs and NH₄OH/PAA-PSiNPs.

Under a vacuum at constant temperature, an inert adsorbate gas (typically nitrogen) is incrementally introduced to a chamber containing the solid sample. Through Van der Waals interactions, an amount of the gas is physisorbed onto the sample surface causing a difference in pressure relative to an empty reference chamber. From this, the quantity of gas adsorbed onto the sample is found and the molar amount required to form a monolayer of adsorbate on the sample surface is computed to give a specific surface area. In the case of micro- and

meso- porous samples, overlapping van der waals potentials inside the pores cause condensation at lower relative pressures than on an unbounded surface, where the pressure of adsorption is dependent on the pore diameter. As such, the adsorption and desorption isotherms (plotted as adsorbed gas quantity as a function of relative pressure) contain information about the pore size distribution, pore shapes, and surface area of the sample.¹¹²

The calculation of the monolayer capacity and hence sample surface area is achieved using the Brunauer–Emmett–Teller (BET) equation:

$$\frac{1}{v\left[\left(\frac{p_0}{p}\right) - 1\right]} = \frac{c - 1}{v_m c} \left(\frac{p}{p_0}\right) + \frac{1}{v_m c}$$

Eq. 2-18

where v is the adsorbed gas quantity, v_m is the monolayer capacity, p/p_0 is the relative pressure in the sample chamber, and c is the BET constant.

The gradient and intercept of a linear plot of $1/v[(p/p_0)-1]$ vs (p/p_0) is used to calculate v_m and c , and the BET surface area is given by:

$$S_{BET} = \frac{v_m N s}{V m}$$

Eq. 2-19

with N as Avagadro's number, s as the absorption cross section of the adsorbate gas, V as the molar volume of adsorbate gas, and m as the mass of the sample.¹¹²

While several theoretical models exist for the calculation of pore size distributions, most notably the t-plot method for micropores and BJH theory for cylindrical mesopores, non-local density functional theory (NLDFT) is currently considered the most accurate method for samples containing micro- and meso-pores. NLDFT modelling of interactions between the adsorptive gas and the substrate is used to generate theoretical isotherms and corresponding pore distributions for differing materials, pore sizes, and pore morphologies. Comparison between theory and the experimental data is used to generate a representative pore size distribution.

For the porosity data presented in Chapter 3, nitrogen gas adsorption-desorption isotherms were recorded using the Micromeritics Tristar 3000 at 77 K with a 10 s equilibration interval. Before measurement, the samples were freeze-dried and degassed under vacuum at 100 °C for 4 h. The specific surface area of the sample was found using the (BET) plot as described

by Roquerol et al. in the relative pressure range of 0.02 – 0.16.¹¹³ The pore size distribution was determined by NLDFIT analysis of the adsorption data in the relative pressure range of 0 – 0.9 using the Micromeritics Microactive analysis software.

2.8 PEI-SiNP/HA and PEI/HA Hydrogel Characterisation

2.8.1 Quantification of the PEI-SiNP/HA Hydrogel Swelling Ratio

Freshly prepared hydrogel samples in the swollen state were weighed before drying under nitrogen flow and then in an oven at 50 °C overnight. Hydrogels were considered dry when the weighed mass reached a stable minimum. The dried gels were then weighed, and the swelling ratio was calculated as the average of three replicates using the equation as follows:

$$\text{Swelling Ratio (\%)} = [(\text{Swollen Mass})/(\text{Dried Mass})] \times 100$$

Eq. 2-20

To study the reversibility of the swelling profile, the hydrogels were then rehydrated in ultrapure water for 24 h and weighed. This mass was used as the ‘swollen mass’ in Eq. 2-20 to find the swelling ratio after drying.

2.8.2 Haemolysis Testing of PEI-SiNP/HA Hydrogel

Whole blood obtained from mice was diluted 25 × with 1 × PBS to obtain a 4% v/v suspension. 0.5 mL of the diluted blood suspension was added to each hydrogel. The samples were incubated for 1 h at 37 °C before centrifugation at 1000 × g for 5 min. 0.1 mL of the supernatant was subsequently transferred to each well of a 96-well plate. The absorbance was measured at 576 nm using a microplate spectrophotometer (Molecular Devices SpectraMax M2e). Whole blood suspension incubated with PBS was used as negative control and red blood cells lysed with 0.05 % v/v Triton X-100 was used as the positive control. The percentage haemolysis was calculated using the following formula:

$$\text{Haemolysis (\%)} = \frac{[(\text{OD576 nm of hydrogel sample} - \text{OD576 nm of negative control}) / (\text{OD576 nm of positive control} - \text{OD576 nm of negative control})] \times 100}{}$$

Eq. 2-21

2.8.3 Rheological Characterisation of PEI-SiNP/HA Hydrogels

For a sample under shear deformation, 3 properties can be defined: the shear stress σ , in terms of the applied force, F , and the cross-sectional area, A ; the shear strain γ in terms of the deformation length L , and the material height, H ; and the shear rate $\dot{\gamma}$, the time derivative of γ .¹¹⁴

$$\sigma = \frac{F}{A}$$

Eq. 2-22

$$\gamma = \frac{L}{H}$$

Eq. 2-23

$$\dot{\gamma} = \frac{d\gamma}{dt}$$

Eq. 2-24

which for oscillatory strains are related by the following equations:

$$\sigma = G\gamma_0 \sin(\omega t)$$

Eq. 2-25

$$\sigma = \eta \dot{\gamma}(t) = \eta \gamma_0 \omega \cos(\omega t) = \eta \gamma_0 \omega \sin\left(\omega t + \frac{\pi}{2}\right)$$

Eq. 2-26

where G is the shear modulus, η is the viscosity, and ω angular frequency. Eq. 2-25 describes the stress response of a perfect Hookian solid, while Eq. 2-26 describes that of a Newtonian fluid. The stress response of a visco-elastic material characterised by both solid and fluid behaviours will be an oscillatory function out of phase with the applied strain by some phase angle δ between 0 and $\pi/2$. This gives rise to the complex shear modulus, G^* :

$$G^* = \frac{|\sigma_0|}{|\gamma_0|} e^{i\delta} = G' + iG''$$

Eq. 2-27

where the storage modulus, G' , describes the elastic component of the response, and the loss modulus, G'' , details the energy lost during deformation and hence the viscous component. These are defined independently as:

$$G' = \frac{|\sigma_0|}{|\gamma_0|} \cos(\delta)$$

Eq. 2-28

$$G'' = \frac{|\sigma_0|}{|\gamma_0|} \sin(\delta)$$

Eq. 2-29

The ratio of these two moduli is the loss factor, $\tan(\delta)$, is thus the ratio between the viscous to elastic effects, and is used to describe the relative dominance of each regime.¹¹⁴

$$\tan(\delta) = \frac{G''}{G'}$$

Eq. 2-30

The rheological properties of PEI/HA and PEI-SiNP/HA hydrogels were characterised with the Anton Paar MCR 302. Freshly prepared hydrogels were used with an 8 mm parallel plate geometry and a 0.5 mm gap at 20 °C for all experiments. Frequency sweep measurements were performed at 1 % shear strain between 0.1 – 10 Hz, and strain sweep measurements were performed at a frequency of 1 Hz between 1 – 1000% shear strain. The self-healing properties of the hydrogels were assessed with cyclical low (1%) and high (1000%) shear strain periods of 30 s at a frequency of 1 Hz.

2.8.4 Macroscopic Self Healing Test of PEI-SiNP/HA Hydrogels

To demonstrate the macroscopic self-healing of PEI-SiNP/HA hydrogels, two hydrogels were prepared with and without CBBG dye. For the incorporation of blue dye into the hydrogel, 30 μ L of 0.1 mg/mL CBBG was added to the PEI-SiNPs prior to the addition of HA and HCl described in section 2.5. The freshly prepared hydrogels were cut with a scalpel and the cut

surfaces were placed together in close contact in a sealed container at room temperature. After 1 h, the hydrogel was suspended under its own weight, and stretched by hand to test the network healing.

2.9 Drug Loading and Release of Methotrexate from PEI-SiNP/HA Hydrogels

The anticancer drug, methotrexate (MTX) was incorporated during hydrogel formation. 10 μL of 33 mg mL^{-1} MTX aqueous solution and 200 μL of PEI-SiNP stock containing 67.2 μM of silica surface bound PEI were combined and then added to 58.4 μL of 10 μM HA and 26.6 μL of ultrapure water before mixing with a vortex mixer. 5 μL of 2 M hydrochloric acid was added and the solution was mixed again with a vortex mixer. The supernatant was removed and the gel was rinsed thrice with ultrapure water. To determine the loading efficiency, the amount of non-encapsulated drug in the supernatants was quantified by UV-vis spectroscopy at 303 nm and compared to a standard calibration curve of known MTX concentrations.

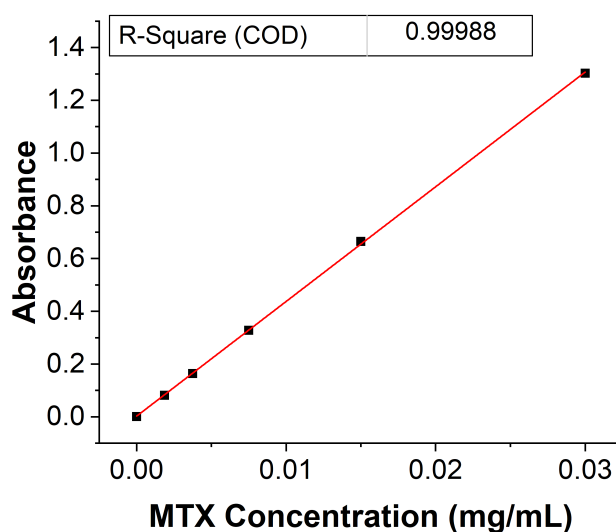


Figure 2.11 An optical absorbance calibration plot collected for MTX at 303 nm for use in quantifying the MTX loading efficiency and release rates with PEI-SiNP/HA hydrogels.

To determine the mass of drug loaded into the hydrogel, the total mass of non-encapsulated drug was subtracted from the initial drug mass added. The loading efficiency was calculated using the following formula:

$$\text{Drug Loading Efficiency (\%)} = ((\text{Mass of loaded drug})/(\text{Mass of drug added})) \times 100$$

Eq. 2-31

To assess the drug release rate, freshly prepared MTX loaded PEI-SiNP/HA and PEI/HA gels were dispersed in 1.0 mL of PBS (pH 7.4) under shaking at 37 °C. At set time points, 500 μL of the supernatant was removed and replaced with fresh PBS. The concentration of released drug in the supernatant was quantified with absorption spectroscopy at 303 nm, and the total released mass was calculated. The drug release kinetics and mechanisms were evaluated using the Korsmeyer-Peppas model as described in Section 2.3.

3 Synthesis and Characterisation of Arginine/Polyacrylic Acid Polyelectrolyte Complex Templated Porous Silica Nanoparticles

3.1 Motivation

Porous silica nanoparticles (PSiNPs) are amongst the most promising vehicles for drug delivery. Made of chemically inert silica, their biocompatibility, large internal pore volumes, high surface areas, and ease of functionalisation, have long attracted attention in medical research¹¹⁵ and spurred the approval of silica-based ‘C dots’ for Phase 2 clinical trials.^{116,117}

PSiNPs are most commonly synthesised through a modified Stöber method, a sol-gel process using the surfactant, cetyltrimonium bromide (CTAB), as a template for the porous structure. Particle size and morphological control is achieved through varying reagent concentrations, reaction temperature, and pH. However, this method does not typically allow the synthesis of highly uniform sub-100 nm particles, which are optimal for prolonged blood circulation, tumour accumulation, and enhanced cell uptake.^{118,119} Adaptations of this method have been used to access the sub-100 nm range, but they often lead to poor monodispersity, poor reproducibility, or require complex synthetic protocols.^{120–122} In addition, all of these protocols require additional calcination or chemical extraction steps to remove the templating surfactant to access the porous structures, modify the chemical properties of the final products, and possibly reduce toxicity before biological application.

To achieve efficient drug delivery, there is a strong impetus for the chemical functionalisation of PSiNPs with cancer targeting ligands and/or stimuli-responsive moieties for controlled or triggered drug release.¹²³ However, the current preparation of functionalised PSiNPs typically involves lengthy post-synthetic modifications with multiple synthesis, purification, and characterisation steps, significantly increasing the time and cost of synthesis. This in turn greatly decreases the likelihood of their successful translation into industrial and clinical use. Therefore, there remains a crucial need for a facile, reproducible, and cost-effective synthetic method to obtain monodisperse sub-100 nm PSiNPs with

intrinsic cancer targeting and stimuli-responsive drug release properties without the requirement for further post-synthetic modifications.

The polyelectrolyte complex (PEC) templated synthesis method has emerged as a promising strategy for the facile preparation of nanoparticles. As introduced in Chapter 1, the mixing of oppositely charged polymers or charged polymers with small counterions forms PECs whose size, polydispersity, surface properties, and chemical functionality may be precisely tuned. However, their application is limited by their poor stability under changes to the pH, ionic strength, and temperature of their surrounding media. Their use as scaffolds for the formation of nanoparticles, however, can enhance their stability and has been used for various types of nanoparticles suitable for drug delivery or biological imaging such as PSiNPs,^{72,100} CaCO₃,^{124,125} zeolitic imidazolate framework-8,¹²⁶ and lanthanide-doped gadolinium oxide nanoparticles.¹²⁷

Recently, the superior ability of divalent cations to crosslink PAA chains and form small, monodisperse PECs was demonstrated. The use of Mg²⁺ and Ca²⁺ to complex with PAA in hollow silica particle synthesis gave both smaller particle sizes and narrower size distributions compared to monovalent cations NH₄⁺, K⁺, and Na⁺.⁹⁹ However, the PAA templates within the synthesised HSNPs were easily removed by rinsing with water during purification, resulting in the loss of potential functionality. In contrast, the use of polyvalent poly(L-glutamic acid) with poly(2-(*N,N*-diethylamino) ethylmethacrylate) was found to give more stable PEC templates that were retained after PSiNP synthesis and purification.⁷² The hybrid PSiNPs were shown to permit doxorubicin (Dox) loading and confer pH responsive drug release. Similarly, the retention of PAA within CaCO₃ and zeolitic imidazolate framework-8 nanoparticles templated from PAA/Ca²⁺ and PAA/Zn²⁺, respectively^{125,126} after synthesis has afforded a high drug loading capacity and a pH responsive drug release kinetic. However for these systems, electron microscope imaging showed that the size distributions of the synthesised nanoparticles remained broad. There is thus a need to further explore and tailor the use of other PEC combinations to improve the uniformity and retain the PEC constituents within the nanoparticles to provide desirable functionalities for biomedical applications in a facile and cost-effective manner.

Herein, we report a novel one-pot synthesis method to obtain monodisperse, sub-100 nm PSiNPs with intrinsic cancer targeting, efficient drug loading, and pH responsive drug release behaviour by exploiting the unique alcohol induced polyelectrolyte complexation of L-arginine (Arg) and PAA (Figure 3.1). The efficacy of Arg in the formation of PECs and its ability to template the synthesis of PSiNPs is further compared to a second cation. The key

motivations behind the choice of Arg and PAA in the PEC template are as follows: (1) Cationic Arg is expected to undergo strong electrostatic interactions with anionic PAA to form highly uniform, colloiddally stable PECs, and act as a basic catalyst for silane mineralisation on the Arg/PAA PEC network to yield PSiNPs with high porosity and surface areas. (2) The retention of both PAA and Arg within the PSiNPs facilitates efficient anticancer drug loading through enhanced electrostatic interactions, as well as promoting acidic pH responsive drug release. (3) Surface presentation of Arg on the PSiNPs is expected to confer excellent colloidal stability and cancer targeting capabilities. Due to argininosuccinate synthetase (ASS) deficiencies in many solid cancers such as glioblastoma multiforme (GBM), melanoma, and prostate, auxotrophic tumour cells greatly rely on exogenous Arg to sustain their development and progression.^{128–130} The Arg transporter, cationic amino acid transporter-1 (CAT-1), has been found to be overexpressed in many malignancies to enhance Arg uptake and accumulation in tumour cells.¹³¹ There is thus significant potential to improve the delivery of anticancer therapeutics to tumour cells *via* Arg functionalisation of nanocarriers. Indeed, Wang *et al.* recently demonstrated efficient delivery of Mn²⁺ and Dox using Arg-capped manganese silicate nanobubbles to give significant tumour suppression in a Huh7 xenograft nude mice model.¹³² Despite the promising results, this cancer targeting strategy remains poorly exploited in nanoparticle mediated drug delivery systems.

In this chapter we discuss the design and synthesis of the PSiNPs. The parameters influencing the formation of optimal PEC templates for PSiNP synthesis are explored and then the size control, pore structures, and chemical functionalities of the PSiNPs are discussed in the context of cancer targeted drug delivery. The application of these particles, including drug delivery and release profiles, biocompatibility evaluation, and an assessment of targeting efficacy, is discussed in Chapter 4

3.2 Effect of Isopropanol/Water Volume Ratio on the Formation and Size of Arg/PAA Polyelectrolyte Droplets

For the formation of monodispersed PECs, PAA and Arg were mixed in water at a molar ratio of 1:230 before the addition of IPA to induce formation of aqueous PEC droplets, which act as templates for the subsequent hydrolysis and condensation of silanes (Figure 3.1).

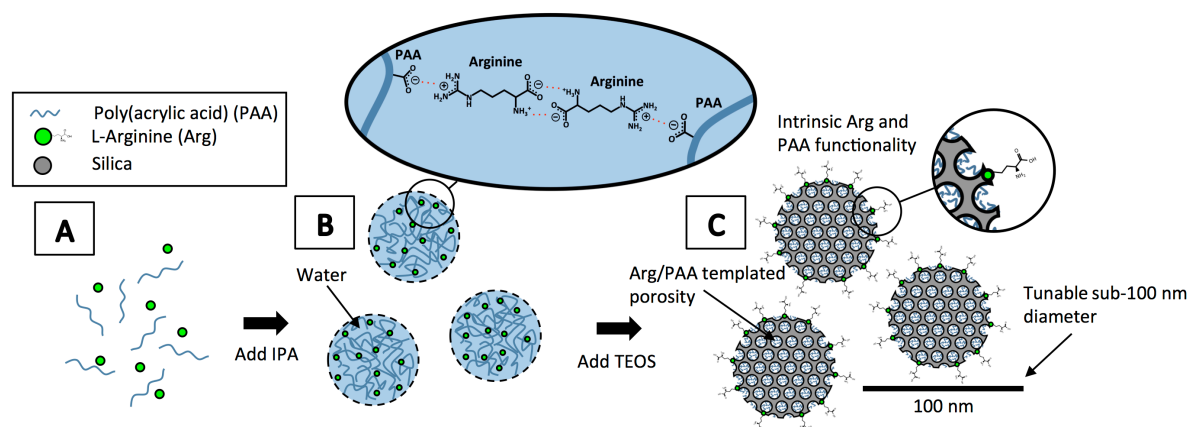


Figure 3.1 A schematic showing the polyelectrolyte templated synthesis of Arg/PAA-PSiNPs. (A) PAA and Arg are initially dissolved in water, and (B) upon addition of 2-propanol (IPA), the electrostatically associated PAA and Arg assemble into aqueous PECs in bulk IPA. (C) The PECs act as a template for the hydrolysis and condensation of the silica precursor triethoxysilane (TEOS) to form hybrid Arg/PAA-PSiNPs with intrinsic PAA and amino acid surface functionality.

It is widely reported that aqueous PAA and counterion mixtures form PECs in binary water/alcohol solvents at high alcohol volume fractions,^{74,95,99} but the effect of varying the binary solvent ratios on the properties the resultant PEC is less understood. Hence, the influence of increasing the IPA volume on the formation and stability of the PECs was first investigated using dynamic light scattering (DLS). The correlation function curve, which is a plot of the intensity signal autocorrelation over a very short time scale, provides important information on the size and polydispersity of a particle suspension undergoing Brownian motion. To monitor colloid formation, the correlation function curves of Arg/PAA,

$\text{NH}_4\text{OH}/\text{PAA}$, and PAA formed under different IPA volume fractions were collected. Figure 3.2 shows that for each PEC or PAA, a critical IPA volume is required for the formation of a stable particle suspension, which is characterised by a smooth, single exponential decay of the correlation function curve. For ease of interpreting the relationship and to explain the mechanisms involved in the IPA-induced colloid formation and stabilisation, a plot of the correlation function y-intercept against the IPA to water volume fraction is presented (Figure 3.3). The correlation function y-intercept gives an indication of the signal-to-noise ratio of the sample. A value closer to 1 indicates that the signal from a measured sample is high and taken together with the smooth exponential decays seen in correlation function curves shown in Figure 3.2, signifies that stable particles were formed.

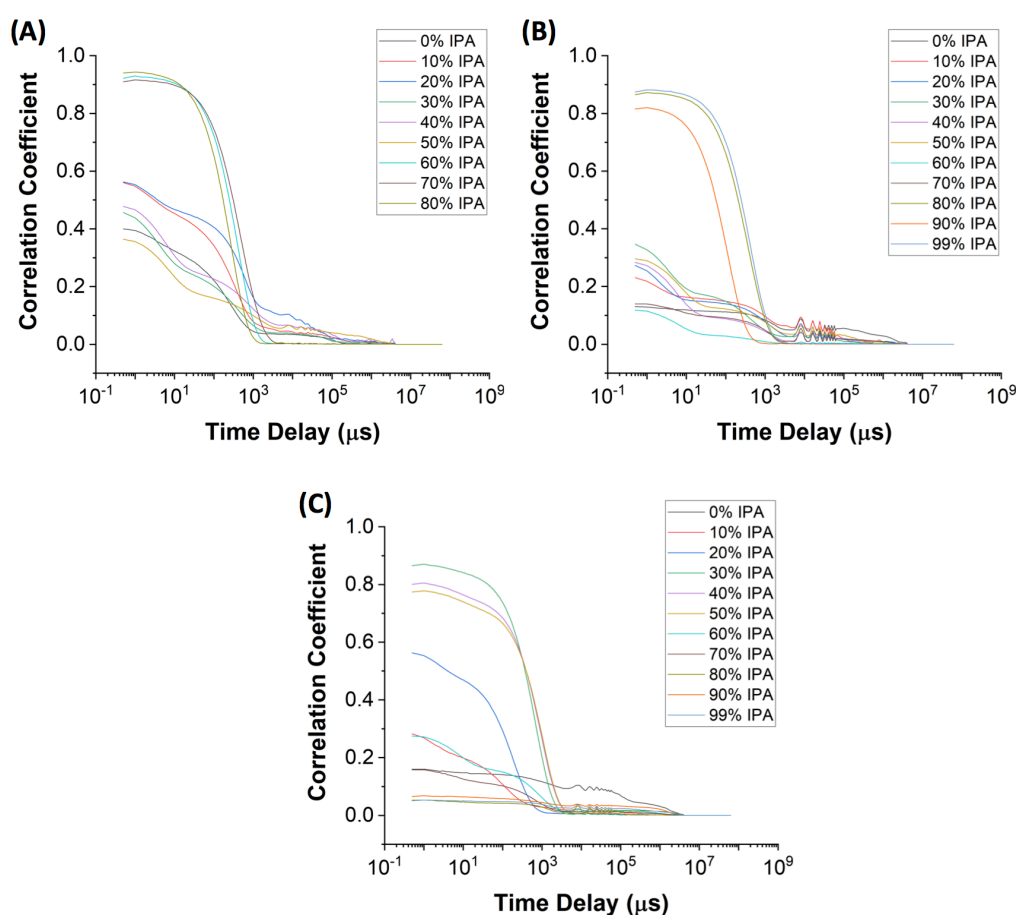


Figure 3.2 DLS correlation function curves for (A) Arg/PAA, (B) $\text{NH}_4\text{OH}/\text{PAA}$, and (C) PAA complexes formed at different IPA volume fractions.

As seen from Figure 3.3, the correlation function y-intercepts of the Arg/PAA PECs remained approximately constant between 0.3 – 0.6 when the IPA volume fraction was increased from 0 – 50%. Within this range, the correlation function curves are not described by a single exponential decay, rather they all show multiple decay regimes indicative of polydisperse complexes. From 60 – 80% v/v IPA, a marked increase of the correlation function y-intercept to ~ 0.97 was observed, indicating that PECs with much greater stability were formed. A further increase in IPA to more than 80% v/v resulted in the precipitation of the PECs. The complexation of the basic amino acid, Arg, with a polyanion such as polyoxometalates has been reported to occur via electrostatic interactions with the guanidinium group of Arg and salt-bridged hydrogen bonds between the $\alpha\text{-NH}_4^+$ and $\alpha\text{-COO}^-$ of adjacent Arg molecules.^{133,134} Due to the presence of excess Arg (acrylic acid monomer to Arg stoichiometric ratio = 1 : 9), the charged stabilised PECs are expected to be well dispersed in water, with low solubility in IPA. As the dielectric constant of the binary mixture decreases with increasing IPA volume fractions¹³⁵, the electrostatic interaction parameter, which contributes to the solution free energy for the oppositely charged Arg and PAA, is enhanced as it is inversely proportional to $\epsilon^{-3/2}$.^{36,136} This effectively promotes liquid-liquid phase separation of aqueous Arg/PAA PEC droplets which are stable and exist in equilibrium with the continuous phase at a critical IPA volume of 60%.

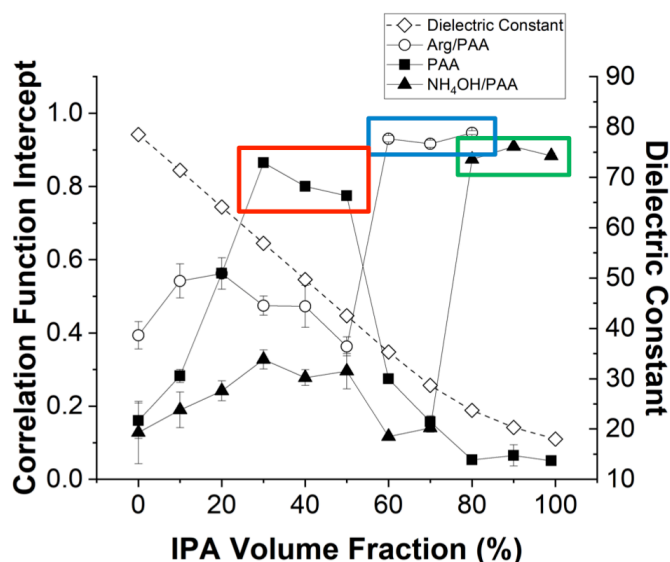


Figure 3.3 A summary of data presented in Figure 3.2. Changes in the dynamic light scattering measured correlation function y-intercepts of Arg/PAA, NH₄OH/PAA, and PAA as a function of IPA volume and dielectric constants¹³⁷.

A similar trend was observed with NH_4OH and PAA in which stable $\text{NH}_4\text{OH}/\text{PAA}$ PECs were formed only between 80 – 99% v/v IPA. Below this concentration range, the y-axis intercept values are between 0.12 – 0.33 and the decay profiles are all characterised by multiple exponentials. The lower IPA volume required to induce Arg/PAA PEC formation could be attributed to the higher cationic charge density of Arg in its guanidinium group, and its ability to act as a crosslinker through salt-bridged hydrogen bonds between anionic PAA chains, thus giving rise to stronger electrostatic interactions within the PEC. It is also worth noting that Arg/PAA PECs had higher correlation function y-intercept values than the 0.23 – 0.56 seen for $\text{NH}_4\text{OH}/\text{PAA}$ at all concentrations below the critical IPA volumes.

The behaviour of PAA alone with varying IPA/water volume fractions was also evaluated for comparison. Unlike the Arg/PAA and $\text{NH}_4\text{OH}/\text{PAA}$ PECs systems, PAA undergoes liquid-liquid phase separation to form single component particles at much lower IPA volumes of 30 – 50% v/v. This phenomenon is due to a different mechanism in which the solubility and conformation of PAA were affected by changes in solvent quality due to the complexation of the added IPA with water molecules.⁶¹ Whilst PAA is separately soluble in water and IPA, its solubility is affected in the mixture. Initially, the PAA chains were ionised and fully solvated due to hydrogen bonding with water. However, as more water/IPA complexes formed with the addition of increasing IPA volumes (0 – 30% v/v), PAA gradually becomes desolvated due to the reduced availability of free water molecules. This resulted in the stepwise increase in the signal-to-noise ratio or correlation function y-intercept observed. Despite the formation of water/IPA complexes, the water molecules remained in excess to solubilise the PAA chains. At a critical IPA range (30 – 50% v/v), the mixture is composed almost entirely of water/IPA complexes, which are a poor solvent for PAA. The PAA droplets were thus the most stable with correlation function y-intercepts of > 0.75 and smooth correlation function curves obtained. Above this concentration, all the water molecules were sequestered within the water/IPA complexes and any additional IPA exists simply in bulk and is thus able to re-solubilise the PAA chains through hydrogen bonding. This results in the dissolution of PAA droplets and a decrease in the correlation function y-intercepts to baseline levels (~ 0.3) above 80% v/v IPA.

The size distributions of stable droplets obtained at the critical IPA volumes were further evaluated. As seen from Figure 3.4A, monodisperse Arg/PAA PECs with hydrodynamic diameters of 114 ± 3 nm (polydispersity index, PDI = 0.03) and 77 ± 1 nm (PDI = 0.01) were obtained at 60 and 80% v/v IPA, respectively. This result contrasts favourably with the

NH₄OH/PAA PECs, which had considerably broader size distributions with hydrodynamic diameters of 103 ± 1 nm (PDI = 0.23) and 122 ± 3 nm (PDI = 0.13) at 80 and 99 % v/v IPA, respectively (Figure 3.4B). As 80% v/v IPA yields stable PECs with comparable sizes in both Arg/PAA and NH₄OH/PAA, this solvent condition was selected for subsequent experiments investigating PEC size control and their use as templates for PSiNP synthesis. Although stable, narrowly dispersed colloids with hydrodynamic diameters ranging from 194 – 273 nm (PDIs of 0.04 – 0.11) were observed with PAA (Figure 3.4C), the low pH of the reaction mixture renders the colloidal system unsuitable for use as templates for PSiNP synthesis (to be discussed in Section 3.3).

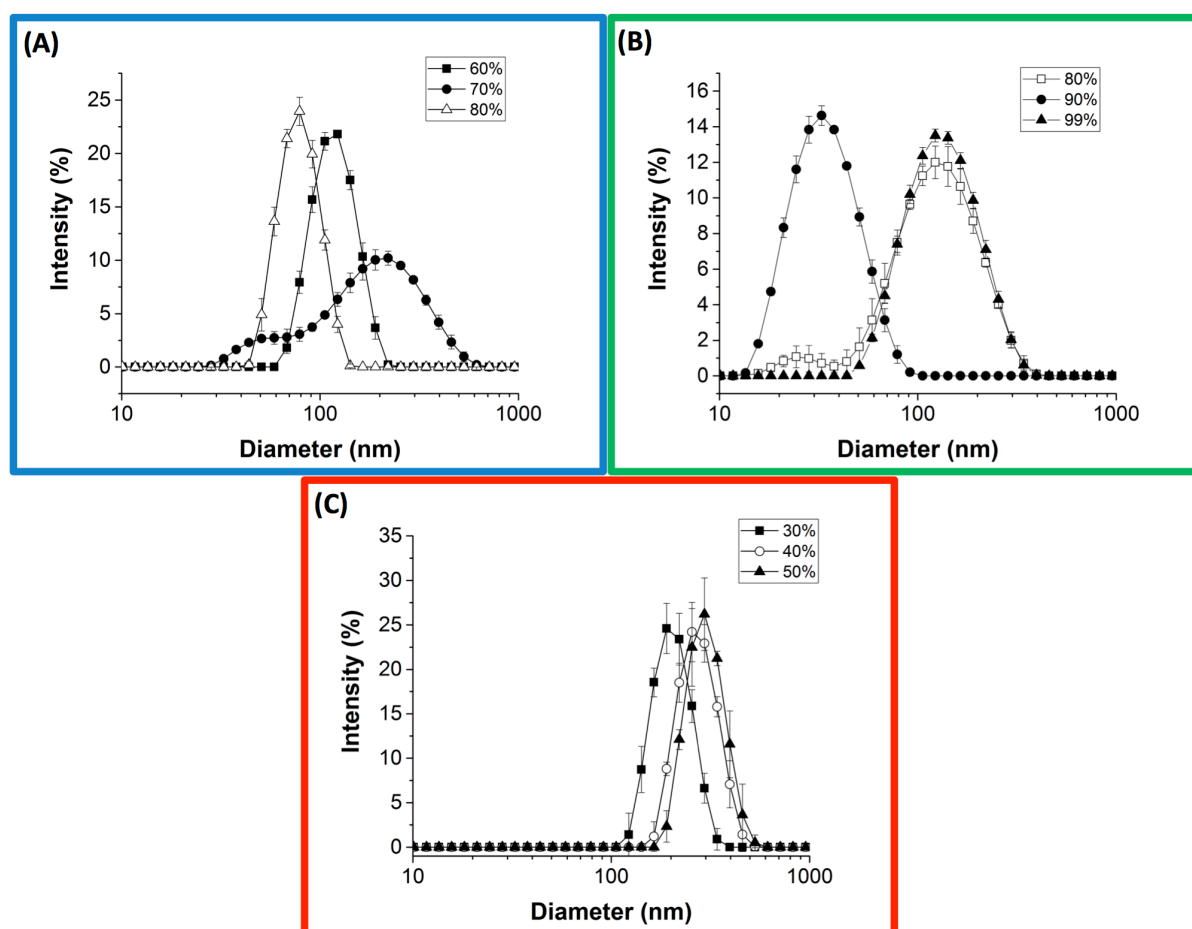


Figure 3.4 Intensity weighted size distributions of stable (A) Arg/PAA, (B) NH₄OH/PAA, and (C) PAA droplets formed at the critical range of IPA/water volume fractions corresponding to the coloured boxes shown in Figure 3.3.

3.3 Effect of Varying Arg, NH₄OH, and PAA on the Size and Dispersity of Arg/PAA and NH₄OH/PAA Templates

Application in targeted drug delivery places stringent restrictions on the size and dispersity of PECs that can be used as templates in PSiNP synthesis. As discussed previously, the particle size is a key determinant in blood circulation time, cellular uptake, and ultimately, particle accumulation at the tumour site. It hence follows that for well-defined uptake, toxicity, and drug delivery properties, one also requires excellent monodispersity. As such, we next investigated the influence of varying Arg, NH₄OH, and PAA on the size of the PEC colloidal templates using DLS. It was determined in Section 3.2 that the 80 % (v/v) IPA solvent condition was optimum for the formation of stable PECs with comparable sizes for both Arg/PAA and NH₄OH/PAA mixtures. Hence, in varying the concentrations of Arg, NH₄OH, and PAA, the total aqueous and IPA volumes were maintained, such that the IPA volume fraction was fixed at 80 % for all reported conditions.

By keeping the PAA concentration constant at 111.1 μ M, an increase in Arg from 2.0 to 30.8 mM led to an increment of Arg/PAA PEC sizes from 389 ± 1 to 72 ± 2 nm; with the PDIs remaining below 0.05 (Figure 3.5). This represents an increase in PAA monomer:Arg ratio from 1:0.7 to 1:11. As a corresponding pH rise from 6.5 to 9.5 with Arg addition was observed (Table 2), the greater deprotonation of carboxyl groups in PAA (pK_a 4.5)¹³⁸ could have led to increased electrostatic interactions and sequestration of Arg as it is being added. The ability of Arg to crosslink adjacent PAA chains via electrostatic interactions and salt-bridged hydrogen bonding (Figure 3.1) also further acts to enhance packing of more PAA and Arg, thereby resulting in the greater PEC diameters observed.

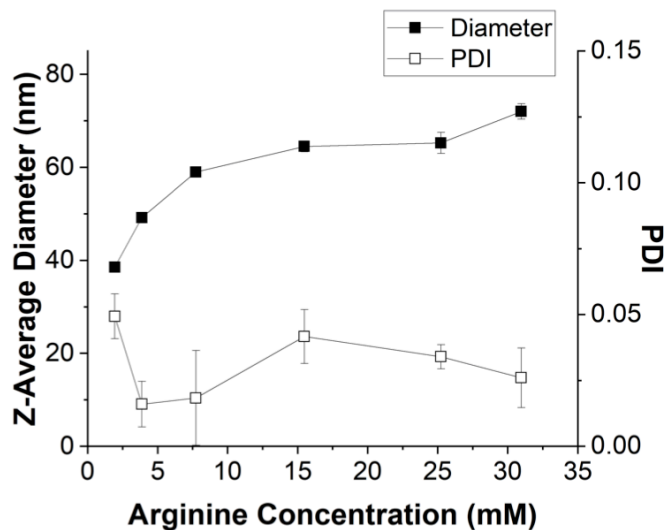


Figure 3.5 Changes in the dynamic light scattering measured hydrodynamic diameters and polydispersity index of Arg/PAA PECs formed by varying Arg with PAA fixed at 111 μM .

Table 2 pH values of PEC mixtures prepared with 2.0 – 30.8 mM of Arg or NH_4OH with a fixed 111 μM of PAA in 80% v/v solution of IPA in water.

Arg or NH_4OH concentration (mM)	pH of Arg/PAA PEC mixtures	pH of NH_4OH /PAA PEC mixtures
2.0	6.5	6.0
3.9	6.8	6.3
7.7	7.3	7.0
15.5	8.0	7.5
25.4	9.0	9.0
30.8	9.5	9.3

Despite possessing the same concentrations and PAA monomer/counter ion ratios, and having comparable pH values, the size trend observed for NH₄OH/PAA complexes is not the same as that for Arg/PAA PECs. Increasing NH₄OH from 2.0 – 15.5 mM gave an increase in peak NH₄OH/PAA complex size from 70 ± 2 to 90 ± 1 nm but then followed by a decrease to 56.6 ± 1.0 nm for 30.8 mM NH₄OH (Figure 3.6). The size distributions of the NH₄OH/PAA complexes were also significantly broader compared to the Arg/PAA complexes, with PDI values in excess of 0.24 over the range of NH₄OH tested. This result could be attributed to the lower charge density of the monovalent NH₄⁺ compared to Arg which results in diminished electrostatic interactions with PAA, and could cause the PECs to be more loosely packed. It has also been shown in recent literature that monovalent counter ions form larger and more polydisperse PECs in similar water/alcohol systems than multivalent ions.⁹⁹ .

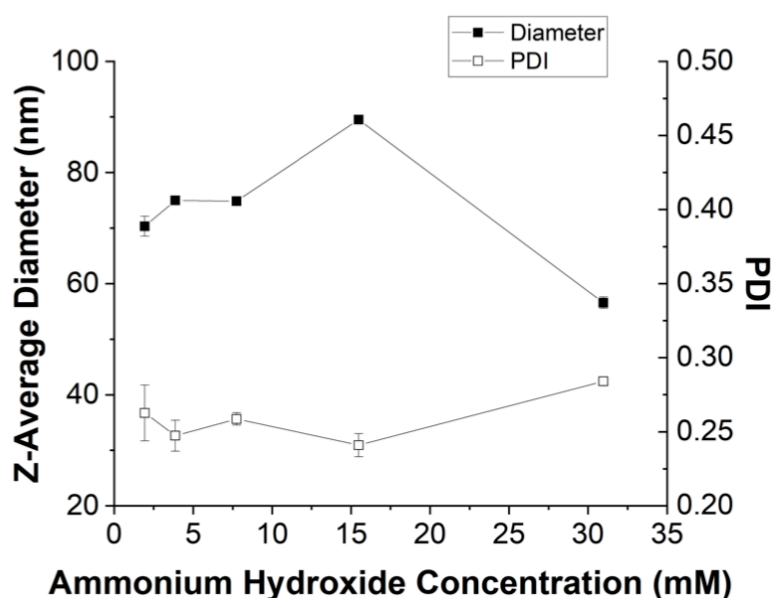


Figure 3.6 Changes in the dynamic light scattering measured hydrodynamic diameters and polydispersity index of NH₄OH/PAA PECs formed by varying NH₄OH with PAA fixed at 111 μM.

The effect of varying PAA on the Arg/PAA template size was next investigated. PAA was found to have a greater influence on the size of the PECs formed at a fixed Arg concentration of 25.4 mM. As seen from Figure 3.7, increasing PAA concentration from 25 to 400 μM led to a greater diameter increase from 50 to 130 nm for the Arg/PAA PECs. Throughout this

concentration increase there is a large excess of Arg (PAA monomer:Arg stoichiometric ratio tuned from 1:37 to 1:3), and hence free Arg in solution is readily available to complex additional PAA leading to size increase across the full tested concentration range. The large size increase seen with varying PAA content (versus the relatively small increase under Arg variation) is likely due to the enhanced packing of more PAA chains into each PEC, which have much larger molecular weights than Arg, within the PECs. This finding is in agreement with the work by Nakashima *et al.* in which increased PAA/NH₄⁺ aggregate sizes with increasing PAA concentrations in ethanol/water mixtures were observed.⁷⁴ Importantly, the low PDI values ranging from 0.02 – 0.12 were maintained through the significant size increase, hence presenting an efficient means to provide larger monodisperse (PDI < 0.2) colloidal templates for accessing larger functionalised PSiNPs.

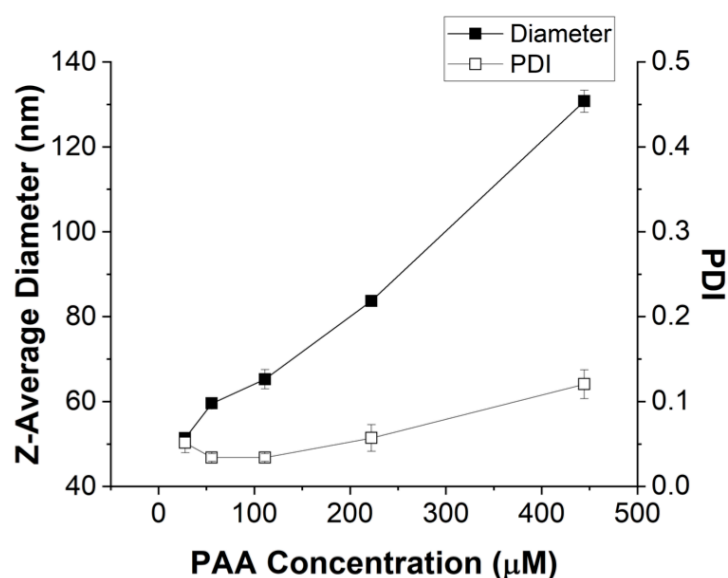


Figure 3.7 Changes in the dynamic light scattering measured hydrodynamic diameters and polydispersity index of PECs formed by varying PAA with Arg fixed at 25.4 mM.

3.4 PAA/Arg PEC Template Directed Porous Silica Nanoparticle Synthesis

Upon identification of the optimal condition that leads to the formation of monodisperse PEC particles, the Arg/PAA PECs were next investigated as colloidal templates for the hydrolysis and condensation of silanes to yield multifunctional PSiNPs. It was found previously that increasing Arg from 7.7 to 30.8 mM led to a pH increase in the reaction mixture from 7.25 to 9.5 (Table 2). As silane hydrolysis, condensation, and depolymerisation rates are higher at alkaline pH⁸⁶, we first evaluated the influence of Arg content, and hence the pH of the reaction mixture on PSiNP formation. TEM images of Arg/PAA-PSiNPs formed at a near neutral pH of 7.25 revealed that small, poorly defined clusters in addition to a dominant population of PSiNPs with an average diameter of 26 ± 3 nm were formed (Figure 3.8), suggesting the incomplete reaction of silica precursors within the 24 h reaction period. In contrast, single PSiNP populations ranging from 36 ± 3 to 50 ± 5 nm in diameter were obtained at a more alkaline pH of 8.0 – 9.5. To ensure complete reaction of the silanes and thus greater reproducibility, all further syntheses were performed at pH 9.0 with 25.4 mM of Arg.

The effect of varying the volume of the silica precursor triethoxysilane (TEOS) added to ~73 nm (by DLS) Arg/PAA PEC templates on the final PSiNP size and zeta-potential was subsequently studied. In general, an increase in TEOS volume from 20-500 μ L led to a progressive increase in the size of the Arg/PAA-PSiNPs obtained (Figure 3.9A).

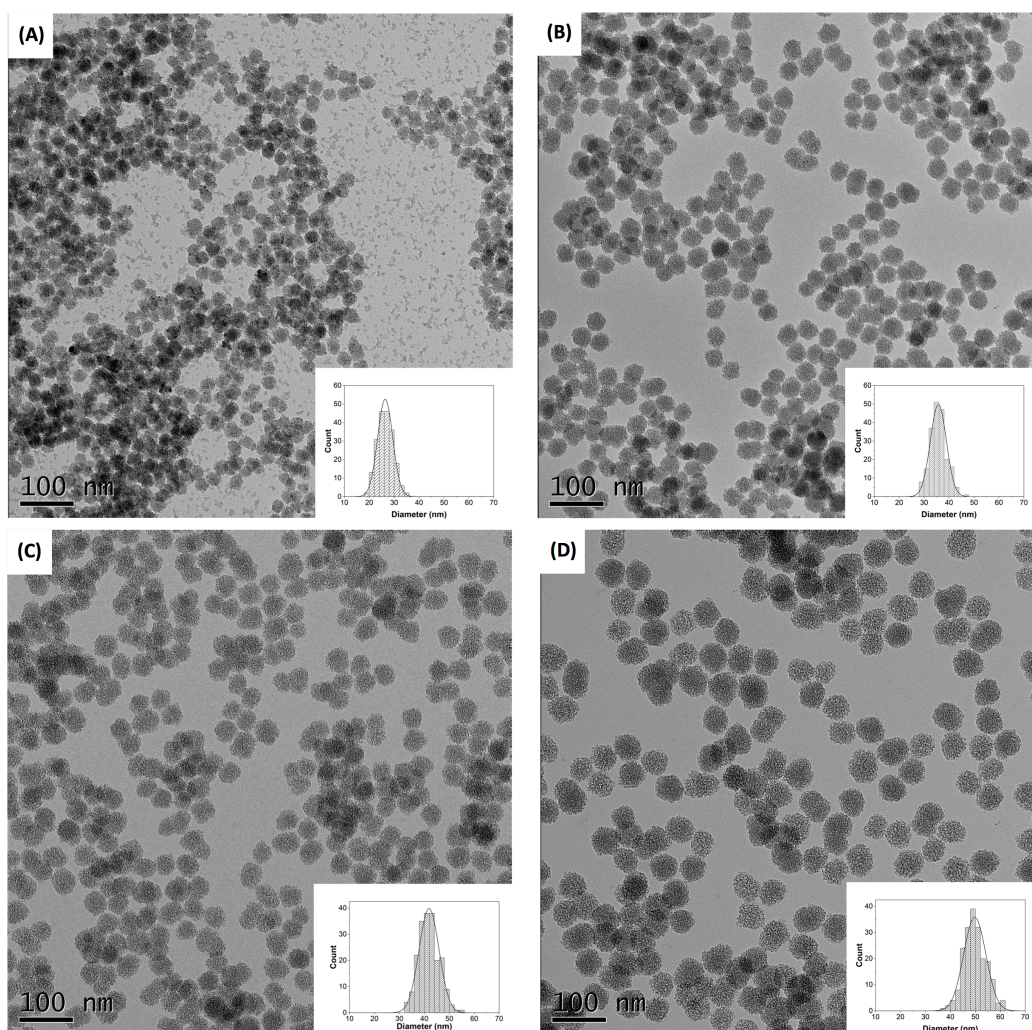


Figure 3.8 TEM images and corresponding size histograms for Arg/PAA-PSiNPs synthesised with (A) 7.7 mM, (B) 15.5 mM, (C) 25.4 mM, and (D) 30.8 mM Arg. The average diameters are 26 ± 3 nm (ignoring the presence small particles arising form unreacted reagents post-synthesis), 36 ± 3 nm, 42 ± 4.0 , and 50 ± 5 nm respectively ($n = 200$ for all).

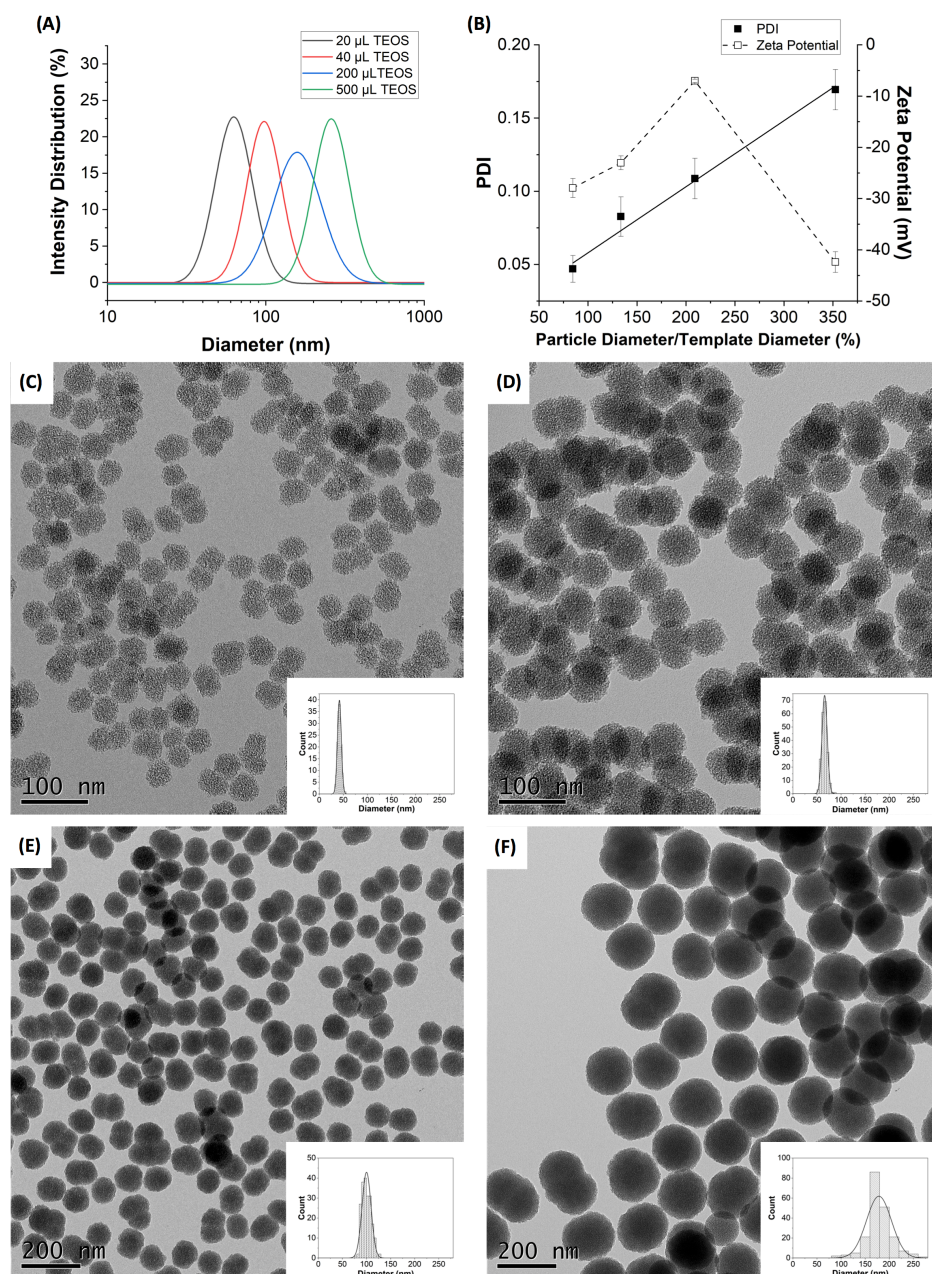


Figure 3.9 (A) Intensity weighted DLS size distributions of the Arg/PAA-PSiNPs displayed in (C-F) with Z-average diameters of 61 ± 1 nm, 97 ± 3 nm, 152 ± 2 nm, and 256 ± 4 nm synthesised with 20, 40, 200, and 500 μ L TEOS respectively. (B) The polydispersity index and zeta-potentials at pH 7.4 of the Arg/PAA-PSiNPs expressed shown in (A) as a function of the ratio of the particle and the polyelectrolyte template diameter showing the effect of the under- and over-growth regimes. TEM images and diameter histograms for Arg/PAA-PSiNPs synthesised by adding (C) 20, (D) 40, (E) 200, and (F) 500 μ L of TEOS to 70 nm (by DLS) polyelectrolyte colloidal templates. The average diameters determined from the TEM images

are (C) 42 ± 4 nm, (D) 66 ± 5 nm, (E) 100 ± 9 nm, and (F) 178 ± 28 nm, respectively (n = 200).

When 20 μ L TEOS was added, Arg/PAA-PSiNPs with Z-average diameter of 61 ± 1 nm were obtained. This corresponded to approximately 85% of the original template diameter. The further addition of TEOS resulted in an overgrowth effect in which the size of the Arg/PAA-PSiNPs obtained exceeded the template size. For instance, at the highest TEOS volume of 500 μ L, the PSiNPs obtained had a diameter of 256 ± 4 nm, which was 350% larger than the original PEC template diameter. The overgrowth of the PSiNPs beyond the PEC template diameter elicited a significant stepwise increase in PDIs from 0.05 to 0.17 (Figure 3.9B). Consistent with the DLS results, TEM images confirmed that highly uniform and spherical Arg/PAA-PSiNPs with average diameters between 42-100 nm and with standard deviations of $< 10\%$ were obtained when 20 - 200 μ L TEOS were added (Figure 3.9C-E). The addition of 500 μ L TEOS resulted in the largest PSiNPs with a size of 178 nm and with a standard deviation increase to 15%. These results clearly demonstrate the relationship between the colloidal template size and the amount of silane added on the size and uniformity of the Arg/PAA PEC templated PSiNPs obtained. A similar observation has also been made by Hu *et al.* where silica overgrowth brought about by an increase in silane mineralisation time with PAA/poly(L-lysine) PECs led to the formation of more dispersed silica nanoparticles with a loss of spherical morphology¹⁰⁰.

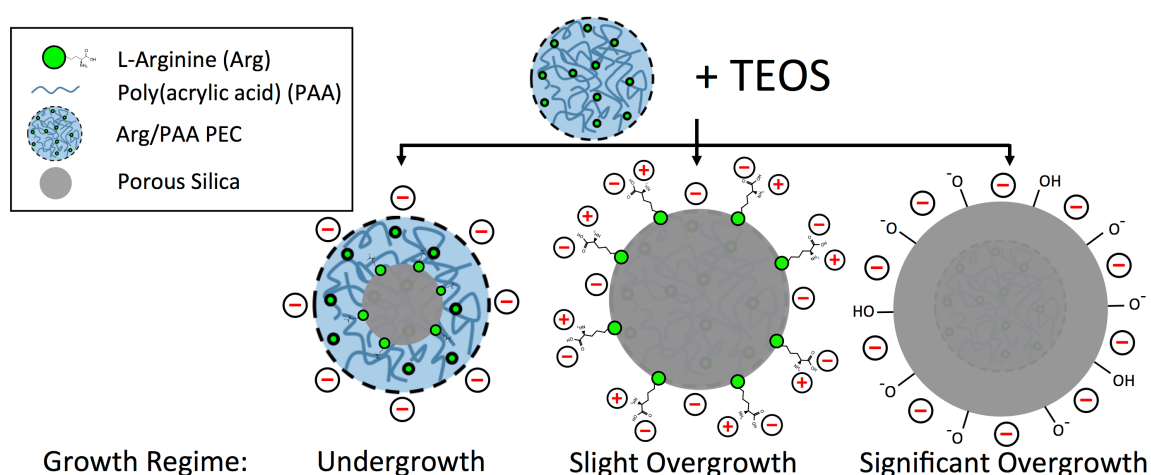


Figure 3.10 A schematic depiction of the three possible undergrowth and overgrowth regimes and their impact on surface functionality.

The zeta-potential of the Arg/PAA-PSiNPs in PBS (pH 7.4) was -27.9 ± 1.9 mV at 85% diameter of the colloidal template (Figure 3B). This is likely due to the decoration of the PSiNP surface with Arg whose guanidinium and α -amino groups (pKa 12.1 and 9.0 respectively)¹³⁹ have positive charges, and PAA whose deprotonated carboxyl groups (pKa 4.5) impart a strongly negative surface charge.^{90,139} PAA, however, extends from the surface like a brush partially covering the surface bound Arg and thus contributes more strongly to the zeta-potential under this growth regime (Scheme 2). The zeta potential increased to -7.0 ± 0.3 mV at 200% overgrowth. This result suggests a reduced surface presentation of the negatively charged PAA as the silica network filled the colloidal templates, although the Arg surface capping of the PSiNPs was retained due to the large excess of Arg present in the amino acid catalysed silica synthesis.¹⁴⁰ However, at the maximum TEOS volume of 500 μ L which gave a PSiNP/template diameter ratio of 350%, a drastic drop in zeta-potential to -42.4 ± 2.0 mV was observed, suggesting that the particle surface was mainly comprised of deprotonated silanol groups without the presence of PAA or Arg. Beyond the addition of a critical amount of TEOS, the full occupation of the Arg/PAA PECs by the silica and complete consumption of the individual reagents in the drastically overgrowth regime plausibly led to the loss of surface functionalisation by these moieties. Taken together, these results demonstrate that to maintain the desired surface presentation of Arg and PAA on the PSiNPs, which have important consequences on cellular targeting effects, the amount of TEOS added needs to be optimised in order to obtain a PSiNP diameter that does not significantly exceed that of the template. Correspondingly, to access larger PSiNPs sizes that retain their monodispersity and surface functionality, the size of the Arg/PAA PEC template used could be increased according to the conditions discussed in Section 3.3.

In contrast, the addition of 20 – 500 μ L of TEOS to \sim 100 nm (by DLS) NH_4OH /PAA PECs templates did not give the same effect on the size and zeta-potential of the resultant PSiNPs obtained (Figure 3.11). The smallest TEOS volumes of 20 and 40 μ L respectively gave the largest particles with hydrodynamic diameters of 112 and 153 nm (PDI 0.11 and 0.13) compared to 62 and 97 nm (PDI 0.05 and 0.08) for the Arg/PAA-PSiNPs. This is likely caused by template instability and resultant particle coalescence during synthesis due the inability of NH_4OH to efficiently crosslink with PAA during PEC formation. Contrary also to Arg/PAA-PSiNPs, the TEOS volume added to the NH_4OH /PAA PECs showed no correlation with the zeta-potentials of the PSiNPs obtained, which were found to be between -30 to -40 mV independent of the particle growth regime (Figure 3.11). As will be seen later, the

absence of PAA functionality within the $\text{NH}_4\text{OH}/\text{PAA}$ -PSiNPs was confirmed with ATR-FTIR and TGA, hence the surface charge could be predominantly attributed to the surface silanol groups. Notably, the zeta-potential value of the significantly overgrown Arg/PAA-PSiNPs (PSiNP/template diameter ratio of 350%) is close to the values obtained for the $\text{NH}_4\text{OH}/\text{PAA}$ -PSiNPs, suggesting the lack of surface PAA or Arg functionality discussed above.

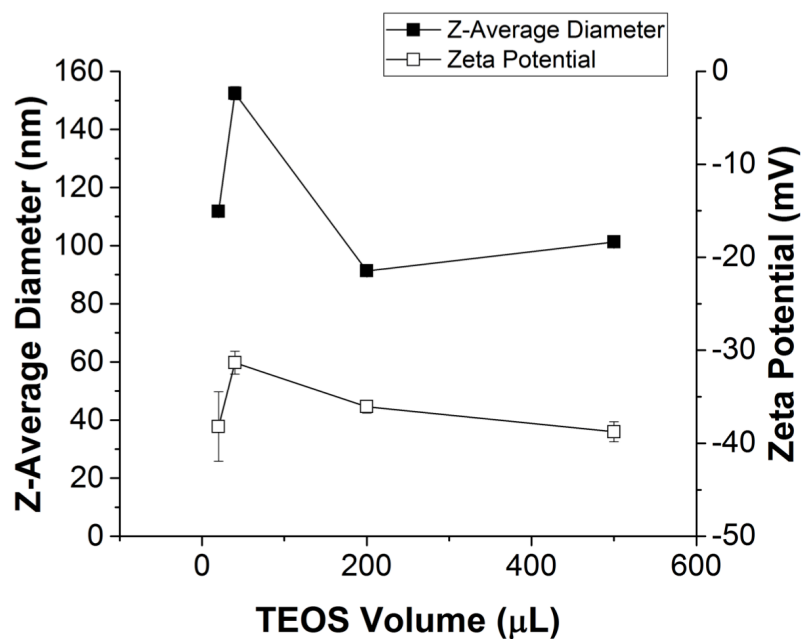


Figure 3.11 Z-average diameters and zeta-potentials of $\text{NH}_4\text{OH}/\text{PAA}$ -PSiNPs synthesised with $50 \mu\text{M}$ PAA and $25.4 \mu\text{M}$ NH_4OH over a range of TEOS volumes.

3.5 The Scalability of Arg/PAA-PSiNP and NH₄OH/PAA-PSiNP Syntheses

For the successful clinical translation of the Arg/PAA-PSiNPs as drug carriers, the scalability and reproducibility of the synthesis are imperative, and as such were tested herein.

Following the same protocol but increasing the volumes of each reagent used, the synthesis can be reproducibly scaled-up 25-fold to a 250 mL volume with a dried particle mass yield of approximately 100 mg. As shown in Figure 3.12, the larger scale synthesis had no detrimental effects on the PSiNP morphology and monodispersity. The diameter as measured by TEM showed a modest decrease in diameter 49.3 ± 5 nm, compared to 66 ± 5 nm produced from a 10 mL synthesis volume (Figure 3.9; Section 3.4), while maintaining the spherical shape and ~ 10 % standard deviation. The synthesis reproducibility was evidenced by DLS analysis of repeat syntheses, where the Z-average diameters of PSiNPs synthesised from three different batches (250 mL) had a variation of less than 5 nm.

In contrast, PSiNPs synthesised with NH₄OH/PAA colloidal PEC templates were found to have much poorer size uniformity and reproducibility. Representative TEM images showed a wide size distribution with average diameter of 55.4 ± 8.5 nm (Figure 3.13). As mentioned earlier in Section 3.4, the polydispersity of the NH₄OH/PAA PECs likely arose from the lower charge density of NH₄⁺, which results in weaker electrostatic interactions with PAA. The batch-to-batch variability was also found to be large, with Z-average diameters ranging between 73 – 151 nm across 3 repeat syntheses (Figure 3.13C). The broad PEC size distribution results in the non-uniform deposition and growth of porous silica to cause significant size variations between batches. These results underscore the benefits of using Arg/PAA PECs as templates for producing highly uniform PSiNPs for biomedical applications.

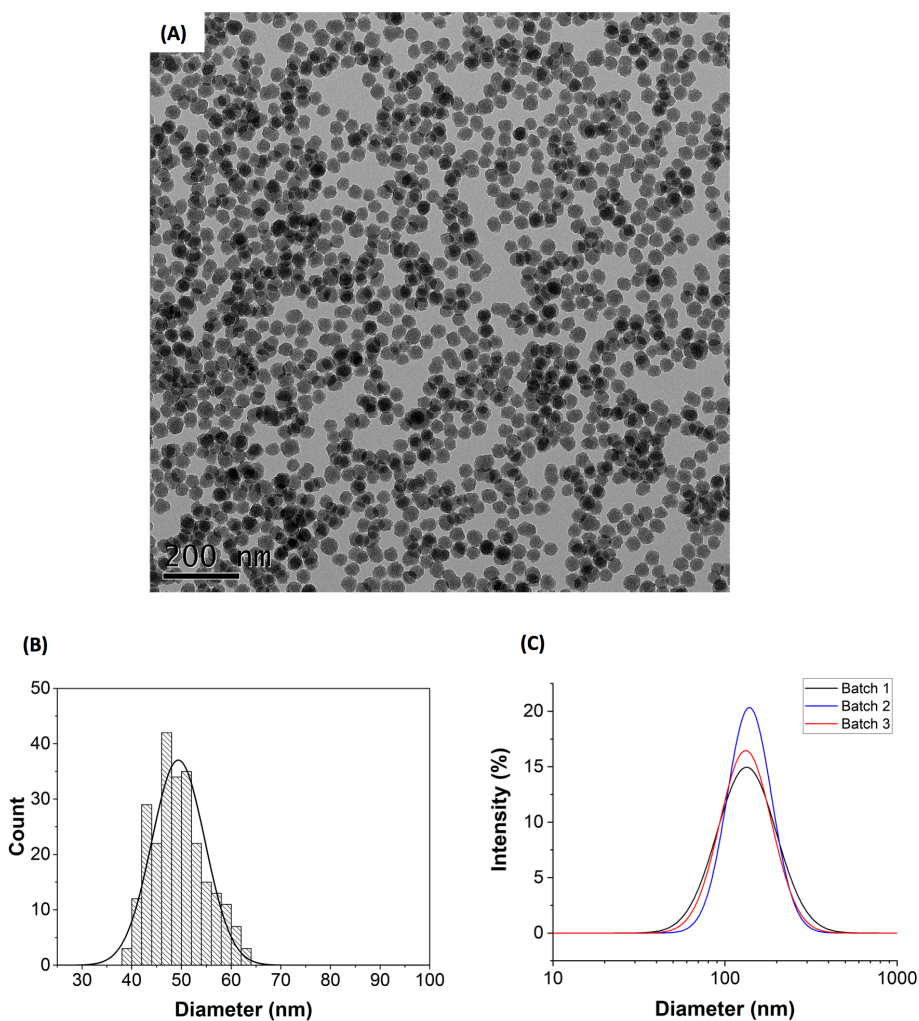


Figure 3.12 Size distributions for Arg/PAA-PSiNPs synthesised in a 25-fold scaled-up synthesis. (A) Representative TEM image, (B) corresponding diameter histogram showing an average diameter of 49 ± 5 nm ($n = 248$), and (C) DLS size intensity distributions for 3 repeat syntheses with Z-average diameters of 131 ± 1 nm, 134 ± 1 nm, and 128 ± 2 nm (batch 1, 2, and 3). The PDI values from the 3 independent synthesis batches are 0.17, 0.10, and 0.13, respectively.

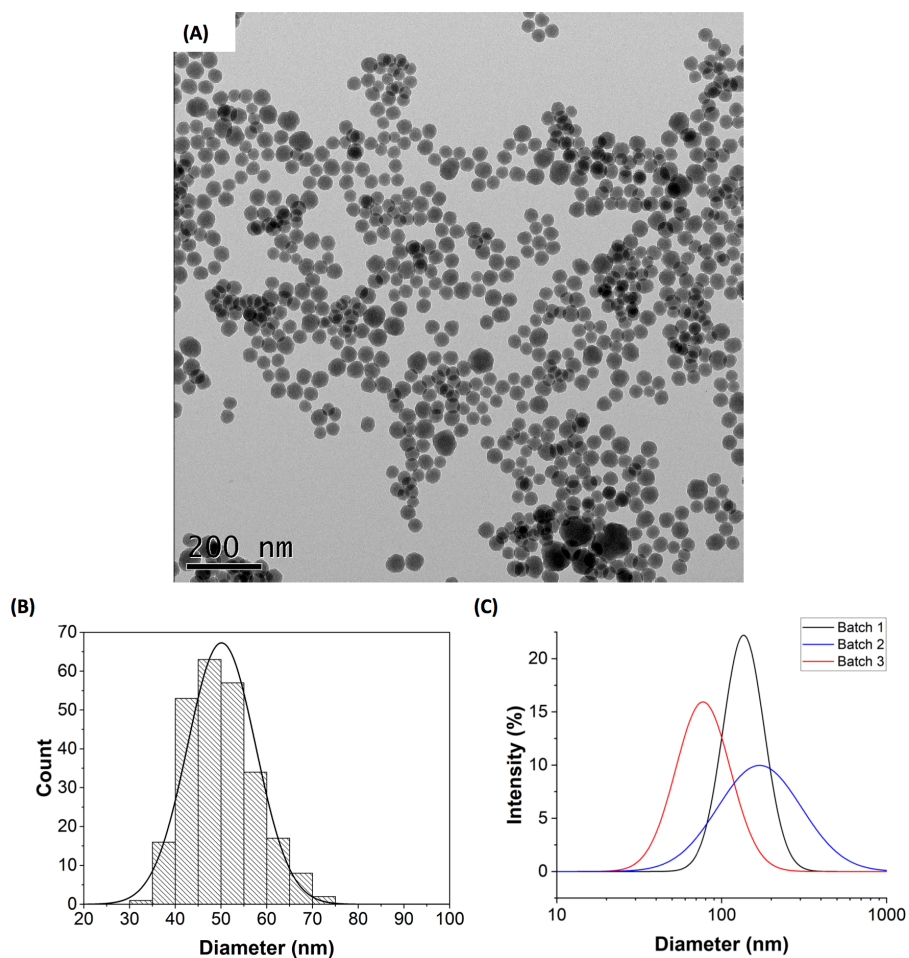


Figure 3.13 (A) TEM image and (B) the corresponding size distribution histogram for $\text{NH}_4\text{OH}/\text{PAA}$ -PSiNPs produced in a 250 mL scaled-up synthesis. The average diameter of the $\text{NH}_4\text{OH}/\text{PAA}$ -PSiNPs is 55 ± 9 nm ($n = 260$). (B) The intensity size distribution determined using dynamic light scattering for 3 repeat syntheses with Z-average diameters of 132 ± 1 nm, 151 ± 1 nm, and 73 ± 2 nm for batch 1, 2, and 3, respectively. The PDI values from the 3 independent synthesis batches are 0.09, 0.25, and 0.12, respectively.

3.6 Chemical Characterisation of Arg/PAA-PSiNPs and NH₄OH/PAA-PSiNPs

One of the key benefits of using PEC templates for PSiNP synthesis is the in-synthesis functionalisation of the PSiNPs to confer desirable properties for cancer targeted drug delivery, obviating the need for any post-synthetic modifications. Hence, there is a need to evaluate the retention of the PEC constituents within the synthesised PSiNPs. In Section 3.4, zeta potential measurements were used to assess the surface functionality in 3 different growth regime. In this section, attenuated total reflection-fourier transform infrared spectroscopy (ATR-FTIR) and thermogravimetric analysis (TGA) were used to confirm the presence of Arg and PAA in Arg/PAA-PSiNPs and NH₄OH/PAA-PSiNPs synthesised at comparable reagent conditions.

For both particle types, typical silica vibration modes corresponding to Si–O–Si asymmetric stretching as well as Si–O and Si–OH stretching were observed at 1000 – 1250, 794, and 935 cm⁻¹, respectively (Figure 3.14A).¹⁴¹ The presence of Arg on the Arg/PAA-PSiNP was confirmed from the presence of common vibrational modes in the Arg and Arg/PAA-PSiNP spectra. The absorption bands which correspond to asymmetric –NH– bending, asymmetric –C–O– stretching, and symmetric –C–O– stretching were observed at 1675, 1558, and 1475 cm⁻¹, respectively for Arg,^{132,142} and at 1679, 1555, and 1474 cm⁻¹ for Arg/PAA-PSiNPs. Although the in-plane –C–O–H bending, asymmetric CH₂ stretching, and C=O stretching modes typical of PAA appeared at 1413, 1450, and 1698 cm⁻¹ in the Arg/PAA spectra, they also coincide with peaks assigned to Arg¹⁴³. Furthermore, broad peaks for the CH₂ rocking and C–O symmetric stretching occurring at 792 and 918 cm⁻¹ for PAA also coincide with the sharper peaks for Si–O and Si–OH stretching, thus preventing conclusive confirmation of PAA functionalisation in the PSiNPs using ATR-FTIR. As such, TGA was further employed as a complementary technique to confirm the presence of PAA. The absorption spectrum for NH₄OH/PAA-PSiNPs showed comparatively fewer spectral features. As expected, none of the peaks attributed to Arg were present and the above discussed in-plane –C–O–H bending, asymmetric CH₂ stretching, and C=O stretching for PAA peaks were also not observed, hence indicating the absence of both Arg and PAA functionality on the NH₄OH/PAA-PSiNPs. TGA analyses further confirmed the retention of PAA and Arg functionality within Arg/PAA-PSiNPs whereas no detectable organic functionality was observed for NH₄OH/PAA-PSiNPs. The thermal degradation profile of Arg/PAA-PSiNPs revealed distinct

weight loss peaks beginning at 229 and 316 °C which were close to the 220 and 305 °C observed for Arg (Figure 3.14B), thus indicating the presence of Arg within the PSiNPs. The existence of PAA within the Arg/PAA-PSiNPs was confirmed through the appearance of a weight loss peak at around 157 °C which was close to that observed at 149 °C for PAA alone (Figure 3.14C and D). Consistent with the ATR-FTIR data, no discernible weight loss ascribed to the presence of PAA was found with the NH₄OH/PAA-PSiNPs (Figure 3.14E). It is thus evident that electrostatic interactions between NH₄⁺ and PAA were not sufficient to retain the polymer during the repeated washing steps used to remove excess reagents after TEOS condensation. Wan and Yu have also previously reported a similar result in which PAA was found to be completely removed from hollow silica nanoparticles templated from PAA/NH₄⁺ in ethanol solutions by washing⁹⁶. Conversely, the increased charge density and efficient crosslinking ability of Arg enhances retention of PAA in the PECs and the final PSiNP product, which will be seen later to contribute greatly to the increased porosity and pH responsive drug release capabilities of the Arg/PAA-PSiNPs.

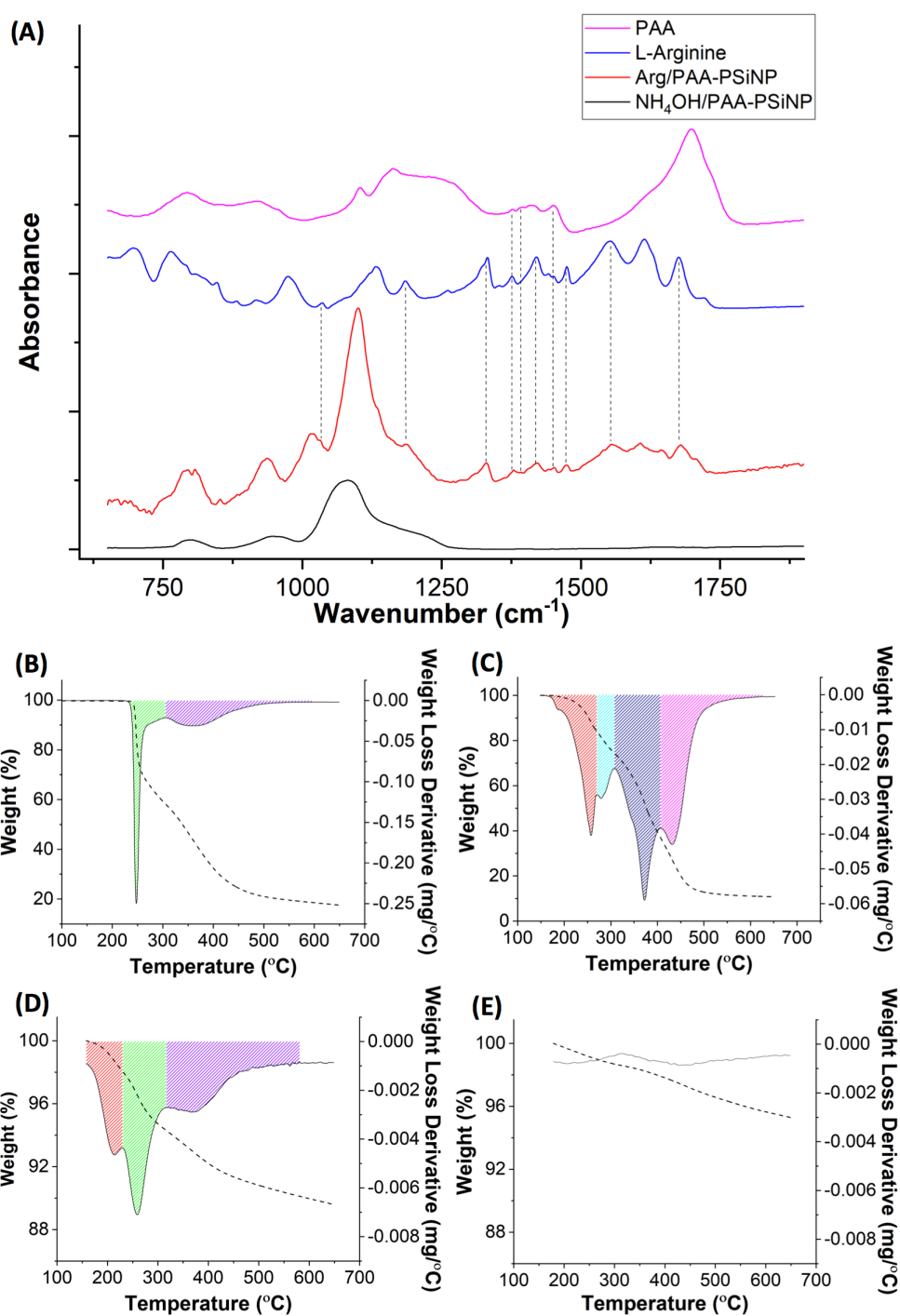


Figure 3.14 Chemical characterisation of Arg/PAA-PSiNPs and NH₄OH/PAA-PSiNPs. (A) Stacked ATR-FTIR spectra showing the fingerprint regions for PAA, Arg, Arg/PAA-PSiNP, and NH₄OH/PAA-PSiNP. TGA curves and the 1st derivatives of the weight loss curves for (B) Arg, (C) PAA, (D) Arg/PAA-PSiNPs and (E) NH₄OH/PAA-PSiNPs, where coloured peaks indicate the presence of a common organic compound between samples.

3.7 Porosity Measurements of Arg/PAA-PSiNPs and NH₄OH/PAA-PSiNPs

A dominant feature of PSiNPs responsible for their success as drug delivery vehicles is their porous structure. The presence of micro- (< 2 nm diameter) and meso- (2 – 50 nm diameter) pores facilitates the loading of therapeutics into the internal particle spaces for retention and later release at the target site. To determine the surface area and porosity of the Arg/PAA-PSiNPs and NH₄OH/PAA-PSiNPs, N₂ adsorption-desorption measurements were performed. From Figure 3.15A, the N₂ adsorption-desorption isotherms of both types of PSiNPs displayed a characteristic type IV behaviour, with the presence of type H3 hysteresis loops which indicates the presence of porous structures. The surface area of Arg/PAA-PSiNP determined using BET analysis was found to be 549 m²/g. Pore size distributions of the Arg/PAA-PSiNPs determined using NLDFT analysis showed pore diameters ranging from 1.1 – 2.7 nm, with a dominant peak at 1.8 nm, clearly demonstrating the presence of disordered pore structures (Figure 3.15B). The corresponding data for NH₄OH/PAA-PSiNP displayed pore distributions over a comparable diameter size range, but with significantly reduced pore volumes, and a lower BET surface area of 118 m²/g.

It was previously discussed in Section 3.4 that the increased charge density and crosslinking ability of Arg leads to greater retention of PAA chains during the hydrolysis and condensation of silane species and the presence of this polyelectrolyte network gives rise to the particle porosity. This is consistent with the reduced electrostatic interaction between NH₄OH and PAA and the resulting poor polymer retention within the PECs, which ultimately leads to reduced surface area and comparatively poor porosity for NH₄OH/PAA-PSiNPs.

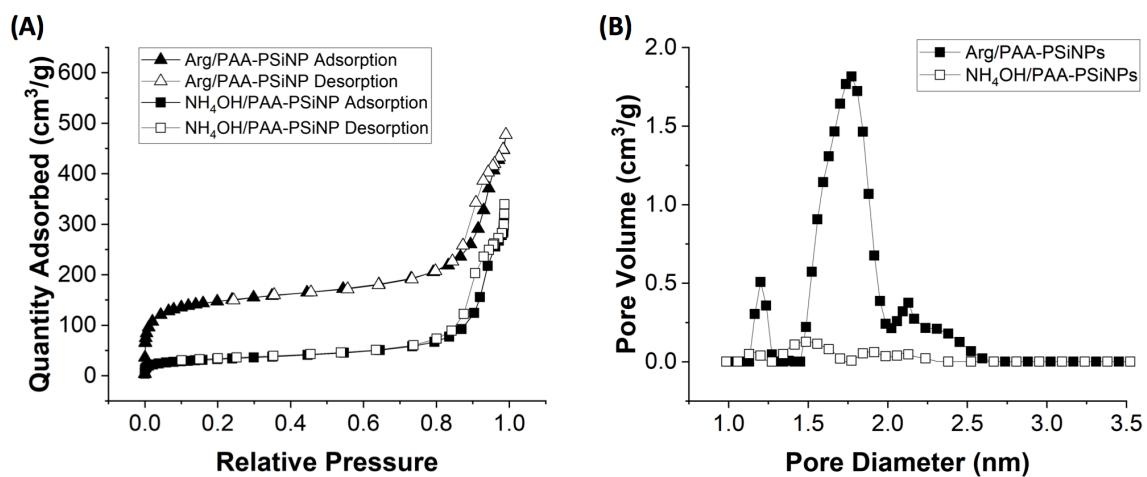


Figure 3.15 (A) N₂ gas adsorption/desorption isotherms collected at 77K for Arg/PAA-PSiNPs and NH₄OH/PAA-PSiNPs and (B) the corresponding pore size distributions determined using non-local density function theory analysis.

3.8 Synthesis of FITC-Labelled Arg/PAA and NH₄OH/PAA Templated PSiNPs

To facilitate imaging and quantitative analysis of cellular internalisation (discussed in the following Chapter 4), the synthesis protocol presented above was adapted to yield fluorescent FITC-labelled Arg/PAA-PSiNPs and NH₄OH/PAA-PSiNPs. This was achieved via the preparation of PECs as described followed by the co-condensation of TEOS and FITC-PEG-silane. The inclusion of just 0.1 mol % of the FITC-PEG-Silane led to the incorporation of FITC into the as-synthesised PSiNPs which had a fluorescence emission peak at 518 nm after excitation at 490 nm (Figure 3.16).

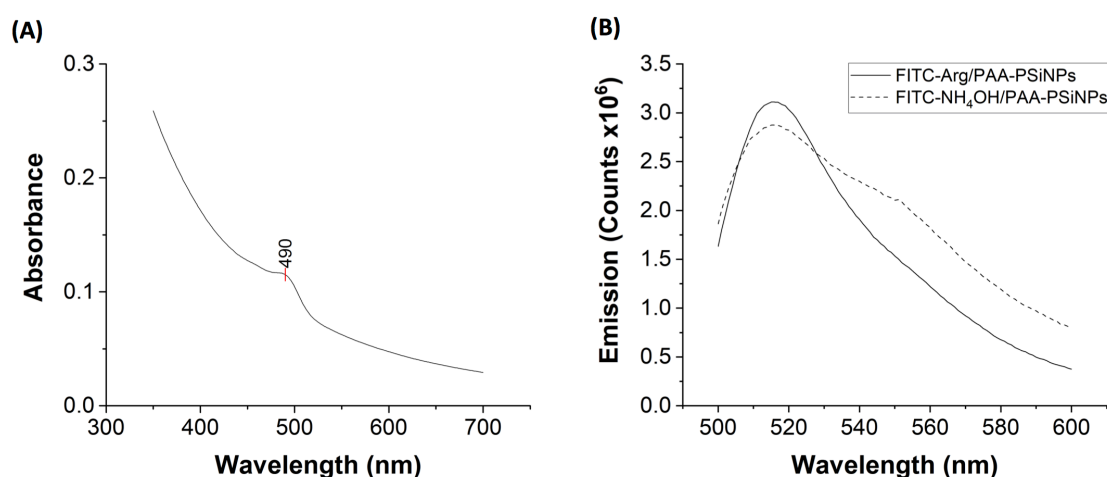


Figure 3.16 (A) A typical UV-Vis absorbance trace and (B) fluorescence emission spectra for FITC-Arg/PAA-PSiNPs and FITC-NH₄OH/PAA-PSiNPs excited at 490 nm.

As previously described, the Arg/PAA-PSiNPs size may be finely controlled while maintaining monodispersity by varying the amount of silane added to a fixed PEC template diameter (Section 3.4). The fine size control and size uniformity is not adversely affected by the inclusion of the FITC-labelled silica precursor. TEM imaging revealed that those synthesised with 75 μ L, 400 μ L and 1 mL of TEOS (total synthesis volume 250 mL) with 0.1 mol % FITC-PEG-silane had particle diameters of 22 ± 2 nm, 52 ± 5 nm, and 84 ± 10 nm (Figure 3.17)

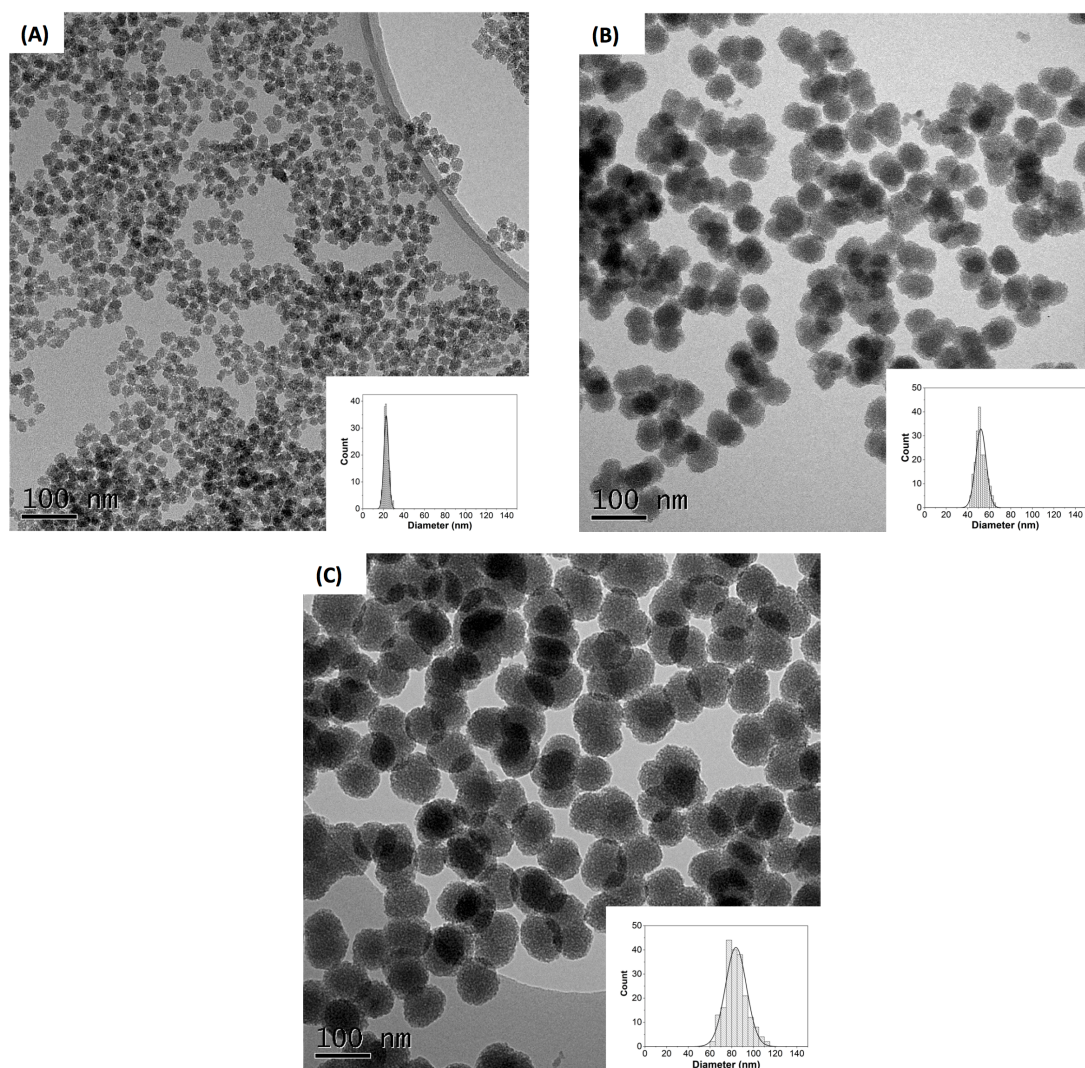


Figure 3.17 TEM images and corresponding size histograms for FITC-Arg/PAA-PSiNPs synthesised using (A) 75 μL , (B) 400 μL , and (C) 1 mL of TEOS with 0.1 molar % of FITC-PEG-Silane. The average diameters are 23 ± 3 nm, 52 ± 5 nm, and 84 ± 10 nm respectively ($n = 200$ for all).

3.9 Conclusion

In this chapter, a simple one-pot synthesis of monodisperse, sub-100 nm PEC templated PSiNPs with intrinsic polymer and amino acid surface functionality has been developed. Monodispersed Arg/PAA PECs with tunable diameters between 50 - 130 nm were formed by variation of the PAA and Arg concentrations. Upon addition of silica precursors, the condensation of silica species occurred selectively inside the PEC templates leading to the formation of monodispersed PSiNPs with intrinsic PAA and Arg surface functionality. The PSiNP diameter was highly tuneable between 42 – 100 nm with spherical morphologies standard deviations below than 10 %. Across 3 repeat syntheses the hydrodynamic diameter varied by less than 5 nm. It was then found that the strong electrostatic interactions between Arg and PAA not only led to enhanced uniformity and fine size control of both PECs and resultant silica nanoparticles when compared to NH_4OH , but also enhanced the particle porosity without the need for template removal.

We went on to evaluate the relationship between the template and silica particle size and defined three growth regimes characterised by differential presentation of the PEC components as surface ligands. To ensure the presentation of both PAA for pH responsive drug release, and Arg for selective uptake and accumulation into cancer cells, the PEC template diameter must exceed that of the silica.

The synthetic pathway presented above provides significant benefit over those reported in literature, both in the particle uniformity and size control achieved below 100 nm, and in the intrinsic Arg and PAA functionalisation for cancer targeting and pH-responsive drug release, respectively. The application of this particle for targeted and pH-responsive therapeutic delivery is discussed in Chapter 4.

4 Application of Arginine/Polyacrylic Acid PEC Templated SiNPs for Cancer Targeted and pH-Responsive Drug Delivery

4.1 Motivation

In the previous chapter, we have developed a novel one-pot synthetic protocol for the PEC templated synthesis of porous silica nanoparticles (PSiNPs). The use of PECs as scaffolds for the condensation of silica species led to the formation of highly uniform PSiNPs with tunable diameters and to the in-synthesis functionalisation of the particles with the PEC components polyacrylic acid (PAA) and arginine (Arg).

PAA carries ionisable carboxyl groups with a negative charge at physiological pH, and is thus able to electrostatically complex cationic doxorubicin hydrochloride (Dox), leading to enhanced loading and retention of the drug in the pores of the PSiNP. In the weakly acidic tumour microenvironment, closer to the pKa of PAA ($pK_a = 4.5$)¹³⁸, the reduced protonation state of the polymer leads to weaker electrostatic interactions with the drug which facilitates drug release.^{92,144}

Arg was chosen as a component of the PECs for its ability to crosslink PAA in the formation of monodispersed coacervate complexes and confer excellent colloidal stability to the as-synthesised PSiNPs. In addition, it was also selected to confer cancer targeting capabilities. It is known that the endogenous arginine synthesis is disrupted by argininosuccinate synthetase (ASS) deficiencies in some malignant tissues, leading to auxotrophy and a dependence on exogenous arginine.¹²⁸⁻¹³⁰ As a result, some cancers up-regulate and overexpress the cationic amino acid transporter-1 (CAT-1) to enhance the cellular uptake and accumulation of arginine.¹³¹ Hence, the surface functionalisation of the PSiNPs with Arg to target towards the CAT-1 transporter was identified as means to enhance their uptake in tumour cells.

Through the presentation of both PAA and Arg at the particle surface we demonstrated the loading and pH responsive release of a model anti-cancer drug Dox, and the selective uptake of the Arg/PAA functionalised PSiNPs by patient derived glioblastoma cells in comparison with non-tumourigenic neural progenitor cells.

4.2 Drug Loading and Release of Doxorubicin Hydrochloride From PAA/Arg PSiNPs

To assess the drug loading and pH responsive drug release capabilities of the PEC templated PSiNPs, Dox, which can interact electrostatically with anionic PAA, was used as a model drug. As previously discussed in Chapter 3, the synthesis of Arg and PAA functionalised porous silica nanoparticles (Arg/PAA-PSiNPs) was achieved through a PEC templated synthesis. Control particles were also produced using NH_4OH in place of Arg ($\text{NH}_4\text{OH}/\text{PAA}$ -PSiNPs), which did not retain the PAA functionalisation and showed significantly reduced porosity.

To achieve drug loading, Arg/PAA-PSiNPs or $\text{NH}_4\text{OH}/\text{PAA}$ -PSiNPs (2 mg/mL) were mixed with Dox (1, 2, or 4, mg/mL) at room temperature for 48 h under dark conditions, to prevent photodegradation, before removal of non-loaded drug by centrifugation. The Arg/PAA-PSiNPs were found to have significantly higher drug loading capacity compared to the $\text{NH}_4\text{OH}/\text{PAA}$ -PSiNPs at 1 and 2 mg/mL of initial Dox loading concentrations (Figure 4.1; $P < 0.05$). With the Arg/PAA-PSiNPs, the highest drug loading capacity of 22% w/w was achieved at 1 mg/mL of initial Dox, which is comparable to that achieved with other porous silica nanoparticles.^{145–149} Although several examples of polymer grafted porous silica particles have exhibited higher loading capacities sometimes in excess of 50%, this is likely due to interaction of Dox with exterior polymer chains, which reduces the possibility for adding targeting or secondary surface functionality.^{92,144,150} A stepwise reduction in drug loading capacity to 16 and 8% w/w at higher Dox concentrations of 2 and 4 mg/mL, respectively was also observed. In contrast, the $\text{NH}_4\text{OH}/\text{PAA}$ -PSiNPs showed a maximum drug loading capacity of only 8% w/w at 1 mg/mL Dox. The higher drug loading capacity of the Arg/PAA-PSiNPs could be attributed to the higher anionic PAA retention afforded by the presence of Arg within the PECs as confirmed earlier by TGA (Section 3.7) and their higher internal pore volumes (Section 3.8). This permits enhanced electrostatic interaction with the cationic Dox to give higher drug encapsulation capacity within the pores of the Arg/PAA-PSiNPs.

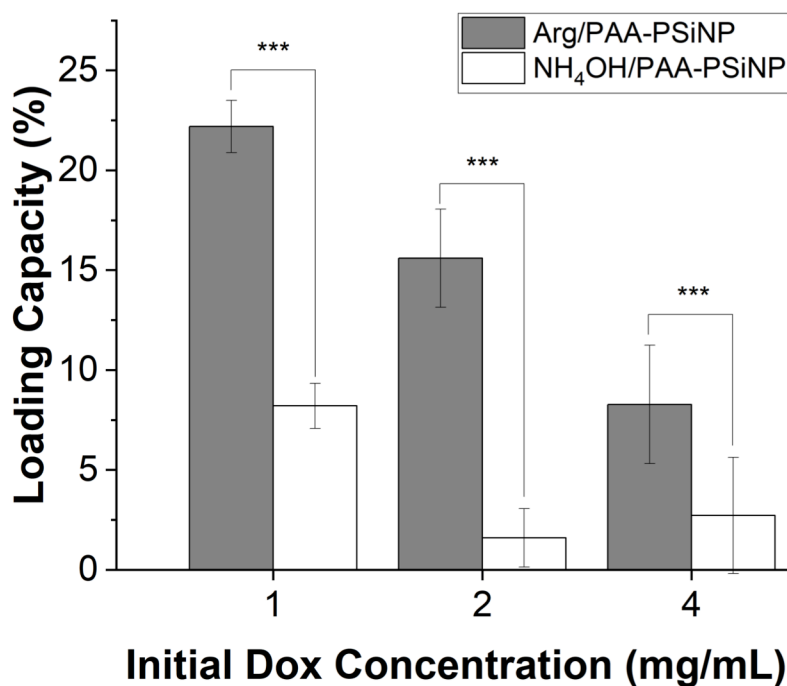


Figure 4.1 Drug loading capacity of Arg/PAA-PSiNPs and NH₄OH/PAA-PSiNPs (1 mg/mL) incubated with 1, 2, and 4 mg/mL Dox for 48 h.

The hydrodynamic diameters of the Dox-loaded Arg/PAA-PSiNPs and NH₄OH-PSiNPs were found to be 162 ± 3 and 152 ± 1 nm, respectively, which were higher than the initial 128 ± 2 and 132 ± 1 nm of the respective empty PSiNPs (Figure 4.2A). This result suggests that some amount of cationic Dox was also adsorbed on the surface of the anionic PSiNPs via electrostatic interactions with surface silanol groups and PAA. Indeed, the Dox-loaded Arg/PAA-PSiNPs and NH₄OH/PAA-PSiNPs were found to have zeta-potentials of -16.0 ± 0.7 and -19.0 ± 0.9 mV, respectively (Figure 4.2B), which were higher than the -24.6 ± 1.1 and -36.9 ± 4.8 mV observed for empty PSiNPs (Section 3.5), hence indicating the presence of positively charged Dox on the surface. Notably however, neither particle carried a positive charge after dox loading; the measured electrophoretic mobility and hence zeta potential is a reflection of the net particle charge, and accounts for both cationic doxorubicin and also anionic PAA and surface silanols. A significantly higher drug loading was observed with the Arg/PAA-PSiNPs compared to the NH₄OH/PAA-PSiNPs. In the case of the latter, a significant proportion of the loaded Dox was likely to have been adsorbed on the exterior surface, whilst the majority of Dox retained by Arg/PAA-PSiNPs was contained within the

pores with a proportionally smaller amount adsorbed on the surface. This conjecture is supported by the BET and NLDFT data described earlier in which the dominant pore size for Arg/PAA-PSiNPs was 1.8 nm (Section 3.7). This was sufficiently large for the loading of Dox, which has a maximum diameter of 1.5 nm.¹⁵⁰ The smaller pore volumes and peak pore diameter of 1.5 nm for the NH₄OH/PAA-PSiNPs led to reduced loading and retention of drug within the pore network compared to the Arg/PAA-PSiNPs.

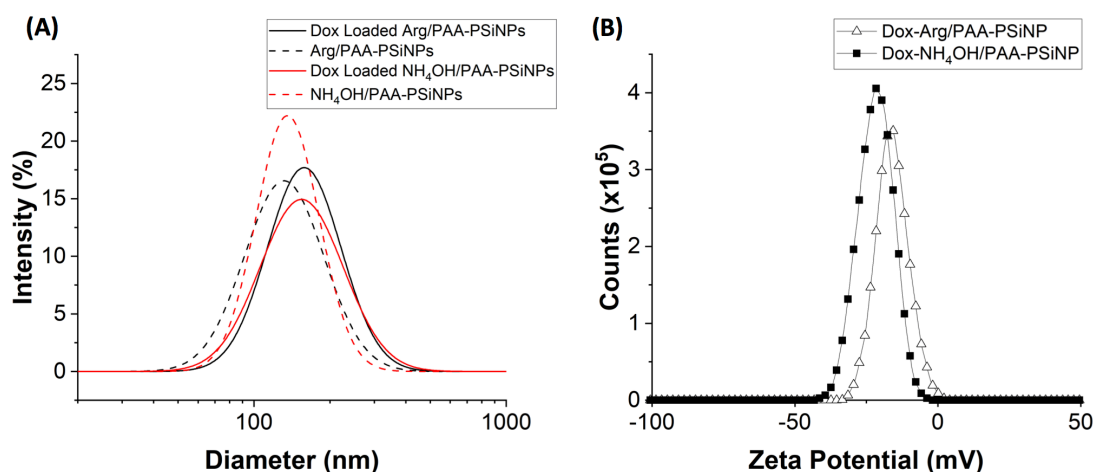


Figure 4.2 (A) Intensity size distributions of empty and Dox-loaded Arg/PAA-PSiNPs and NH₄OH/PAA-PSiNPs measured by dynamic light scattering. Z-average diameters of empty Arg/PAA-PSiNP and NH₄OH/PAA-PSiNPs were 128.4 ± 2.4 and 132.1 ± 0.1 nm, respectively, while that of Dox-loaded Arg/PAA-PSiNP and NH₄OH/PAA-PSiNPs were 162.4 ± 3.4 and 152.2 ± 0.2 nm, respectively. (B) Zeta-potentials of Dox loaded Arg/PAA-PSiNPs and NH₄OH-PSiNPs measured in PBS (pH 7.4). The zeta-potential values for Dox-loaded Arg/PAA-PSiNP and NH₄OH/PAA-PSiNPs were determined to be -16.0 ± 0.7 and -19.0 ± 0.9 mV, respectively.

An added benefit of incorporating PAA within the colloidal templates used for the synthesis of PSiNPs is the ability to provide stimuli-responsive drug release in response to an acidic tumour microenvironment and/or endosomal environment following cellular uptake. As the carboxylic acid groups in PAA have a pK_a of 4.5, they are predominantly deprotonated at the physiological pH of 7.4, leading to the extension of the polymer chains into the pores due to electrostatic repulsion. This effectively enhances the interaction and retention of the Dox by

the extended PAA chains within the pores of the Arg/PAA-PSiNPs. Under acidic pH, however, the protonation of PAA's carboxylic acid groups leads to reduced interaction between PAA chains and the Dox, thus facilitating drug release from the PSiNPs. As depicted in Figure 4.3, the Arg/PAA-PSiNPs were found to have a significantly higher drug release of 33.3% in sodium acetate buffer (pH 5.0) compared to only 8% in PBS (pH 7.4) over 48 h. The low levels of Dox released at physiological pH could be attributed to charge screening effects by ions in the PBS to reduce electrostatic interactions between the adsorbed drug with deprotonated PAA and/or surface silanol groups. Although a similar pH-responsive Dox release profile was also observed with the $\text{NH}_4\text{OH}/\text{PAA-PSiNPs}$, it is important to note that the maximum drug release attained at pH 5.0 was much lower at 17.4%. The enhanced Dox release from the $\text{NH}_4\text{OH}/\text{PAA-PSiNPs}$ under acidic pH is likely to be due to the fact that most of the Dox molecules were adsorbed on the surface through electrostatic interaction with surface silanol groups (pK_a 4.5),¹⁵¹ and thus a decrease in pH to 5.0 leads to the partial protonation of the silanol groups and Dox displacement from the surface of the PSiNPs. The absence of PAA in the $\text{NH}_4\text{OH}/\text{PAA-PSiNPs}$ was confirmed earlier by TGA, thus the mechanism of drug loading and release is ascribed to electrostatic interactions between the surface silanol groups and cationic Dox.

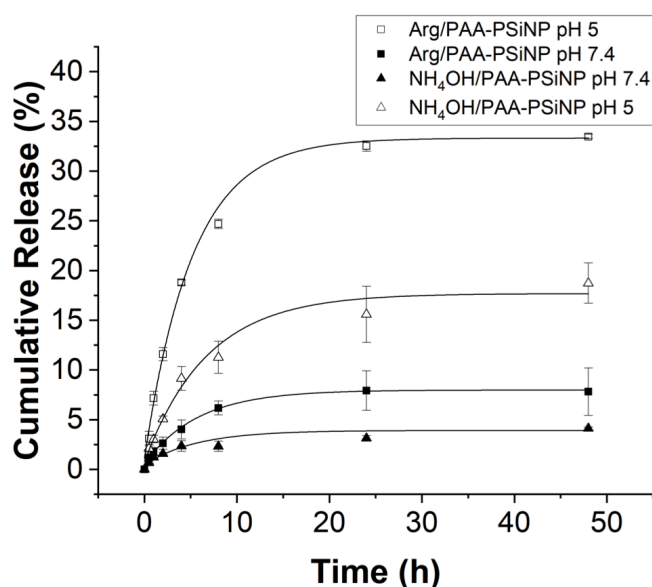


Figure 4.3 Cumulative Dox release curves from the Arg/PAA-PSiNPs and $\text{NH}_4\text{OH}/\text{PAA-PSiNPs}$ over 48 h in PBS (pH 7.4) and sodium acetate buffer (pH 5.0).

The *in vitro* drug release kinetics and mechanisms at different pH were further evaluated using the Korsmeyer-Peppas model.¹⁰¹ Good linearity with high correlation coefficients (R^2) of greater than 0.98 were found for all the samples thus indicating the appropriateness of this model for evaluating the drug release kinetics (Figure 4.4 and Table 3). As discussed previously, the increased protonation of PAA chains within the Arg/PAA-PSiNPs with a decrease in pH from 7.4 to 5.0 leads to greater and faster drug release in acidic pH. Indeed, a rise in the kinetic constant, k_m from 1.78 to 6.84 was seen with the Arg/PAA-PSiNPs, hence indicating more rapid drug release in acidic pH. In contrast, a smaller increase in the k_m from 1.05 to 3.11 was observed for the $\text{NH}_4\text{OH}/\text{PAA-PSiNPs}$ with pH reduction (Table 2). This result indicates that a slower rate of drug release from the $\text{NH}_4\text{OH}/\text{PAA-PSiNPs}$ is occurring in acidic pH possibly *via* the pH-dependent displacement of surface adsorbed Dox. The release exponent, n , was found to range from 0.58 – 0.73 for all samples, hence indicating that the drug release from the Arg/PAA-PSiNPs and $\text{NH}_4\text{OH}/\text{PAA-PSiNPs}$ occurred by non-Fickian diffusion ($n > 0.43$) involving both diffusion and polymer swelling. Although PAA was only detected in the Arg/PAA-PSiNPs and not in the $\text{NH}_4\text{OH}/\text{PAA-PSiNPs}$, the similar n values observed for both particle types at the same pH suggest a diffusion mechanism that is dependent on pH and electrostatic interactions.

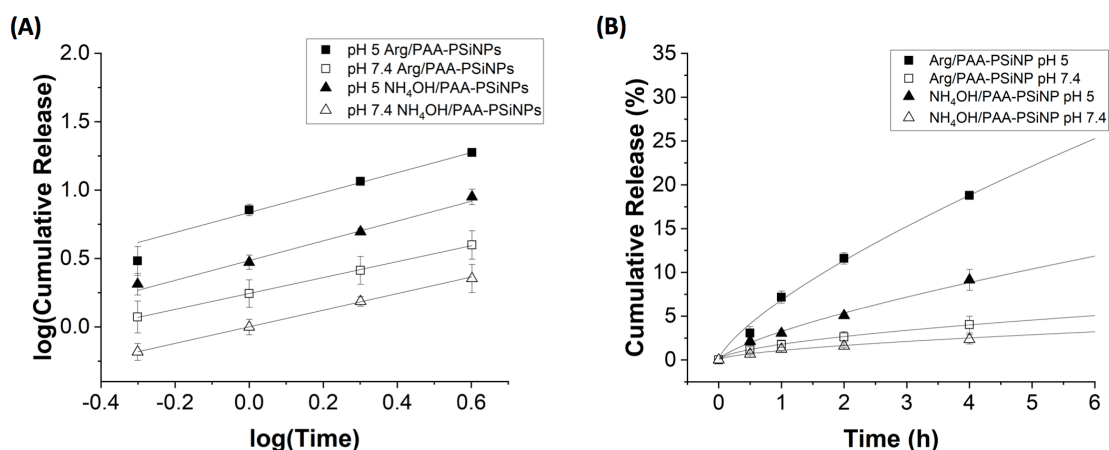


Figure 4.4 (A) A log-log plot of the first 60% of the drug release data where the gradient is the release exponent, n . (B) The Korsmeyer-Peppas fit, where n was found from (A) and used in Eq. 2-2 to determine the kinetic constant, k_m .

Table 3 The release exponent, n , and kinetic constant, k_m , describing the pH responsive release kinetics, and R^2 values for Arg/PAA-PSiNPs and NH_4OH /PAA-PSiNPs.

Particle type	pH of release medium	n	k_m	R^2
Arg/PAA-PSiNPs	5	0.73 ± 0.04	6.84 ± 0.08	0.996
	7.4	0.58 ± 0.01	1.78 ± 0.01	0.999
NH_4OH /PAA-PSiNPs	5	0.72 ± 0.06	3.11 ± 0.07	0.988
	7.4	0.61 ± 0.01	1.05 ± 0.03	0.981

4.3 *In vitro* Cytotoxicity Testing and Selective Uptake of Arg/PAA-PSiNPs in Primary Human Glioblastoma Cells

The biosafety and cancer specific uptake of the Arg/PAA-PSiNPs and NH₄OH/PAA-PSiNPs were assessed using two different patient-derived GBM cell lines, GBM1 and GBM20. The GBM1 cell line was derived from a primary tumour with no prior treatment and the GBM20 cell line originated from recurrent GBM post radiotherapy, temozolomide, and IMA950 treatment.^{102,103} Both cell models exhibit stem cell-like features as well as transcriptional heterogeneity at the single cell level representing classical, proneural, and mesenchymal GBM tumour cell subpopulations. In addition, the non-tumorigenic human adult neural progenitor cell line, NP1, derived from primary tissue obtained from a patient undergoing epileptic surgery, was included as a control.^{102,103}

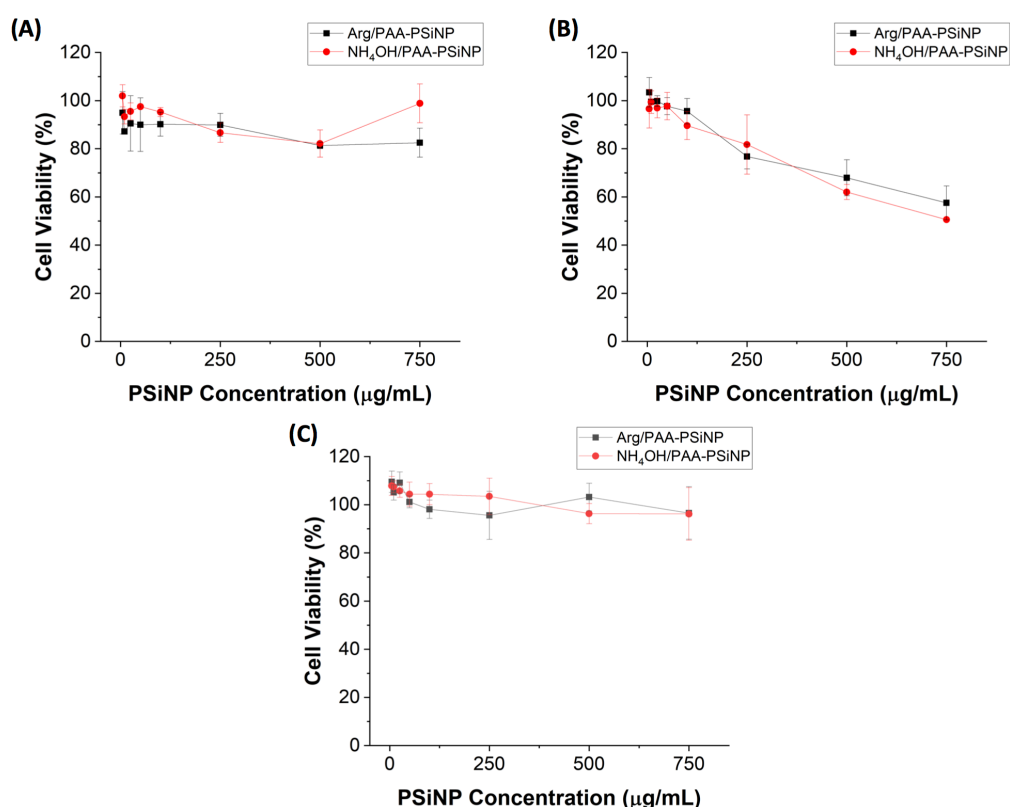


Figure 4.5 Cytotoxicity of Arg/PAA-PSiNPs and NH₄OH/PAA-PSiNPs in patient-derived glioblastoma cell lines. Graphs show cellular viability of GBM1 (A), GBM20 (B), and the (C) non-tumourigenic human adult neural progenitor NP1 cells treated with 0-750 µg/mL of Arg/PAA-PSiNPs and NH₄OH/PAA-PSiNPs for 24 h.

The cytotoxicity of the Arg/PAA-PSiNPs and NH₄OH/PAA-PSiNPs towards the various cell lines was first evaluated using the WST-1 assay. No significant cytotoxicity was observed in GBM1 and NP1, with > 80% cell viability observed up to high concentrations of 750 µg/mL after 24 h treatment (Figure 4.5A and C). Although a slight dose-dependent toxicity was observed in GBM20, the cell viability remained ≥ 77% up to a supraphysiological concentration of 250 µg/mL, which was much higher than the concentrations used in subsequent cellular uptake and drug delivery studies (Figure 4.5B). As Arg/PAA-PSiNPs and NH₄OH/PAA-PSiNPs have similar cytotoxicity profiles in GBM20 at high concentrations, it is likely that the induced cytotoxicity observed is intrinsic of silica nanoparticles and is not due to the added Arg or PAA surface functionality.

To assess the tumour cell selectivity, fluorescent FITC-labelled Arg/PAA-PSiNPs and NH₄OH/PAA-PSiNPs were synthesised by the co-condensation of FITC-PEG-silane with TEOS. By varying the volume of silanes added, the diameters of the FITC-labelled Arg/PAA-PSiNPs were readily tuned between 22.8 ± 2.3 nm – 83.9 ± 9.7 nm; with narrow size distributions obtained. The FITC-labelled Arg/PAA-PSiNPs demonstrated strong absorbance at 490 nm, with a clear fluorescence emission peak at 518 nm with excitation at 490 nm (Section 3.8). GBM1, GBM20, and NP1 cells were incubated with FITC-labelled Arg/PAA-PSiNPs and NH₄OH/PAA-PSiNPs with comparable Z-average diameters of 112.9 ± 2.2 and 127.6 ± 2.6 nm, respectively for 24 h. After removal of non-internalised PSiNPs, the cells were lysed and quantified for cellular uptake using fluorescence spectroscopy. To account for differences in cell number and size between cell lines, the fluorescent intensity values obtained were normalised for protein expression determined by BCA assay. A significantly higher uptake of Arg/PAA-PSiNPs compared to the non-targeting NH₄OH/PAA-PSiNPs was observed in both GBM cell models (Figure 4.6A; P < 0.001); with a 2.9- and 3.7-fold higher uptake of Arg/PAA-PSiNPs in GBM1 and GBM20, respectively. Notably, there was no significant difference in uptake of Arg/PAA-PSiNPs and NH₄OH/PAA-PSiNPs in the non-tumourigenic NP1 cells (P > 0.05). To further confirm the cellular internalization of the Arg/PAA-PSiNPs and NH₄OH/PAA-PSiNPs, confocal imaging of the GBM20 and NP1 cells was performed. Consistent with the cellular uptake data, GBM20 cells treated with the cancer targeting Arg/PAA-PSiNPs exhibited stronger fluorescence intensities compared to the non-targeting NH₄OH/PAA-PSiNPs and Arg/PAA-PSiNP treated non-tumourigenic NP1 cells (Figure 4.6B). No apparent difference in fluorescence intensities between confocal images of NP1 cells treated with Arg/PAA-PSiNP

and $\text{NH}_4\text{OH/PAA-PSiNPs}$ was observed. These results demonstrate a marked enhancement of cellular uptake capabilities of the Arg/PAA-PSiNPs towards the GBM cells over non-tumorigenic NP1 cells, thus demonstrating their potential for use as selective cancer targeted drug delivery vehicles.

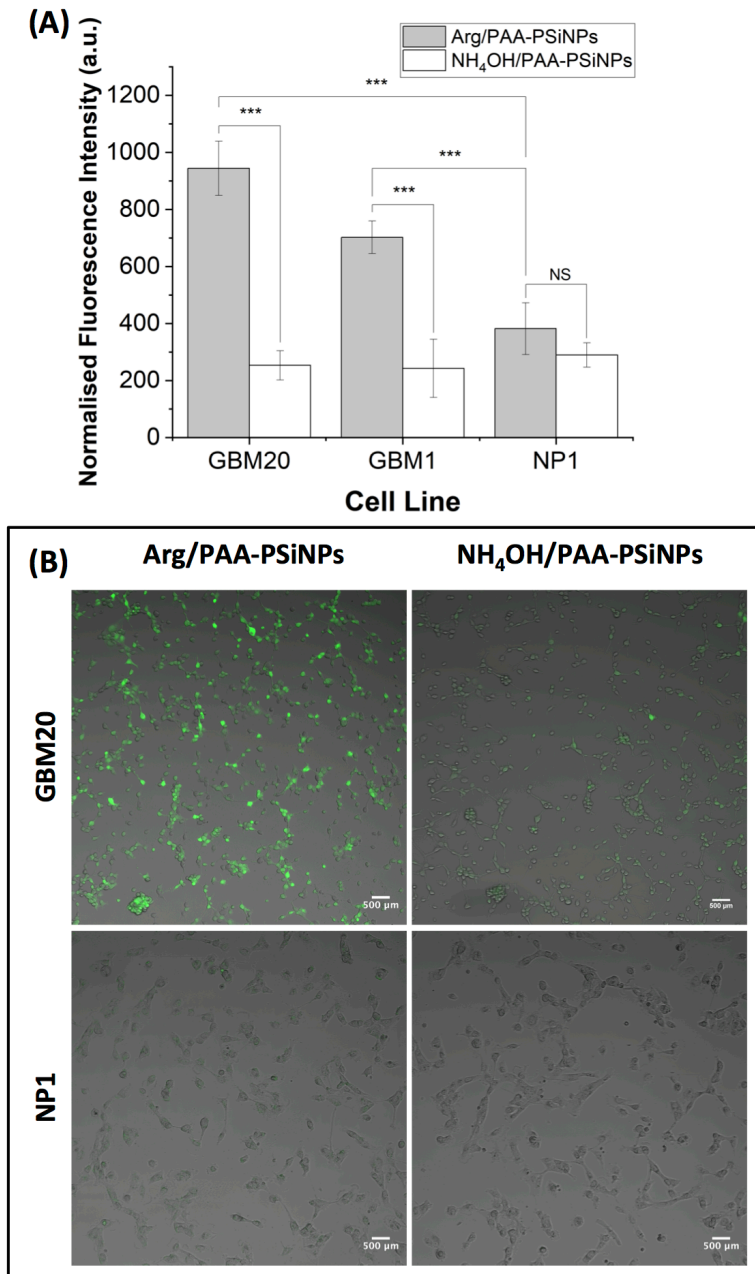


Figure 4.6 Enhanced targeting and uptake of Arg/PAA-PSiNPs by patient-derived glioblastoma cells. (A) Cellular uptake of FITC-labelled Arg/PAA-PSiNPs and NH₄OH/PAA-PSiNPs after treating GBM1, GBM20, and non-tumourigenic neural progenitor NP1 cells with 200 μ g/mL of PSiNPs for 4 h. The fluorescence intensities of the internalized particles were normalized for cellular protein content using the bicinchoninic acid assay. Each data point represent mean \pm standard deviation from at least two independent experiments performed with six replicates. *** $P < 0.001$; NS indicates lack of statistical significance ($P > 0.05$). (B) Confocal images of GBM20 and NP1 cells following treatment with FITC-labelled Arg/PSiNPs and NH₄OH/PAA-PSiNPs.

4.4 The Effect of Arg/PAA-PSiNP Overgrowth on Cellular Uptake

As discussed in Section 3.4, the relationship between the PEC template diameter and the PAA/Arg-PSiNP diameter can be used to modulate the presentation of both PAA and Arg at the particle surface (Figure 3.10). Three possible growth regimes were described and are summarised here:

- ‘Undergrowth’. The Arg/PAA-PSiNP diameter is less than that of the PEC template leading to presentation of both PAA and Arg at the surface.
- ‘Slight Overgrowth’. The Arg/PAA-PSiNP diameter is larger than the PEC so as to cover the PAA scaffold and prevent its surface presentation. Free Arg in solution may still catalyse the silica condensation and functionalise the PSiNP surface via electrostatic interaction between protonated amines in the guanidinium group of Arg, and anionic silanol groups at the silica particle surface.
- ‘Significant Overgrowth’. The Arg/PAA-PSiNP diameter far exceeds that of the PEC template such that the PAA and Arg of the PEC scaffold may not present at the surface, and all free Arg in solution has been exhausted. Only silanol groups decorate the PSiNP surface.

Considering the proposed role of Arg in the cancer-selective cellular uptake behaviour, and its modulation with overgrowth regime, the cellular uptake of the significantly overgrown Arg/PAA-PSiNPs was thus further investigated using GBM20 cells. For this, the amount of TEOS added to the initial PEC template was increased to obtain significantly overgrown Arg/PAA-PSiNPs (final PSiNP/template diameter ratio of 311%) with a zeta-potential of -37.2 mV (Figure 4.7), which was indicative of deprotonated silanol groups at a particle surface devoid of Arg functionalisation.

Compared to the Arg/PAA-PSiNPs synthesised with 40 μ L of TEOS (PSiNP to PEC template diameter ratio of 157 %), which have shown tumour specific targeting earlier (Figure 4.6A), a significant decrease in the normalised fluorescent intensity from 933 a.u. to 558 a.u. was seen, thus demonstrating a reduced cellular uptake of the overgrown Arg/PAA-PSiNPs, although this is not a true comparison as the particle diameters between these experiments are significantly different (undergrowth particle diameter = 112.9 ± 2.2 nm; overgrowth particle diameter = 226 ± 6.4 nm) . Confirmation of the effect of overgrowth, and hence lack of

surface Arg, comes from a direct comparison of the cellular uptake of overgrown Arg/PAA-PSiNPs and NH₄OH/PAA-PSiNPs with comparable hydrodynamic diameters of 226.3 ± 6.4 and 194.3 ± 2.9 nm, respectively (Figure 4.7), which did not give a significant difference in cellular uptake ($P > 0.05$; Figure 4.8).

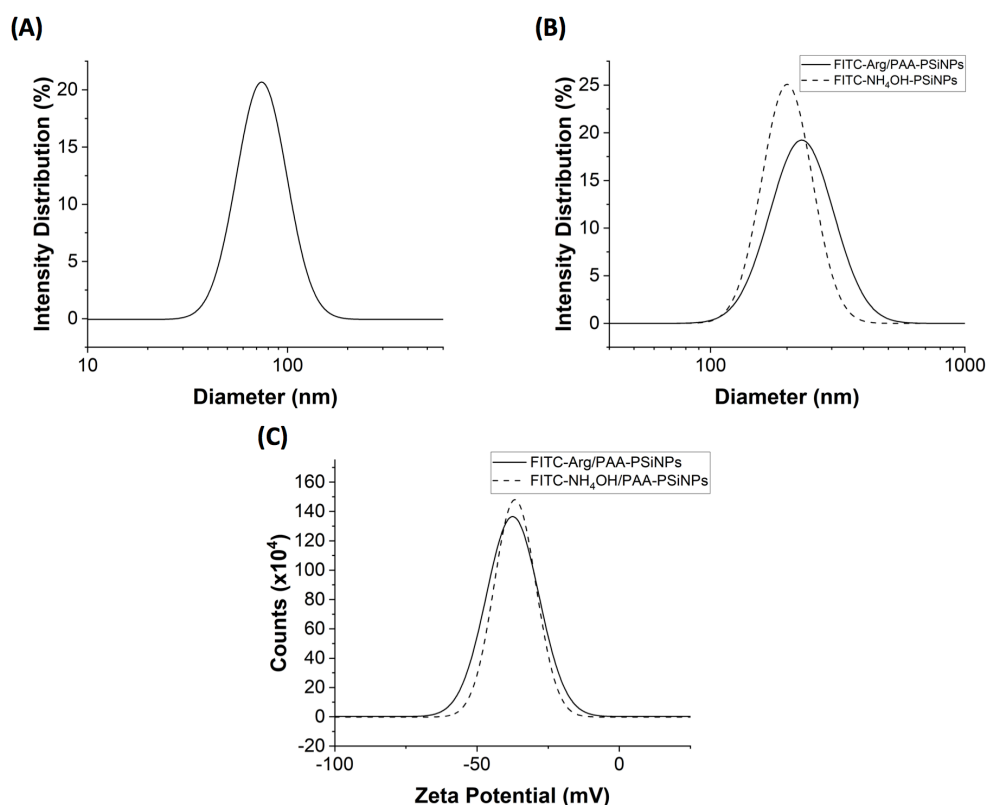


Figure 4.7 (A) The intensity size distribution determined by DLS for Arg/PAA PECs with a Z-average diameter of 72.5 ± 1.3 nm used for the overgrowth synthesis of FITC-labeled Arg/PAA-PSiNPs. (B) Intensity size distributions for FITC-labelled Arg/PAA-PSiNPs and NH₄OH/PAA-PSiNPs synthesised in the overgrowth regime for use in nanoparticle uptake studies with z-average sizes of 226 ± 6.4 and 194.3 ± 2.9 nm respectively. (C) The zeta-potential distributions for the FITC-labelled Arg/PAA-PSiNPs and NH₄OH/PAA-PSiNPs with average values of -37.2 ± 1.2 and -36.7 ± 1.3 mV, respectively.

This result clearly indicates a loss of cancer targeting abilities when Arg/PAA-PSiNPs were prepared in a drastically overgrown regime from the initial PEC colloid template. When small amounts of TEOS were added, sufficient Arg and PAA remained available within the colloidal system to present on the surfaces of the Arg/PAA-PSiNPs formed. Beyond the

addition of a critical amount of TEOS, most of the Arg and PAA in the system were likely to have been used up as scaffolds for the hydrolysis and condensation of the silanes, hence resulting in the formation of PSiNPs with minimal or no Arg surface functionalisation for cancer targeting (Figure 3.10). Taken together, these results strongly highlight the need to consider appropriate colloidal template sizes for the preparation of polyelectrolyte templated PSiNPs used in cancer targeting applications to ensure that the cell targeting moieties are retained on the surface of the final products. It is plausible that to obtain larger monodisperse PSiNPs that retain the surface presentation and hence functional properties of each polyelectrolyte used in the PECs, correspondingly larger colloidal templates would need to be used in the synthesis.

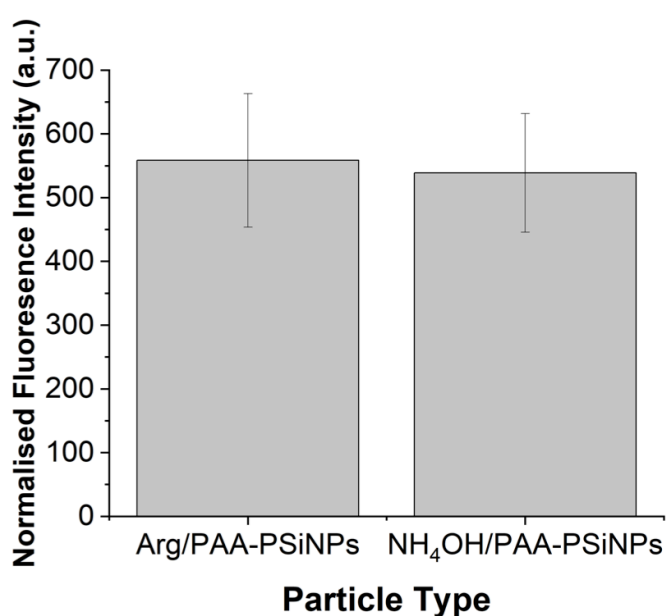


Figure 4.8 Cellular uptake of overgrown FITC-labelled Arg/PAA-PSiNPs and NH₄OH/PAA-PSiNPs. GBM20 cells were treated with 200 µg/mL of PSiNPs for 4 h and the fluorescence intensity of the internalised particles was normalised for cellular protein content.

4.5 Enhanced Anticancer Efficacy in Patient-Derived Glioblastoma Cells

The anticancer drug delivery potential of the Arg/PAA-PSiNPs with combined tumour targeting and pH-responsiveness was demonstrated using patient derived GBM1 cells. Following 24 h incubation with either Dox-loaded Arg/PAA-PSiNPs, Dox-loaded NH₄OH/PAA-PSiNPs or free Dox, the cell viability was assessed by WST-1 assay. The enhanced tumour cell uptake (Section 4.3) and increased Dox release in acidic pH environments such as the weakly acidic endosomes following cellular internalisation (Section 4.2) effectively led to a significantly reduced half maximal inhibitory concentration (IC₅₀) of 5.3 μM with Dox-loaded Arg/PAA-PSiNPs compared to 14.0 μM of NH₄OH/PAA-PSiNPs (Figure 4.9). The observed IC₅₀ value of Dox-loaded Arg/PAA-PSiNPs equates to 13.2 μg/mL of empty Arg/PAA-PSiNPs, which is a concentration previously shown to induce minimal or no toxicity in GBM1 cells (Figure 4.4). This result clearly demonstrates that the enhanced anticancer effect seen with Dox-loaded Arg/PAA-PSiNPs was due to the anticancer drug released and not a result of PSiNP induced toxicity. The higher IC₅₀ value observed with Dox-loaded Arg/PAA-PSiNP compared to free Dox (1.8 μM) can be explained by the slower drug release, where only approximately 30% of the loaded Dox was released from the Arg/PAA-PSiNPs after 24 h (Figure 4.3). In spite of this result, the strong tumour cell selectivity and pH-responsiveness of the Arg/PAA-PSiNPs are expected to be more advantageous to promote in vivo tumour accumulation of the Dox-loaded Arg/PAA-PSiNPs, where enhanced Dox release can occur in response to the acidic tumour microenvironment and in the endosomes following uptake by tumour cells.

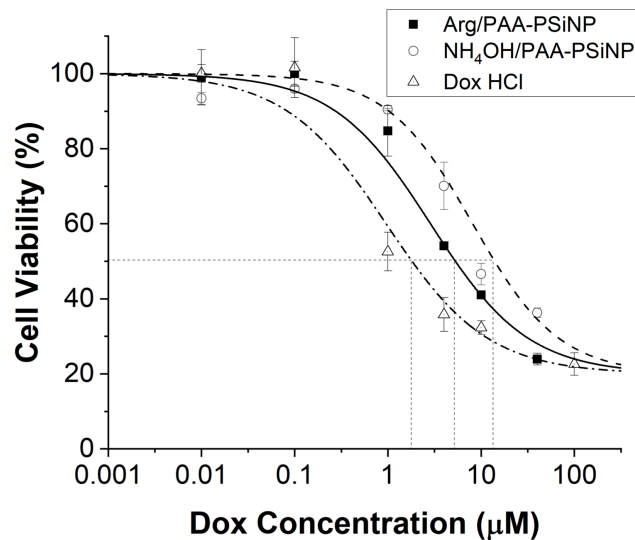


Figure 4.9 Cell viability of GBM1 cells following 24 h treatment with Dox-loaded Arg/PAA-PSiNPs and NH₄OH-PSiNPs as determined using the WST-1 assay and fitted with a dose-response curve (Eq. 2-4). The dotted lines indicate the IC₅₀ values. The results represent mean ± standard deviation from two independent experiments performed with six replicates.

4.6 Conclusion

In this chapter, the efficacy of the Arg/PAA-PSiNPs as GBM-targeted and stimuli-responsive drug delivery vehicles has been demonstrated.

The anticancer drug, Dox, was successfully retained in the internal pore network of the PSiNPs with a high loading capacity of 22 % w/w, and through the pH responsive activity of retained PAA, enhanced drug release was observed under weakly acidic conditions. It was discussed previously (Chapter 3) that the use of NH_4OH in place of Arg during synthesis reduced the particle porosity and retention of PAA in the final PSiNPs. In this chapter, we showed that this caused a significant reduction in the loading capacity for $\text{NH}_4\text{OH}/\text{PAA}$ -PSiNPs when compared to Arg/PAA-PSiNPs.

The Arg/PAA-SiNPs and $\text{NH}_4\text{OH}/\text{PAA}$ -PSiNPs did not induce overt cytotoxicities in patient derived GBM cells. A significantly higher cellular uptake was observed for Arg/PAA-PSiNPs compared to $\text{NH}_4\text{OH}/\text{PAA}$ -PSiNPs with GBM20 and GBM1 cells, while no significant difference was observed with non-tumorigenic NP1 cells. Furthermore, when PSiNPs were synthesised in the 'overgrowth' regime where no Arg surface functionalisation is present, no significant difference in uptake was observed between the Arg/PAA- and $\text{NH}_4\text{OH}/\text{PAA}$ -PSiNPs ($P > 0.05$). This resulted in a significantly reduced IC_{50} for Dox loaded Arg/PAA-PSiNPs versus $\text{NH}_4\text{OH}/\text{PAA}$ -PSiNPs. As the enhanced uptake of Arg is common amongst aggressive malignancies, the Arg/PAA-PSiNPs are expected to have wider drug delivery applications in other cancer types.

5 Synthesis and Characterisation of Poly(ethyleneimine)/Glutamic Acid Polyelectrolyte Complex Templated Porous Silica Nanoparticles

5.1 Motivation

In this chapter, we present a PEC templated SiNP synthesis for poly(ethylenimine) functionalised SiNPs (PEI-SiNPs) which are later used in Chapter 6 as multifunctional crosslinkers for electrostatic interaction with hyaluronic acid in the formation of physical nanocomposite hydrogels.

In Chapter 3, we reported that polyelectrolyte complexes (PECs) formed through alcohol-induced coacervation may function as templates for the hydrolysis and condensation of silanes. The PEC constituents, PAA and Arg, were retained in the silica matrix of the SiNPs and on the surface. Herein, we demonstrate the versatility of the PEC templated system and explore the use of other polyelectrolyte pairs containing a positively charged polymer with an anionic amino acid to impart new functionalities to the SiNPs. Similar to that presented in Section 3.2, the required properties of the colloidal templates are as follows: The PECs are monodispersed and of tuneable nanoscale diameter; the aqueous PEC microenvironment has a pH suitable for the basic catalysis of silane condensation; and their molecular interactions with the silica matrix are sufficient to cause retention of the PEC components as SiNP surface functionalities.

It was hypothesised that the large number of ionisable groups of the polycationic poly(ethylenimine) (PEI) would provide both an alkaline environment in the PECs for the condensation of silica precursors, and a strongly positive surface charge when presented at the surface of the SiNPs. For the choice of counter ion, it is known from published studies that the use of multivalent ions can permit the retention of the PEC constituents in the final SiNPs.⁹⁹ This effect was also observed in Chapter 3 where the use of cationic NH_4^+ to interact electrostatically with anionic PAA did not lead to retention of the polymer within the SiNPs, while the use of Arg which has a higher charge density permitted the synthesis of

PAA-functionalised SiNPs. In addition, we showed that this higher charge density of Arg resulted in greater monodispersity to the PEC templates, which was conferred to the SiNPs. As such, we used glutamic acid (Glu) whose two ionisable carboxyl groups (both of which are deprotonated at alkaline pH) were able to crosslink between PEI molecules leading to the formation of monodispersed PECs. Further, this PEC composition led to the retention of PEI and hence its presentation at the SiNP surface.

5.2 Formation and Size Control of PEI/Glu PEC Templates

For the synthesis of PEI-SiNPs a PEC templated protocol was developed. Monodisperse PECs formed from the mixing of PEI and Glu in a binary water-alcohol solvent act as scaffolds for the spatially selective hydrolysis and condensation of silanes. After synthesis and particle purification, the PEC constituents were retained and presented at the particle surface to yield PEI-SiNPs (Figure 5.1).

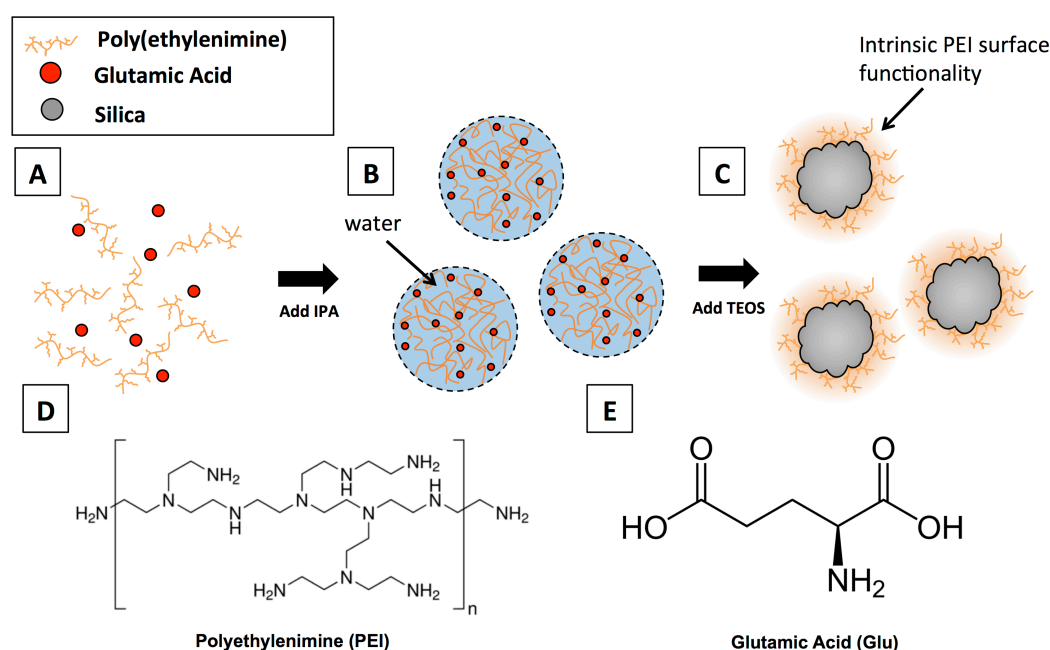


Figure 5.1 A schematic representation of the PEC templated synthesis of PEI functionalised SiNPs. (A) PEI and Glu are dissolved in water, and (B) on the addition of IPA assemble into stable, monodispersed, aqueous PECs in bulk IPA. (C) On the addition of tetraethoxysilane (TEOS), the PECs act as scaffolds for the hydrolysis and condensation of silica. (D,E) The chemical structures of PEI and Glu respectively.

5.2.1 The Effect of Alcohol Co-Solvent Choice on Alcohol-Induced PEC Formation

Similar to Chapter 3, DLS was used to determine the optimum solvent condition for the formation of stable, monodispersed PECs with PEI and Glu. The correlation function, derived from the correlation between successive light scattering events, contains information about the diameter and polydispersity of particles where a stable and monodisperse suspension is characterised by a single smooth exponential decay. Further, the extrapolated y-intercept of the correlation function can describe the scattering signal-to-noise ratio and hence a high value indicates the formation of scattering bodies. As such, observation of the correlation functions collected at progressively increasing alcohol volume fractions can be used to determine the optimum solvent conditions for the alcohol-induced formation of coacervate droplets.

A plot of the DLS correlation function y-intercept for increasing alcohol volume fraction in mixtures of water with IPA, ethanol, or methanol, is shown in Figure 5.2A. For IPA volume fractions between 0 - 60 %, correlation function y-intercept values between 0.31 – 0.51 are observed forming an approximately constant baseline. Over this range, the measured correlation is either comparable to, or less than that observed for 0 % IPA (pure water solvent) suggesting that the complex formation is purely electrostatic and no alcohol-induced assembly of PEI and Glu has occurred. A further increase in IPA to 70 – 90 % v/v led to a sharp increase to 0.73 for 70 % and then to ≈ 0.85 for 80 and 90 % showing an increase in signal-to-noise ratio and hence the alcohol induced assembly of PECs. This combined with the single smooth exponential decay profiles shown in Figure 5.2B indicate that the optimum IPA concentration for the formation of stable, monodisperse complexes is between 80 – 90 % v/v. While in this experiment the complexation occurred in the presence of an excess of glutamic acid (PEI monomer to glutamic acid ratio = 1 : 2.7), the four tertiary amines and approximately two of the three secondary amines of PEI (pKa 11.6 and 6.7 respectively¹⁵²) are protonated (solution pH ≈ 7) and hence each monomer will complex multiple glutamic acid molecules (Figure 5.1D and E).

When ethanol was used as the alcohol co-solvent, a similar profile was observed. Between 0 – 70 % v/v ethanol an approximately constant y-intercept value is found, again showing a comparable value to that observed for the pure water solvent. On increase to 80 – 90 % v/v the same sharp increase in y-intercept from ~ 0.4 to > 0.75 occurs indicating the alcohol-induced formation of PECs.

For the use of methanol, however, this characteristic increase in correlation function y-intercept and high signal-to-noise ratio at high alcohol volume fractions is not observed. In fact, the observed correlation function y-axis intercept remains below 0.58 and the correlation function curves shown in Figure 5.2C remain comparable in shape to the 0 % alcohol condition. From this, it is inferred that any self-assembly or coacervation occurring in the solution is independent of the co-solvent, and based purely on cooperative electrostatic interactions between oppositely charged PEI and Glu.

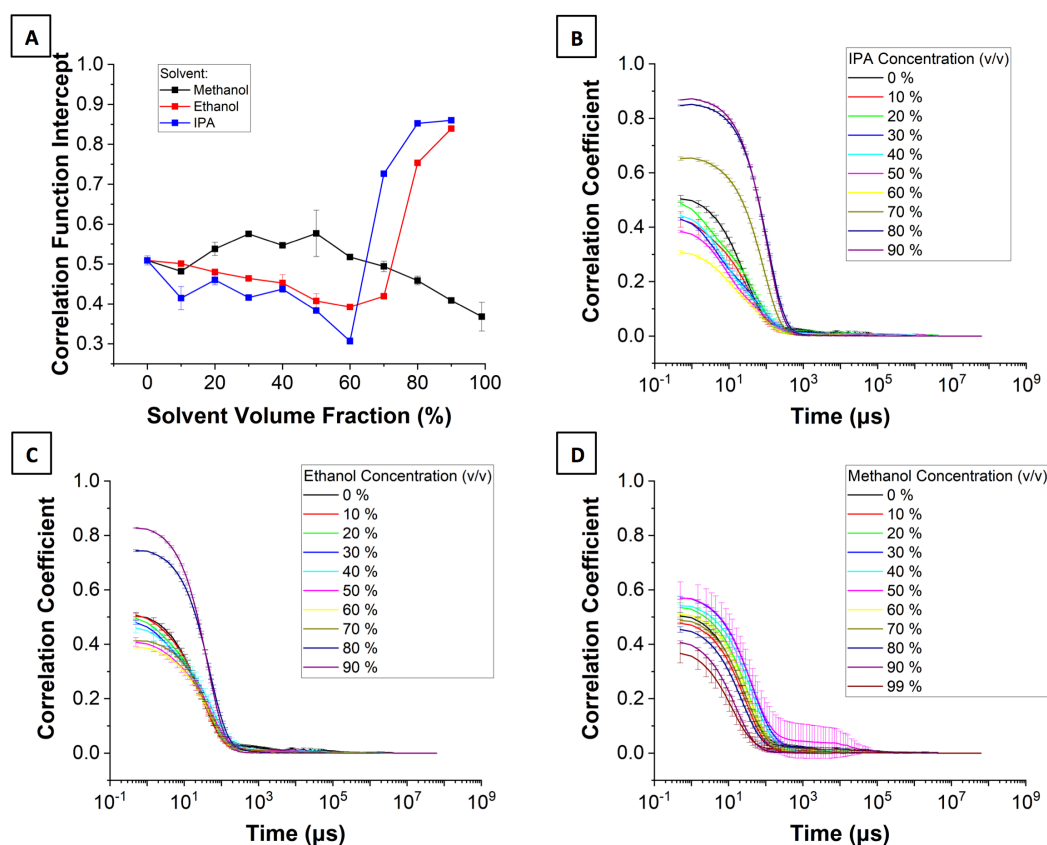


Figure 5.2 Dynamic light scattering correlation data for PEI/Glu PECs prepared in mixtures of water and differing alcohol co-solvents. (A) Changes in the dynamic light scattering correlation function y-axis intercept as a function of alcohol volume fraction and (B-D) the respective correlation curves for mixtures IPA, ethanol, and methanol.

This behaviour can be explained by considering the electrostatic interaction parameter from Debye-Huckle theory for weakly interacting electrolytes in solution and its contribution to the free energy of the polyelectrolyte solution. It is described in Section 1.2.1 that the electrostatic free energy contributes negatively to the total free energy, and is dependent on

$\varepsilon^{-\frac{3}{2}}$. That is to say that decreasing the dielectric constant of the solvent will decrease the total free energy, and at a critical value, cause liquid-liquid phase separation.

Figure 5.3 shows the relationship between the dielectric constant and the volume fraction of alcohol for binary mixtures of water with IPA, ethanol, and methanol¹³⁷, and their effect on the alcohol induced coacervation of PEI/Glu PECs. When IPA was used as the co-solvent, the onset of alcohol-induced PEC formation occurred for ε between approximately 40 and 33 (between 60 – 70 % IPA v/v), while for ethanol the threshold value was observed between 70 – 80 % v/v, corresponding to ε between 41 and 36. Assuming that other differences between the two alcohols (for example polarity and the water-alcohol miscibility) are negligible, one could approximate the threshold dielectric constant for alcohol-induced coacervation of PEI/Glu PECs to be between 40 and 36. However, when the observations of water/methanol mixtures are considered, these approximations break down. It was demonstrated before that no alcohol-induced coacervation occurred between 0 – 99 % v/v methanol, and it is shown in Figure 5.3B that these dielectric constant values are below the proposed critical threshold.

From this, it was concluded that other factors such as the miscibility of the co-solvent or specific interactions between the co-solvent and polyelectrolytes are significant and a critical dielectric constant for coacervation may not be applied universally across all water-alcohol systems.

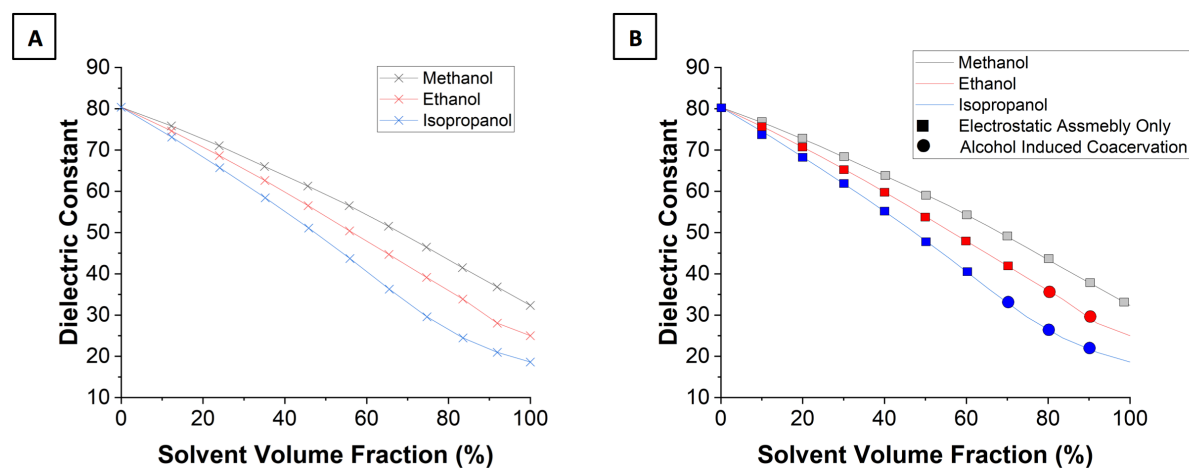


Figure 5.3 (A) The dielectric constant for binary mixtures of water and alcohol¹³⁷. Circular or square points superimposed onto the dielectric constant data presented in panel A to indicate whether or not alcohol-induced coacervation of PEI/Glu was observed for (B) methanol, ethanol, and IPA.

5.2.2 The Effect of PEI Molecular Weight on the Alcohol-Induced Coacervation of PEI/Glu

To evaluate the effect of the PEI molecular weight on the formation of alcohol-induced coacervates, we first studied its simple coacervation in binary water-IPA solvents. By comparison of the DLS correlation functions collected between 0 – 90 % v/v IPA, a sharp increase in correlation function y-axis intercept value accompanied by a single smooth exponential decay in the correlation curve at high alcohol concentrations was observed. This is indicative of alcohol-induced coacervation and the formation of single component complexes. As shown in Figure 5.4, when the PEI molecular weight was decreased from 25 to 2 kDa, the volume fraction of IPA required to elicit coacervation increased from 70 to 90 %. As the molecular weight is decreased at constant mass concentration, the degree of polymerisation for each chain decreases also, which increases the Flory-Huggins free energy of mixing contribution to Voorn-Overbeek theory as outlined in Chapter 1. This serves to effectively increase the energy barrier for coacervation, which is compensated by the increased alcohol concentrations required for phase separation.

Unlike the y-intercept graphs shown above for mixtures of PEI/Glu (Figure 5.2) with an approximately constant value at low IPA volume fractions, the samples of pristine PEI show a peak in scattering correlation at 20 – 30 % v/v IPA. This occurs through a different mechanism in which a re-entrant coil-globule transition is affected by changes in the solvent quality by the formation of water/IPA complexes⁶¹. PEI is soluble in both water and IPA independently, but the water/IPA complexes formed on addition of the alcohol to increasing concentrations are a poor solvent for the polymer. From an initially aqueous state the solvating water molecules are complexed by added IPA and the polymer chains become desolvated and collapse into the globule form. This manifests as an increase in the DLS signal to noise ratio and scattering correlation. At progressively higher IPA concentrations, the water/IPA complexation becomes saturated, and any additional IPA may re-solvate the PEI chains, which serves to reduce the correlation between successive scattering events and the observed y-intercept between 40 – 60 % IPA (Figure 5.4A).

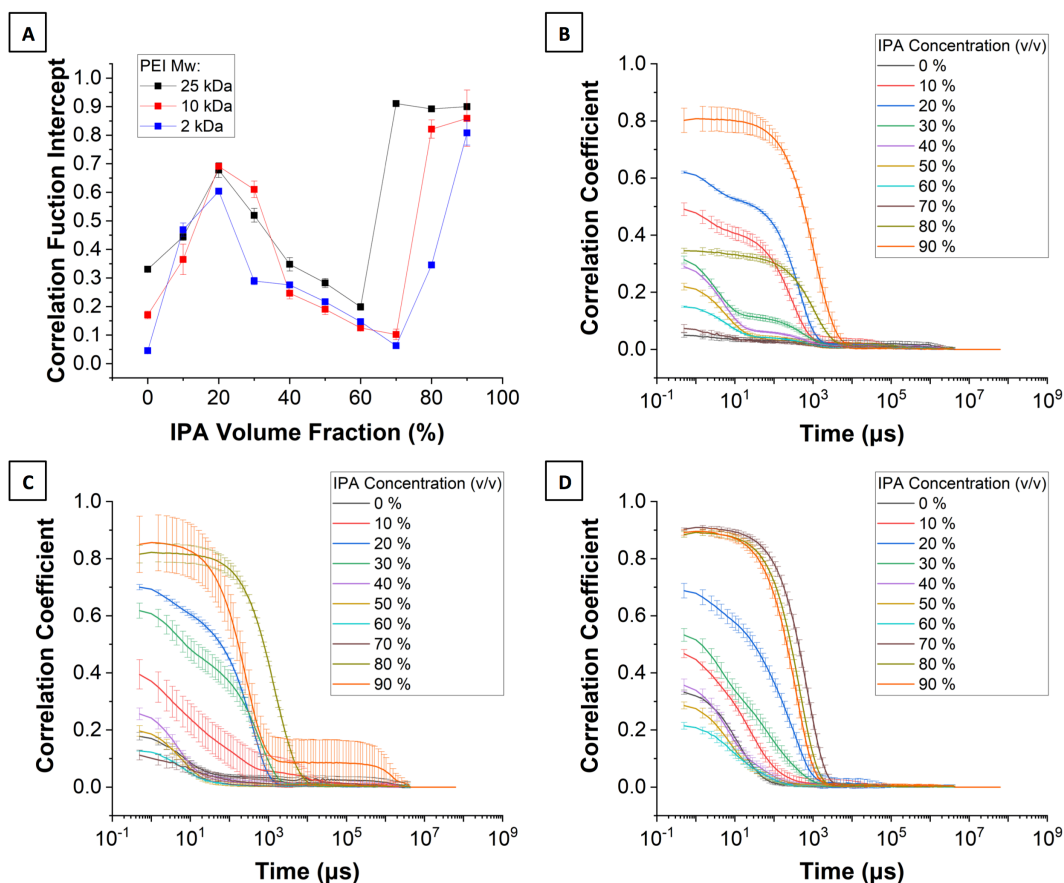


Figure 5.4 (A) Dynamic light scattering data for 2, 10, and 25 kDa PEI in binary water/IPA solvents as a function of IPA volume fraction, and (B – D) the contributing correlation function curves for 2, 10, and 25 kDa PEI respectively. Each data point represents the mean \pm standard deviation of 3 repeat measurements.

When Glu is incorporated for the formation of complex PEI/Glu coacervates, the re-entrant conformation change was not observed, but the dependence of the critical volume fraction on the PEI molecular weight was retained (Figure 5.5). For each molecular weight, approximately constant correlation y-intercept values are observed for low IPA volume fractions. When 2 kDa PEI was used, the intercept values remained between 0.11 and 0.26 for alcohol concentrations up to 60 %, and the correlation curves shown in Figure 5.5B are approximately comparable to that collected at 0 % IPA. For 80 – 90 % IPA correlation curves with single exponential decay profiles and high y-intercept values are observed typical of alcohol-induced coacervation. For the higher molecular weights, the same y-intercept

‘baseline’ is observed relative to their 0 % IPA conditions, but the onset of coacervation occurred by 70 % IPA.

Notably, in comparison to the simple coacervation observed with PEI alone, the onset of coacervation of the PEI/Glu PECs occurred at lower alcohol volume fractions for the 2 and 10 kDa PEI when Glu is incorporated. Glu, whose carboxyl groups carry a negative charge at alkaline pH may act as an electrostatic crosslinker between the cationic PEI molecules. This encourages coacervation and decreases the critical alcohol concentration from 90 to 80 % for 2 kDa PEI, and 80 to 70 % for 10 kDa PEI.

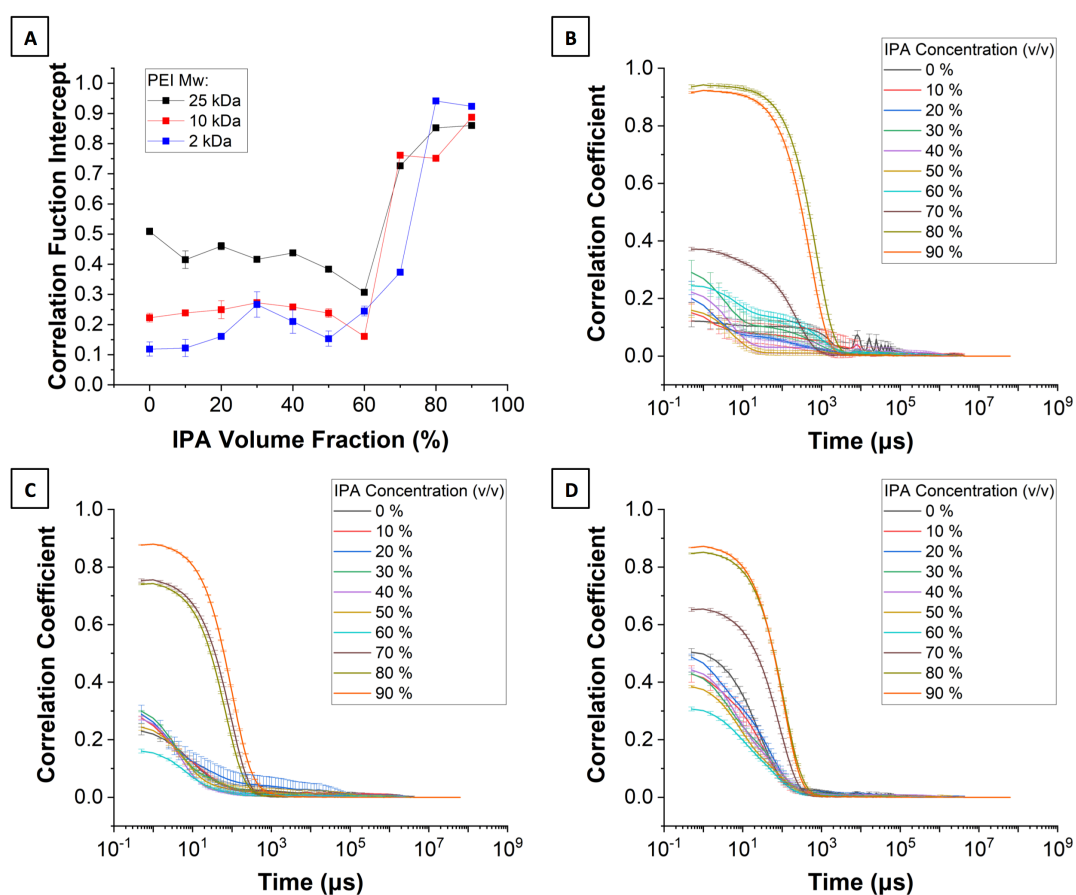


Figure 5.5 (A) Dynamic light scattering data for mixtures of PEI/Glu with varied PEI molecular weight in binary water/IPA solvents, and (B – D) the contributing correlation function curves for 2, 10, and 25 kDa PEI respectively. Each data point represents the mean \pm standard deviation of 3 repeat measurements.

5.2.3 The Effect of Varying PEI and Glu concentrations on the PEI/Glu PEC Templates

It was observed in Chapters 3 that to ensure the presentation of PEC constituents at the silica particle surface, the PEC size must be greater than or comparable to the final particle size; further, the PEC monodispersity is conferred to the as-synthesised silica particle population¹⁵³. Thus, we next investigated the effect of PEI and Glu concentrations on the size and monodispersity of the PECs, and its variation between differing PEI molecular weights.

For 25 kDa PEI/Glu PECs prepared with constant Glu concentration (1.09 mM), an increase in PEI concentration from 4 – 64 μ M elicited a PEC diameter increase from 18 ± 1 to 153 ± 4 nm and a decrease in PDI from 0.159 ± 0.006 to 0.042 ± 0.014 (Figure 5.6A). For all but the highest PEI concentration presented herein, there is a large excess of Glu compared to PEI monomers, such that even if multiple Glu molecules may associate with each PEI monomer, free glutamic acid in solution is still available to complex additional PEI leading to the observed PEC diameter increase with PEI concentration. Even at the highest PEI concentration the relative number of Glu and PEI monomers are close enough (PEI:Glu monomer ratio = 1.5:1) that we expect every PEI polymer to participate in PEC formation. The increase in PEI concentration also increased the synthesis pH from 5 to 9 suggesting that those PECs with a higher PEI will be more suitable for the basic catalysis of silica condensation. Given that the silica hydrolysis and condensation rates are known to be higher at alkaline pH⁸⁶, the PEC size must be comparable to the resultant particles, and the PEC PDI must be low, the highest PEI concentration was chosen for future experiments. While keeping the concentration of the 25 kDa constant, the Glu concentration was increased from 0 – 2.2 mM for the PEC formation (Figure 5.6B). For PEI only samples, comparatively small and polydisperse clusters of 11.4 ± 1.1 nm with a PDI of 0.37 ± 0.08 were formed. The inclusion of 0.2 mM Glu increased the hydrodynamic diameter to 307.5 ± 45.5 nm, which decreased to 139.2 ± 0.6 nm with the progressive increase in Glu concentration to 2.2 mM. This decrease in hydrodynamic diameter can be attributed to the larger number of Glu molecules that are able to increase the extent of crosslinking between PEI monomers without affecting the global pH, which leads to a decrease in PDI to 0.045 ± 0.02 over the tested range. Again considering the size, PDI, and pH requirements of the PECs, 1.09 mM Glu was chosen for future nanoparticle syntheses.

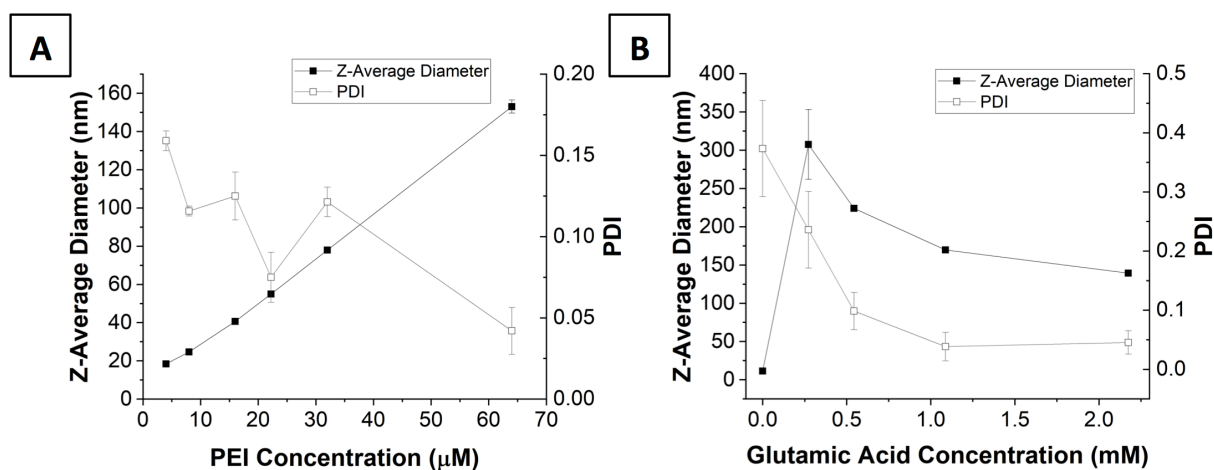


Figure 5.6 Hydrodynamic diameters and PDI values for 25 kDa PEI/Glu PECs formed at 80 % IPA with (A) 64 μM PEI and varied glutamic acid, and (B) 1.09 mM glutamic acid and varied PEI.

When the same concentration variations were assessed with PECs formed from 10 kDa and 2 kDa PEI, however, the magnitude of size change increased significantly. A PEI increase of the same mass concentrations led to an increase in PEC diameter from 19.4 ± 5.8 to 530 ± 9.3 nm for 10 kDa PEI and 40.8 ± 0.3 to 2539.0 ± 213.5 nm for 2 kDa PEI (Figure 5.7A). Similarly when the same variation in Glu concentration change was applied to the lower molecular weight PEI, very broad size ranges were achieved. The 10 kDa PEI/Glu PECs varied between 65.8 ± 54.5 nm and $5306. \pm 9.3$ nm while the diameter changed from 83 ± 30.9 to 3626.5 ± 19.1 nm when 2 kDa PEI was used (Figure 5.7B).

Longer chain polymers are known to show greater stability in the formation of PECs than those with lower degrees of polymerisation³⁸, which could explain why the diameters of low molecular weight PECs prepared in this work are highly sensitive to changes in reagent concentration. Also, while the ratio of Glu to PEI monomers is the same for each molecular weight in Figure 5.7, the number of Glu monomers per PEI molecule is lower for the 10 and 2 kDa PEI conditions. This could lead to a decreased ability of Glu to crosslink between PEI chains causing lower PEC stability and greater liability to size change when the reagent ratios are varied.

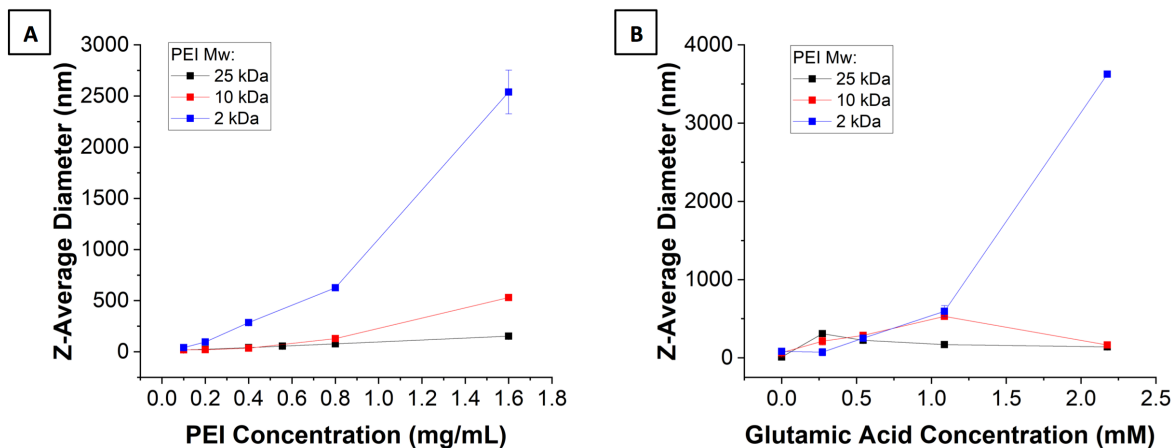


Figure 5.7 The Z-average diameter determined by DLS for PEI/Glu PECs prepared at 80 % v/v IPA with 2, 10, or 25 kDa PEI for varied (A) PEI concentration and (B) Glu concentration.

It was shown in Chapter 3 that for the preparation of PECs as templates for silica nanoparticle synthesis, fine size control and uniformity of the template is conferred to the silica nanoparticle. As such, PECs prepared with 64 μ M (1.6 mg/mL) of 25 kDa PEI with 1.09 mM Glu were used for the subsequent synthesis of the SiNPs.

To produce sufficient quantities for the formation of nanocomposite hydrogel (discussed Chapter 6), the PEC formation was scaled up 25-fold while maintaining reagent concentrations and ratios. Under the scaled-up condition with 64 μ M PEI and 1.09 mM Glu in an 80 % IPA (v/v) solvent, the PEC size increased from 169.7 ± 2.3 to 205.2 ± 4.1 nm with a PDI of 0.15 ± 0.02 .

5.3 PEC Templated Synthesis of PEI-Functionalised SiNPs

Following optimisation of the PEI/Glu PECs for size, pH, and monodispersity, their efficacy as colloidal templates in the formation of PEI-functionalised SiNPs was evaluated.

On the addition of tetraethoxysilane (TEOS) to the PEC solution, silica condensation occurred inside the PEI/Glu templates to yield PEI-functionalised silica nanoparticles (PEI-SiNPs) of 135.5 ± 37.7 nm with asymmetrical popcorn structures (Figure 5.8A). The hydrodynamic diameters of the PEI-SiNP were found by DLS to be 187.3 ± 4.2 nm and with a low PDI of 0.07 (Figure 5.9A). The broader size distribution seen by TEM was likely due to the presence of larger aggregates which arise through the clustering of particles during drying.

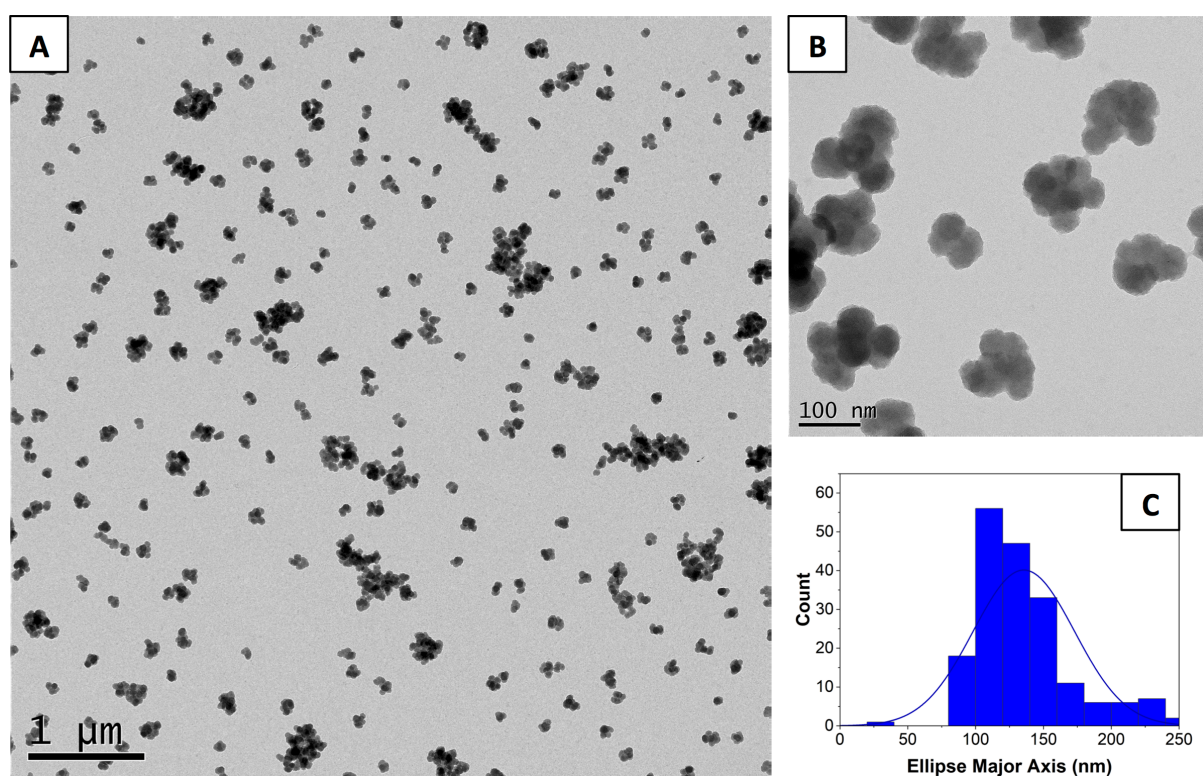


Figure 5.8 (A, B) TEM images showing the size and morphology of PEI-SiNPs and (C) their corresponding size histogram with an average diameter of 135 ± 37.7 nm ($n = 188$).

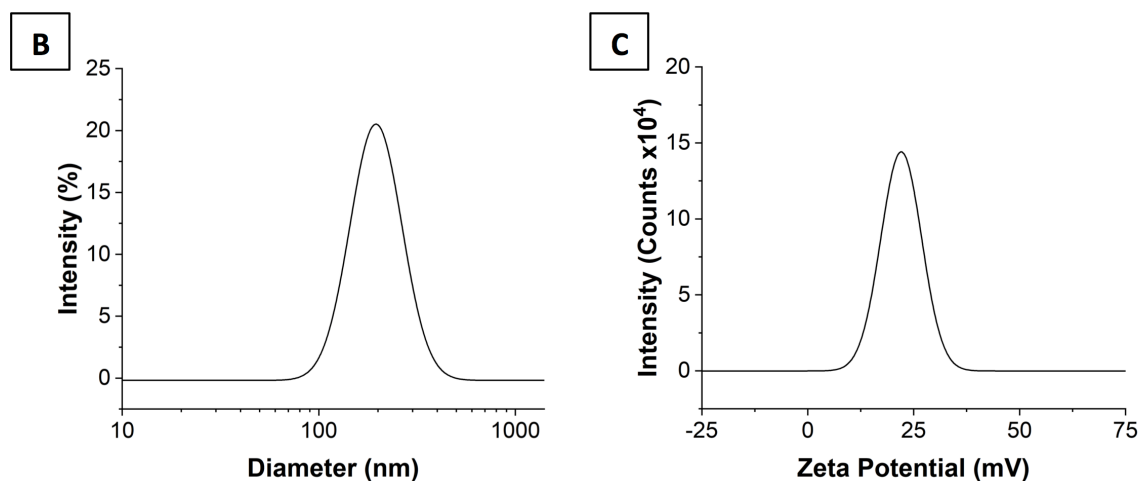


Figure 5.9 (A) Intensity weighted size distribution collected by dynamic light scattering for PEI-SiNPs of diameter 187 ± 4.2 nm and PDI of 0.07 ± 0.02 and (B) The zeta potential of as-synthesised PEI-SiNPs in PBS (pH 7.4) showing a positive surface charge of 22.1 ± 1.1 mV.

As shown in Figure 5.9B, the presentation of the PEI and its protonated tertiary amines at the particle surface conferred a positive zeta potential of 22.1 ± 1.1 mV to the PEI-SiNPs in pH 7.4 PBS. The one-pot functionalisation of silica particles with hyperbranched PEI is expected to facilitate the incorporation of PEI-SiNPs into a supramolecular hydrogel with oppositely charged hyaluronic acid (HA).

The retention of PEI on the PEI-SiNP surface was further confirmed by the presence of FTIR peaks common to both spectra. Within the fingerprint region, peaks for Glu and PEI are too close in wavenumber to separate in the PEI-SiNP spectra. However, the PEI spectrum shows a broad vibrational mode attributed to N-H stretching with peaks at 3382 and 3351 cm^{-1} , which occurred at 3293 and 3417 cm^{-1} for PEI-SiNPs and is not present for Glu. A PEI absorption band corresponding to CH_2 stretching at 2820 cm^{-1} was also present in the PEI-SiNP spectrum and not for Glu, but shifted to higher wavenumber at 2854 cm^{-1} (Figure 5.10A)^{154,155}.

In addition, TGA analysis was used to confirm the retention of the PEC constituents and hence organic functionality of the PEI-SiNPs. As shown in Figure 5.10B-E, the first weightloss for PEI-SiNPs at ~ 200 $^{\circ}\text{C}$ can be attributed to the loss of Glu. Pristine Glu shows a weightloss derivative peak at comparable temperatures (onset of 191 $^{\circ}\text{C}$) and no PEI degradation is observed until 310 $^{\circ}\text{C}$. Above this, the Glu and PEI weightloss profiles overlap and both contribute to the PEI-SiNPs. After the full temperature ramp to 700 $^{\circ}\text{C}$, the PEI and

Glu masses have reduced by 100% and 76% respectively while the PEI-SiNP thermal profile shows a mass loss of 39%, suggesting approximately 60% of the PEI-SiNP mass is derived from silica not PEI or Glu.

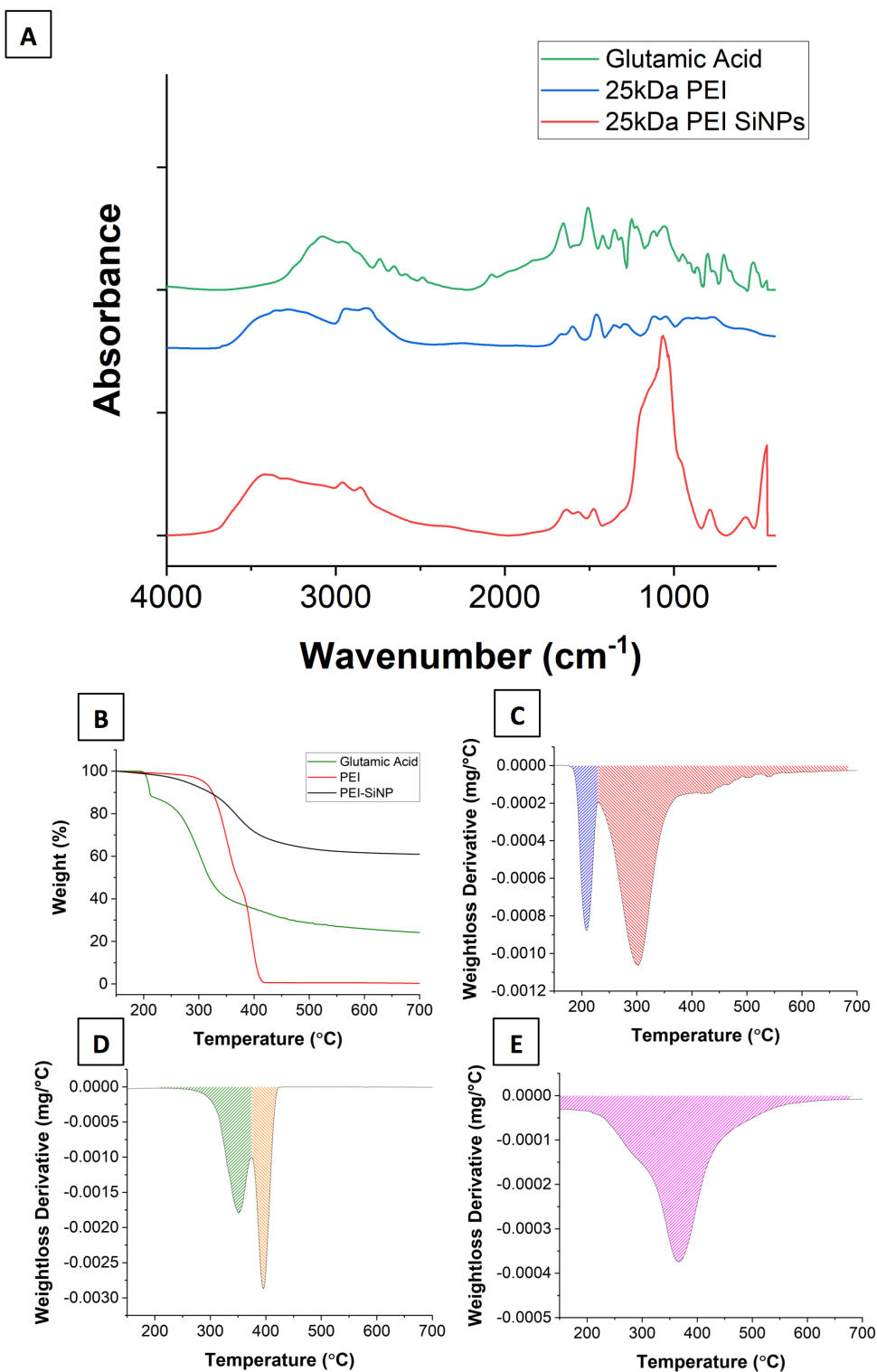


Figure 5.10 (A) Stacked FTIR spectra of glutamic acid, PEI, and PEI-SiNPs. (B) Weight loss curves from TGA analysis for glutamic acid, PEI, and PEI-SiNPs, and (C-E) their corresponding 1st derivatives.

5.4 Conclusions

In this chapter, we have expanded on the PEC templated nanoparticle synthesis described in Chapter 3 with the use of polycationic PEI and anionic Glu for the formation of silica nanoparticles with intrinsic PEI surface functionality. We have also investigated and quantified the effects of alcohol co-solvent choice and PEI molecular weight on the formation of PEI/Glu PECs.

We first demonstrated that the alcohol-induced formation of PECs was highly dependent on the choice of alcohol co-solvent and the resultant dielectric constant of the medium. Methanol, ethanol, and isopropanol were used to show that higher alcohols with lower polarity were able to induce PEI/Glu PEC formation at progressively lower volume fractions, but a single critical dielectric threshold value for the onset of coacervation may not be applied universally to all solvents.

Then the molecular weight of the PEI was found to have significant effect on the required IPA volume for coacervation and on the size tuneability of the PECs. An increase in molecular weight from 2 to 25 kDa caused decrease in the required volume fraction for complex formation from 80 to 70 % (v/v). The use of higher molecular weight PEI also afforded finer size control of the PECs. Increase of the PEI concentration from 0.1 to 1.6 mg/mL increased the PEC diameters from 18.4 ± 0.1 to 153.0 ± 3.5 nm for 25 kDa PEI, and 40.8 ± 0.3 and 2539.0 ± 213.5 nm for 2 kDa PEI.

The PEC formation volume was scaled up 25-fold while maintaining a narrow size distribution and subsequently used in the formation of monodispersed PEI-SiNPs with hydrodynamic diameters of 187 ± 4.2 nm. The presence of PEI at the particle surface was confirmed with zeta potential measurement, FTIR, and thermogravimetric analysis.

The in-synthesis functionalisation of silica particles with PEI removes the need for post synthetic modifications steps traditionally required for polymer-functionalised SiNP synthesis, and in the next chapter will facilitate the synthesis of physical nanocomposite hydrogels.

6 Application of PEI-SiNPs as Multifunctional Crosslinkers in Physical Nanocomposite Hydrogels

6.1 Motivation

Hydrogels are three-dimensional water swollen networks formed from the chemical or physical crosslinking of hydrophilic polymers. Their high water content, porosity, tuneable physiochemical properties, and capacity to encapsulate drugs and cells make them valuable for a wide range of biological applications such as tissue engineering¹⁵⁶, bioadhesive gels and wound healing¹⁵⁷, and therapeutic delivery²¹. However, the successful translation of many hydrogel systems has been limited by poor mechanical properties such as insufficient stiffness, brittleness, and lack of self-healing properties due to the heterogeneous distribution of crosslinking points and the inability of the hydrogel networks to dissipate energy.^{22,23} To improve the mechanical properties and confer added functionalities, nanocomposite hydrogels incorporating silica nanoparticles (SiNPs)¹⁵⁸⁻¹⁶⁰, polymeric nanoparticles¹⁶¹, gold nanoparticles¹⁶², iron oxide nanoparticles¹⁶³, and carbon nanotubes¹⁶⁴ have been utilised. Amongst the various nanoparticle types, SiNPs are most promising for improving the mechanical performance of nanocomposite hydrogels in biomedical applications due to their inherent biocompatibility, biodegradability, colloidal stability, and ease of synthesis.

The most common methods of preparing mechanically robust nanocomposite hydrogels include chemical and/or physical crosslinking of SiNPs with polymeric gelators. In chemically crosslinked nanocomposite hydrogels, surface modified SiNPs are typically used for the covalent grafting of polymers via free radical polymerisation or for crosslinking with polymers bearing complementary functional groups through photo-crosslinking of methacrylates, thiol-thiol, and aldehyde-amine bonds.^{160,165-169} Yang *et al.* reported tough and elastic nanocomposite hydrogels formed by the *in situ* covalent grafting of poly(acrylic acid) (PAA) from vinyl functionalised SiNPs.¹⁶⁰ The polymer-bridged SiNPs acted as multifunctional crosslinking points, enabling the dynamic disentanglement of the PAA chains to facilitate energy dissipation during deformation. Although tough and flexible hydrogels were obtained, predominantly chemically crosslinked hydrogels formed via permanent

covalent bonds tend to lack self-healing and thixotropic properties that are desirable for *in vivo* biomedical applications.

In physical nanocomposite hydrogels, SiNPs are incorporated into the network via electrostatic interactions, hydrophobic interactions, hydrogel bonding, and/or Van der Waal's forces.^{158,170–172} Although SiNPs may be simply embedded into physical hydrogel formulations without any engineered intermolecular interactions or crosslinking, such systems have yielded weak mechanical reinforcement.^{173,174} In contrast, the design of polymer grafted SiNPs as physical crosslinkers for interaction with polymer chains confers desirable mechanical attributes. Zheng *et al.* reported the use of poly(2-dimethylaminoethyl methacrylate) modified SiNPs (SiO₂@PDMAEMA) as multifunctional crosslinkers in an *in situ* polymerised PAA network.¹⁵⁸ The electrostatic interactions between the SiO₂@PDMAEMA and PAA resulted in a supramolecular nanocomposite hydrogel with high tensile strength and self-healing properties. Ternary crosslinked nanocomposite hydrogels formed from the *in situ* copolymerisation of acrylamide and stearyl methacrylate monomers on vinyl functionalised SiNPs have also been reported.¹⁷² In this system, the hydrogel network is formed by hydrogen bonding and hydrophobic interactions between the grafted co-polymer chains and covalent bonds between the SiNPs. Despite the improved mechanical properties observed for the aforementioned SiNP crosslinked nanocomposite hydrogels, the requirement for toxic monomers, initiators and catalysts and/or high temperatures for the *in situ* polymerisation process may limit biological applications and the loading of thermally labile drugs.^{160,172} In addition, the sequestration of free radicals by the SiNPs during the free radical polymerisation could also affect reproducibility of the hydrogel synthesis and mechanical properties.¹⁷⁵ The current synthesis of the polymer brush grafted SiNP crosslinkers also requires multiple steps involving the Stöber synthesis of the SiNPs, followed by surface modification which could increase the time and cost of production.^{158,160} There is thus a need for a simpler and modular approach to produce nanocomposite hydrogels with tunable mechanical stiffness and self-healing properties for biomedical applications. In this Chapter, we present a novel protocol for the formation of mechanically tuneable and self-healing nanocomposite hydrogels using organic-inorganic hybrid PEI-SiNPs (Chapter 5) as multifunctional crosslinkers for electrostatic interaction with hyaluronic acid (HA) (Figure 6.1).

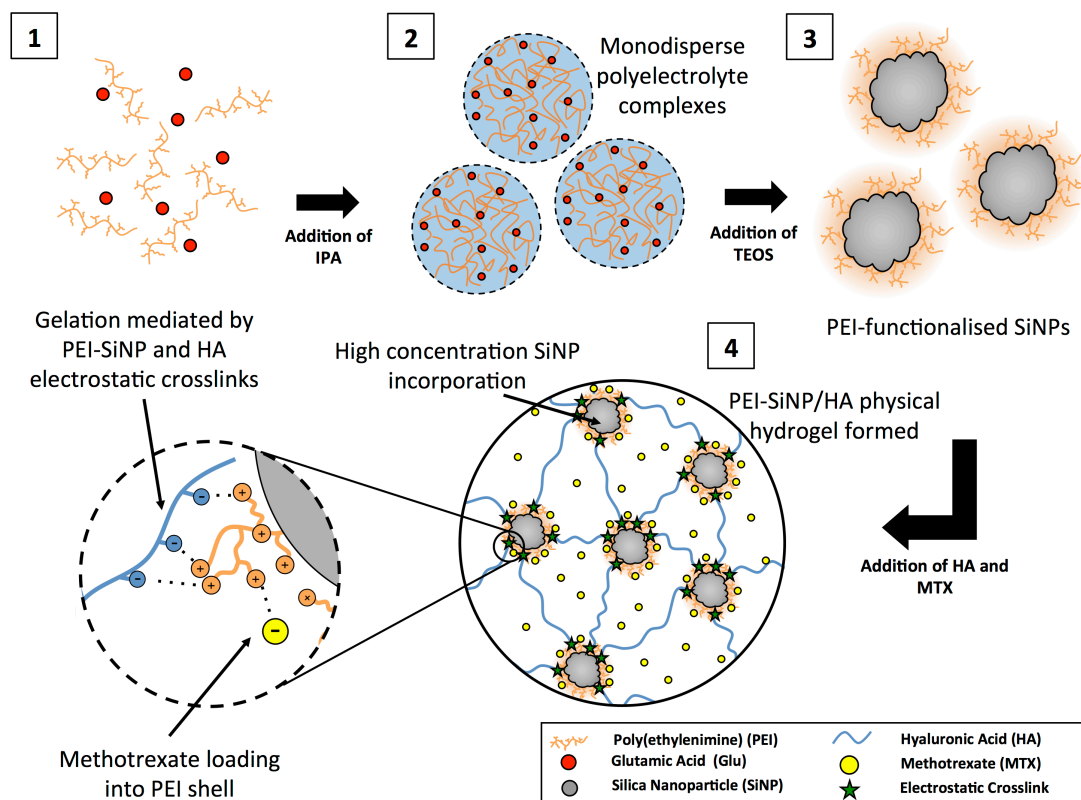


Figure 6.1 A graphical representation of the PEC templated synthesis of core-shell PEI-SiNPs and their subsequent use as multifunctional crosslinking junctions in the formation of coacervate nanocomposite hydrogels. (1) PEI and Glu are initially dispersed in an aqueous solution before (2) the addition of isopropanol (IPA) to form monodispersed nanoscale PECs. (3) On the addition of TEOS, the silanes selectively condense inside the PECs and each one becomes a PEI-functionalised SiNP (PEI-SiNP). (4) The PEI-SiNPs are mixed with HA and MTX to form a drug loaded, physical nanocomposite hydrogel with electrostatic crosslinks.

6.2 PEI-SiNP/HA Hydrogel Formation

Hyaluronic acid (HA), a non-sulfated glycosaminoglycan and extracellular matrix component, exhibits excellent biocompatibility, and biodegradability.¹⁷⁶ As it is negatively charged at physiological pH, HA was used to electrostatically complex with cationic PEI-SiNPs to obtain PEI-SiNP/HA nanocomposite hydrogels. For clarity, the structures of HA and PEI are shown below in Figure 6.2.

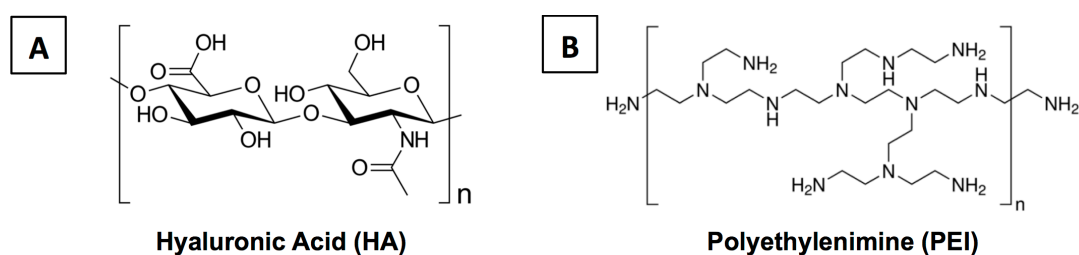


Figure 6.2 The chemical structures of (A) hyaluronic acid and (B) polyethylenimine.

During the initial mixing of PEI-SiNPs and HA, the alkaline environment (pH ~10) induced a low degree of protonation of PEI's primary, secondary, and tertiary amines (pKa 4.5, 6.7, and 11.6, respectively), hence resulting in the formation of a white precipitate following charge neutralisation by the $-\text{COO}^-$ groups present in HA (Figure 6.3A). Upon pH adjustment to ~6 with hydrochloric acid, a greater degree of protonation of PEI's tertiary and secondary amines was achieved. The enhanced electrostatic interaction between PEI and HA resulted in the formation of a complex coacervate hydrogel along with contraction of the polymeric networks during syneresis. This process resulted in the formation of an opaque white hydrogel suspended in a colourless liquid (Figure 6.3B). It is noteworthy that the high-pH mixing of PEI and HA is imperative for the homogeneous mixing of reagents. When the pH of the PEI-SiNP solution was tuned to the weakly acidic range before the addition of HA, a gel formed instantaneously on mixing with visible, heterogeneous PEI-SiNP and HA domains.

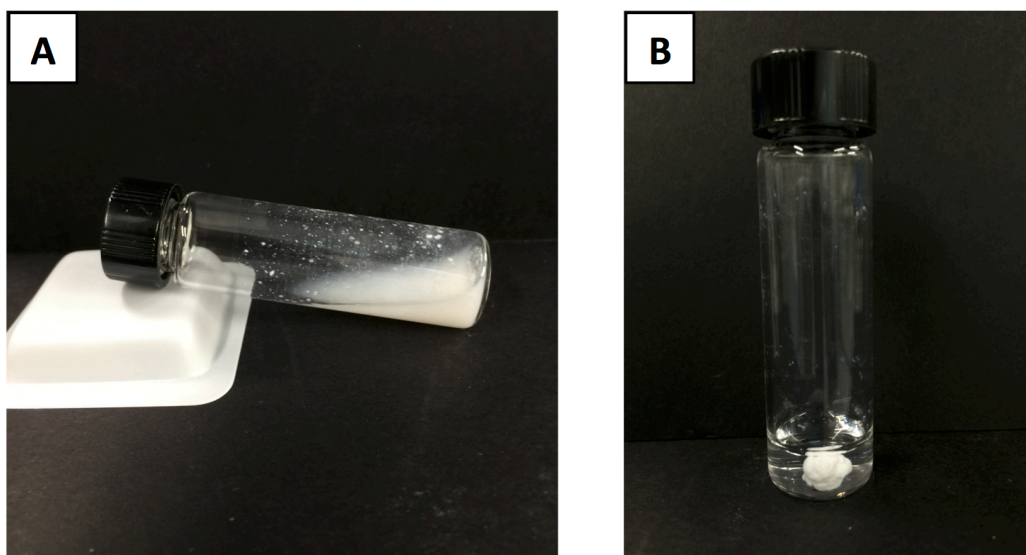


Figure 6.3 Photographs of taken during PEI-SiNP/HA hydrogel synthesis showing (A) the white precipitates formed after the initial mixing of PEI-SiNPs and HA, and (B) the coacervate hydrogel formed in a transparent supernatant after reduction of the pH and the resultant syneresis.

When PEI-SiNPs were replaced with silica nanoparticles without PEI surface functionality, no gelation between the SiNPs and HA was observed. SiNPs of comparable size (hydrodynamic diameter 230 ± 4 nm and PDI 0.17 ± 0.01 ; Figure 6.4A) without cationic surface functionality were prepared from Arg and PAA PECs in the overgrowth regime as described in Chapter 3. The SiNPs had no polymeric surface functionality, and a zeta potential of -29.5 ± 0.7 mV (Figure 6.4B) derived from the presence of surface silanol groups. In the absence of cations for electrostatic complexation, on mixing with HA at equivalent silica mass concentrations to the established PEI-SiNP/HA protocols, no coacervation or syneresis was observed independent of the pH (Figure 6.4C).

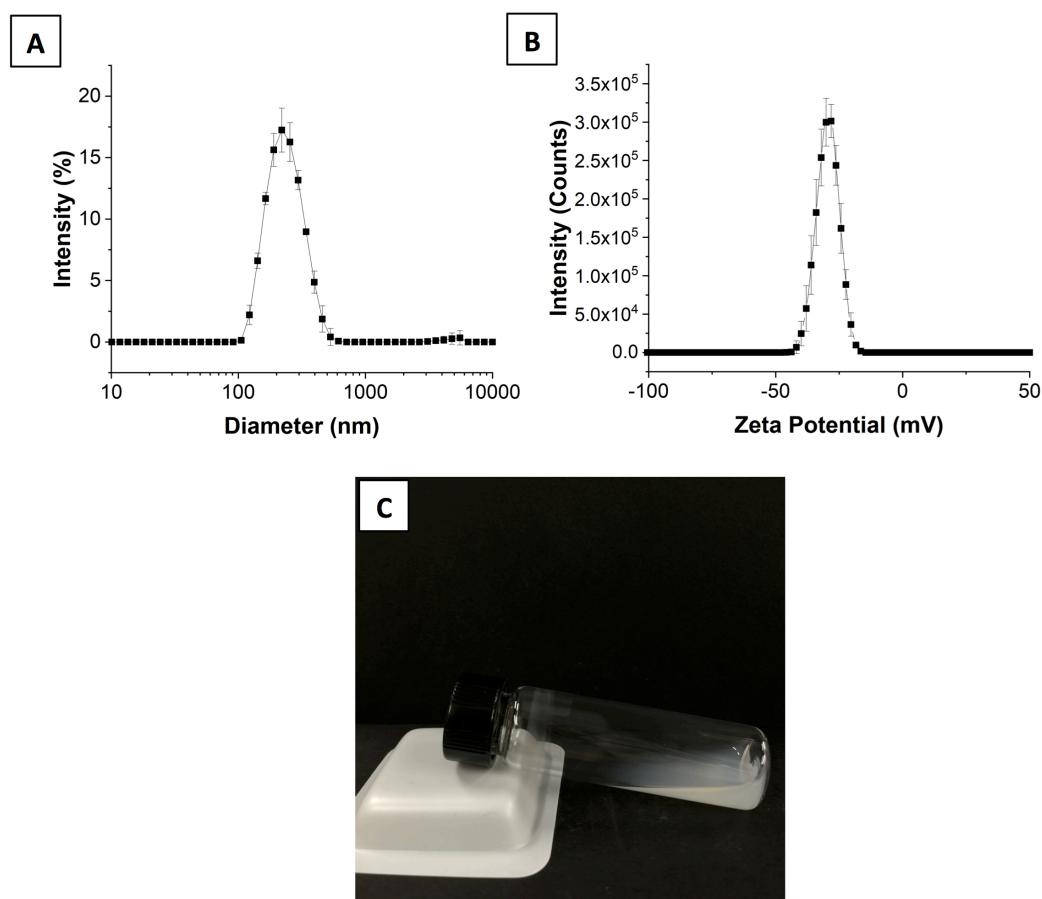


Figure 6.4 The intensity weighted size distribution for unfunctionalised SiNPs measured by DLS with a diameter of 230 ± 4 nm and PDI of 0.17 ± 0.01 . (B) The zeta potential distribution of the SiNPs measured in pH 7.4 PBS with a negative surface charge of -29.5 ± 0.7 mV. (C) A photograph of a mixture of non-PEI functionalised SiNPs and HA showing no coacervation or gelation.

As the driving force for gelation is electrostatic interaction between the ionisable groups of PEI and HA, the effect of their concentrations and stoichiometry were subsequently investigated. For all PEI-SiNP/HA samples with a PEI:HA monomer ratio $\leq 1:1$, hydrogels formed instantaneously on mixing after pH reduction (Figure 6.5A). At the final pH of ~ 6 , each HA monomer possesses one anionic carboxyl group (pKa 3.0¹⁷⁷; Figure 6.2A) and each PEI monomer has seven cationic secondary and tertiary amines (pKa 6.7 and 11.6 respectively; Figure 6.2B), hence it is likely that one PEI monomer may complex several HA monomers. When the PEI:HA monomer ratio was increased to 1:8 (monomer concentrations 0.6 and 4.8 mM) beyond the maximum possible stoichiometry for 1:1 charge matching, gel formation was still observed showing that not all HA monomers need to interact with a

corresponding PEI monomer for gel formation. For PEI:HA monomer ratios $\geq 1:1$ however, phase separation and bulk gelation did not occur suggesting that on average each PEI monomer must complex with more than one HA monomer.

When gels were formed with pristine PEI in place of PEI-SiNPs, the gelation occurred independent of PEI/HA monomer stoichiometry and was more dependent on the concentration of HA. A minimum HA monomer concentration of 2.4 mM was found to be critical for gelation for all PEI concentrations tested (Figure 6.5B). Notably, the total amount of PEI and HA required to induce gelation was found to be lower for the PEI-SiNP/HA compared to PEI/HA samples: Gel synthesis occurred at a 1:1 monomer ratio (PEI and HA monomer concentrations 2.4 and 2.4 mM respectively) where it did not for the corresponding PEI-SiNP/HA mixture, and did not occur for 0.6 mM PEI/1.2 mM HA (ie. 1:2 PEI/HA monomer ratio) where the equivalent PEI-SiNP/HA gel did. Taken together, it is evident that the conjugation of PEI to the silica particle surface significantly affects the network crosslinking mechanics in electrostatic-mediated gelation, and as will be shown in the following discussion, yields gels with notably different physical properties.

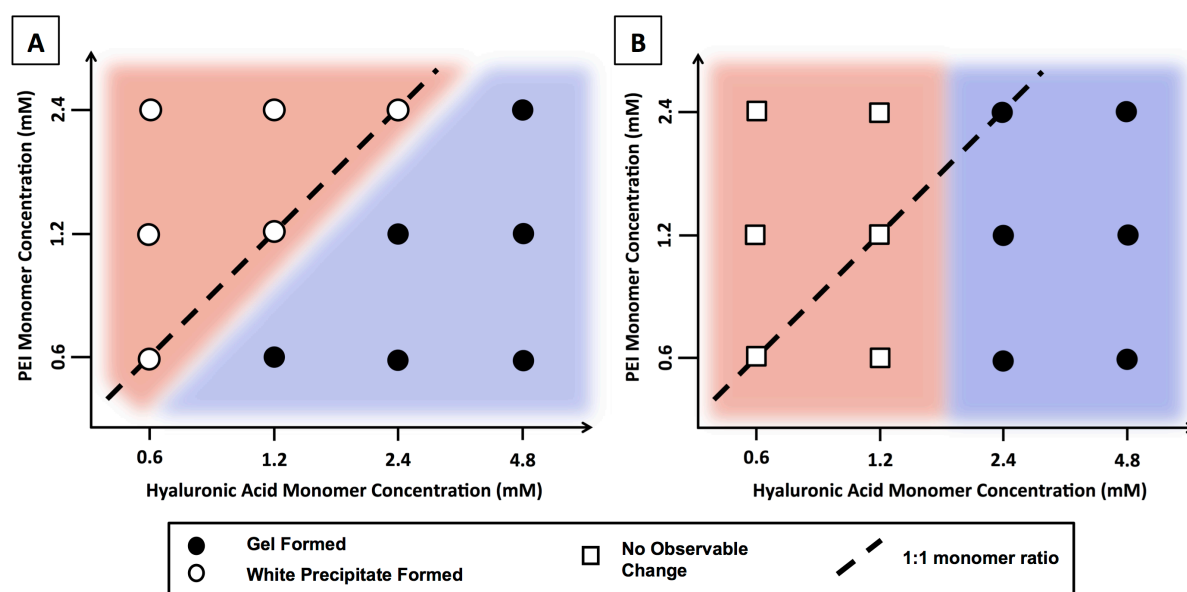


Figure 6.5 Schematics showing the gel forming conditions for (A) PEI-SiNP/HA gels, and (B) PEI/HA gels.

As the hydrogel forms through the formation of a complex coacervate, some of the hydrogel precursor may remain in the dilute supernatant phase. The amount of PEI and HA

incorporated into the PEI-SiNPs/HA hydrogels was estimated by quantifying the concentrations remaining in the expelled liquid following syneresis. With the HA monomer concentration fixed at 4.8 mM, increasing the concentration of SiNP-bound PEI from 0.6 to 3.6 mM led to an increase in the amount of PEI-SiNP and HA incorporated in the hydrogel as the concentration of PEI-SiNP and HA present in the supernatant decreased by 12 % and 10 % relative to the added dose (Figure 6.6A & B). A similar trend was observed when HA was increased from 1.2 to 4.8 mM with PEI fixed at 0.6 mM. With increasing HA, a higher amount of PEI-SiNP was incorporated into the hydrogel whereas the amount of HA incorporated remained high with no significant change across the samples (Figure 6.6C & D). Although a similar trend in which an increased relative incorporation of PEI and HA into the hydrogels was observed for the PEI/HA hydrogels, the total amount of both components present in the hydrogel was lower than the PEI-SiNP/HA hydrogels. These results suggest that the use of PEI-SiNP as multifunctional crosslinkers could lead to an increased local charge density to enhance electrostatic interactions with HA in the complex coacervates, hence resulting in an increased incorporation of PEI-SiNPs and HA into the hydrogel.

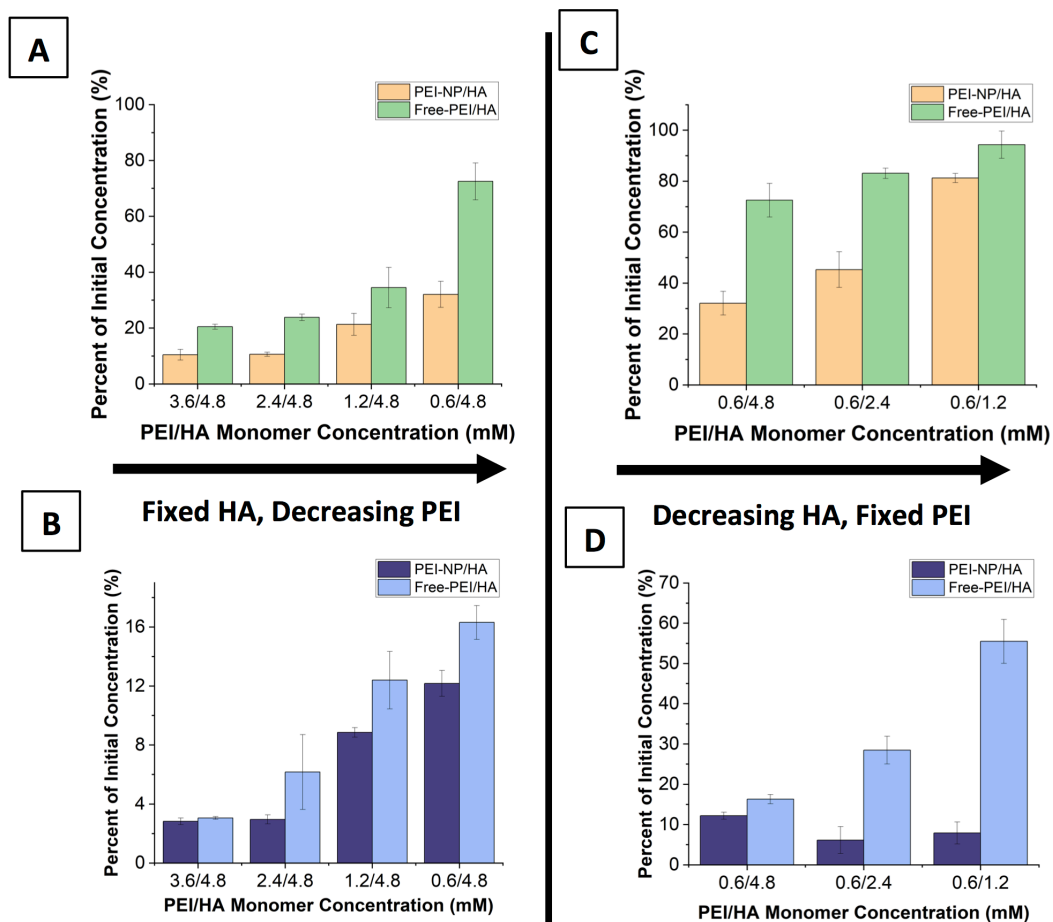


Figure 6.6 Quantification of the PEI and HA concentration in the supernatant after gel formation normalised to the initial reagent concentration. (A,C) The PEI supernatant concentration as a function of decreasing PEI concentration and decreasing HA concentration respectively. (B,D) The HA supernatant concentration as a function of decreasing PEI concentration and decreasing HA concentration respectively.

6.3 The Effect of PEI-SiNP Incorporation on Hydrogel Morphology

As the pore morphology of hydrogels could greatly influence their mechanical properties and drug release kinetics, cryo-SEM, which enables preservation of the hydrated state of the hydrogel, was used to study the microstructural features of the PEI-SiNP/HA nanocomposite hydrogel.

As shown in Figure 6.7A & B, HA only samples possessed a highly porous network structure with thin walls. In contrast, the electrostatic interactions of PEI with HA in the PEI/HA hydrogels resulted in the formation of denser walls between adjacent pores (Figure 6.7C & D). The network structure was also comparatively heterogeneous, showing a wide range of pore sizes and wall thicknesses compared to the HA only sample. With the PEI-SiNP/HA hydrogel, a significant change in network structure occurred. Unlike the smooth continuous walls with typical thickness of $< 1 \mu\text{m}$ seen with the PEI/HA hydrogels, thick walls of densely packed and homogeneously dispersed SiNPs with widths up to several microns were observed for the PEI-SiNP/HA hydrogels (Figure 6.7E & F). The micron-scale pores between the walls present in the PEI-SiNP/HA hydrogels also show a larger diameter and reduced inter-connectivity compared to the PEI/HA hydrogel. Furthermore, the nanoparticle packing in the case of PEI-SiNP/HA gives rise to a secondary nanoscale pore network spanning the meso- and macro- porous range (Figure 6.7G & H).

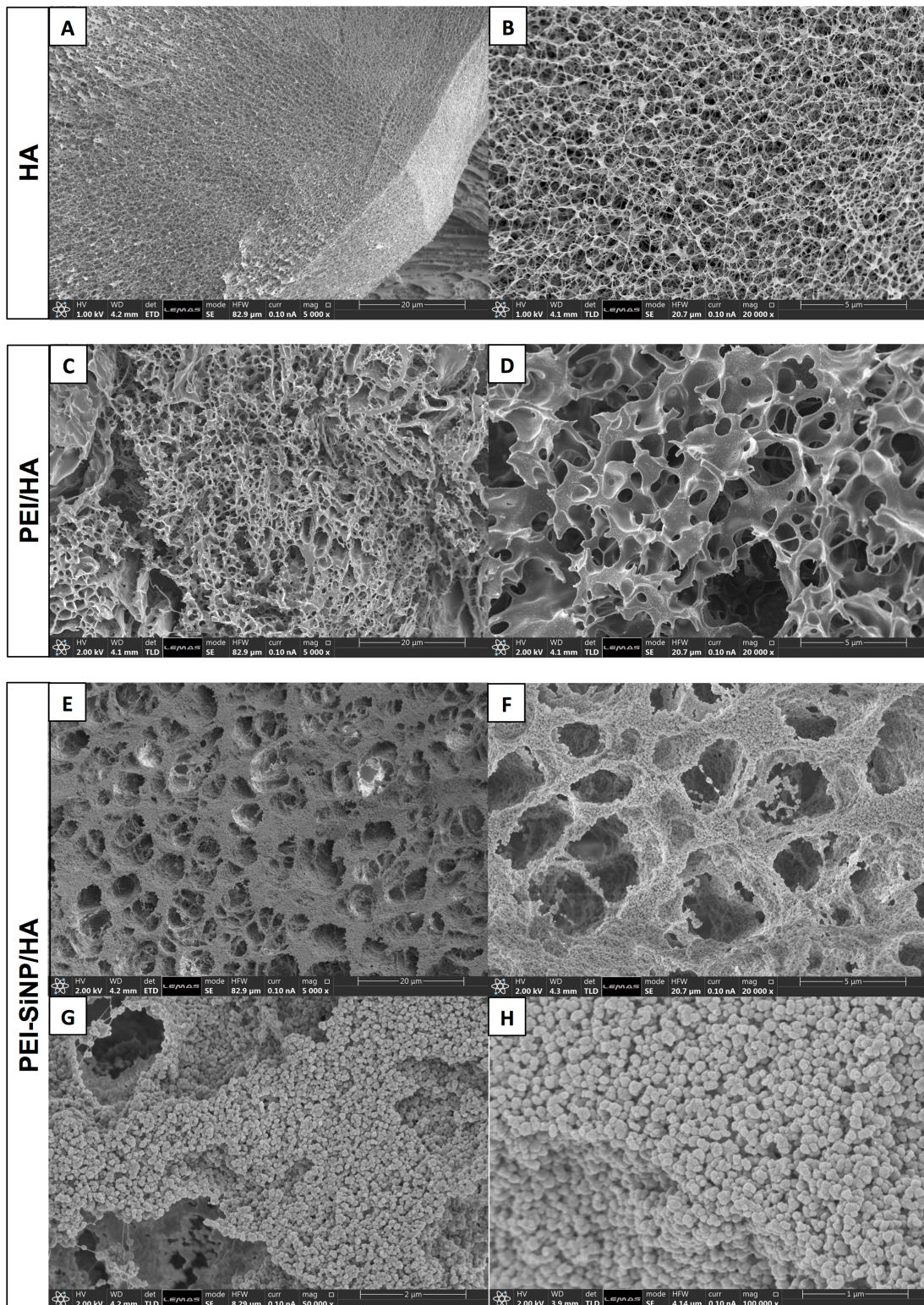


Figure 6.7 The effect of PEI-SiNP incorporation on the structure and morphology of hydrogels. Cryo-SEM images of (A,B) pristine HA, (C,D) PEI/HA hydrogels, and (E-H) PEI-SiNP/HA hydrogels prepared with PEI/HA ratio 3.6/4.8.

6.4 Rheological Characterisation of PEI-SiNP/HA and PEI/HA Hydrogels

Next, the rheological properties of the PEI-SiNP/HA and PEI/HA hydrogels were investigated. It is known that a mismatch in stiffness can cause poor apposition between hydrogels and the surrounding tissues leading to poor drug diffusion, a decrease in efficacy. While very weak hydrogels may experience poor interfacing with the tissue walls and premature degradation in dynamic biological environments, excessive stiffness can cause mechano-chemical injuries and the foreign body reaction.^{178,179} As such, the ability to achieve controllable and tuneable stiffness is highly desirable for the biological application of hydrogels.

The viscoelastic behaviour of the hydrogels was confirmed with a frequency sweep at 1 % strain which displayed significantly higher values of G' than G'' between 0.1 and 10 Hz for both PEI-SiNP/HA and PEI/HA (Figure 6.8A). As seen in Figure 6.8B, the PEI-SiNP/HA hydrogels prepared at various PEI:HA ratios displayed much higher mechanical stiffness than the PEI/HA hydrogels, which could be attributed to the multifunctional crosslinking and high density packing of non-deformable SiNPs. In addition, the conjugation of multiple branched PEI to the SiNP surface may lead to reduced molecular motion and enhanced local charge densities for stronger electrostatic crosslinking with the polyanionic HA.

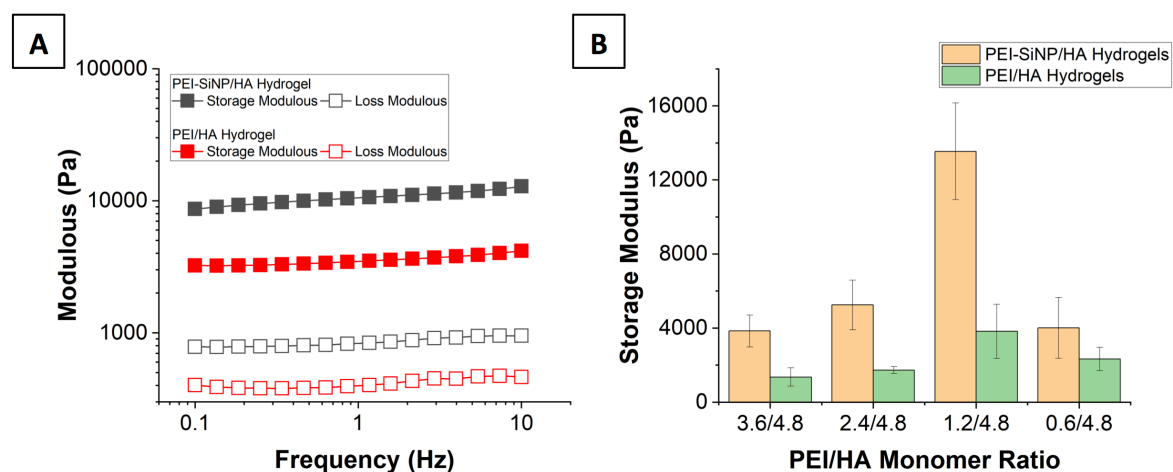


Figure 6.8 (A) A frequency sweep at 1 % shear strain showing the storage and loss moduli for PEI-SiNP/HA and PEI/HA hydrogels synthesised with PEI/HA monomer ratio of 1.2/4.8. (B) The storage moduli measured at 1 % shear strain and a frequency of 1 Hz for PEI-SiNP/HA and PEI/HA hydrogels prepared at different PEI/HA monomer ratios ($n = 3$).

As the charge ratio between oppositely charged polymers in electrostatically crosslinked hydrogels is expected to modulate the mechanical properties,¹⁸⁰ the molar ratio of PEI to HA monomers was systematically varied to study tuneability in the hydrogel stiffness (Figure 6.8B). A reduction in PEI/HA monomer ratio from 3.6/4.8 to 1.2/4.8 led to a stepwise increase in the storage moduli of the PEI-SiNP/HA hydrogels from 3,800 Pa to 13,500 Pa. The reduction of excess cationic charges (Table 4) could have resulted in decreased electrostatic repulsions between the incorporated PEI-SiNPs that led to stronger interactions with the polyanionic HA in the hydrogel network. A further decrease in the PEI/HA monomer ratio to 0.6/4.8, however, led to a marked decrease in hydrogel stiffness. This could be attributed to a weakened hydrogel network due to reduced availability of PEI-SiNPs to electrostatically crosslink with HA, along with increased repulsion between the HA chains. The same trend was observed for PEI/HA where the stiffest network was observed at PEI:HA monomer ratio of 1.2:4.8. The tunable variation of the storage modulus shows that the hydrogel composition may be specifically chosen to match that of the target tissues.

Table 4 Cation:anion charge ratios present in PEI-SiNP/HA and PEI/HA hydrogels prepared at different PEI/HA monomer ratios.

PEI/HA Monomer Ratio	3.6/4.8	2.4/4.8	1.2/4.8	0.6/4.8
Cation:Anion Charge Ratio	4.8:1	3.2:1	1.6:1	0.8:1

The incorporation of PEI-SiNP with HA also decreases the energy dissipation potential as shown by the lower loss factor ($\tan \delta$) obtained for most of the PEI-SiNP/HA nanocomposite hydrogels (Figure 6.9). In the PEI/HA hydrogels, the presence of relatively weak, purely physical crosslinks in the polymer network allows for energy dissipation through the reversible breaking of electrostatic bonds and resultant structural rearrangement. In the PEI-SiNP/HA hydrogels, however, the covalent bonds between PEI and the SiNPs do not reversibly break, which decreases the networks' ability to dissipate energy through structural reconfiguration and induces network elasticity. Yang et al. also observed a similar

relationship with hydrogels formed from hydrogen bonding between poly(acrylamide)-functionalised silica nanoparticles where higher concentrations of silica decreased the loss factor compared to polymer-only hydrogels.¹⁸¹

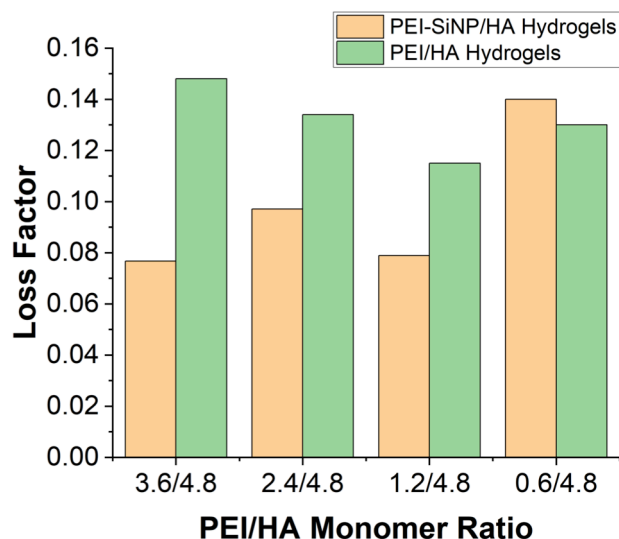


Figure 6.9 The loss factor at 1 % shear strain and 1 Hz for PEI-SiNP/HA and PEI/HA hydrogels prepared with varied composition.

Following implantation in the body, the dynamic biological environment and tissue remodelling could subject the hydrogel to strain, causing network breakage and treatment failure for a hydrogel with insufficient critical strain value^{182,183}. As seen from Figure 6.10, strain sweeps revealed that the electrostatic crosslinking of PEI-SiNPs maintained the viscoelastic properties of PEI-SiNP/HA up to a much higher shear strain compared to that for PEI/HA hydrogels (304 % vs. 46.9 %). These results suggest that the PEI-SiNP/HA nanocomposite hydrogels are more likely to retain their physical properties following *in vivo* application.

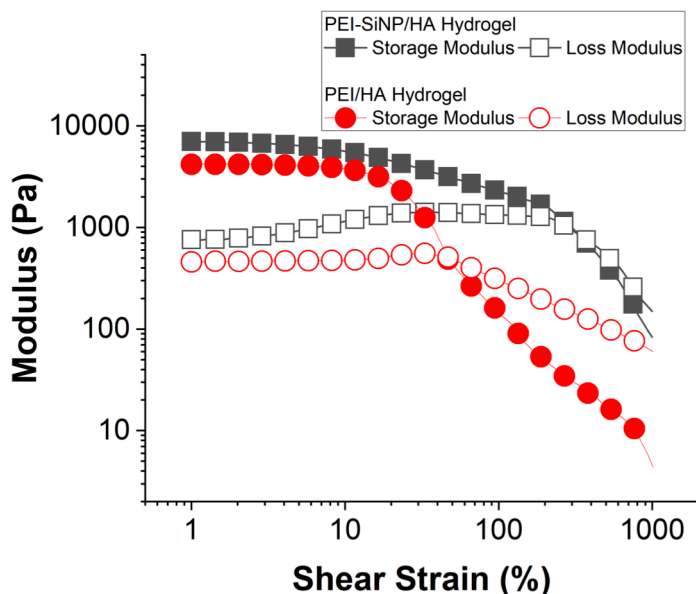


Figure 6.10 A strain sweep for PEI-SiNP/HA and PEI/HA hydrogels (PEI/HA monomer ratio 1.2/4.8) at a frequency of 1 Hz.

6.5 The Equilibrium Swelling Ratio of PEI-SiNP/HA and PEI/HA Hydrogels

To evaluate their swelling ratio, the mass of the freshly prepared hydrogel was compared to that obtained after complete drying under mild conditions. As seen in Figure 6.11A, comparable swelling ratios were observed for both hydrogel types and the changes in gelator ratios had no significant effect on the degree of swelling. The modest decrease in swelling observed on the incorporation of PEI-SiNPs is likely caused by the high concentration of SiNPs (shown in Figure 6.7E-H) and corresponding high mass density of the hydrogel relative to the PEI/HA networks which manifests as a lower (mass normalised) swelling ratio. However, when the hydrogels were dried and subsequently re-hydrated, the swelling behaviour changed significantly. As shown in Figure 6.11B, for each PEI:HA ratio, PEI-SiNP/HA hydrogels show a higher swelling ratio than those made with pristine PEI. In addition, the swelling ratio for PEI-SiNP/HA hydrogels increased from 480% to 1160% when the PEI-SiNP:HA ratio was decreased from 3.6/4.8 to 1.2/4.8, and decreased to 872% on further PEI-SiNP decrease to 0.6/4.8. When compared to the cation:anion charge ratios in

Table 4 and mechanical stiffness in Figure 6.8B, the hydrogel swelling ratio correlates with mechanical stiffness, where those with low charge ratios and high storage moduli retain the largest water content.

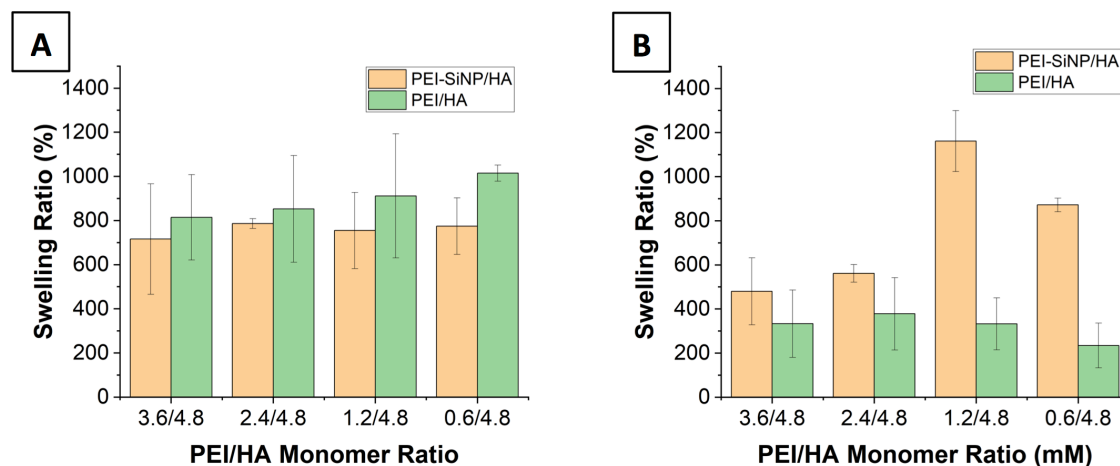


Figure 6.11 Equilibrium swelling ratios determined in ultrapure water for (A) freshly prepared and (B) dried PEI-SiNP/HA and PEI/HA gels ($n = 3$).

The swelling ratios presented herein exceed that of comparable SiNP-hydrogel nanocomposites synthesised with dynamic covalent crosslinks^{169,184}, but are significantly lower than those typically reported for physical nanocomposites. For example, *in-situ* grafted poly(acrylic acid)-functionalised SiNPs with physical crosslinks were shown to have swelling ratios in excess of 10,000 %¹⁶⁰ while a poly(acrylamide)-SiNPs swelled up to 2300 %¹⁸⁵. The lower swelling ratios observed with polyelectrolyte hydrogels could be attributed to the stronger electrostatic interactions within the polymeric networks compared to weaker bonds such as hydrogen bonding.^{186–188}

6.6 Shear Thinning and Self-Healing Properties of PEI-SiNP/HA Hydrogels

The ability of physical hydrogels to undergo shear thinning aids in their injection or application to the body whilst the recovery of networks upon removal of the shear stress enables their mechanical properties to be restored for the intended purpose. When subject to large shear strains (1000 % strain, above the critical strain of 304 % determined in Figure 6.10) the reversible breakage of the physical crosslinks between PEI-SiNPs and HA resulted in a 100-fold decrease in mechanical stiffness and increased flow ($G' < G''$; Figure 6.12A). Reformation of the electrostatic bonds and recovery of the viscoelastic properties occurred almost instantaneously on return to a low shear strain regime (1 % strain). This result is consistent with other reported studies. For example, Arno *et al.* observed a reversible ~100x decrease in G' for electrostatic calcium-alginate hydrogels reinforced with poly(L-lactide)-based nanoparticles under high mechanical strain¹⁸⁹. Similarly, Zhang and co-workers also observed a decrease in stiffness by an order of magnitude for the chitosan-strengthened polyacrylamide-based guest-host hydrogel under high strain, which subsequently recovered within seconds of return to the low strain regime¹⁹⁰. Interestingly, after the high-strain cycle used in our study, the storage modulus of the nanocomposite hydrogel only partially recovered to 7.5 kPa (initial $G' = 9.6$ kPa) in the low strain period. This behaviour suggests that while initial recovery and reformation of the physical crosslinks may occur within seconds, the structural reorganisation required for complete stiffness recovery may take longer than the 30 s afforded in the 1 % shear strain cycle in this experiment.

To assess the self-healing properties of the PEI-SiNP/HA hydrogels, two pieces of hydrogel (one strained blue with CBBG dye) were placed in intimate contact (Figure 6.12B). After incubation at room temperature for 1 h the hydrogels had joined at their interface, could support their own weight, and remained attached under mechanical stretching (Figure 6.12C & D).

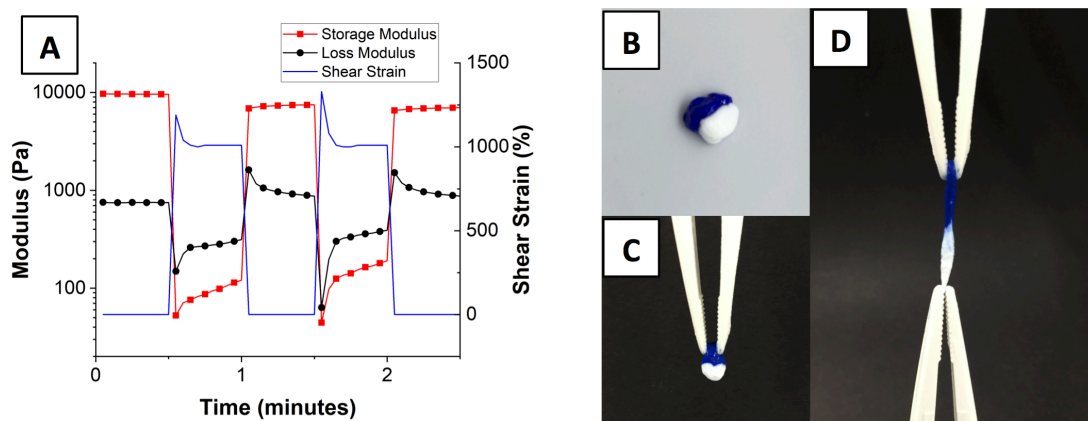


Figure 6.12 (A) The storage modulus for PEI-SiNP/HA hydrogels (PEI/HA ratio 1.2/4.8; measurement frequency 1 Hz) under repeated cycles of 1 % and then 1000 % strain (interval time 30 s). (B) Two pieces of hydrogel, prepared with and without CBBG dye, placed in intimate contact to demonstrate their macroscopic self-healing properties. After 1 h the hydrogels support their own weight (C) and remain connected under mild mechanical stretching (D).

6.7 Hemolytic Activity of PEI-SiNP/HA and PEI/HA Hydrogels

Good biocompatibility with minimal off-target cytotoxicity is imperative for materials in drug delivery and biological application. Hemolysis testing of the hydrogels and their constituents was conducted using mouse mammalian blood to assess their potential toxicity.

As seen in Figure 6.13A, minimal hemolysis ($\leq 3.8\%$) was observed for the PEI-SiNP/HA and PEI/HA hydrogels, hence demonstrating good haemocompatibility. In contrast, free PEI and PEI-SiNPs induced significant haemolysis over the same concentration range (Maximum hydrogel PEI monomer concentration 2.2 mM for PEI/HA ratio of 3.6/4.8; Figure 6.13B & C). As expected, HA, a naturally occurring component of the extracellular matrix, showed negligible haemolysis over the concentration range used in hydrogel preparation ($< 2.6\%$, Figure 6.13D; maximum HA monomer concentration 2.9 mM for 3.6/4.8 PEI/HA ratio). These results clearly demonstrate that the charge screening and electrostatic complexation of high molecular weight PEI by the oppositely charged HA polymer could mitigate the cytotoxicity of the resultant hydrogel. Such charge balanced hydrogels thus offer an advantage over conventional PEI-containing hydrogels which tend to be cytotoxic due to the disruption of mammalian cell membranes by PEI's high cationic charged densities^{191,192}.

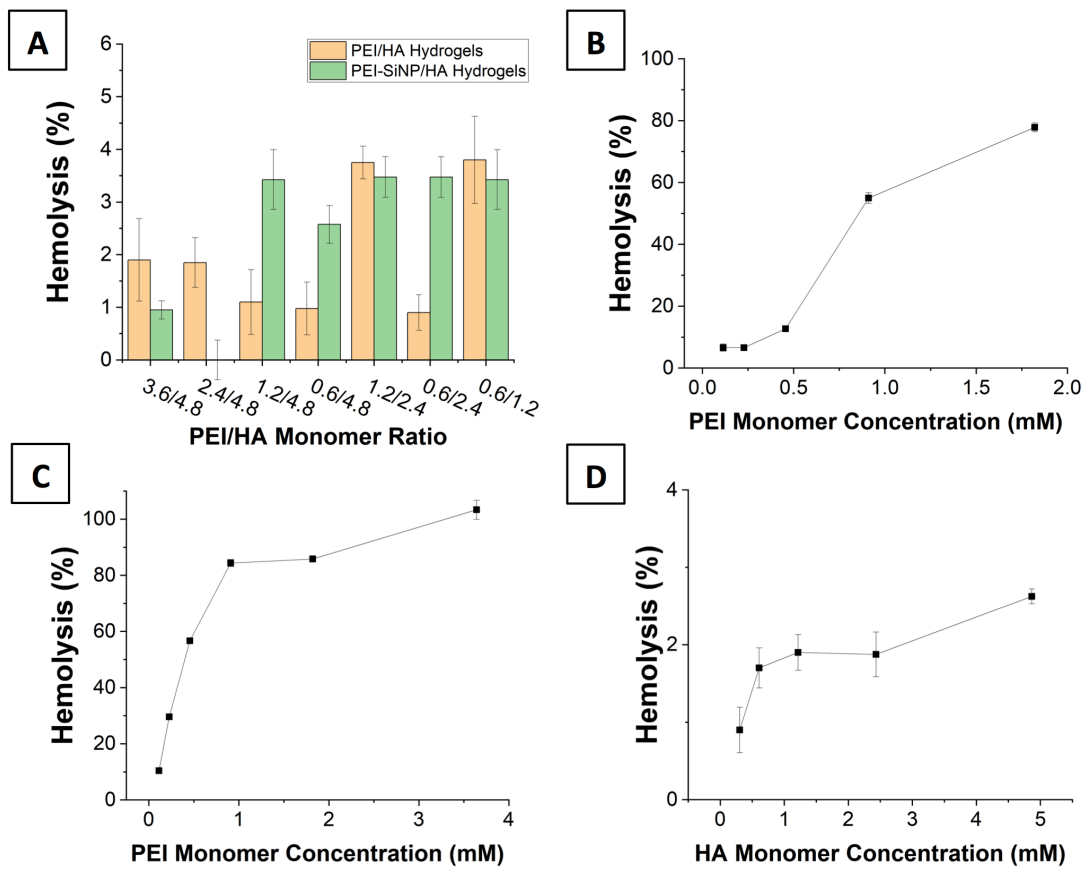


Figure 6.13 Hemolysis testing for (A) PEI-SiNP/HA and PEI/HA gels, and (B-D) HA, PEI, and PEI-SiNPs respectively.

6.8 Methotrexate Drug Loading and Release

Abraham *et al.* recently demonstrated that electrostatic interactions from charged gelators may retard the release of small molecule drugs with complementary charges.¹⁹³ As discussed in Chapter 5, the presence of protonated amines in the silica surface-bound PEI conferred a positive surface charge. Because of the large number of ionisable groups per PEI monomer (7 protonated amines per PEI monomer vs 1 deprotonated carboxyl group per HA monomer at pH 7.4), an excess of cationic groups is still expected to be available for electrostatic interaction with a guest molecule after hydrogel formation. As such, we investigated the loading and release of an oppositely charged cargo. MTX, an anti-metabolite of folic acid is used as an anticancer agent in the treatment of a variety of neoplasms.¹⁹⁴ However, the drug efficacy is limited by its short plasma half-life and low accumulation in tumour tissues following injection or oral administration.¹⁹⁵ Owing to its two ionisable carboxyl groups that carry a negative charge at physiological pH, MTX was incorporated into the PEI-SiNP/HA hydrogel *via* electrostatic interaction with the cationic PEI-SiNPs prior to the addition of HA. Implantation of the MTX loaded PEI-SiNP/HA hydrogel at the disease site could allow for direct delivery of the drug, hence reducing systemic toxicity and overcoming its poor pharmacokinetic properties to increase drug bioavailability.

As shown in Figure 6.14, a significantly higher MTX loading efficiency was observed for the PEI-SiNP/HA compared to PEI/HA hydrogels ($P < 0.05$ for all). Interestingly, the loading of MTX into the PEI-SiNP/HA nanocomposite hydrogels was found to be dependent on the ratio of PEI to HA. When the PEI monomer concentration (and hence PEI-SiNPs) was increased from 1.2 to 3.6 mM, the MTX loading efficiency increased from 79 to a maximum at 93%. This result is consistent with the expected increase in availability of protonated amines for electrostatic complexation with MTX as the PEI concentration increases.

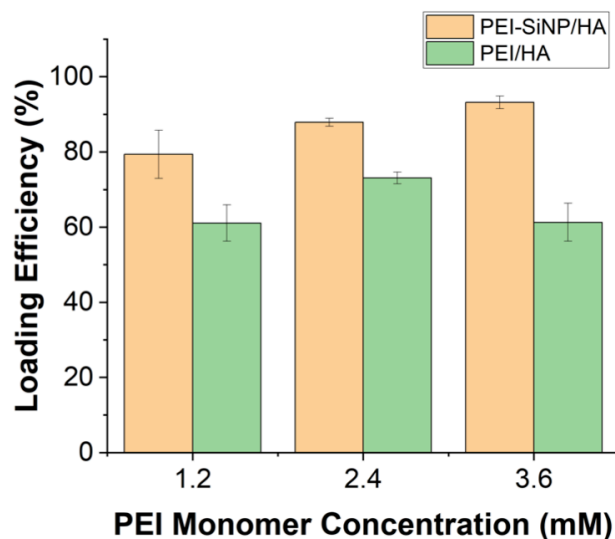


Figure 6.14 MTX loading efficiencies for PEI-SiNP/HA and Free-PEI/HA gels synthesised with varied PEI monomer concentration and HA monomer concentration fixed at 4.8 mM (n = 3).

Next, the drug release profiles and kinetics for PEI-SiNP/HA gels were measured and evaluated with the Korsmeyer-Peppas model.¹⁰¹ As seen from Figure 6.15, slower, more sustained, and tuneable drug release is observed for the PEI-SiNP/HA compared to the HA only hydrogel. Over the first 8 h, a burst release of MTX is observed for the HA only hydrogel with almost 100 % release by 24 h. In comparison, much slower release is shown for the PEI-SiNP/HA hydrogels with 46 % release after 8 h, and only 78 % after 24 h for gels prepared with a 3.6 mM PEI monomers. In addition, the MTX release rates can be tuned by varying the PEI-SiNP concentration. With an increase in the PEI monomer concentration from 0 to 3.6 mM, a decrease in MTX release rate was attained (Table 5). Notably, the release up to 12 h is approximately comparable for the hydrogels with 1.2 – 3.6 mM PEI; this initial release is primarily due to MTX adsorbed in the hydrogel pores. From 24 h onwards the MTX contained in the pores is depleted, and the remaining drug is electrostatically bound to the cationic PEI-SiNPs within the walls of the hydrogel matrix. This electrostatic interaction retards the release of MTX and is greater in the hydrogels prepared with higher PEI-SiNP concentrations. When PEI-SiNPs containing 1.2 mM of PEI monomers were used, 91% of the loaded MTX mass was released over 72 h; this decreased to 83% and 78% for 2.4 and 3.6 mM PEI monomer respectively. These results thus demonstrate the ability to

modulate the release of the anionic anticancer drug MTX by varying PEI-PSiNP concentration within the nanocomposite hydrogels.

Importantly, the electrostatic complexation of PEI-PSiNP with HA to form the nanocomposite hydrogel avoids the near complete burst release observed with the HA only hydrogel. With the HA only hydrogel, 80 % of MTX was released within the first 8 h and the kinetic constant, k_m , observed was approximately double that of the nanocomposite hydrogels ($k_m = 47.8$ vs 23.8 ; Table 2). For all samples, the exponent n was < 0.5 suggesting that diffusion was controlled by fickian diffusion of the guest molecule from within the hydrogel matrix rather than hydrogel swelling or dissolution.

Similar to the increased drug loading efficiency discussed above, the change in total drug release over 72 h between hydrogels of increasing PEI-SiNP content is also caused by the presence of excess PEI. We can consider two mechanisms of drug encapsulation: loading of drug into the hydrogel porous network without specific electrostatic interaction; and electrostatic complexation of MTX with excess cationic amines present in the polymer matrix. It is likely that the initial release observed over the first 48 h arises predominantly from MTX retained in the pore network without significant electrostatic interaction while the non-released drug content observed at 72 h is derived from MTX retained in electrostatic bonds with the surplus PEI. As the amount of surplus PEI not involved with gelation increases with higher PEI-SiNP:HA ratios, the amount of drug retained in the hydrogel matrix after 72 h increases in parallel. To confirm this, the samples composed of only HA and MTX (0/4.8 PEI-SiNP/HA), where no attractive electrostatic interactions exist between the drug and polymer matrix, gives approximately 100 % drug release. We speculate that the retained drug may see a prolonged release profile in tandem with hydrogel degradation under physiological conditions.

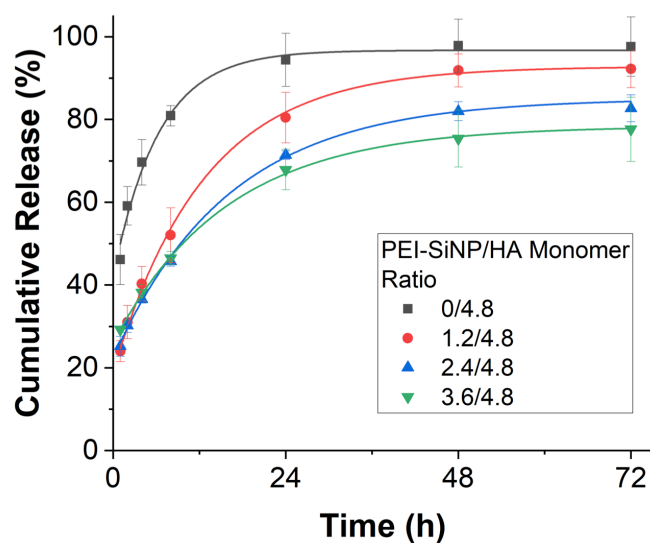


Figure 6.15 Cumulative release of MTX from PEI-SiNP/HA hydrogels of varied composition collected in pH 7.4 PBS at 37 °C (n = 3).

Table 5 The release exponent, n , and kinetic constant, k_m , derived from the Korsmeyer-Peppas model, and R^2 values from the fitting for the drug release profiles presented in Figure 6.15.

Gel Condition	n	k_m	R^2
PEI-SiNP/HA – 0/4.8	0.26	47.8	0.990
PEI-SiNP/HA – 1.2/4.8	0.38	23.8	0.999
PEI-SiNP/HA – 2.4/4.8	0.31	23.9	0.995
PEI-SiNP/HA – 3.6/4.8	0.22	29.2	0.986

6.9 Conclusion

In this chapter we demonstrate the use of PEI functionalised SiNPs developed in Chapter 5 for the formation of complex coacervate-based nanocomposite hydrogels. Due to the reversible electrostatic bonding between PEI-SiNP and HA, the nanocomposite hydrogels possessed desirable shear-thinning and self-healing properties. Furthermore, the incorporation of the hybrid organic-inorganic PEI-SiNPs enhanced the mechanical stiffness of the nanocomposite hydrogels compared to the PEI/HA hydrogels. The mechanical stiffness of the nanocomposite hydrogels could also be readily tailored through tuning the ratio of PEI-SiNP to HA.

It was also found that the electrostatic complexation of PEI-SiNPs with HA could mitigate the cytotoxicity concerns traditionally associated with high molecular weight PEI thus improving their suitability for biological applications. The modular approach used also offers benefit over *in-situ* polymerised SiNP-nanocomposite hydrogels that use potentially cytotoxic reagents^{159,170,196,197}. Finally, we exploited the excess cationic charges present to enhance the loading and retard the release anionic anti-cancer therapeutic MTX. In conclusion, the novel synthetic pathway presented herein affords improved mechanical stiffness, self-healing, as well as enhanced drug loading and release capability while offering greater simplicity and biocompatibility over currently established protocols for the construction of nanocomposite hydrogels for biomedical applications.

7 Conclusions and Future Work

7.1 Conclusions

The aim of this thesis was to combine the ease of formation, customisability, and polymeric functionality of polyelectrolyte complexes (PECs) with the stability of colloidal silica. This was achieved through the use of the PECs as scaffolds for the synthesis of silica nanoparticles (SiNPs) that retained the PEC constituents as intrinsic organic functionalities.

The development of the PEC templated syntheses was initially demonstrated in Chapter 3 with the formation of Arginine (Arg)/Poly(acrylic acid) (PAA) PECs, which served as scaffolds for the formation of Arg/PAA-Porous silica nanoparticles (PSiNPs). PAA was chosen for its pH responsive electrostatic interaction with Dox, while Arg was chosen to give enhanced cellular uptake into tumourigenic tissues. The mixing of anionic polymer PAA, and basic amino acid Arg in an 80 % (v/v) IPA solvent led to the formation of stable, monodispersed PECs. The diameter of the PECs was highly tunable between 50 – 130 nm *via* control of the PAA and Arg concentrations while maintaining a monodispersed population. The use of Arg provided an alkaline pH inside the PECs, which was suitable for the basic catalysis of silica condensation, hence, on the addition of TEOS silica condensation occurred selectively inside the PEC templates for the formation of PSiNPs with intrinsic PAA and Arg surface functionality. The particle diameter was tunable between 42 – 100 nm (determined by TEM imaging), and the hydrodynamic diameter was found to vary by less than 5 nm over 3 repeat syntheses. The packing of the PAA chains in the PECs led to a porous structure in the Arg/PAA-PSiNPs spanning the micro- and meso- porous range. When Arg was replaced with NH_4OH , the weaker electrostatic interactions between PAA and the monovalent NH_4^+ caused poor uniformity in both the PECs and PSiNPs, and led to a reduction in the particle internal pore volumes. Three growth regimes (undergrowth, slight overgrowth, and significant overgrowth) were defined which describe of the relationship between the PEC template and PSiNP diameters. For the presentation of both PEC components in the PSiNP, the template diameter must be less than that of the final particle.

The efficacy of the Arg/PAA-PSiNPs and NH_4OH /PAA-PSiNPs as vehicles for the targeted delivery of anticancer therapeutic doxorubicin (Dox) to glioblastoma (GBM) cells was assessed in Chapter 4. The enhanced porosity of the Arg/PAA-PSiNPs led to a higher Dox

loading capacity of 22 % compared to 8 % for the NH₄OH/PAA-PSiNPs. The incorporation of PAA from the colloidal templates into the PSiNPs provided pH responsive drug release, corresponding to the acidic tumour microenvironment and/or the endosomal environment. At physiological pH, protonation of the carboxyl groups of PAA ($pK_a = 4.5$) caused increased electrostatic interaction with Dox, causing enhanced retention and only 8 % drug release over 48 h. Their protonation under weakly acidic pH reduced the strength of this interaction and led to 33 % Dox release. When NH₄OH/PAA-PSiNPs were used, only 17 % drug release observed at acidic pH over the same timescale.

In vitro viability assays revealed that neither Arg/PAA-PSiNPs nor NH₄OH/PAA-PSiNPs showed overt cytotoxicity against patient derived GBM cells. Increased cellular uptake of Arg/PAA-PSiNPs into GBM20 and GBM1 cells was observed compared to NH₄OH/PAA-PSiNPs and no difference was observed for non-tumorigenic NP1 cells. This was caused by the presentation of Arg at the Arg/PAA-PSiNP particle surface and was confirmed when PSiNPs synthesised in the ‘overgrowth’ regime, which did not lead to Arg surface functionalisation, showed no significant difference in uptake versus NH₄OH/PAA-PSiNPs of comparable diameter. This in turn caused an increase in tumouricidal activity as described by a significantly reduced IC₅₀ value for Dox loaded Arg/PAA-PSiNPs against the NH₄OH/PAA-PSiNPs.

The PEC templated PAA/Arg-PSiNP synthesis and its application presented in Chapters 1 and 2 gave significant benefits over previously established syntheses for SiNPs with responsive drug release and cancer targeting capabilities, both in size, monodispersity, and ease of production. Due to the enhanced uptake of Arg in other tumorigenic tissues, the Arg/PAA-PSiNPs show great potential as drug delivery vehicles for other cancer types.

Chapters 5 and 6 reported the synthesis of poly(ethyleneimine) (PEI)-functionalised SiNPs and their application as multifunctional crosslinkers in physical nanocomposite hydrogels respectively. Analogous to the Arg and PAA used previously, polycationic PEI and anionic glutamic acid (Glu) were used in the alcohol-induced formation of PECs, and their function as templates for PEI-SiNP synthesis. First, DLS was used to assess the effects of the alcohol co-solvent and its polarity on the formation of PECs. In agreement with the predictions of Debye-Huckel theory for weakly interacting polyelectrolytes in solution, a comparison of methanol, ethanol, and IPA, showed that alcohols of lower polarity cause alcohol-induced PEC formation at lower volume fractions.

Following this, the effects of PEI molecular weight on the required IPA concentration and the size of the resultant PECs was assessed. For both PEI/Glu mixtures and PEI alone, the

formation of stable complexes occurred at progressively lower IPA volume fractions for higher molecular weight polymers. In addition, the use of high molecular weight PEI allowed finer size control of the PECs. When the concentration of 2 kDa PEI was varied, the PEC diameter increased from 40 to 2539 nm, while the size changed only between 18 and 153 nm when 25 kDa was used at the same mass concentrations. Using optimised solvent and molecular weight conditions (80 % IPA, and 25 kDa PEI), the PECs were used as scaffolds for the condensation of silica species in the formation of PEI-SiNPs with asymmetric nanopopcorn structures with an average diameter of 135 ± 37.7 nm. The presentation of PEI at the SiNP surface conferred a zeta potential of 22.1 ± 1.1 mV at pH 7.4.

The cationic PEI-SiNPs were able to electrostatically complex with anionic HA in the formation of PEI-SiNP/HA nanocomposite hydrogels (Chapter 6). The hydrogels showed typical viscoelastic behaviour ($G' > G''$) and the presence of the SiNPs significantly enhanced the mechanical stiffness of the hydrogels compared to PEI/HA hydrogels prepared without SiNPs. The critical strain was also increased in the presence of SiNPs from 46.9 % for PEI/HA hydrogels to 304 % for PEI-SiNP/HA hydrogels. Furthermore, the hydrogel storage modulus was tunable between 3276 and 10617 Pa, and was highest near 1:1 cation:anion ratios.

The reversible electrostatic crosslinking between PEI-SiNPs and HA caused shear thinning and self-healing behaviours. When subjected to a 1000 % shear strain, the reversible breakage of the physical crosslinks in the PEI-SiNP/HA hydrogels caused a 100-fold decrease in mechanical stiffness, followed by near instantaneous reformation and stiffness recovery on return to a 1 % shear strain. The self-healing ability was further demonstrated on a macro-scale, where two cleaved pieces of hydrogel could re-join after intimate contact along their cut faces, and remain attached under mechanical stretching.

Haemolysis testing demonstrated that the electrostatic complexation and neutralisation of charges effectively mitigated the haemolytic activity and resultant cytotoxicity concerns associated with high molecular weight PEI, including the hydrogel formulations with an excess of charged cations. Further, these charged cations facilitated the loading of anionic antifolate and cancer therapeutic MTX to a loading efficiency of 93 %. Approximately comparable release of MTX from the hydrogel pores was observed over the first 24 h for all PEI-SiNP/HA hydrogels, until only the MTX electrostatically associated with PEI-SiNPs remains. The electrostatic interaction slowed the drug release and was greater in the hydrogels prepared with higher PEI-SiNP concentrations, giving tunable drug release rates.

Firstly, the work presented in Chapters 5 and 6 expanded on the earlier PEC templated SiNP synthesis to use a cationic polymer and anionic counterion demonstrating the versatility of this pathway and its potential application to other cation/anion pairs. In addition, new insight into the formation of alcohol-induced PECs was provided through investigation of the effects of co-solvent choice and polymer molecular weight. Secondly, the nanocomposite hydrogel offered improved and tuneable mechanical properties, self-healing, and enhanced drug loading and release capabilities while offering greater simplicity over previously reported methods for the formation of nanocomposite hydrogels in biomedical applications.

Taken together this thesis demonstrates the ability of PECs to act as scaffolds of the selective condensation of silica species hence improving the stability of PECs to changes in pH, temperature, and ionic strength; and obviating the need for lengthy synthetic protocols commonly required for the formation of surface functionalised SiNPs for biomedical application.

7.2 Future Work

7.2.1 Additional Assessment of Selective Arg/PAA-PSiNP Uptake into Malignant Tissues

In Chapter 4, the enhanced cellular uptake of Arg/PAA-PSiNPs over NH₄OH/PAA-PSiNPs was demonstrated against GBM1 and GBM20 cells lines *in vitro*, and determined to be due to the presence of Arg at the particle surface. In over 70 % of tumours, argininosuccinate synthase 1 (ASS1), an enzyme required for endogenous Arg synthesis, is suppressed leading to a dependence on extracellular Arg. Correspondingly, many tumours overexpress the solute transporters responsible for Arg influx.¹⁹⁸ Hence, a next step in the testing of Arg/PAA-PSiNPs would be an assessment of their uptake into a wide range of tumorigenic tissues known to exhibit Arg auxotrophy, and a comparison to NH₄OH/PAA-PSiNPs which do not present Arg at their surface. A bank of cell lines would be incubated with fluorescently labeled PSiNPs, and the uptake efficiency assessed by measurement of the fluorescence intensity in the cells.

This work did not probe the specific uptake pathway and intracellular localisation of the Arg/PAA-PSiNPs. Competition assays would be completed using high concentrations of Arg to saturate the Arg transporters and hence Arg/PAA-PSiNP uptake to confirm that

overexpressed solute transporters were responsible for the enhanced cellular uptake. Additionally, confocal microscopy and transmission electron microscopy of the cells after PSiNP uptake could be used to determine the fate of the Arg/PAA-PSiNPs after cellular internalisation.

Finally, an *in vivo* assessment of particle toxicity and tumour targeting would add valuable insight to their efficacy as drug delivery vehicles.

7.2.2 Cellular Toxicity and Anti-Tumour Efficacy of PEI-SiNP/HA Hydrogels

In chapter 6, the haemocompatibility of the PEI-SiNP/HA and PEI/HA hydrogels was assessed, and it was shown that the electrostatic complexation of PEI with HA could mitigate the toxicity typically associated with high molecular weight PEI. The next step would be an *in vitro* cytotoxicity assessment of the hydrogels against both tumorigenic and non-tumorigenic cell lines without the loading of MTX. This would aid in describing the biosafety of the formulations.

The anticancer efficacy of the MTX loaded PEI-SiNP/HA hydrogels should also be assessed with an *in vivo* study. The MTX loaded PEI-SiNP/HA hydrogels would be surgically applied directly to the tumour site and compared with the conventional intravenous delivery of MTX.

7.2.3 Assessment of the PEC Internal Structure, and its Influence on the SiNP Properties

As described in Chapter 3, the pore sizes and volumes observed for PSiNPs synthesised from Arg/PAA PECs were much higher than those of NH₄OH/PAA-PSiNPs. It is possible that this is due to differences in the internal structure of the PECs and the packing of PAA chains in the complexes. A thorough understanding of the influence of the choice of polyelectrolytes on the internal PEC structure and resultant PSiNP properties may provide greater morphological control and tunability of the porosity. For example, this could be used to increase the pore size for the encapsulation of larger therapeutic molecules, or for control of the drug release rate through manipulation of the pore diameters.

It is also noted that similar protocols reported in literature, which used ethanol/water mixtures to prepare PAA/cation PECs, produced hollow SiNPs while only solid particles were made in this work.⁹⁹ A description of the relationship between PEC formation conditions and structure

of the SiNPs would be of interest both for completeness of understanding and for greater morphological control in future syntheses.

Small angle neutron scattering has been used to study the polyelectrolyte complex continuum for solutions of KBr doped poly(styrenesulfonate) to describe the inter-chain distances and polymer concentrations in the coacervates.¹⁹⁹ A similar approach combined with electron microscopy observation of SiNP morphology and gas adsorption porosity analysis may help to describe the structural relationship between the PECs and SiNPs.

Bibliography

- (1) Zhao, L.; Skwarczynski, M.; Toth, I. Polyelectrolyte-Based Platforms for the Delivery of Peptides and Proteins. *ACS Biomater. Sci. Eng.* **2019**, *5* (10), 4937–4950. <https://doi.org/10.1021/acsbiomaterials.9b01135>.
- (2) Jing, H.; Du, X.; Mo, L.; Wang, H. Self-Coacervation of Carboxymethyl Chitosan as a PH-Responsive Encapsulation and Delivery Strategy. *Int. J. Biol. Macromol.* **2021**, *192* (July), 1169–1177. <https://doi.org/10.1016/j.ijbiomac.2021.10.072>.
- (3) Water, J. J.; Schack, M. M.; Velazquez-Campoy, A.; Maltesen, M. J.; Van De Weert, M.; Jorgensen, L. Complex Coacervates of Hyaluronic Acid and Lysozyme: Effect on Protein Structure and Physical Stability. *Eur. J. Pharm. Biopharm.* **2014**, *88* (2), 325–331. <https://doi.org/10.1016/j.ejpb.2014.09.001>.
- (4) Wu, D.; Zhu, L.; Li, Y.; Zhang, X.; Xu, S.; Yang, G.; Delair, T. Chitosan-Based Colloidal Polyelectrolyte Complexes for Drug Delivery: A Review. *Carbohydr. Polym.* **2020**, *238* (December 2019). <https://doi.org/10.1016/j.carbpol.2020.116126>.
- (5) Tan, M. L.; Friedhuber, A. M.; Dunstan, D. E.; Choong, P. F. M.; Dass, C. R. The Performance of Doxorubicin Encapsulated in Chitosan-Dextran Sulphate Microparticles in an Osteosarcoma Model. *Biomaterials* **2010**, *31* (3), 541–551. <https://doi.org/10.1016/j.biomaterials.2009.09.069>.
- (6) Tapia, C.; Escobar, Z.; Costa, E.; Sapag-Hagar, J.; Valenzuela, F.; Basualto, C.; Gai, M. N.; Yazdani-Pedram, M. Comparative Studies on Polyelectrolyte Complexes and Mixtures of Chitosan-Alginate and Chitosan-Carrageenan as Prolonged Diltiazem Chlorhydrate Release Systems. *Eur. J. Pharm. Biopharm.* **2004**, *57* (1), 65–75. [https://doi.org/10.1016/S0939-6411\(03\)00153-X](https://doi.org/10.1016/S0939-6411(03)00153-X).
- (7) Aluani, D.; Tzankova, V.; Kondeva-Burdina, M.; Yordanov, Y.; Nikolova, E.; Odzhakov, F.; Apostolov, A.; Markova, T.; Yoncheva, K. Evaluation of

- Biocompatibility and Antioxidant Efficiency of Chitosan-Alginate Nanoparticles Loaded With Quercetin. *Int. J. Biol. Macromol.* **2017**, *103*, 771–782. <https://doi.org/10.1016/j.ijbiomac.2017.05.062>.
- (8) Rahaiee, S.; Hashemi, M.; Shojaosadati, S. A.; Moini, S.; Razavi, S. H. Nanoparticles Based on Crocin Loaded Chitosan-Alginate Biopolymers: Antioxidant Activities, Bioavailability and Anticancer Properties. *Int. J. Biol. Macromol.* **2017**, *99*, 401–408. <https://doi.org/10.1016/j.ijbiomac.2017.02.095>.
- (9) Mohanta, B. C.; Javed, M. N.; Hasnain, M. S.; Nayak, A. K. *Polyelectrolyte Complexes of Alginate for Controlling Drug Release*; INC, 2020. <https://doi.org/10.1016/b978-0-12-817640-5.00012-1>.
- (10) Coppi, G.; Iannuccelli, V. Alginate/Chitosan Microparticles for Tamoxifen Delivery to the Lymphatic System. *Int. J. Pharm.* **2009**, *367* (1–2), 127–132. <https://doi.org/10.1016/j.ijpharm.2008.09.040>.
- (11) Chu, H.; Johnson, N. R.; Mason, N. S.; Wang, Y. A [Polycation:Heparin] Complex Releases Growth Factors with Enhanced Bioactivity. *J. Control. Release* **2011**, *150* (2), 157–163. <https://doi.org/10.1016/j.jconrel.2010.11.025>.
- (12) Park, U.; Lee, M. S.; Jeon, J.; Lee, S.; Hwang, M. P.; Wang, Y.; Yang, H. S.; Kim, K. Coacervate-Mediated Exogenous Growth Factor Delivery for Scarless Skin Regeneration. *Acta Biomater.* **2019**, *90*, 179–191. <https://doi.org/10.1016/j.actbio.2019.03.052>.
- (13) Janes, K. A.; Fresneau, M. P.; Marazuela, A.; Fabra, A.; Alonso, M. J. Chitosan Nanoparticles as Delivery Systems for Doxorubicin. *J. Control. Release* **2001**, *73* (2–3), 255–267. [https://doi.org/10.1016/S0168-3659\(01\)00294-2](https://doi.org/10.1016/S0168-3659(01)00294-2).
- (14) Timilsena, Y. P.; Akanbi, T. O.; Khalid, N.; Adhikari, B.; Barrow, C. J. Complex Coacervation: Principles, Mechanisms and Applications in Microencapsulation. *Int. J.*

- Biol. Macromol.* **2019**, *121*, 1276–1286.
<https://doi.org/10.1016/j.ijbiomac.2018.10.144>.
- (15) Blocher McTigue, W. C.; Perry, S. L. Design Rules for Encapsulating Proteins into Complex Coacervates. *Soft Matter* **2019**, *15* (15), 3089–3103.
<https://doi.org/10.1039/C9SM00372J>.
- (16) Saravanan, M.; Rao, K. P. Pectin-Gelatin and Alginate-Gelatin Complex Coacervation for Controlled Drug Delivery: Influence of Anionic Polysaccharides and Drugs Being Encapsulated on Physicochemical Properties of Microcapsules. *Carbohydr. Polym.* **2010**, *80* (3), 808–816. <https://doi.org/10.1016/j.carbpol.2009.12.036>.
- (17) Black, K. A.; Priftis, D.; Perry, S. L.; Yip, J.; Byun, W. Y.; Tirrell, M. Protein Encapsulation via Polypeptide Complex Coacervation. *ACS Macro Lett.* **2014**, *3* (10), 1088–1091. <https://doi.org/10.1021/mz500529v>.
- (18) Nishida, K.; Tamura, A.; Yui, N. PH-Responsive Coacervate Droplets Formed from Acid-Labile Methylated Polyrotaxanes as an Injectable Protein Carrier. *Biomacromolecules* **2018**, *19* (6), 2238–2247.
<https://doi.org/10.1021/acs.biomac.8b00301>.
- (19) Lim, J. Y. C.; Lin, Q.; Xue, K.; Loh, X. J. Recent Advances in Supramolecular Hydrogels for Biomedical Applications. *Mater. Today Adv.* **2019**, *3*, 100021.
<https://doi.org/10.1016/j.mtadv.2019.100021>.
- (20) Cai, H.; Ni, C.; Zhang, L. Preparation of Complex Nano-Particles Based on Alginic Acid/Poly[(2-Dimethylamino) Ethyl Methacrylate] and a Drug Vehicle for Doxorubicin Release Controlled by Ionic Strength. *Eur. J. Pharm. Sci.* **2012**, *45* (1–2), 43–49. <https://doi.org/10.1016/j.ejps.2011.10.020>.
- (21) Li, J.; Mooney, D. J. Designing Hydrogels for Controlled Drug Delivery. *Nat. Rev. Mater.* **2016**, *1* (12). <https://doi.org/10.1038/natrevmats.2016.71>.

- (22) Li, W.; Feng, R.; Wang, R.; Li, D.; Jiang, W.; Liu, H.; Guo, Z.; Serpe, M. J.; Hu, L. Polyelectrolyte-Based Physical Adhesive Hydrogels with Excellent Mechanical Properties for Biomedical Applications. *J. Mater. Chem. B* **2018**, *6* (29), 4799–4807. <https://doi.org/10.1039/c8tb01160e>.
- (23) Zeimaran, E.; Pourshahrestani, S.; Fathi, A.; Razak, N. A. bin A.; Kadri, N. A.; Sheikhi, A.; Baino, F. Advances in Bioactive Glass-Containing Injectable Hydrogel Biomaterials for Tissue Regeneration. *Acta Biomater.* **2021**. <https://doi.org/10.1016/j.actbio.2021.09.034>.
- (24) Zhao, X.; Wang, L.; Gao, J.; Chen, X.; Wang, K. Hyaluronic Acid/Lysozyme Self-Assembled Coacervate to Promote Cutaneous Wound Healing. *Biomater. Sci.* **2020**, *8* (6), 1702–1710. <https://doi.org/10.1039/c9bm01886g>.
- (25) Voorhaar, L.; Hoogenboom, R. Supramolecular Polymer Networks: Hydrogels and Bulk Materials. *Chem. Soc. Rev.* **2016**, *45* (14), 4013–4031. <https://doi.org/10.1039/c6cs00130k>.
- (26) Zhu, Y.; Luo, Q.; Zhang, H.; Cai, Q.; Li, X.; Shen, Z.; Zhu, W. A Shear-Thinning Electrostatic Hydrogel with Antibacterial Activity by Nanoengineering of Polyelectrolytes. *Biomater. Sci.* **2020**, *8* (5), 1394–1404. <https://doi.org/10.1039/c9bm01386e>.
- (27) Zhou, D.; Pierucci, L.; Gao, Y.; O’Keeffe Ahern, J.; Huang, X.; Sigen, A.; Wang, W. Thermo- and PH-Responsive, Coacervate-Forming Hyperbranched Poly(β -Amino Ester)s for Selective Cell Binding. *ACS Appl. Mater. Interfaces* **2017**, *9* (7), 5793–5802. <https://doi.org/10.1021/acsami.6b15005>.
- (28) Wang, W.; Xu, Y.; Li, A.; Li, T.; Liu, M.; Von Klitzing, R.; Ober, C. K.; Kayitmazer, A. B.; Li, L.; Guo, X. Zinc Induced Polyelectrolyte Coacervate Bioadhesive and Its Transition to a Self-Healing Hydrogel. *RSC Adv.* **2015**, *5* (82), 66871–66878. <https://doi.org/10.1039/c5ra11915d>.

- (29) Dobrynin, A. V.; Rubinstein, M. Theory of Polyelectrolytes in Solutions and at Surfaces. *Prog. Polym. Sci.* **2005**, *30* (11), 1049–1118. <https://doi.org/10.1016/j.progpolymsci.2005.07.006>.
- (30) Sing, C. E.; Perry, S. L. Recent Progress in the Science of Complex Coacervation. *Soft Matter* **2020**. <https://doi.org/10.1039/d0sm00001a>.
- (31) Meka, V. S.; Sing, M. K. G.; Pichika, M. R.; Nali, S. R.; Kolapalli, V. R. M.; Kesharwani, P. A Comprehensive Review on Polyelectrolyte Complexes. *Drug Discov. Today* **2017**, *22* (11), 1697–1706. <https://doi.org/10.1016/j.drudis.2017.06.008>.
- (32) Kudlay, A.; Ermoshkin, A. V.; De La Cruz, M. O. Complexation of Oppositely Charged Polyelectrolytes: Effect of Ion Pair Formation. *Macromolecules* **2004**, *37* (24), 9231–9241. <https://doi.org/10.1021/ma048519t>.
- (33) Castelnovo, M.; Joanny, J. F. Complexation between Oppositely Charged Polyelectrolytes: Beyond the Random Phase Approximation. **2001**, No. 6, 377–386. <https://doi.org/10.1007/s10189-001-8051-7>.
- (34) Wang, Q.; Schlenoff, J. B. The Polyelectrolyte Complex/Coacervate Continuum. *Macromolecules* **2014**, *47* (9), 3108–3116. <https://doi.org/10.1021/ma500500q>.
- (35) Sing, C. E. Development of the Modern Theory of Polymeric Complex Coacervation. *Adv. Colloid Interface Sci.* **2017**, *239*, 2–16. <https://doi.org/10.1016/j.cis.2016.04.004>.
- (36) Overbeek, J. T. G.; Voorn, M. J. Phase Separation in Polyelectrolyte Solutions. Theory of Complex Coacervation. *J. Cell. Comp. Physiol.* **1957**, *49* (S1), 7–26. <https://doi.org/10.1002/jcp.1030490404>.
- (37) Adhikari, S.; Leaf, M. A.; Muthukumar, M. Polyelectrolyte Complex Coacervation by Electrostatic Dipolar Interactions. *J. Chem. Phys.* **2018**, *149* (16). <https://doi.org/10.1063/1.5029268>.

- (38) Spruijt, E.; Westphal, A. H.; Borst, J. W.; Cohen Stuart, M. A.; Van Der Gucht, J. Binodal Compositions of Polyelectrolyte Complexes. *Macromolecules* **2010**, *43* (15), 6476–6484. <https://doi.org/10.1021/ma101031t>.
- (39) Andreev, M.; Chremos, A.; De Pablo, J.; Douglas, J. F. Coarse-Grained Model of the Dynamics of Electrolyte Solutions. *J. Phys. Chem. B* **2017**, *121* (34), 8195–8202. <https://doi.org/10.1021/acs.jpcc.7b04297>.
- (40) Radhakrishna, M.; Basu, K.; Liu, Y.; Shamsi, R.; Perry, S. L.; Sing, C. E. Molecular Connectivity and Correlation Effects on Polymer Coacervation. *Macromolecules* **2017**, *50* (7), 3030–3037. <https://doi.org/10.1021/acs.macromol.6b02582>.
- (41) Qin, J.; De Pablo, J. J. Criticality and Connectivity in Macromolecular Charge Complexation. *Macromolecules* **2016**, *49* (22), 8789–8800. <https://doi.org/10.1021/acs.macromol.6b02113>.
- (42) Perry, S. L.; Sing, C. E. PRISM-Based Theory of Complex Coacervation: Excluded Volume versus Chain Correlation. *Macromolecules* **2015**, *48* (14), 5040–5053. <https://doi.org/10.1021/acs.macromol.5b01027>.
- (43) Qin, J.; Priftis, D.; Farina, R.; Perry, S. L.; Leon, L.; Whitmer, J.; Hoffmann, K.; Tirrell, M.; De Pablo, J. J. Interfacial Tension of Polyelectrolyte Complex Coacervate Phases. *ACS Macro Lett.* **2014**, *3* (6), 565–568. <https://doi.org/10.1021/mz500190w>.
- (44) Yeo, G. C.; Keeley, F. W.; Weiss, A. S. Coacervation of Tropoelastin. *Adv. Colloid Interface Sci.* **2011**, *167* (1–2), 94–103. <https://doi.org/10.1016/j.cis.2010.10.003>.
- (45) Reichheld, S. E.; Muiznieks, L. D.; Keeley, F. W.; Sharpe, S. Direct Observation of Structure and Dynamics during Phase Separation of an Elastomeric Protein. *Proc. Natl. Acad. Sci. U. S. A.* **2017**, *114* (22), E4408–E4415. <https://doi.org/10.1073/pnas.1701877114>.

- (46) Narayanan, A.; Menefee, J. R.; Liu, Q.; Dhinojwala, A.; Joy, A. Lower Critical Solution Temperature-Driven Self-Coacervation of Nonionic Polyester Underwater Adhesives. *ACS Nano* **2020**, *14* (7), 8359–8367. <https://doi.org/10.1021/acsnano.0c02396>.
- (47) Seo, S.; Das, S.; Zalicki, P. J.; Mirshafian, R.; Eisenbach, C. D.; Israelachvili, J. N.; Waite, J. H.; Ahn, B. K. Microphase Behavior and Enhanced Wet-Cohesion of Synthetic Copolyampholytes Inspired by a Mussel Foot Protein. *J. Am. Chem. Soc.* **2015**, *137* (29), 9214–9217. <https://doi.org/10.1021/jacs.5b03827>.
- (48) Wei, W.; Tan, Y.; Martinez Rodriguez, N. R.; Yu, J.; Israelachvili, J. N.; Waite, J. H. A Mussel-Derived One Component Adhesive Coacervate. *Acta Biomater.* **2014**, *10* (4), 1663–1670. <https://doi.org/10.1016/j.actbio.2013.09.007>.
- (49) Zhang, Z.; Li, H.; Kasmi, S.; Van Herck, S.; Deswarte, K.; Lambrecht, B. N.; Hoogenboom, R.; Nuhn, L.; De Geest, B. G. A Synthetic, Transiently Thermoresponsive Homopolymer with UCST Behaviour within a Physiologically Relevant Window. *Angew. Chemie - Int. Ed.* **2019**, *58* (23), 7866–7872. <https://doi.org/10.1002/anie.201900224>.
- (50) Seuring, J.; Agarwal, S. First Example of a Universal and Cost-Effective Approach: Polymers with Tunable Upper Critical Solution Temperature in Water and Electrolyte Solution. *Macromolecules* **2012**, *45* (9), 3910–3918. <https://doi.org/10.1021/ma300355k>.
- (51) Perro, A.; Giraud, L.; Coudon, N.; Shanmugathan, S.; Lapeyre, V.; Goudeau, B.; Douliez, J. P.; Ravaine, V. Self-Coacervation of Ampholyte Polymer Chains as an Efficient Encapsulation Strategy. *J. Colloid Interface Sci.* **2019**, *548*, 275–283. <https://doi.org/10.1016/j.jcis.2019.04.033>.
- (52) Abbas, M.; Lipiński, W. P.; Wang, J.; Spruijt, E. Peptide-Based Coacervates as Biomimetic Protocells. *Chem. Soc. Rev.* **2021**, *50* (6), 3690–3705. <https://doi.org/10.1039/d0cs00307g>.

- (53) Tauer, K.; Gau, D.; Schulze, S.; Völkel, A.; Dimova, R. Thermal Property Changes of Poly(N-Isopropylacrylamide) Microgel Particles and Block Copolymers. *Colloid Polym. Sci.* **2009**, *287* (3), 299–312. <https://doi.org/10.1007/s00396-008-1984-x>.
- (54) Ali, S.; Bleuel, M.; Prabhu, V. M. Lower Critical Solution Temperature in Polyelectrolyte Complex Coacervates. *ACS Macro Lett.* **2019**, *8* (3), 289–293. <https://doi.org/10.1021/acsmacrolett.8b00952>.
- (55) Das, E.; Matsumura, K. Tunable Phase-Separation Behavior of Thermoresponsive Polyampholytes through Molecular Design. *J. Polym. Sci. Part A Polym. Chem.* **2017**, *55* (5), 876–884. <https://doi.org/10.1002/pola.28440>.
- (56) Seuring, J.; Agarwal, S. Polymers with Upper Critical Solution Temperature in Aqueous Solution: Unexpected Properties from Known Building Blocks. *ACS Macro Lett.* **2013**, *2* (7), 597–600. <https://doi.org/10.1021/mz400227y>.
- (57) Shimada, N.; Nakayama, M.; Kano, A.; Maruyama, A. Design of UCST Polymers for Chilling Capture of Proteins. *Biomacromolecules* **2013**, *14* (5), 1452–1457. <https://doi.org/10.1021/bm400120y>.
- (58) Mohanty, B.; Bohidar, H. B. Systematic of Alcohol-Induced Simple Coacervation in Aqueous Gelatin Solutions. *Biomacromolecules* **2003**, *4* (4), 1080–1086. <https://doi.org/10.1021/bm034080l>.
- (59) Shimokawa, K. I.; Saegusa, K.; Wada, Y.; Ishii, F. Physicochemical Properties and Controlled Drug Release of Microcapsules Prepared by Simple Coacervation. *Colloids Surfaces B Biointerfaces* **2013**, *104*, 1–4. <https://doi.org/10.1016/j.colsurfb.2012.11.036>.
- (60) Gupta, A.; Reena; Bohidar, H. B. Free-Energy Landscape of Alcohol Driven Coacervation Transition in Aqueous Gelatin Solutions. *J. Chem. Phys.* **2006**, *125* (5). <https://doi.org/10.1063/1.2219745>.

- (61) Zhang, G.; Wu, C. Reentrant Coil-to-Globule-to-Coil Transition of a Single Linear Homopolymer Chain in a Water/Methanol Mixture. *Phys. Rev. Lett.* **2001**, *86* (5), 822–825. <https://doi.org/10.1103/PhysRevLett.86.822>.
- (62) Zhang, G.; Wu, C. The Water/Methanol Complexation Induced Reentrant Coil-to-Globule-to-Coil Transition of Individual Homopolymer Chains in Extremely Dilute Solution. *J. Am. Chem. Soc.* **2001**, *123* (7), 1376–1380. <https://doi.org/10.1021/ja003889s>.
- (63) Naassaoui, I.; Aschi, A. Influence of Temperature and Salt on Coacervation in an Aqueous Mixture of Poly-L-Lysine (PLL) and Poly-(Sodium Styrene Sulfonate) (PSSNa). *Eur. Biophys. J.* **2021**, *50* (6), 877–887. <https://doi.org/10.1007/s00249-021-01542-4>.
- (64) Guo, L.; Fang, Y.; Shao, Z.; Fang, S.; Li, Y.; Chen, J.; Meng, Y. PH-Induced Structural Transition during Complexation and Precipitation of Sodium Caseinate and ϵ -Poly-L-Lysine. *Int. J. Biol. Macromol.* **2020**, *154*, 644–653. <https://doi.org/10.1016/j.ijbiomac.2020.03.062>.
- (65) Kayitmazer, A. B.; Koksall, A. F.; Kilic Iyilik, E. Complex Coacervation of Hyaluronic Acid and Chitosan: Effects of PH, Ionic Strength, Charge Density, Chain Length and the Charge Ratio. *Soft Matter* **2015**, *11* (44), 8605–8612. <https://doi.org/10.1039/c5sm01829c>.
- (66) Perry, S. L.; Li, Y.; Priftis, D.; Leon, L.; Tirrell, M. The Effect of Salt on the Complex Coacervation of Vinyl Polyelectrolytes. *Polymers (Basel)*. **2014**, *6* (6), 1756–1772. <https://doi.org/10.3390/polym6061756>.
- (67) Perry, S. L.; Leon, L.; Hoffmann, K. Q.; Kade, M. J.; Priftis, D.; Black, K. A.; Wong, D.; Klein, R. A.; Pierce, C. F.; Margossian, K. O.; Whitmer, J. K.; Qin, J.; De Pablo, J. J.; Tirrell, M. Chirality-Selected Phase Behaviour in Ionic Polypeptide Complexes. *Nat. Commun.* **2015**, *6*. <https://doi.org/10.1038/ncomms7052>.

- (68) Chollakup, R.; Beck, J. B.; Dirnberger, K.; Tirrell, M.; Eisenbach, C. D. Polyelectrolyte Molecular Weight and Salt Effects on the Phase Behavior and Coacervation of Aqueous Solutions of Poly(Acrylic Acid) Sodium Salt and Poly(Allylamine) Hydrochloride. *Macromolecules* **2013**, *46* (6), 2376–2390. <https://doi.org/10.1021/ma202172q>.
- (69) Priftis, D.; Tirrell, M. Phase Behaviour and Complex Coacervation of Aqueous Polypeptide Solutions. *Soft Matter* **2012**, *8* (36), 9396–9405. <https://doi.org/10.1039/c2sm25604e>.
- (70) Schatz, C.; Lucas, J. M.; Viton, C.; Domard, A.; Pichot, C.; Delair, T. Formation and Properties of Positively Charged Colloids Based on Polyelectrolyte Complexes of Biopolymers. *Langmuir* **2004**, *20* (18), 7766–7778. <https://doi.org/10.1021/la049460m>.
- (71) Yilmaz, T.; Maldonado, L.; Turasan, H.; Kokini, J. Thermodynamic Mechanism of Particulation of Sodium Alginate and Chitosan Polyelectrolyte Complexes as a Function of Charge Ratio and Order of Addition. *J. Food Eng.* **2019**, *254* (March), 42–50. <https://doi.org/10.1016/j.jfoodeng.2019.03.002>.
- (72) Shiu, C. C.; Wang, S.; Chang, C. H.; Jan, J. S. Poly(l -Glutamic Acid)-Decorated Hybrid Colloidal Particles from Complex Particle-Templated Silica Mineralization. *J. Phys. Chem. B* **2013**, *117* (34), 10007–10016. <https://doi.org/10.1021/jp403753z>.
- (73) Nakashima, Y.; Takai, C.; Razavi-Khosroshahi, H.; Shirai, T.; Fuji, M. Effects of Primary- and Secondary-Amines on the Formation of Hollow Silica Nanoparticles by Using Emulsion Template Method. *Colloids Surfaces A Physicochem. Eng. Asp.* **2016**, *506*, 849–854. <https://doi.org/10.1016/j.colsurfa.2016.07.052>.
- (74) Nakashima, Y.; Takai, C.; Razavi-Khosroshahi, H.; Fuji, M. Influence of the PAA Concentration on PAA/NH₃emulsion Template Method for Synthesizing Hollow Silica Nanoparticles. *Colloids Surfaces A Physicochem. Eng. Asp.* **2018**, *546*, 301–306. <https://doi.org/10.1016/j.colsurfa.2018.03.033>.

- (75) Nakashima, Y.; Takai, C.; Wanghui, C.; Razavi-Khosroshahi, H.; Shirai, T.; Fuji, M. Control Size Distribution of Hollow Silica Nanoparticles by Viscosity of Emulsion Template. *Colloids Surfaces A Physicochem. Eng. Asp.* **2016**, *507*, 164–169. <https://doi.org/10.1016/j.colsurfa.2016.07.091>.
- (76) Mechtaeva, E. V.; Zorin, I. M.; Gavrilova, D. A.; Fetin, P. A.; Zorina, N. A.; Bilibin, A. Y. Polyelectrolyte Complexes of Polyacrylic Acid with Oligovalent Organic Counterions. *J. Mol. Liq.* **2019**, *293*, 111418. <https://doi.org/10.1016/j.molliq.2019.111418>.
- (77) Chang, L. W.; Lytle, T. K.; Radhakrishna, M.; Madinya, J. J.; Vélez, J.; Sing, C. E.; Perry, S. L. Sequence and Entropy-Based Control of Complex Coacervates. *Nat. Commun.* **2017**, *8* (1), 1–7. <https://doi.org/10.1038/s41467-017-01249-1>.
- (78) Sun, J.; Perry, S. L.; Schiffman, J. D. Electrospinning Nanofibers from Chitosan/Hyaluronic Acid Complex Coacervates. *Biomacromolecules* **2019**, *20* (11), 4191–4198. <https://doi.org/10.1021/acs.biomac.9b01072>.
- (79) Meng, S.; Liu, Y.; Yeo, J.; Ting, J. M.; Tirrell, M. V. Effect of Mixed Solvents on Polyelectrolyte Complexes with Salt. *Colloid Polym. Sci.* **2020**, *298* (7), 887–894. <https://doi.org/10.1007/s00396-020-04637-0>.
- (80) Abe, K.; Koide, M.; Tsuchida, E. Complexes of Poly(L-Glutamic Acid) with Oligo(Ethyleneimine)s and Their Quaternary Derivatives: Effect of the Chain Length of the Oligomers on Complexation. *Polym. J.* **1977**, *9* (1), 73–78. <https://doi.org/10.1295/polymj.9.73>.
- (81) Asefa, T.; Tao, Z. Biocompatibility of Mesoporous Silica Nanoparticles. *Chem. Res. Toxicol.* **2012**, *25* (11), 2265–2284. <https://doi.org/10.1021/tx300166u>.
- (82) Möller, K.; Bein, T. Degradable Drug Carriers: Vanishing Mesoporous Silica Nanoparticles. *Chem. Mater.* **2019**, *31* (12), 4364–4378.

<https://doi.org/10.1021/acs.chemmater.9b00221>.

- (83) Tzur-Balter, A.; Shatsberg, Z.; Beckerman, M.; Segal, E.; Artzi, N. Mechanism of Erosion of Nanostructured Porous Silicon Drug Carriers in Neoplastic Tissues. *Nat. Commun.* **2015**, *6*, 1–8. <https://doi.org/10.1038/ncomms7208>.
- (84) Manzano, M.; Vallet-Regí, M. Mesoporous Silica Nanoparticles for Drug Delivery. *Adv. Funct. Mater.* **2020**, *30* (2), 3–5. <https://doi.org/10.1002/adfm.201902634>.
- (85) Tang, F.; Li, L.; Chen, D. Mesoporous Silica Nanoparticles: Synthesis, Biocompatibility and Drug Delivery. *Adv. Mater.* **2012**, *24* (12), 1504–1534. <https://doi.org/10.1002/adma.201104763>.
- (86) Brinker, C. Hydrolysis and Condensation of Silicates: Effects on Structure. *J. Non-Cryst. Solids* **1988**, *100*, 31–50. <https://doi.org/10.1017/CBO9781107415324.004>.
- (87) Ghimire, P. P.; Jaroniec, M. Renaissance of Stöber Method for Synthesis of Colloidal Particles: New Developments and Opportunities. *J. Colloid Interface Sci.* **2021**, *584*, 838–865. <https://doi.org/10.1016/j.jcis.2020.10.014>.
- (88) Matsoukas, T.; Gulari, E. Dynamics of Growth of Silica Particles from Ammonia-Catalyzed Hydrolysis of Tetra-Ethyl-Orthosilicate. *J. Colloid Interface Sci.* **1988**, *124* (1), 252–261. [https://doi.org/10.1016/0021-9797\(88\)90346-3](https://doi.org/10.1016/0021-9797(88)90346-3).
- (89) Bogush, G. H.; Zukoski IV, C. F. Studies of the Kinetics of the Precipitation of Uniform Silica Particles through the Hydrolysis and Condensation of Silicon Alkoxides. *J. Colloid Interface Sci.* **1991**, *142* (1), 1–18. [https://doi.org/10.1016/0021-9797\(91\)90029-8](https://doi.org/10.1016/0021-9797(91)90029-8).
- (90) Li, H.; Yu, H.; Zhu, C.; Hu, J.; Du, M.; Zhang, F.; Yang, D. Cisplatin and Doxorubicin Dual-Loaded Mesoporous Silica Nanoparticles for Controlled Drug Delivery. *RSC Adv.* **2016**, *6* (96), 94160–94169. <https://doi.org/10.1039/c6ra17213j>.

- (91) Peralta, M. E.; Jadhav, S. A.; Magnacca, G.; Scalarone, D.; Mártire, D. O.; Parolo, M. E.; Carlos, L. Synthesis and in Vitro Testing of Thermoresponsive Polymer-Grafted Core-Shell Magnetic Mesoporous Silica Nanoparticles for Efficient Controlled and Targeted Drug Delivery. *J. Colloid Interface Sci.* **2019**, *544*, 198–205. <https://doi.org/10.1016/j.jcis.2019.02.086>.
- (92) Tian, B.; Liu, S.; Wu, S.; Lu, W.; Wang, D.; Jin, L.; Hu, B.; Li, K.; Wang, Z.; Quan, Z. PH-Responsive Poly (Acrylic Acid)-Gated Mesoporous Silica and Its Application in Oral Colon Targeted Drug Delivery for Doxorubicin. *Colloids Surfaces B Biointerfaces* **2017**, *154*, 287–296. <https://doi.org/10.1016/j.colsurfb.2017.03.024>.
- (93) Saroj, S.; Rajput, S. J. Tailor-Made PH-Sensitive Polyacrylic Acid Functionalized Mesoporous Silica Nanoparticles for Efficient and Controlled Delivery of Anti-Cancer Drug Etoposide. *Drug Dev. Ind. Pharm.* **2018**, *44* (7), 1198–1211. <https://doi.org/10.1080/03639045.2018.1438467>.
- (94) Jadhav, S. A.; Miletto, I.; Brunella, V.; Berlier, G.; Scalarone, D. Controlled Post-Synthesis Grafting of Thermoresponsive Poly(N-Isopropylacrylamide) on Mesoporous Silica Nanoparticles. *Polym. Adv. Technol.* **2015**, *26* (9), 1070–1075. <https://doi.org/10.1002/pat.3534>.
- (95) Takai-Yamashita, C.; Ando, M.; Noritake, M.; Khosroshahi, H. R.; Fuji, M. Emulsion Templating of Poly (Acrylic Acid) by Ammonium Hydroxide/Sodium Hydroxide Aqueous Mixture for High-Dispersed Hollow Silica Nanoparticles. *Adv. Powder Technol.* **2017**, *28* (2), 398–405. <https://doi.org/10.1016/j.apt.2016.10.010>.
- (96) Wan, Y.; Yu, S. H. Polyelectrolyte Controlled Large-Scale Synthesis of Hollow Silica Spheres with Tunable Sizes and Wall Thicknesses. *J. Phys. Chem. C* **2008**, *112* (10), 3641–3647. <https://doi.org/10.1021/jp710990b>.
- (97) Wei, Y.; Quan, L.; Zhou, C.; Zhan, Q. Factors Relating to the Biodistribution & Clearance of Nanoparticles & Their Effects on in Vivo Application. *Nanomedicine* **2018**, *13* (12), 1495–1512. <https://doi.org/10.2217/nmm-2018-0040>.

- (98) Danaei, M.; Dehghankhold, M.; Ataei, S.; Hasanzadeh Davarani, F.; Javanmard, R.; Dokhani, A.; Khorasani, S.; Mozafari, M. R. Impact of Particle Size and Polydispersity Index on the Clinical Applications of Lipidic Nanocarrier Systems. *Pharmaceutics* **2018**, *10* (2), 1–17. <https://doi.org/10.3390/pharmaceutics10020057>.
- (99) Nakashima, Y.; Takai, C.; Razavi-Khosroshahi, H.; Fuji, M. Effects of Cations on the Size and Silica Shell Microstructure of Hollow Silica Nanoparticles Prepared Using PAA/Cation/NH₄OH Template. *Colloids Surfaces A Physicochem. Eng. Asp.* **2020**, *593* (February), 124582. <https://doi.org/10.1016/j.colsurfa.2020.124582>.
- (100) Hu, J. J.; Hsieh, Y. H.; Jan, J. S. Polyelectrolyte Complex-Silica Hybrid Colloidal Particles Decorated with Different Polyelectrolytes. *J. Colloid Interface Sci.* **2015**, *438*, 94–101. <https://doi.org/10.1016/j.jcis.2014.09.063>.
- (101) Korsmeyer, R. W.; Gurny, R.; Doelker, E.; Buri, P.; Peppas, N. A. Mechanisms of Solute Release from Porous Hydrophilic Polymers. *Int. J. Pharm.* **1983**, *15* (1), 25–35. [https://doi.org/10.1016/0378-5173\(83\)90064-9](https://doi.org/10.1016/0378-5173(83)90064-9).
- (102) Polson, E. S.; Kuchler, V. B.; Abbosh, C.; Ross, E. M.; Mathew, R. K.; Beard, H. A.; Silva, B. Da; Holding, A. N.; Ballereau, S.; Chuntharpursat-Bon, E.; Williams, J.; Griffiths, H. B.; Shao, H.; Patel, A.; Davies, A. J.; Droop, A.; Chumas, P.; Short, S. C.; Lorger, M.; Gestwicki, J. E.; Roberts, L. D.; Bon, R. S.; Allison, S. J.; Zhu, S.; Markowitz, F.; Wurdak, H. KHS101 Disrupts Energy Metabolism in Human Glioblastoma Cells and Reduces Tumor Growth in Mice. *Sci. Transl. Med.* **2018**, *10* (454). <https://doi.org/10.1126/scitranslmed.aar2718>.
- (103) Wurdak, H.; Zhu, S.; Romero, A.; Lorger, M.; Watson, J.; Chiang, C. yuan; Zhang, J.; Natu, V. S.; Lairson, L. L.; Walker, J. R.; Trussell, C. M.; Harsh, G. R.; Vogel, H.; Felding-Habermann, B.; Orth, A. P.; Miraglia, L. J.; Rines, D. R.; Skirboll, S. L.; Schultz, P. G. An RNAi Screen Identifies TRRAP as a Regulator of Brain Tumor-Initiating Cell Differentiation. *Cell Stem Cell* **2010**, *6* (1), 37–47. <https://doi.org/10.1016/j.stem.2009.11.002>.

- (104) Oueslati, N.; Leblanc, P.; Harscoat-Schiavo, C.; Rondags, E.; Meunier, S.; Kapel, R.; Marc, I. CTAB Turbidimetric Method for Assaying Hyaluronic Acid in Complex Environments and under Cross-Linked Form. *Carbohydr. Polym.* **2014**, *112*, 102–108. <https://doi.org/10.1016/j.carbpol.2014.05.039>.
- (105) Mailer, A. G.; Clegg, P. S.; Pusey, P. N. Particle Sizing by Dynamic Light Scattering: Non-Linear Cumulant Analysis. *J. Phys. Condens. Matter* **2015**, *27* (14). <https://doi.org/10.1088/0953-8984/27/14/145102>.
- (106) Finsy, R. Particle Sizing in the Submicron Range by Dynamic Light Scattering. *KONA Powder Part. J.* **1993**, *11* (0), 17–32. <https://doi.org/10.14356/kona.1993007>.
- (107) Stetefeld, J.; McKenna, S. A.; Patel, T. R. Dynamic Light Scattering: A Practical Guide and Applications in Biomedical Sciences. *Biophys. Rev.* **2016**, *8* (4), 409–427. <https://doi.org/10.1007/s12551-016-0218-6>.
- (108) Morrison, I. D.; Grabowski, E. F.; Herb, C. A. Improved Techniques for Particle Size Determination by Quasi-Elastic Light Scattering. *Langmuir* **1985**, *1* (4), 496–501. <https://doi.org/10.1021/la00064a016>.
- (109) Provencher, S. W. Contin: A General Purpose Constrained Regularization Program for Inverting Noisy Linear Algebraic and Integral Equations. *Comput. Phys. Commun.* **1984**, *35*, C-818-C–819. [https://doi.org/10.1016/s0010-4655\(84\)82935-5](https://doi.org/10.1016/s0010-4655(84)82935-5).
- (110) Jones, M. Diagram of zeta potential and slipping planeV2 [available online: https://en.wikipedia.org/wiki/Zeta_potential#/media/File:Diagram_of_zeta_potential_and_slipping_planeV2.svg], 2012.
- (111) Hunter, R. J. Electrokinetics and the Zeta Potential. In *Foundations of colloid science*. Oxford University Press, New York; Oxford University Press, 2001; pp 373–434.
- (112) Thommes, M.; Kaneko, K.; Neimark, A. V.; Olivier, J. P.; Rodriguez-Reinoso, F.;

- Rouquerol, J.; Sing, K. S. W. Physisorption of Gases, with Special Reference to the Evaluation of Surface Area and Pore Size Distribution (IUPAC Technical Report). *Pure Appl. Chem.* **2015**, *87* (9–10), 1051–1069. <https://doi.org/10.1515/pac-2014-1117>.
- (113) Rouquerol, J.; Llewellyn, P.; Rouquerol, F. *Is the BET Equation Applicable to Microporous Adsorbents?*; Elsevier B.V., 2007; Vol. 160. [https://doi.org/10.1016/s0167-2991\(07\)80008-5](https://doi.org/10.1016/s0167-2991(07)80008-5).
- (114) Ferry, J. D. *Viscoelastic Properties of Polymers*; John Wiley & Sons, Inc, 1980. <https://doi.org/10.1149/1.2428174>.
- (115) Slowing, I. I.; Vivero-Escoto, J. L.; Wu, C.-W.; Lin, V. S. Y. Mesoporous Silica Nanoparticles as Controlled Release Drug Delivery and Gene Transfection Carriers. *Adv. Drug Deliv. Rev.* **2008**, *60* (11), 1278–1288. <https://doi.org/http://dx.doi.org/10.1016/j.addr.2008.03.012>.
- (116) Chen, S.; Greasley, S. L.; Ong, Z. Y.; Naruphontjirakul, P.; Page, S. J.; Hanna, J. V.; Redpath, A. N.; Tsigkou, O.; Rankin, S.; Ryan, M. P.; Porter, A. E.; Jones, J. R. Biodegradable Zinc-Containing Mesoporous Silica Nanoparticles for Cancer Therapy. *Mater. Today Adv.* **2020**, *6*, 100066. <https://doi.org/10.1016/j.mtadv.2020.100066>.
- (117) Anselmo, A. C.; Mitragotri, S. Nanoparticles in the Clinic: An Update. *Bioeng. Transl. Med.* **2019**, *4* (3), 1–16. <https://doi.org/10.1002/btm2.10143>.
- (118) Wu, S.-H.; Mou, C.-Y.; Lin, H.-P. Synthesis of Mesoporous Silica Nanoparticles. *Chem. Soc. Rev.* **2013**, *42* (9), 3862. <https://doi.org/10.1039/c3cs35405a>.
- (119) Lu, F.; Wu, S. H.; Hung, Y.; Mou, C. Y. Size Effect on Cell Uptake in Well-Suspended, Uniform Mesoporous Silica Nanoparticles. *Small* **2009**, *5* (12), 1408–1413. <https://doi.org/10.1002/sml.200900005>.

- (120) Lin, H.-P.; Tsai, C.-P. Synthesis of Mesoporous Silica Nanoparticles from a Low-Concentration CnTMAX–Sodium Silicate Components. *Chem. Lett.* **2003**, *32* (12), 1092–1093. <https://doi.org/10.1246/cl.2003.1092>.
- (121) Fowler, C. E.; Khushalani, D.; Lebeau, B.; Mann, S. Nanoscale Materials with Mesostructured Interiors. *Adv. Mater.* **2001**, *13* (9), 649–652. [https://doi.org/10.1002/1521-4095\(200105\)13:9<649::AID-ADMA649>3.0.CO;2-G](https://doi.org/10.1002/1521-4095(200105)13:9<649::AID-ADMA649>3.0.CO;2-G).
- (122) Lv, X.; Zhang, L.; Xing, F.; Lin, H. Controlled Synthesis of Monodispersed Mesoporous Silica Nanoparticles: Particle Size Tuning and Formation Mechanism Investigation. *Microporous Mesoporous Mater.* **2016**, *225*, 238–244. <https://doi.org/10.1016/j.micromeso.2015.12.024>.
- (123) Castillo, R. R.; Lozano, D.; González, B.; Manzano, M.; Izquierdo-Barba, I.; Vallet-Regí, M. Advances in Mesoporous Silica Nanoparticles for Targeted Stimuli-Responsive Drug Delivery: An Update. *Expert Opin. Drug Deliv.* **2019**, *16* (4), 415–439. <https://doi.org/10.1080/17425247.2019.1598375>.
- (124) Lauth, V.; Maas, M.; Rezwan, K. Coacervate-Directed Synthesis of CaCO₃ Microcarriers for PH-Responsive Delivery of Biomolecules. *J. Mater. Chem. B* **2014**, *2* (44), 7725–7731. <https://doi.org/10.1039/c4tb01213e>.
- (125) Shi, H.; Li, L.; Zhang, L.; Wang, T.; Wang, C.; Zhu, D.; Su, Z. Designed Preparation of Polyacrylic Acid/Calcium Carbonate Nanoparticles with High Doxorubicin Payload for Liver Cancer Chemotherapy. *CrystEngComm* **2015**, *17* (26), 4768–4773. <https://doi.org/10.1039/c5ce00708a>.
- (126) Ren, H.; Zhang, L.; An, J.; Wang, T.; Li, L.; Si, X.; He, L.; Wu, X.; Wang, C.; Su, Z. Polyacrylic Acid@zeolitic Imidazolate Framework-8 Nanoparticles with Ultrahigh Drug Loading Capability for PH-Sensitive Drug Release. *Chem. Commun.* **2014**, *50* (8), 1000–1002. <https://doi.org/10.1039/c3cc47666a>.

- (127) Ren, H.; Zhang, L.; Wang, T.; Li, L.; Su, Z.; Wang, C. Universal and Facile Synthesis of Multicolored Upconversion Hollow Nanospheres Using Novel Poly(Acrylic Acid Sodium Salt) Microspheres as Templates. *Chem. Commun.* **2013**, *49* (54), 6036–6038. <https://doi.org/10.1039/c3cc41284a>.
- (128) Syed, N.; Langer, J.; Janczar, K.; Singh, P.; Lo Nigro, C.; Lattanzio, L.; Coley, H. M.; Hatzimichael, E.; Bomalaski, J.; Szlosarek, P.; Awad, M.; O’Neil, K.; Roncaroli, F.; Crook, T. Epigenetic Status of Argininosuccinate Synthetase and Argininosuccinate Lyase Modulates Autophagy and Cell Death in Glioblastoma. *Cell Death Dis.* **2013**, *4* (1), 1–11. <https://doi.org/10.1038/cddis.2012.197>.
- (129) Ensor, C. M.; Holtsberg, F. W.; Bomalaski, J. S.; Clark, M. A. Pegylated Arginine Deiminase (ADI-SS PEG20,000 Mw) Inhibits Human Melanomas and Hepatocellular Carcinomas in Vitro and in Vivo. *Cancer Res.* **2002**, *62* (19), 5443–5450.
- (130) Kim, R. H.; Coates, J. M.; Bowles, T. L.; McNerney, G. P.; Sutcliffe, J.; Jung, J. U.; Gandour-Edwards, R.; Chuang, F. Y. S.; Bold, R. J.; Kung, H. J. Arginine Deiminase as a Novel Therapy for Prostate Cancer Induces Autophagy and Caspase-Independent Apoptosis. *Cancer Res.* **2009**, *69* (2), 700–708. <https://doi.org/10.1158/0008-5472.CAN-08-3157>.
- (131) Lu, Y.; Wang, W.; Wang, J.; Yang, C.; Mao, H.; Fu, X.; Wu, Y.; Cai, J.; Han, J.; Xu, Z.; Zhuang, Z.; Liu, Z.; Hu, H.; Chen, B. Overexpression of Arginine Transporter CAT-1 Is Associated with Accumulation of L-Arginine and Cell Growth in Human Colorectal Cancer Tissue. *PLoS One* **2013**, *8* (9), 1–8. <https://doi.org/10.1371/journal.pone.0073866>.
- (132) Wang, S.; Li, F.; Qiao, R.; Hu, X.; Liao, H.; Chen, L.; Wu, J.; Wu, H.; Zhao, M.; Liu, J.; Chen, R.; Ma, X.; Kim, D.; Sun, J.; Davis, T. P.; Chen, C.; Tian, J.; Hyeon, T.; Ling, D. Arginine-Rich Manganese Silicate Nanobubbles as a Ferroptosis-Inducing Agent for Tumor-Targeted Theranostics. *ACS Nano* **2018**, *12* (12), 12380–12392. <https://doi.org/10.1021/acsnano.8b06399>.

- (133) Xu, J.; Li, X.; Li, J.; Li, X.; Li, B.; Wang, Y.; Wu, L.; Li, W. Wet and Functional Adhesives from One-Step Aqueous Self-Assembly of Natural Amino Acids and Polyoxometalates. *Angew. Chemie - Int. Ed.* **2017**, *56* (30), 8731–8735. <https://doi.org/10.1002/anie.201703774>.
- (134) Liu, X.; Xie, X.; Du, Z.; Li, B.; Wu, L.; Li, W. Aqueous Self-Assembly of Arginine and K₈SiW₁₁O₃₉: Fine-Tuning the Formation of a Coacervate Intended for Sprayable Anticorrosive Coatings. *Soft Matter* **2019**, *15* (45), 9178–9186. <https://doi.org/10.1039/c9sm01511f>.
- (135) Park, J.-G.; Lee, S.-H.; Ryu, J.-S.; Hong, Y.-K.; Kim, T.-G.; Busnaina, A. A. Interfacial and Electrokinetic Characterization of IPA Solutions Related to Semiconductor Wafer Drying and Cleaning. *J. Electrochem. Soc.* **2006**, *153* (9), G811. <https://doi.org/10.1149/1.2214532>.
- (136) Gupta, A.; Bohidar, H. B. Kinetics of Phase Separation in Systems Exhibiting Simple Coacervation. *Phys. Rev. E - Stat. Nonlinear, Soft Matter Phys.* **2005**, *72* (1), 1–9. <https://doi.org/10.1103/PhysRevE.72.011507>.
- (137) Åkerlöf, G. Dielectric Constants of Some Organic Solvent-Water Mixtures at Various Temperatures. *J. Am. Chem. Soc.* **1932**, *54* (11), 4125–4139. <https://doi.org/10.1021/ja01350a001>.
- (138) Swift, T.; Swanson, L.; Geoghegan, M.; Rimmer, S. The PH-Responsive Behaviour of Poly(Acrylic Acid) in Aqueous Solution Is Dependent on Molar Mass. *Soft Matter* **2016**, *12* (9), 2542–2549. <https://doi.org/10.1039/c5sm02693h>.
- (139) Lide, D. R.; Ed. *CRC Handbook of Chemistry and Physics*, Internet V.; CRC Press: Boca Ranton, FL, 2005; Vol. Internet V. <https://doi.org/10.5860/CHOICE.41-4368>.
- (140) Yokoi, T.; Wakabayashi, J.; Otsuka, Y.; Fan, W.; Iwama, M.; Watanabe, R.; Aramaki, K.; Shimojima, A.; Tatsumi, T.; Okubo, T. Mechanism of Formation of Uniform-Sized

- Silica Nanospheres Catalyzed by Basic Amino Acids. *Chem. Mater.* **2009**, *21* (15), 3719–3729. <https://doi.org/10.1021/cm900993b>.
- (141) Du, X.; He, J. Carrier Effect in the Synthesis of Rattle-Type Au@hollow Silica Nanospheres by Impregnation and Thermal Decomposition Method. *Microporous Mesoporous Mater.* **2012**, *163*, 201–210. <https://doi.org/10.1016/j.micromeso.2012.06.045>.
- (142) Roy, E.; Patra, S.; Madhuri, R.; Sharma, P. K. Development of an Imprinted Polymeric Sensor with Dual Sensing Property for Trace Level Estimation of Zinc and Arginine. *Mater. Sci. Eng. C* **2015**, *49*, 25–33. <https://doi.org/10.1016/j.msec.2014.12.066>.
- (143) Kam, W.; Liew, C. W.; Lim, J. Y.; Ramesh, S. Electrical, Structural, and Thermal Studies of Antimony Trioxide-Doped Poly(Acrylic Acid)-Based Composite Polymer Electrolytes. *Ionics (Kiel)*. **2014**, *20* (5), 665–674. <https://doi.org/10.1007/s11581-013-1012-0>.
- (144) Yuan, L.; Tang, Q.; Yang, D.; Zhang, J. Z.; Zhang, F.; Hu, J. Preparation of PH-Responsive Mesoporous Silica Nanoparticles and Their Application in Controlled Drug Delivery. *J. Phys. Chem. C* **2011**, *115* (20), 9926–9932. <https://doi.org/10.1021/jp201053d>.
- (145) Yan, J.; Xu, X.; Zhou, J.; Liu, C.; Zhang, L.; Wang, D.; Yang, F.; Zhang, H. Fabrication of a PH/Redox-Triggered Mesoporous Silica-Based Nanoparticle with Microfluidics for Anticancer Drugs Doxorubicin and Paclitaxel Codelivery. *ACS Appl. Bio Mater.* **2020**, *3* (2), 1216–1225. <https://doi.org/10.1021/acsabm.9b01111>.
- (146) Li, J.; Shen, S.; Kong, F.; Jiang, T.; Tang, C.; Yin, C. Effects of Pore Size on: In Vitro and in Vivo Anticancer Efficacies of Mesoporous Silica Nanoparticles. *RSC Adv.* **2018**, *8* (43), 24633–24640. <https://doi.org/10.1039/c8ra03914c>.
- (147) Xie, M.; Shi, H.; Li, Z.; Shen, H.; Ma, K.; Li, B.; Shen, S.; Jin, Y. A Multifunctional

- Mesoporous Silica Nanocomposite for Targeted Delivery, Controlled Release of Doxorubicin and Bioimaging. *Colloids Surfaces B Biointerfaces* **2013**, *110*, 138–147. <https://doi.org/10.1016/j.colsurfb.2013.04.009>.
- (148) Yue, J.; Luo, S. zhong; Lu, M. meng; Shao, D.; Wang, Z.; Dong, W. fei. A Comparison of Mesoporous Silica Nanoparticles and Mesoporous Organosilica Nanoparticles as Drug Vehicles for Cancer Therapy. *Chem. Biol. Drug Des.* **2018**, *92* (2), 1435–1444. <https://doi.org/10.1111/cbdd.13309>.
- (149) Shen, J.; He, Q.; Gao, Y.; Shi, J.; Li, Y. Mesoporous Silica Nanoparticles Loading Doxorubicin Reverse Multidrug Resistance: Performance and Mechanism. *Nanoscale* **2011**, *3* (10), 4314–4322. <https://doi.org/10.1039/c1nr10580a>.
- (150) Bilalis, P.; Tziveleka, L. A.; Varlas, S.; Iatrou, H. PH-Sensitive Nanogates Based on Poly(l-Histidine) for Controlled Drug Release from Mesoporous Silica Nanoparticles. *Polym. Chem.* **2016**, *7* (7), 1475–1485. <https://doi.org/10.1039/c5py01841b>.
- (151) Leung, K.; Nielsen, I. M. B.; Criscenti, L. J. Elucidating the Bimodal Acid-Base Behavior of the Water-Silica Interface from First Principles. *J. Am. Chem. Soc.* **2009**, *131* (51), 18358–18365. <https://doi.org/10.1021/ja906190t>.
- (152) Willner, I.; Eichen, Y.; Frank, A. J.; Fox, M. A. Photoinduced Electron-Transfer Processes Using Organized Redox-Functionalized Bipyridinium-Polyethylenimine-TiO₂ Colloids and Particulate Assemblies. *J. Phys. Chem.* **1993**, *97* (28), 7264–7271. <https://doi.org/10.1021/j100130a024>.
- (153) Newham, G.; Mathew, R. K.; Wurdak, H.; Evans, S. D.; Ong, Z. Y. Polyelectrolyte Complex Templated Synthesis of Monodisperse, Sub-100 Nm Porous Silica Nanoparticles for Cancer Targeted and Stimuli-Responsive Drug Delivery. *J. Colloid Interface Sci.* **2021**, *584*, 669–683. <https://doi.org/10.1016/j.jcis.2020.10.133>.
- (154) Kasprzak, A.; Popławska, M.; Bystrzejewski, M.; Łabędź, O.; Grudziński, I. P.

- Conjugation of Polyethylenimine and Its Derivatives to Carbon-Encapsulated Iron Nanoparticles. *RSC Adv.* **2015**, *5* (104), 85556–85567. <https://doi.org/10.1039/c5ra17912b>.
- (155) Navarrete, J. T. L.; Hernández, V.; Ramírez, F. J. Vibrational Study of Aspartic Acid and Glutamic Acid Dipeptides. *J. Mol. Struct.* **1995**, *348*, 249–252. [https://doi.org/10.1016/0022-2860\(95\)08635-9](https://doi.org/10.1016/0022-2860(95)08635-9).
- (156) Talebian, S.; Mehrali, M.; Taebnia, N.; Pennisi, C. P.; Kadumudi, F. B.; Foroughi, J.; Hasany, M.; Nikkhah, M.; Akbari, M.; Orive, G.; Dolatshahi-Pirouz, A. Self-Healing Hydrogels: The Next Paradigm Shift in Tissue Engineering? *Adv. Sci.* **2019**, *6* (16). <https://doi.org/10.1002/advs.201801664>.
- (157) Xiong, Y.; Zhang, X.; Ma, X.; Wang, W.; Yan, F.; Zhao, X.; Chu, X.; Xu, W.; Sun, C. A Review of the Properties and Applications of Bioadhesive Hydrogels. *Polym. Chem.* **2021**, *12* (26), 3721–3739. <https://doi.org/10.1039/d1py00282a>.
- (158) Zheng, J.; Xiao, P.; Liu, W.; Zhang, J.; Huang, Y.; Chen, T. Mechanical Robust and Self-Healable Supramolecular Hydrogel. *Macromol. Rapid Commun.* **2016**, *37* (3), 265–270. <https://doi.org/10.1002/marc.201500571>.
- (159) Shi, F.-K.; Wang, X.-P.; Guo, R.-H.; Zhong, M.; Xie, X.-M. Highly Stretchable and Super Tough Nanocomposite Physical Hydrogels Facilitated by the Coupling of Intermolecular Hydrogen Bonds and Analogous Chemical Crosslinking of Nanoparticles. *J. Mater. Chem. B* **2015**, *3* (7), 1187–1192. <https://doi.org/10.1039/C4TB01654H>.
- (160) Yang, J.; Han, C. R.; Duan, J. F.; Xu, F.; Sun, R. C. In situ Grafting Silica Nanoparticles Reinforced Nanocomposite Hydrogels. *Nanoscale* **2013**, *5* (22), 10858–10863. <https://doi.org/10.1039/c3nr04252a>.
- (161) Wu, C.; Wang, C.; Sun, L.; Xu, K.; Zhong, W. PLGA Nanoparticle-Reinforced

- Supramolecular Peptide Hydrogels for Local Delivery of Multiple Drugs with Enhanced Synergism. *Soft Matter* **2020**, *16* (46), 10528–10536. <https://doi.org/10.1039/d0sm01152e>.
- (162) Yu, J.; Ha, W.; Sun, J. N.; Shi, Y. P. Supramolecular Hybrid Hydrogel Based on Host-Guest Interaction and Its Application in Drug Delivery. *ACS Appl. Mater. Interfaces* **2014**, *6* (22), 19544–19551. <https://doi.org/10.1021/am505649q>.
- (163) Wu, H.; Song, L.; Chen, L.; Zhang, W.; Chen, Y.; Zang, F.; Chen, H.; Ma, M.; Gu, N.; Zhang, Y. Injectable Magnetic Supramolecular Hydrogel with Magnetocaloric Liquid-Conformal Property Prevents Post-Operative Recurrence in a Breast Cancer Model. *Acta Biomater.* **2018**, *74*, 302–311. <https://doi.org/10.1016/j.actbio.2018.04.052>.
- (164) Mihajlovic, M.; Mihajlovic, M.; Dankers, P. Y. W.; Masereeuw, R.; Sijbesma, R. P. Carbon Nanotube Reinforced Supramolecular Hydrogels for Bioapplications. *Macromol. Biosci.* **2019**, *19* (1). <https://doi.org/10.1002/mabi.201800173>.
- (165) Yang, J.; Shi, F. K.; Gong, C.; Xie, X. M. Dual Cross-Linked Networks Hydrogels with Unique Swelling Behavior and High Mechanical Strength: Based on Silica Nanoparticle and Hydrophobic Association. *J. Colloid Interface Sci.* **2012**, *381* (1), 107–115. <https://doi.org/10.1016/j.jcis.2012.05.046>.
- (166) Yang, J.; Gong, C.; Shi, F. K.; Xie, X. M. High Strength of Physical Hydrogels Based on Poly(Acrylic Acid)-g-Poly(Ethylene Glycol) Methyl Ether: Role of Chain Architecture on Hydrogel Properties. *J. Phys. Chem. B* **2012**, *116* (39), 12038–12047. <https://doi.org/10.1021/jp303710d>.
- (167) Schäfer, S.; Kickelbick, G. Self-Healing Polymer Nanocomposites Based on Diels-Alder-Reactions with Silica Nanoparticles: The Role of the Polymer Matrix. *Polymer (Guildf)*. **2015**, *69*, 357–368. <https://doi.org/10.1016/j.polymer.2015.03.017>.
- (168) Zhang, C.; Liang, K.; Zhou, D.; Yang, H.; Liu, X.; Yin, X.; Xu, W.; Zhou, Y.; Xiao, P.

- High-Performance Photopolymerized Poly(Vinyl Alcohol)/Silica Nanocomposite Hydrogels with Enhanced Cell Adhesion. *ACS Appl. Mater. Interfaces* **2018**, *10* (33), 27692–27700. <https://doi.org/10.1021/acsami.8b09026>.
- (169) Zengin, A.; Castro, J. P. O.; Habibovic, P.; van Rijt, S. H. Injectable, Self-Healing Mesoporous Silica Nanocomposite Hydrogels with Improved Mechanical Properties. *Nanoscale* **2021**, *13* (2), 1144–1154. <https://doi.org/10.1039/D0NR07406C>.
- (170) Zhong, M.; Liu, X. Y.; Shi, F. K.; Zhang, L. Q.; Wang, X. P.; Cheetham, A. G.; Cui, H.; Xie, X. M. Self-Healable, Tough and Highly Stretchable Ionic Nanocomposite Physical Hydrogels. *Soft Matter* **2015**, *11* (21), 4235–4241. <https://doi.org/10.1039/c5sm00493d>.
- (171) Yang, J.; Wang, X. P.; Xie, X. M. In Situ Synthesis of Poly(Acrylic Acid) Physical Hydrogels from Silica Nanoparticles. *Soft Matter* **2012**, *8* (4), 1058–1063. <https://doi.org/10.1039/c1sm06647a>.
- (172) Shi, F. K.; Zhong, M.; Zhang, L. Q.; Liu, X. Y.; Xie, X. M. Robust and Self-Healable Nanocomposite Physical Hydrogel Facilitated by the Synergy of Ternary Crosslinking Points in a Single Network. *J. Mater. Chem. B* **2016**, *4* (37), 6221–6227. <https://doi.org/10.1039/c6tb01606e>.
- (173) Alvarez, G. S.; Hélarý, C.; Mebert, A. M.; Wang, X.; Coradin, T.; Desimone, M. F. Antibiotic-Loaded Silica Nanoparticle-Collagen Composite Hydrogels with Prolonged Antimicrobial Activity for Wound Infection Prevention. *J. Mater. Chem. B* **2014**, *2* (29), 4660–4670. <https://doi.org/10.1039/c4tb00327f>.
- (174) Shi, Y.; Hélarý, C.; Coradin, T. Exploring the Cell–Protein–Mineral Interfaces: Interplay of Silica (Nano)Rods@collagen Biocomposites with Human Dermal Fibroblasts. *Mater. Today Bio* **2019**, *1* (April), 1–10. <https://doi.org/10.1016/j.mtbio.2019.100004>.

- (175) Adibnia, V.; Taghavi, S. M.; Hill, R. J. Roles of Chemical and Physical Crosslinking on the Rheological Properties of Silica-Doped Polyacrylamide Hydrogels. *Rheol. Acta* **2017**, *56* (2), 123–134. <https://doi.org/10.1007/s00397-016-0989-5>.
- (176) Xu, X.; Jha, A. K.; Harrington, D. A.; Farach-Carson, M. C.; Jia, X. Hyaluronic Acid-Based Hydrogels: From a Natural Polysaccharide to Complex Networks. *Soft Matter* **2012**, *8* (12), 3280–3294. <https://doi.org/10.1039/c2sm06463d>.
- (177) Liao, Y. H.; Jones, S. A.; Forbes, B.; Martin, G. P.; Brown, M. B. Hyaluronan: Pharmaceutical Characterization and Drug Delivery. *Drug Deliv. J. Deliv. Target. Ther. Agents* **2005**, *12* (6), 327–342. <https://doi.org/10.1080/10717540590952555>.
- (178) Sadtler, K.; Wolf, M. T.; Ganguly, S.; Moad, C. A.; Chung, L.; Majumdar, S.; Housseau, F.; Pardoll, D. M.; Elisseeff, J. H. Divergent Immune Responses to Synthetic and Biological Scaffolds. *Biomaterials* **2019**, *192* (October 2018), 405–415. <https://doi.org/10.1016/j.biomaterials.2018.11.002>.
- (179) Axpe, E.; Orive, G.; Franze, K.; Appel, E. A. Towards Brain-Tissue-like Biomaterials. *Nat. Commun.* **2020**, *11* (1), 10–13. <https://doi.org/10.1038/s41467-020-17245-x>.
- (180) Zhu, F.; Lin, X. Y.; Wu, Z. L.; Cheng, L.; Yin, J.; Song, Y.; Qian, J.; Zheng, Q. Processing Tough Supramolecular Hydrogels with Tunable Strength of Polyion Complex. *Polymer (Guildf)*. **2016**, *95*, 9–17. <https://doi.org/10.1016/j.polymer.2016.04.043>.
- (181) Yang, J.; Zhao, J. J.; Han, C. R.; Duan, J. F. Keys to Enhancing Mechanical Properties of Silica Nanoparticle Composites Hydrogels: The Role of Network Structure and Interfacial Interactions. *Compos. Sci. Technol.* **2014**, *95*, 1–7. <https://doi.org/10.1016/j.compscitech.2014.02.003>.
- (182) Atalar, B.; Choi, C. Y. H.; Harsh, G. R.; Chang, S. D.; Gibbs, I. C.; Adler, J. R.; Soltys, S. G. Cavity Volume Dynamics after Resection of Brain Metastases and

- Timing of Postresection Cavity Stereotactic Radiosurgery. *Neurosurgery* **2013**, *72* (2), 180–185. <https://doi.org/10.1227/NEU.0b013e31827b99f3>.
- (183) Jarvis, L. A.; Simmons, N. E.; Bellerive, M.; Erkmen, K.; Eskey, C. J.; Gladstone, D. J.; Hug, E. B.; Roberts, D. W.; Hartford, A. C. Tumor Bed Dynamics after Surgical Resection of Brain Metastases: Implications for Postoperative Radiosurgery. *Int. J. Radiat. Oncol. Biol. Phys.* **2012**, *84* (4), 943–948. <https://doi.org/10.1016/j.ijrobp.2012.01.067>.
- (184) Wu, M.; Chen, J.; Huang, W.; Yan, B.; Peng, Q.; Liu, J.; Chen, L.; Zeng, H. Injectable and Self-Healing Nanocomposite Hydrogels with Ultrasensitive PH-Responsiveness and Tunable Mechanical Properties: Implications for Controlled Drug Delivery. *Biomacromolecules* **2020**, *21* (6), 2409–2420. <https://doi.org/10.1021/acs.biomac.0c00347>.
- (185) Yang, J.; Deng, L. H.; Han, C. R.; Duan, J. F.; Ma, M. G.; Zhang, X. M.; Xu, F.; Sun, R. C. Synthetic and Viscoelastic Behaviors of Silica Nanoparticle Reinforced Poly(Acrylamide) Core-Shell Nanocomposite Hydrogels. *Soft Matter* **2013**, *9* (4), 1220–1230. <https://doi.org/10.1039/c2sm27233d>.
- (186) He, M.; Shi, L.; Wang, G.; Cheng, Z.; Han, L.; Zhang, X.; Wang, C.; Wang, J.; Zhou, P.; Wang, G. Biocompatible and Biodegradable Chitosan/Sodium Polyacrylate Polyelectrolyte Complex Hydrogels with Smart Responsiveness. *Int. J. Biol. Macromol.* **2020**, *155*, 1245–1251. <https://doi.org/10.1016/j.ijbiomac.2019.11.092>.
- (187) Chen, Y.; Yan, X.; Zhao, J.; Feng, H.; Li, P.; Tong, Z.; Yang, Z.; Li, S.; Yang, J.; Jin, S. Preparation of the Chitosan/Poly(Glutamic Acid)/Alginate Polyelectrolyte Complexing Hydrogel and Study on Its Drug Releasing Property. *Carbohydr. Polym.* **2018**, *191* (February), 8–16. <https://doi.org/10.1016/j.carbpol.2018.02.065>.
- (188) Treenate, P.; Monvisade, P. In Vitro Drug Release Profiles of PH-Sensitive Hydroxyethylacryl Chitosan/Sodium Alginate Hydrogels Using Paracetamol as a Soluble Model Drug. *Int. J. Biol. Macromol.* **2017**, *99*, 71–78.

<https://doi.org/10.1016/j.ijbiomac.2017.02.061>.

- (189) Arno, M. C.; Inam, M.; Weems, A. C.; Li, Z.; Binch, A. L. A.; Platt, C. I.; Richardson, S. M.; Hoyland, J. A.; Dove, A. P.; O'Reilly, R. K. Exploiting the Role of Nanoparticle Shape in Enhancing Hydrogel Adhesive and Mechanical Properties. *Nat. Commun.* **2020**, *11* (1). <https://doi.org/10.1038/s41467-020-15206-y>.
- (190) Zhang, X.; Liu, Y.; Wen, J.; Zhao, Z.; Chen, H.; Liu, X.; Liu, S. Host-Guest Interaction-Mediated Fabrication of a Hybrid Microsphere-Structured Supramolecular Hydrogel Showing High Mechanical Strength. *Soft Matter* **2020**, *16* (14), 3416–3424. <https://doi.org/10.1039/d0sm00271b>.
- (191) Chang, C. W.; Ho, H. O.; Lo, Y. J.; Lee, S. Y.; Yang, Y. R.; Sheu, M. T. Development of Swellable Local Implants of a Polyethyleneimine-Poly(Vinyl Pyrrolidone) (PEI-PVP) Hydrogel as a Socket Filler. *J. Biomater. Sci. Polym. Ed.* **2012**, *23* (17), 2171–2184. <https://doi.org/10.1163/092050611X611684>.
- (192) Satapathy, M. K.; Nyambat, B.; Chiang, C. W.; Chen, C. H.; Wong, P. C.; Ho, P. H.; Jheng, P. R.; Burnouf, T.; Tseng, C. L.; Chuang, E. Y. A Gelatin Hydrogel-Containing Nano-Organic PEI-Ppy with a Photothermal Responsive Effect for Tissue Engineering Applications. *Molecules* **2018**, *23* (6). <https://doi.org/10.3390/molecules23061256>.
- (193) Abraham, B. L.; Toriki, E. S.; Tucker, N. J.; Nilsson, B. L. Electrostatic Interactions Regulate the Release of Small Molecules from Supramolecular Hydrogels. *J. Mater. Chem. B* **2020**, *8* (30), 6366–6377. <https://doi.org/10.1039/D0TB01157F>.
- (194) Koźmiński, P.; Halik, P. K.; Chesori, R.; Gniazdowska, E. Overview of Dual-Acting Drug Methotrexate in Different Neurological Diseases, Autoimmune Pathologies and Cancers. *Int. J. Mol. Sci.* **2020**, *21* (10). <https://doi.org/10.3390/ijms21103483>.
- (195) Abolmaali, S. S.; Tamaddon, A. M.; Dinarvand, R. A Review of Therapeutic Challenges and Achievements of Methotrexate Delivery Systems for Treatment of

- Cancer and Rheumatoid Arthritis. *Cancer Chemother. Pharmacol.* **2013**, *71* (5), 1115–1130. <https://doi.org/10.1007/s00280-012-2062-0>.
- (196) Jia, Y.; Chen, J.; Liu, W.; Yin, D. Construction of Highly Stretchable Silica/Polyacrylamide Nanocomposite Hydrogels through Hydrogen Bond Strategy. *J. Polym. Res.* **2019**, *26* (5), 1–9. <https://doi.org/10.1007/s10965-019-1761-1>.
- (197) Xia, S.; Song, S.; Ren, X.; Gao, G. Highly Tough, Anti-Fatigue and Rapidly Self-Recoverable Hydrogels Reinforced with Core-Shell Inorganic-Organic Hybrid Latex Particles. *Soft Matter* **2017**, *13* (36), 6059–6066. <https://doi.org/10.1039/c7sm01253e>.
- (198) Chen, C. L.; Hsu, S. C.; Ann, D. K.; Yen, Y.; Kung, H. J. Arginine Signaling and Cancer Metabolism. *Cancers (Basel)*. **2021**, *13* (14), 1–29. <https://doi.org/10.3390/cancers13143541>.
- (199) Fares, H. M.; Ghousoub, Y. E.; Delgado, J. D.; Fu, J.; Urban, V. S.; Schlenoff, J. B. Scattering Neutrons along the Polyelectrolyte Complex/Coacervate Continuum. *Macromolecules* **2018**, *51* (13), 4945–4955. <https://doi.org/10.1021/acs.macromol.8b00699>.